N°d'ordre NNT : 2019LYSEI016

THESE de DOCTORAT DE L'UNIVERSITE DE LYON
opérée au sein de
L'Institut National des Sciences Appliquées de Lyon

Ecole Doctorale 160
Électronique, Électrotechnique, Automatique

Spécialité / discipline de doctorat : Traitement du Signal et de l'Image

Soutenue publiquement le 13/03/2019, par :
Boliang Yu

3D analysis of bone ultra structure from phase nano-CT imaging

---

Devant le jury composé de :

LAUGIER Pascal	Directeur de Recherche, CNRS, Univ Paris	Président
ROUSSEAU David	Professeur, Univ Angers	Rapporteur
VAN LENTHE Harry	Professeur, Univ Louvain	Rapporteur
VICO Laurence	Directeur de Recherche, Univ Lyon, St Etienn	Examinateur
LAUGIER Pascal	Directeur de Recherche, CNRS, Univ Paris	Examinateur
GOURRIER Aurelien	Chargé de Recherche, CNRS, Univ Grenoble	Examinateur
CLOETENS Peter	Chercheur, ESRF, Grenoble	Examinateur
PEYRIN Françoise	Directeur de Recherche, Univ Lyon	Directrice de thèse

Département FEDORA – INSA Lyon - Ecoles Doctorales – Quinquennal 2016-2020

SIGLE	ECOLE DOCTORALE	NOM ET COORDONNEES DU RESPONSABLE
CHIMIE	**CHIMIE DE LYON** **http://www.edchimie-lyon.fr** Sec. : Renée EL MELHEM Bât. Blaise PASCAL, 3e étage **secretariat@edchimie-lyon.fr** INSA : R. GOURDON	M. Stéphane DANIELE Institut de recherches sur la catalyse et l'environnement de Lyon IRCELYON-UMR 5256 Équipe CDFA 2 Avenue Albert EINSTEIN 69 626 Villeurbanne CEDEX **directeur@edchimie-lyon.fr**
E.E.A.	**ÉLECTRONIQUE, ÉLECTROTECHNIQUE, AUTOMATIQUE** **http://edeea.ec-lyon.fr** Sec. : M.C. HAVGOUDOUKIAN **ecole-doctorale.eea@ec-lyon.fr**	M. Gérard SCORLETTI École Centrale de Lyon 36 Avenue Guy DE COLLONGUE 69 134 Écully Tél : 04.72.18.60.97 Fax 04.78.43.37.17 **gerard.scorletti@ec-lyon.fr**
E2M2	**ÉVOLUTION, ÉCOSYSTÈME, MICROBIOLOGIE, MODÉLISATION** **http://e2m2.universite-lyon.fr** Sec. : Sylvie ROBERJOT Bât. Atrium, UCB Lyon 1 Tél : 04.72.44.83.62 INSA : H. CHARLES **secretariat.e2m2@univ-lyon1.fr**	M. Philippe NORMAND UMR 5557 Lab. d'Ecologie Microbienne Université Claude Bernard Lyon 1 Bâtiment Mendel 43, boulevard du 11 Novembre 1918 69 622 Villeurbanne CEDEX **philippe.normand@univ-lyon1.fr**
EDISS	**INTERDISCIPLINAIRE SCIENCES-SANTÉ** **http://www.ediss-lyon.fr** Sec. : Sylvie ROBERJOT Bât. Atrium, UCB Lyon 1 Tél : 04.72.44.83.62 INSA : M. LAGARDE **secretariat.ediss@univ-lyon1.fr**	Mme Emmanuelle CANET-SOULAS INSERM U1060, CarMeN lab, Univ. Lyon 1 Bâtiment IMBL 11 Avenue Jean CAPELLE INSA de Lyon 69 621 Villeurbanne Tél : 04.72.68.49.09 Fax : 04.72.68.49.16 **emmanuelle.canet@univ-lyon1.fr**
INFOMATHS	**INFORMATIQUE ET MATHÉMATIQUES** **http://edinfomaths.universite-lyon.fr** Sec. : Renée EL MELHEM Bât. Blaise PASCAL, 3e étage Tél : 04.72.43.80.46 Fax : 04.72.43.16.87 **infomaths@univ-lyon1.fr**	M. Luca ZAMBONI Bât. Braconnier 43 Boulevard du 11 novembre 1918 69 622 Villeurbanne CEDEX Tél : 04.26.23.45.52 **zamboni@maths.univ-lyon1.fr**
Matériaux	**MATÉRIAUX DE LYON** **http://ed34.universite-lyon.fr** Sec. : Marion COMBE Tél : 04.72.43.71.70 Fax : 04.72.43.87.12 Bât. Direction **ed.materiaux@insa-lyon.fr**	M. Jean-Yves BUFFIÈRE INSA de Lyon MATEIS - Bât. Saint-Exupéry 7 Avenue Jean CAPELLE 69 621 Villeurbanne CEDEX Tél : 04.72.43.71.70 Fax : 04.72.43.85.28 **jean-yves.buffiere@insa-lyon.fr**
MEGA	**MÉCANIQUE, ÉNERGÉTIQUE, GÉNIE CIVIL, ACOUSTIQUE** **http://edmega.universite-lyon.fr** Sec. : Marion COMBE Tél : 04.72.43.71.70 Fax : 04.72.43.87.12 Bât. Direction **mega@insa-lyon.fr**	M. Jocelyn BONJOUR INSA de Lyon Laboratoire CETHIL Bâtiment Sadi-Carnot 9, rue de la Physique 69 621 Villeurbanne CEDEX **jocelyn.bonjour@insa-lyon.fr**
ScSo	ScSo* **http://ed483.univ-lyon2.fr** Sec. : Viviane POLSINELLI Brigitte DUBOIS INSA : J.Y. TOUSSAINT Tél : 04.78.69.72.76 **viviane.polsinelli@univ-lyon2.fr**	M. Christian MONTES Université Lyon 2 86 Rue Pasteur 69 365 Lyon CEDEX 07 **christian.montes@univ-lyon2.fr**

*ScSo : Histoire, Géographie, Aménagement, Urbanisme, Archéologie, Science politique, Sociologie, Anthropologie

Acknowledgment

First and foremost, I would like to thank my supervisor, Prof. Francoise Peyrin, for the introduction and guidance in the research work during the past three years of my PhD. I miss our regular and interesting chats in Grenoble, to let me know how to think in a scientific way and overcome the challenges of my tasks all the time. It is a little pity that although I have been to Grenoble more than sixty times, I never explored this beautiful city except the ESRF and train station. Scientific life is always busy.

Then, I am thankful for Prof. David Rousseau and Prof. Harry Van Lenthe to review my PhD manuscript and give valuable advice about the improvement of segmentation and quantification methods. I would like also to thank the other members of my jury Prof. Pascal Laugier, Prof. Laurence Vico, Prof. Aurelien Gourrier and Prof. Peter Cloetens for their insightful comments which incented me to widen research from perspectives.

A very special gratitude goes to Madam Cecile Olivier for the help in life and work during the whole PhD. I will miss the time when we take the lunch so many times in the ESRF. The same gratitude goes to Dr. Loriane Weber for the help of the research work in the beginning time of my PhD, and Dr. Max Langer for the introduction of tomographic reconstruction. I would like to thank Prof. Peter Cloetens again and Dr. Alexandra Pacureanu for the help during sample scanning, the explanation about the phase retrieval method and the advice in the publications.

With a special mention to Dr. Yufei Li, I would like to thank her for the help during my whole PhD, especially in the beginning when I first came to France. We worked in the same office more than three years and talked about many problems in Academy and life. Hope she all the best in future and achieve great success. Similarly, I am especially thankful to Dr. Teng Zhang for sharing the PhD time with me together, which really encouraged me a lot when I got lost in myself. Cheers for the animations we watched in the past three years. I would like also to thank Dr. Yangdi Li and Dr. Xiaoyang Zhu for helping me adapt to new life in a different country three years ago when I just came to France. Besides, I would like to thank Bingqing Xie, Fei Ge, Yuemeng Feng and Pei Niu for the help in life and sometimes the discussion in science. I will always remember the happy time we spent together in drinking, talking and playing board games. Hope they can pass through the doctoral defense successfully.

Finally, last but not the least, I would like to thank my parents for supporting me to pursue my doctor's degree in France. It was the first time that I studied abroad so it was really a challenge for me in the beginning. I experienced and learned a lot during the past 42 months. I am grateful for your understanding, consistent care and support.

Thanks for all your encouragement!

Contents

Abstract

Osteoporosis is a bone fragility disease resulting in abnormalities in bone mass and density. In order to prevent osteoporotic fractures, it is important to have a better understanding of the processes involved in fracture at various scales. Recently, osteocytes, which play an important role in bone remodeling and are considered related to the mechanisms of bone fragility, have attracted an increasing attention. As the most abundant bone cells, osteocytes may act as orchestrators of bone remodeling which regulate the activities of both osteoclasts and osteoblasts. The osteocyte system is deeply embedded inside the bone matrix and also called lacuno-canalicular network (LCN). The network is organized as a complex mesh structure where lacunae serve as nodes housing the osteocytes connected with each other through processes included in the canaliculi.

Although several imaging techniques have recently been proposed, the 3D observation and analysis of the LCN at high spatial resolution is still challenging. In the past, the LCN was mainly investigated by various 2D imaging modalities such as light microscopy (LM), transmission electron microscope (TEM) and scanning electron microscope (SEM). Some 3D imaging techniques such as confocal laser scanning microscopy (CLSM), serial focused ion beam SEM (serial FIB SEM) and Ptychographic X-ray CT have also been used but they still have either a limited spatial resolution or a limited field of view. The 3D visualization of the osteocyte system with a large field of views has recently been achieved using full field synchrotron radiation (SR) CT techniques.

The aim of this work was to investigate and analyze the LCN in human cortical bone in three dimensions with an isotropic spatial resolution using magnified X-ray phase nano-CT.

We performed image acquisition at the beamlines ID16A and ID16B of the European Synchrotron Radiation Facility (ESRF). Both beamlines are long beamlines offering a spatially coherent beam and equipped with a Kirkpatrick-Baez (KB) device permitting nanofocusing. In magnified X-ray phase nano-CT, tomographic datasets are acquired at different focus-to-sample distances (typically 4). ID16A is optimized to reach spatial resolutions of a few tens of nanometers. We scanned 13 samples on this beamline at different voxel sizes of 120 nm, 100 nm, 50 nm and 30 nm. Compared with the case of ID16A, we could scan more samples (27 in total) at ID16B with a voxel size of 100 nm, which will be helpful for the statistical analysis.

Our first study concerned phase retrieval, which is the first step of data processing and consists in solving a non-linear inverse problem. We proposed an extension of Paganin's method suited to multi-distance acquisitions, which has been used to retrieve phase maps in our experiments. The method was compared theoretically and experimentally to the contrast transfer function (CTF) approach for homogeneous object. Our results showed a gain in image quality in terms of the signal-to-noise ratio and spatial resolution when using four distances instead of one. The extended Paganin's method followed by an iterative refinement step provides the best reconstructions while the homogeneous CTF method delivers comparable results for our data

The analysis of the 3D reconstructed images requires first to segment the LCN, including both the segmentation of lacunae and of canaliculi. We had to select suitable methods to cope with the large datasets (32 GB for ID16A and 52.7 GB for ID16B). We developed a workflow based on median filter, hysteresis thresholding and morphology filters to segment lacunae. Concerning the segmentation of canaliculi, we first used vesselness enhancement to improve the visibility of canaliculi based on calculating hessian matrix and eigenvalue decomposition. After this, we used the maximum entropy thresholding to get the initial image which would then be used as the seed map of Variational Region Growing (VRG) method to detect the canaliculi. Finally, we also used the connected components analysis to clear out residual noise.

For the quantitative assessment of the LCN, we calculated morphological descriptors based on an automatic and efficient 3D analysis method developed in our group. For the lacunae, we calculated some parameters like the number of lacunae (Lc.N), the bone volume (BV), the total volume of all lacunae (Lc.TV), lacunar volume density (Lc.TV/BV), the average lacunae volume (Lc.V), the average lacunae surface (Lc.S), the average length, width and depth of lacunae (Lc.L1, Lc.L2, Lc.L3). For the canaliculi, we first computed the total volume of all the canaliculi (Ca.TV) and canalicular volume density (Ca.TV/BV). Moreover, we counted the number of canaliculi at different distances from the surface of each lacuna by an automatic method, which could be used to evaluate the ramification of canaliculi.

We reported the statistical results obtained on the different groups and at different spatial resolutions, providing unique information about the organization of the LCN in human bone in three dimensions.

In conclusion, magnified X-ray phase nano-CT is an efficient technique to analyze cellular networks such as the LCN. In terms of image processing, the main challenge is to extract the canaliculi. It is still necessary to look for an efficient segmentation method which can process large datasets fast, keep the connectivity of canaliculi and filter out noise at the same time. In terms of quantification, further works could be performed to define additional parameters about the network structure. Nevertheless, this work offers a better understanding of bone microstructure which may help learn about bone mechanical and figure out the mechanisms of bone fragility in disease.

Résumé étendu

Introduction

L'ostéoporose est une maladie de la fragilité osseuse associée à une perte de masse osseuse et des anomalies de l'architecture osseuse. Selon les critères diagnostiques publiés par l'Organisation mondiale de la santé (OMS), environ 6% des hommes et 21% des femmes qui ont plus de 50 ans sont touchés. Dans l'Union européenne (UE) en 2010, 22 millions de femmes et 5,5 millions d'hommes souffraient d'ostéoporose, et 3,5 millions de nouveaux cas de fractures de fragilité sont survenus, incluant des fractures du col de la hanche, de la colonne vertébrale, et de l'avant-bras. Toutes les fractures de fragilité ont représenté une charge économique de 37 milliards d'euros à l'UE, et ces montants devraient augmenter de 25% en 2025. Malheureusement, les mécanismes de la fragilité osseuse dans des maladies comme l'ostéoporose ne sont encore que partiellement compris.

L'os est un tissu dynamique et vivant qui va réguler sa densité et sa force avec l'âge et les changements environnementaux. Si la microarchitecture trabéculaire a largement été investiguée dans les deux dernières décennies, depuis quelques années une attention croissante est portée au système ostéocytaire. Celui-ci joue un rôle important dans le remodelage osseux et dans maintien des activités métaboliques quotidiennes telles que le transfert des nutriments et des déchets. Les ostéocytes agissent comme des mécanos capteurs pour la détection de la pression mécanique par une grande surface exposée au fluide interstitiel, qui modifie les propriétés structurelles de l'os pour s'adapter aux stimuli mécaniques. Le système ostéocytaire qui est profondément ancré à l'intérieur de la matrice osseuse réside dans un réseau poreux appelé réseau lacuno-canaliculaire (LCN). Le réseau est organisé sous la forme d'une structure maillée complexe dans laquelle les lacunes servent de nœuds abritent le corps cellulaire des ostéocytes qui sont connectés entre eux par des processus inclus dans les canalicules. A travers ce réseau, de nombreux signaux biochimiques peuvent être transportés entre les différents ostéocytes permettant la communication entre les cellules osseuses. En raison de leur emplacement stratégique et de l'arrangement spatial au sein de la matrice osseuse, le système d'ostéocytes intègre les informations biologiques et environnementales pour orchestrer les activités des ostéoblastes et des ostéoclastes pour le remodelage osseux. Toutefois, il existe encore peu de données quantitatives sur le LCN ainsi que sur les mécanismes de conversion du stimulus en signal à l'intérieur du système ostéocytaire

Malgré le développement des techniques d'imagerie, l'observation et l'analyse 3D du LCN à haute résolution spatiale est encore difficile. Dans le passé, le LCN était principalement étudié par des modalités d'imagerie 2D limitées par la profondeur d'observation et ne permettant pas d'obtenir une image complète du réseau 3D. Certaines techniques d'imagerie 3D, telles que le FIB/SEM ont été proposées mais leur champ de vue limité ne permet d'observer que quelques ostéocytes (ou portions d'ostéocytes). De plus, peu de travaux ont porté sur le développement de méthodes d'analyse d'images (segmentation et quantification) adaptées au LCN, et les résultats obtenus sur échantillons humains sont rares.

L'objectif de cette thèse était de quantifier le LCN dans une série d'échantillons humains à partir d'images 3D acquises en nano CT synchrotron de phase. Ceci nécessitera d'optimiser les processus d'acquisition et de reconstruction de phase, ainsi que de développer des méthodes efficaces de traitement d'images pour segmenter et quantifier le LCN en 3D. Ce travail a été mené dans le cadre du projet ANR MULTIPS visant à une étude des propriétés de l'os cortical humain par tout un panel de méthodes d'investigation (ultrasons, mécanique, biochimique, diffraction)

La thèse est divisée en cinq parties différentes comme suit :

(1) Dans l'introduction, nous présentons brièvement certaines connaissances de base sur l'ostéoporose et le fonctionnement du système ostéocytaire et précisons l'objectif et la structure de la thèse.

(2) Nous présentons 3 chapitres pour décrire le contexte de notre travail. Dans le chapitre 1, nous décrivons la structure hiérarchique de l'os, les fonctions des cellules osseuses et les principales activités dynamiques de l'os de l'embryon à l'âge adulte. Nous soulignons l'importance du LCN qui joue un rôle essentiel dans la régulation du remodelage osseux et faisons une synthèse des techniques d'imagerie 2D et 3D utilisées pour étudier le LCN. Compte tenu de la méthode d'imagerie retenue dans de travail, le chapitre 2 fait un bref bilan des sources de rayonnement synchrotron de troisième génération du monde entier, et décrit plus en détail l'Installation européenne de rayonnement synchrotron (ESRF) et le projet d'upgrade ESRF - Extremely Brilliant Source. Nous décrivons plus particulièrement les deux lignes ID16A et ID16B de l'ESRF où nous avons scanné nos échantillons, ainsi que le principe des méthodes de reconstruction de phase en nano CT de phase. Dans le chapitre 3, nous décrivons avons fait le bilan de l'évaluation quantitative du LCN qui a suscité un intérêt croissant au paramètres utilisés pour quantifier les lacunes et les canalicules et synthétisons les résultats rapportés dans les travaux antérieurs.

(3) Cette partie comprend 4 chapitres qui décrivent nos contributions. Le chapitre 4 concerne notre étude sur les algorithmes de reconstruction de phase. Nous avons généralisé la méthode de Paganin à seule distance à des acquisitions multi-distance et l'avons comparée à la méthode de la fonction de transfert de contraste (CTF) utilisant un a priori d'homogénéité pour la reconstruction de nos échantillons à des résolutions spatiales nanométriques. Dans le chapitre 5, nous décrivons les méthodes de segmentation que nous avons utilisées pour extraire les lacunes et les canalicules des volumes reconstruits, et les paramètres calculés pour l'évaluation du LCN. Nous présentons les résultats obtenus sur le LCN à partir des images scannées sur ID16A à une taille de voxel de 120 nm. Dans le chapitre 6, nous nous sommes intéressés à la quantification du LCN à partir d'images ID16A à des résolutions spatiales plus élevées (tailles de voxel 50 nm et 30 nm). De plus, nous avons comparé les quantifications à 30 nm avec celles des mêmes volumes à 120 nm après une étape de recalage. Le chapitre 7 fournit les paramètres quantifiés sur l'ensemble des échantillons du projet MULTIPS scannés sur la ligne ID16B (taille du voxel 100 nm).

(4) Conclusion et perspectives.

(5) Annexe. Cette partie rassemble les images des différents échantillons en complément du texte.

Chapitre 1: Structures osseuses et techniques d'imagerie

L'os joue un rôle très important dans le corps humain parce qu'il permet à la fois de soutenir le poids, de protéger les organes internes et de stocker des minéraux. Pour maintenir une fonction motrice normale, l'os doit posséder des propriétés naturelles complexes. D'une part, les os doivent être rigides car ils doivent supporter des charges et tolérer la compression. D'autre part, l'os doit être souple et élastique pour changer de forme et absorber l'énergie des déformations. De plus, l'os doit être léger pour faciliter le mouvement. Toutes ces propriétés apparemment contradictoires sont déterminées par la composition de l'os et sa conception structurelle.

Structure osseuse

Les os humains sont divisés en différents types tels que les os longs, les os courts, les os plats et les os irréguliers.

À l'échelle macroscopique, l'os est constitué de deux tissus osseux majeurs (os compact et os spongieux) et de certains autres composants comme le périoste, l'endoste, le cartilage articulaire, la moelle, les vaisseaux sanguins et les nerfs. L'os compact ou cortical, se situe dans les régions proches de l'extérieur de la diaphyse et de l'épiphyse. Il est traversé de canaux perforants qui traversent des lamelles circonférentielles et servent de conduits aux petits vaisseaux sanguins et aux nerfs pour fournir énergie et nutrition. L'os spongieux ou trabéculaire, situé à l'intérieur de l'os, se compose d'un grand nombre de travées osseuses et constitue un réseau poreux complexe. La cavité du réseau, appelée cavité médullaire, est pleine de moelle rouge pour fournir des cellules sanguines.

À l'échelle microscopique, l'unité anatomique de l'os compact est appelée ostéon. Les ostéons sont des structures à peu près cylindriques et situées dans les régions situées entre les lamelles Les canaux Harversiens sont au centre des ostéons et reliés entre eux par les canaux de Volkmann. Des lamelles organisées en cercles concentriques entourent le canal central. Elles sont constituées de fibres de collagène s'étendant en spirale et dans le sens inverse des couches voisines. De nombreuses petites cavités, appelées lacunes, contenant les ostéocytes, se trouvent au bord des lamelles.

A l'échelle nanométrique, de minuscules canaux, appelés canalicules, sont observables. Ils connectent les lacunes adjacentes et forment un réseau complexe, le réseau lacuno-canaliculaire (LCN). Les canalicules servent de conduits de transport pour permettre aux ostéocytes de communiquer entre eux, de recevoir l'apport en nutriments et d'éliminer les déchets par des jonctions de séparation. Par ailleurs, des fibrilles de collagène sont observées en même temps. En tant qu'unité de base du matériau osseux, les fibrilles de collagène sont constituées de molécules de collagène sécrétées par des ostéoblastes de 300 nm de long et 1,5 nm d'épaisseur. Le mode de rotation et de disposition des fibrilles et des lamelles peut améliorer les propriétés isotropes et augmenter la ténacité de l'os.

Cellules osseuses

Dans le tissu osseux, les cellules osseuses jouent un rôle crucial dans l'ajustement des propriétés structurelles osseuses en réponse aux changements environnementaux. Il y a principalement quatre types de cellules osseuses: les ostéoblastes, les ostéocytes, les cellules ostéogéniques et les ostéoclastes.
Les ostéoblastes situés à la surface des zones de croissance de l'os et normalement disposés en couche, sont impliqués dans la formation osseuse. Les ostéoblastes peuvent sécréter des molécules de collagène et une matrice organique pour former une matrice extracellulaire non minéralisée. Pendant ce temps, les ostéoblastes sécrètent également des vésicules matricielles par bourgeonnement de la membrane cellulaire. Après la rupture des vésicules, des cristaux de sel sont libérés dans la matrice osseuse, ce qui

augmente le dépôt des sels osseux et mène finalement à la minéralisation. De plus, les ostéoblastes deviennent des ostéocytes lorsqu'ils sont piégés dans la matrice minéralisée.

Les ostéocytes sont les cellules osseuses les plus abondantes et se trouvent entre les lamelles. L'ostéocyte mature ressemble à un ellipsoïde, dont le corps cellulaire se trouve dans la lacune alors que les processus sont hébergés dans les canalicules. Les ostéocytes parviennent à communiquer leurs activités métaboliques avec les cellules adjacentes par des jonctions d'interstices qui traversent les canalicules. Le liquide interstitiel dans les lacunes et les canalicules peut nourrir les ostéocytes, maintenir l'équilibre calcique et éliminer les déchets.

Les cellules ostéogéniques sont dérivées de cellules souches mésenchymateuses et situées dans les couches profondes du périoste et de la moelle. La fonction principale des cellules ostéogéniques est de pouvoir se différencier et se développer en ostéoblastes sous la stimulation de facteurs tels que les protéines morphogénétiques osseuses, en raison de l'absence d'activité mitotique des ostéoblastes.

Les ostéoclastes qui se situent dans les baies de résorption de la surface sont impliqués dans la résorption osseuse. Contrairement aux ostéoblastes et aux ostéocytes, les ostéoclastes sont dérivés des unités formant les colonies de granulocytes et de macrophages. Les ostéoclastes agissent principalement pour la dissolution et la résorption des os anciens, endommagés ou inutiles.

Formation, croissance et remodelage osseux

L'os commence à se former dans le mésenchyme au cours de l'embryon et continuera à croître après la naissance. L'os arrête sa croissance après l'âge adulte, mais le remodelage osseux dure toute la vie et son taux diminue progressivement avec l'âge.

Il y a deux types de formation osseuse: l'ossification intramembranaire et l'ossification endochondrale. Seulement quelques os sont formés par ossification intramembranaire, comme les os plats du crâne, de la mandibule et de la clavicule. Ce processus commence sous forme de membranes fibreuses à l'état embryonnaire. L'ossification endochondrale est un processus relativement complexe qui remplace le cartilage hyalin par l'os et forme la plupart des os du corps humain. Le processus d'ossification endochondrale dure de l'embryon à l'enfance. Après ossification, le cartilage hyalin à la surface des épiphyses est conservé sous forme de cartilage articulaire, et le cartilage hyalin entre l'épiphyse et la diaphyse sous forme de plaque épiphysaire qui est liée à la croissance osseuse ultérieurement.

La croissance osseuse se compose de deux types différents: la croissance de l'épaisseur et la croissance de la longueur. L'augmentation de l’épaisseur de l'os est due à une croissance par l'apposition périostée avec le dépôt de lamelles. La croissance de la longueur de l'os est basée sur la plaque épiphysaire. Lorsque l'os grandit en longueur, un nouveau cartilage se forme à la surface du cartilage articulaire et sur le côté externe de la plaque épiphysaire. Pendant ce temps, le cartilage ancien du côté interne est remplacé par de l'os et la cavité médullaire est élargie par la résorption des ostéoclastes.

Le remodelage osseux comporte quatre étapes différentes : résorption, réversion, formation et quiescence. La résorption osseuse commence par l'attraction des précurseurs d'ostéoclastes mononucléaires vers la région de remodelage à la surface de l'os. Ensuite, ces précurseurs d'ostéoclastes mononucléaires se différencient et fusionnent pour former des ostéoclastes multi nucléés. Au stade de réversion, les ostéoclastes partent et les cellules ostéogéniques prennent la surface pour se préparer aux régulateurs et se différencier en ostéoblastes. Ensuite, la formation osseuse est réalisée par des ostéoblastes sécrétant de l'ostéoïde qui sera ensuite calcifié, piégeant ainsi les ostéoblastes se transformant en ostéocytes. De cette façon, l’os ancien est résorbé et progressivement remplacé par du nouvel os. Une fois le remplacement terminé, il y a une étape de quiescence lorsque les cellules du revêtement osseux recouvrent la surface et se préparent à un nouveau cycle de remodelage.

La fonction des ostéocytes

Les ostéocytes agissent comme des orchestrateurs du remodelage osseux pour réguler l'activité des ostéoclastes et des ostéoblastes. On suppose actuellement que l'apoptose ostéocytaire pourrait localement fonctionner comme un signal de recrutement des ostéoclastes, ce qui augmenterait la résorption osseuse. Les ostéocytes pourraient donc être utiles pour un remodelage osseux ciblé, et de plus, pourraient libérer des facteurs qui ont des effets directs sur l'activité des ostéoblastes.

Le système ostéocytaire est profondément enfoui à l'intérieur de la matrice osseuse et contenu dans le réseau lacuno-canaliculaire (LCN). Par les jonctions interstitielles, les processus cytoplasmiques des ostéocytes se relient à ceux des ostéocytes voisins, et des ostéoblastes proches de la surface osseuse. Le LCN permet la communication entre de nombreux signaux biochimiques pour réaliser l'intégration de l'information et stimuler l'interaction.

Imagerie des ostéocytes

Le LCN a été principalement étudié par des techniques d'imagerie 2D mais leur imagerie 3D a suscité des travaux récents.

Imagerie 2D. La microscopie optique (LM) a été utilisée pour investiguer LCN pendant de nombreuses années. La microscopie optique n'endommage pas les échantillons pendant le balayage mais sa résolution est limitée à environ 200 nm par la limite de diffraction de la lumière visible. La microscopie électronique à transmission (TEM) a un principe similaire à celui de la microscopie optique. Il détecte les électrons qui traversent l'objet et les informations reflétant la structure et les propriétés du spécimen sont enregistrées par une caméra. Le microscope électronique à balayage (SEM) utilise un faisceau d'électrons focalisé pour balayer l'échantillon selon un motif matriciel, qui est différent du TEM. La microscopie à force atomique (AFM) scanne la surface de l'échantillon par un cantilever avec une sonde pointue à son extrémité qui peut percevoir et amplifier les forces entre atomes. Mais ces techniques ne permettent pas d'obtenir une image complète du LCN et sont parfois limitées par la profondeur d'observation.

Imagerie 3D. La microscopie confocale à balayage laser (CLSM) utilise une source lumineuse ponctuelle pour éclairer l'échantillon. La fluorescence réfléchie est captée par les lentilles de l'objet et envoyée à la photo détectrice. En enregistrant une série de tranches 2D, une image 3D peut être créée. Le SEM à rayon ionique focalisé en série (FIB SEM) utilise un faisceau d'ions focalisé au lieu d'un faisceau d'électrons focalisé dans le SEM classique. Après avoir scanné la surface, le faisceau d'ions focalisé est utilisé pour fraiser l'échantillon. De même, une séquence d'images peut être produite à travers l'échantillon. La Ptychographie par rayons X est une technique d'imagerie sans lentilles qui permet de reconstruire la fonction de transmission de l'objet en enregistrant une série de diagrammes de diffraction en champ lointain. Si elle permet d’atteindre des résolutions spatiales très élevées cette technique est lourde en termes de temps d’acquisition et de traitement, et souvent limitée à champs de vue faibles. La nano-CT par rayonnement synchrotron (SR) présente un certain nombre d’avantages. Grâce au haut degré de cohérence et de brillance du faisceau synchrotron, cette technique permet d'obtenir une image de l'échantillon avec un bon contraste et un fort rapport signal sur bruit en des temps relativement courts de balayage. Dans les travaux antérieurs du groupe, il a été prouvé que cette technique permettait d'imager les structures 3D du LCN avec un champ de vision relativement large permettant de réaliser des analyses statistiques. C’est cette technique qui sera utilisée dans la suite de ce travail.

Chapitre 2: Sources de rayonnement synchrotron et l'imagerie tomographique par rayons X

Le rayonnement synchrotron (SR) est généré lorsque des particules chargées accélérées à la vitesse de la lumière maintenues sur une trajectoire circulaire sous l'action de champs magnétiques. Jusqu'à présent, il y a eu trois générations de sources synchrotron. Les sources de rayonnement synchrotron de première génération étaient parasitaires parce que les dispositifs expérimentaux étaient développés pour la physique des hautes énergies ou la physique nucléaire. Les conditions expérimentales requises par la physique des hautes énergies, comme les courants ou les énergies de faible intensité, limitaient souvent les possibilités de rayonnement synchrotron. Par conséquent, des installations de rayonnement synchrotron spécialisées ont été conçues et ont produit les sources de rayonnement synchrotron de deuxième génération. Au fur et à mesure que les expériences avec le rayonnement synchrotron se multiplient, les chercheurs se sont progressivement rendu compte de l'importance d'une brillance accrue. Celle-ci est obtenue grâce à des dispositifs d'insertion tels que des wigglers et des ondulateurs. La première installation de rayonnement synchrotron de troisième génération utilisant des dispositifs d'insertion a été l'Installation européenne de rayonnement synchrotron (ESRF) à Grenoble. Suite à l'ESRF, de plus en plus d'installations de troisième génération ont été construites dans le monde entier ou sont en cours de construction.

Sources de rayonnement synchrotron de troisième génération

Les sources de rayonnement synchrotron de troisième génération ont des applications dans un grand nombre de domaines de domaines tels que la biologie, la médecine, la physique, la science des matériaux et leurs applications industrielles. Avec une brillance supérieure par rapport aux sources de première et deuxième génération, l'information spatiale peut être obtenue avec une résolution plus haute et un temps d'acquisition plus court. Nous passons brièvement en revue les sources de troisième génération qui sont classifiées en deux types différents en fonction de l'énergie du faisceau d'électrons dans l'anneau de stockage.

Les sources à grande échelle ont des circonférences grandes (> 800 m), des énergies électroniques hautes (> 5 GeV) et un nombre comparable de lignes de faisceaux. Ces installations se spécialisent dans la gamme des rayons X de courte longueur d'onde. Par exemple, il y a trois sources à grande échelle: l'Advanced Photon Source (APS) située au Laboratoire National d'Argonne, Illinois, USA; SPring-8 située à Harima Science Park City, Hyogo, Japon; PETRA III, située à DESY à Hambourg, Allemagne.

Les sources à échelle intermédiaire ont des circonférences plus petites (100~700 m), des énergies électroniques plus faibles (~ 3 GeV) et relativement peu de lignes de faisceaux. Ces installations utilisent principalement des rayons ultraviolets et des rayons X de grande longueur d'onde. Nous décrivons ici 4 exemples: SOLEIL (Source Optimisée de Lumière d'énergie intermédiaire du LURE) située à Saint-Aubin, Paris; Diamond, la source nationale de l'Angleterre, située sur le Harwell Science and Innovation Campus, Oxfordshire; NSLS-II (Source nationale de rayonnement synchrotron) du Brookhaven National Laboratory (BNL), situé à Upton, New York, USA; MAX IV, le centre national suédois de rayonnement synchrotron situé à Lund.

ESRF

Toutes les expériences de cette thèse ont été réalisées à l'ESRF, première installation de rayonnement synchrotron de troisième génération. Nous donnons des informations plus détaillées sur l'ESRF et les lignes de faisceaux qui ont été utilisées dans ce travail.

En 1988, l'ESRF avec un anneau de stockage d'électrons de 6 GeV et 844 m a commencé à être construit à Grenoble, en France, avec l'investissement de 12 pays européens. À l'heure actuelle,le consortium inclut 22 pays partenaires. Grâce à la brillance et à la qualité de ses rayons X, il est possible d'observer des matériaux et des matières vivantes à haute résolution dans les domaines de la chimie, des matériaux, de la physique, de la biologie structurale et des applications médicales, des sciences environnementales et de l'information.

Les faisceaux de rayons X émis par les électrons sont canalisés dans les lignes de lumière tangentes à l'orbite. Une ligne de lumière est composée de trois parties: la cabine optique, qui contient des dispositifs optiques (fentes, filtres, monochromateurs et miroirs) pour donner au faisceau les caractéristiques visées; la cabine expérimentale, où les échantillons sont placés et les détecteurs enregistrent les images; la cabine de contrôle, où les utilisateurs contrôlent les expériences. Actuellement, l'ESRF dispose de 43 lignes de lumière équipées d'instruments dédiés.

Le projet d'upgrade ESRF-Extremely Brilliant Source (ESRF-EBS) a été lancé en 2015 afin de consolider le rôle de pionnier de la science synchrotron et de préparer le développement d'une nouvelle génération de sources. Deux des tâches les plus importantes du projet sont la rénovation de l'anneau de stockage afin de produire des faisceaux de rayons X plus intenses, cohérents et stables et l'installation de nouvelles lignes de faisceaux ultramodernes. La réalisation débutera en Décembre 2018 et devrait être terminée en 2020.

NINA faisceaux

Le projet NINA (Nano-imagerie et nano-analyse) du programme UPBL4 de l'ESRF a permis de développer deux nouvelles lignes de faisceaux, ID16A et ID16B utilisant des faisceaux de rayons X nano-focalisés. Toutes nos données expérimentales ont été acquises sur ces deux lignes de faisceaux à des tailles de voxel nanométriques différentes pendant les deux premières années de mon doctorat.

Ligne ID16A

La ligne ID16A combine des techniques d'imagerie par rayons X à la résolution spatiale ultime. Cette ligne d'une longueur de 185 m est actuellement la plus longue de l'ESRF. Elle fonctionne à deux énergies spécifiques, 17,05 keV et 33,6 keV, avec un flux allant de 6×10^9 à 4×10^{12} photons par seconde.

ID16A a obtenu une taille de tache focale de rayons X limitée par diffraction inférieure à 13 nm avec 6×10^9 photons par seconde à l'énergie de 33,6 keV en utilisant des miroirs multicouches de Kirkpatrick-Baez (KB), qui est le record à cette énergie dans le monde. Le système optique de focalisation KB peut être divisé en deux parties indépendantes qui sont perpendiculaires l'une à l'autre. La première partie est responsable de la mise au point dans le sens vertical et la seconde dans le sens horizontal. Après traitement par des miroirs KB, le faisceau de rayons X parallèle entrant est focalisé sur un point focal dont la taille limite la résolution de l'image. Il existe deux configurations de miroirs KB indépendants qui peuvent être réglés en fonction de l'énergie spécifique de chaque expérimentation, 17,05 keV ou 33,6 keV.

Pendant le scan, l'échantillon est placé dans un support sous vide. L'échantillon est placé et retiré par des pinces qui sont contrôlées avec précision par un système électronique. Après avoir traversé l'échantillon, le faisceau de rayons X est converti en lumière visible par le scintillateur et est enregistré par les détecteurs qui ont différents types à sélectionner en fonction des techniques d'imagerie par rayons X appliquées. Par exemple, une caméra FReLoN (Fast Readout Low Noise) couplée à l'objectif, développée à l'ESRF avec un capteur CCD de 2048×2048 pixels, a été utilisée pour la nano-CT aux rayons X.

Il y a principalement trois techniques d'imagerie à l'ID16A : la fluorescence par rayons X (XRF), l'imagerie en phase par rayons X et la ptychographie par rayons X. XRF est une microscopie à balayage détectant l'émission secondaire des rayons X de l'échantillon qui a été bombardé par des rayons de haute énergie, pour analyser la composition élémentaire dans la zone focale du faisceau source. La taille nanométrique du spot à l'ID16A peut produire une image de fluorescence à très haute résolution. L'imagerie en phase par rayons X, qui se combine à la tomographie conduisant à la nano CT de phase, utilise des images de phase pour réaliser la reconstruction tomographique à la place d’images d'absorption come en CT X classique. L'acquisition d'images consiste à enregistrer plusieurs scans tomographiques pour différentes positions de l'échantillon entre la focale et le détecteur. La ptychographie par rayons X à l'ID16A permet d’acquérir des images à très haute résolution spatiale. Son avantage est qu'elle permet non seulement de retrouver l'indice de réfraction complexe de l'échantillon, mais aussi l'éclairage. Cela peut réduire l'impact des artefacts sur les images reconstruites en raison de l'inhomogénéité du faisceau de rayons X incident.

Ligne ID16B

La ligne faisceau ID16B offre une approche multimodale (spectroscopie - diffraction - imagerie) pour l'analyse 2D ou 3D d'échantillons hétérogènes à l'échelle nanométrique. Comparé à ID16A, ID16B a une longueur relativement plus courte de 165 m et peut fournir des nano faisceaux monochromatiques accordables sur une plus large gamme énergétique (5-70 keV) et est un complément à l'ID16A.

Le système KB d'ID16B utilise des optiques à revêtement multicouches en combinaison avec des miroirs courbés dynamiquement pour donner l'énergie spécifiée sur une plage variable en continu. Le faisceau ID16B a été conçu à partir des mêmes concepts que la ligne précédente ID22. Le faisceau de rayons X incident produit par un onduleur sous vide U26 entièrement accordable passe d'abord par un miroir à double faisceau blanc et un monochromateur à double cristal situé à environ 30~35 m de l'onduleur, qui sont principalement utilisés pour maintenir la cohérence et la stabilité élevées du faisceau. Les miroirs KB sont placés très près de l'échantillon pour maintenir une forte démagnétisation.

Différentes techniques d'imagerie sont mises en œuvre à l'ID16B telles que XRF, la spectroscopie d'absorption par rayons X (XAS), la diffraction par rayons X (XRD), la luminescence optique excitée par rayons X (XEOL) et le nano-CT par rayons X. Le XRF a été utilisé pour diverses applications, par exemple pour détecter des fragments de météorite, analyser la composition des cellules solaires et étudier les nanoparticules d'argent. XAS est une sous-classe de spectroscopie d'absorption qui peut coopérer avec XRF pour la détermination d'un élément chimique dans l'échantillon et la structure géométrique locale des matériaux. XRD est une technique de diffusion qui se base sur l'interférence d'ondes diffusées lorsque le faisceau de rayons X incident interagit avec des matériaux à structure régulière. XEOL est un type de technique d'entrée et de sortie de photons qui se produit lorsque les électrons énergétiques sont ionisés et excités après absorption des photons de rayons X. Par ailleurs, ID16B permet de réaliser de la nano-CT de phase en appliquant le même principe qu’ID16A. Dans ce cas, l'environnement expérimental n'est pas dans le vide, et la taille du voxel est supérieure à celle d’ID16A.

L’imagerie tomographique par rayons X

Dans ce travail, nous avons utilisé le nano-CT en phase par rayons X à la fois sur les faisceaux de l'ESRF ID16A et ID16B. Nous introduisons ensuite les bases de la reconstruction de phase et plus de détails seront donnés dans le prochain chapitre.

La modulation de phase présente dans les images d'intensité enregistrée n'est pas directement accessible car ces images contiennent un contraste de phase et d'amplitude induit par l'échantillon. Ainsi, pour reconstruire l'information de phase, il faut d'abord récupérer les informations de phase des images d'intensité enregistrées à différentes distances de propagation pour chaque angle spécifique des projections. Ce processus est également appelé la reconstruction de phase.

La reconstruction de phase est un problème inverse non-linéaire qui a été résolu par diverses approches. La majorité des approches résolvent une version linéarisée du problème. Un article a fait la synthèse de sept méthodes et les a regroupées dans un cadre général. Bien que les méthodes reposent sur des approximations et des hypothèses différentes, ils suivent le même modèle et peuvent être mis en œuvre numériquement en utilisant des méthodes similaires.

Nous considérons deux approches importantes pour résoudre ce problème. La première est la méthode l'équation de transport d'intensité (TIE) qui linéarise l'intensité par un développement en série de Taylor du propagateur au premier ordre par rapport à la distance de propagation. La dérivée partielle résultante dans la direction de propagation est alors approchée par une différence finie, qui n'est valable que pour de faibles distances de propagation et de faibles fréquences spatiales. L'autre méthode est la fonction de transfert de contraste (CTF) qui linéarise l'intensité en étendant la fonction de transmission au premier ordre en ce qui concerne l'amplitude et la phase. Il en résulte une relation linéaire valable pour une absorption faible et une variation lente de la phase. Un algorithme pratique a été dérivé du modèle TIE par Paganin en ajoutant une hypothèse sur l'homogénéité de l'objet. La méthode CTF peut bénéficier de l'utilisation de plusieurs distances pour réduire l'impact des passages à zéro. Plus de détails sur ces méthodes seront donnés dans le Chapitre 5.

Après avoir été calculées, les images de phase extraites des images d'intensité détectées sont utilisées comme entrée pour la reconstruction tomographique. A l'ESRF, ce processus peut être réalisé sur la base de l'algorithme standard de rétroprojection filtrée (FBP) par le logiciel PyHST (Python High Speed Tomography).

En conclusion, toutes les images utilisées dans cette thèse ont été enregistrées sur les lignes ID16A et ID16B de l'ESRF. Nous avons utilisé le nano-CT de phase pour scanner nos échantillons. Nous espérons ainsi observer et quantifier le LCN à des résolutions spatiales relativement hautes et avec de large champ de vue.

Chapitre 3: Bilan des paramètres du réseau lacuno-canaliculaire

Afin de mieux comprendre la fonction du LCN pendant le remodelage osseux, il est important d'obtenir des informations quantitatives sur les propriétés géométriques et structurelles de ce réseau complexe. Dans ce chapitre, nous passons en revue un certain nombre d'études qui ont permis de mesurer les paramètres morphologiques et topologiques du LCN à partir d’images 2D ou 3D. Selon la méthode d'imagerie, soit on voit directement les ostéocytes, comme en imagerie optique, soit on voit les lacunes, comme en imagerie radiographique. Dans ce dernier cas, les propriétés des ostéocytes seront quantifiées indirectement par les propriétés des lacunes.

Densité et porosité des lacunes

La densité de lacunes ou d'ostéocytes a été mesurée de différentes manières et sur différentes espèces. Pour les images 2D, la densité est définie comme le nombre total de lacunes (ostéocytes) divisé par la surface osseuse (Lc.N/BA ou Ot.N/BA) en excluant les zones des canaux de Havers ou de Volkmann ou par la surface du tissu (Lc.N/TA ou Ot.N/TA). En 3D, la densité est calculée en utilisant le nombre total de lacunes (ostéocytes) divisé par le volume osseux (Lc.N/BV ou Ot.N/BV) ou le volume tissulaire (Lc.N/TV ou Ot.N/TV). Dans la littérature, la densité lacunaire chez l'homme est d'environ 200–700 mm^{-2} en 2D et 10,000–35,000 mm^{-3} en 3D, ce qui est inférieur à la densité lacunaire chez les animaux tels que lapins, moutons, rats et souris, environ 700–1200 mm^{-2} et 40,000–80,000 mm^{-3}.

Comme la densité, la porosité lacunaire peut avoir des expressions différentes. En 2D, la porosité est généralement calculée par la surface totale des lacunes divisée par la surface osseuse (Lc.TA/BA) alors qu'en 3D elle est définie comme le volume total des lacunes divisé par le volume osseux ou le volume du tissu (Lc.TV/BV ou Lc.TV/TV). Une étude récente a rapporté que la porosité 2D des lacunaires est d'environ 3.2% chez les jeunes femmes (20–23 ans) et 2.5% chez les femmes âgées (70–86 ans). En 3D, la porosité lacunaire semble être plus faible chez l'humain (0.84 % ou 0.68 %) et entre 1 et 2 % chez le rat et la souris.

Paramètres morphologiques des lacunes

Il y a peu de paramètres morphologiques qui peuvent être calculés à partir d'images 2D mais ils sont limités par les techniques d'imagerie. En général, trois paramètres sont considérés: la surface lacunaire moyenne (Lc.A), la longueur lacunaire moyenne (Lc.L1) et la largeur (Lc.L2). De plus, certains paramètres sont proposés pour évaluer l'espace péricellulaire entre le corps des cellules ostéocytaires et la paroi lacunaire, tels que la surface moyenne du de l’espace péricellulaire (Lc.PA) et son épaisseur (Lc.PT). La surface lacunaire moyenne pour l'homme est d'environ 20–70 μm^2, la longueur moyenne environ 14–25 μm et la largeur moyenne environ 10 μm. De plus, la surface moyenne de l’espace péricellulaire lacunaire est d'environ 7 μm^2 et son épaisseur 0.45 μm. Toutefois, nous notons que ces paramètres sont des paramètres apparents puisque leurs valeurs dépendent de la direction de coupe.

Comparé au 2D, les images 3D peuvent fournir des paramètres non biaisés: le volume lacunaire moyen (Lc.V), la surface lacunaire moyenne (Lc.S), la longueur lacunaire moyenne (Lc.L1), la largeur (Lc.L2) et la profondeur (Lc.L3) ainsi que l'orientation lacunaire moyenne. La longueur, la largeur et la profondeur peuvent être définies comme l'axe long, l'axe moyen et l'axe court de l'ellipsoïde qui correspond à la lacune. Carter a obtenu ces paramètres en utilisant les valeurs propres de la matrice de covariance calculées grâce au logiciel AMIRA (Lc.λ1 > Lc.λ2 > Lc.λ3). Dong a utilisé une méthode interne basée sur le calcul de la matrice des moments du second ordre. Carter a également introduit d'autres paramètres dérivés de ces trois valeurs propres pour décrire la forme des lacunes qui sont exprimés comme suit:

$$Lc.St = \frac{\lambda_1-\lambda_3}{\lambda_1}, Lc.Ob = 2 * \frac{\lambda_2-\lambda_3}{\lambda_1-\lambda_3} - 1$$
$$Lc.Eq = \frac{\lambda_3}{\lambda_1}, Lc.El = 1 - \frac{\lambda_2}{\lambda_1}, Lc.Fl = 1 - \frac{\lambda_3}{\lambda_2}.$$

Il faut noter que ces paramètres utilisent directement les valeurs propres et sont donc proportionnels aux longueurs au carré des dimensions des lacunes.

Pour l'orientation lacunaire, il existe plusieurs méthodes de calcul. Cette orientation peut être définie par le calcul de l'angle entre l'axe long de la lacune et l'axe longitudinal de l'os (Lc.θ). Carter a mesuré l'orientation comme l'angle entre l'axe long de la lacune et l'axe horizontal de l'échantillon (Lc.Φ). Repp a proposé deux angles pour décrire l'orientation: l'angle polaire et l'angle azimutal. Deux systèmes de coordonnées peuvent être utilisés pour calculer ces angles: le système de coordonnées de Haversian qui définit un axe central au milieu du canal et ensuite la direction radiale comme la direction la plus courte vers cet axe; le système de coordonnées lamellaire qui définit la direction radiale perpendiculaire à la lamelle osseuse et ensuite une autre direction perpendiculaire à la direction radiale et parallèle au canal de Haversian.

D'après la littérature, le volume moyen des lacunes chez l'homme varie de 50 μm^3 à 730 μm^3 et la surface moyenne de 90 μm^2 à 430 μm^2. La longueur, la largeur et la profondeur moyennes des lacunes chez l'homme sont d'environ 15 µm, 12 µm et 6 µm, ce qui est plus grand que chez le rat, environ 12 µm, 8 µm et 3 µm. Pour l'orientation lacunaire, l'angle entre l'axe long de la lacune et l'axe longitudinal de l'os varie entre 7° et 30° alors que l'angle par rapport à l'axe horizontal de l'échantillon est de 55° environ.

Densité et porosité des canalicules

Dans les travaux basés sur l'imagerie 2D, la densité des canalicules a été définie comme le nombre de canalicules par 10 µm de longueur (Ca.N/10 µm) variant entre 2.9–3.7 (#/10 µm), ou le nombre de canalicules par unité de surface (Ca.N/μm^2) qui est environ 0.85 μm^{-2} pour les bovins. Dans le cas de l'imagerie 3D, la densité peut être calculée par le nombre total de canalicules divisé par la surface lacunaire (Ca.N/Lc.S). On a constaté que la valeur était d'environ 0.20 µm/μm^3 pour les souris, soit la longueur totale des canalicules par unité de volume (Ca.TL/μm^3), environ 0.076 µm/μm^3 pour les humains.

Comme pour la définition de la porosité des lacunes, la porosité des canalicules peut être exprimée comme la surface totale des canalicules divisée par la surface osseuse (Ca.TA/BA) en 2D. En 3D, on peut l'évaluer comme le volume total des canalicules divisé par le volume osseux (Ca.TV/BV). Il existe peu de travaux sur les valeurs de porosité canaliculaire..

Paramètres morphologiques des canalicules

Dans des études récentes 2D, certains paramètres morphologiques des canalicules ont été rapportés, tels que le diamètre canaliculaire moyen (Ca.D), la surface canaliculaire moyenne (Ca.A) et le nombre moyen de canalicules par lacune (Ca.N). De plus, avec l'imagerie à nano résolution, d'autres paramètres à l'intérieur de chaque canalicule peuvent être mesurés comme la surface péricellulaire moyenne (Ca.PA) et l'épaisseur péricellulaire moyenne (Ca.PT). D'après les résultats précédents, on peut voir que le diamètre canalaire moyen est d'environ 259 nm pour les souris et 443 nm pour les bovins, et que le nombre moyen de canaux par lacune en 2D est d'environ 16 pour les humains et 32 pour les ovins. Chez la souris, la surface canaliculaire moyenne est d'environ 0.074 μm^2 et la surface péricellulaire moyenne est d'environ 0.059 μm^2. De plus, l'épaisseur péricellulaire moyenne varie entre 78–101 µm selon les rapports.

Il y a peu de paramètres 3D de canalicules car l'émergence des images 3D du LCN est relativement nouvelle et provient principalement de CSLM ou de la nano CT. Le diamètre canaliculaire moyen est d'environ 370 nm et le nombre moyen de canaux par lacune est d'environ 88.5 chez l'humain, contre 286.6 nm et 86.8 chez le rat, respectivement. De plus, le volume canaliculaire est d'environ 144.3 μm^3 et la surface canaliculaire de 1350.6 μm^2 pour l'homme, 123 μm^3 et 461 μm^2 pour le poulet ainsi que 688 μm^3 et 1587 μm^2 pour la souris.

Caractérisation du LCN

Si on considère les lacunes et les canalicules comme un réseau entier, la porosité du LCN est définie comme la surface totale du LCN divisée par la surface osseuse excluant la surface du canal de Haversian et vasculaire (LCN.TA/BA) en 2D, et le volume total du LCN divisé par le volume du tissu (LCN.TV/TV) en 3D. D'après les résultats limités du rapport, la porosité 2D du LCN varie de 10.5 % à 17.6 % chez l'humain selon l'âge. Par ailleurs, la porosité 3D du LCN varie beaucoup pour différentes espèces d'animaux, comme 5% pour les moutons, 16% pour les souris et environ 2.88% pour les rats.

En conclusion, nous avons brièvement passé en revue l'état de l'art de l'évaluation quantitative du LCN. La caractérisation des lacunes au niveau de la porosité, de la densité et de la morphologie a fait l’objet de plusieurs études mais moins de recherches ont été effectuées sur la quantification des canalicules en utilisant des techniques d'imagerie 3D. Par conséquent, il est toujours d’actualité et crucial d'obtenir des images 3D du LCN à haute résolution et de mesurer des paramètres quantitatifs pour décrire les propriétés structurelles du LCN.

Chapitre 4: Évaluation des approches de reconstruction de phase pour la nano CT X du tissu osseux

L'imagerie de l'organisation tridimensionnelle de la micro architecture osseuse a été une application pionnière en micro-CT. En couplant cette technique au rayonnement synchrotron (SR) permet d'utiliser des sources monochromatiques à haut flux, conduisant à des images de meilleure qualité, à haut signal sur bruit et sans artefacts de durcissement de faisceau. Au cours des deux dernières décennies, un certain nombre de sources SR de troisième génération ont été développées et la plupart d'entre elles implémenté des systèmes de micro-CT synchrotron.

Un autre avantage de la micro-CT synchrotron est la possibilité de mettre en œuvre l'imagerie en phase par rayons X avec un haut degré de cohérence spatiale. Cette technique est plus sensible, de trois ordres de grandeur, que l'imagerie basée sur l'atténuation, et permet l'imagerie d'échantillons faiblement absorbants tels que les tissus mous ou de matériaux présentant de faibles variations d'atténuation. La micro-CT de phase est depuis peu utilisée dans les domaines biomédical pour l'imagerie du petit animal ou d'échantillons biologiques jusqu'à à l'échelle micrométrique.

Le contraste de phase peut être obtenu expérimentalement par diverses techniques, soit sur des sources synchrotron, soit en laboratoire. Ici, nous nous concentrerons sur l'imagerie par contraste de phase basée sur la propagation, car il fournit la résolution spatiale la plus haute possible. Cette technique peut être utilisée avec une ou plusieurs distances de propagation. La reconstruction de la phase peut être exprimée comme la résolution d'un problème inverse non linéaire. Le problème direct correspondant peut être modélisé par l'optique de Fourier et la diffraction de Fresnel. Dans nos conditions, l'intensité enregistrée par le détecteur peut être exprimée sous la forme du carré de la transformée de Fresnel de la fonction de transmittance de l'objet.

Bien que non linéaire, ce problème est le plus souvent inversé après une linéarisation qui peut être réalisée par diverses approches. La première est l'équation de transport d'intensité (TIE) qui linéarise l'intensité par le développement en série de Taylor au premier ordre du propagateur par rapport à la distance de propagation. La dérivée partielle résultante dans la direction de propagation est alors approchée par une différence finie. L'autre est la fonction de transfert de contraste (CTF) qui linéarise l'intensité en développant la fonction de transmission au premier ordre par rapport à l'amplitude et la phase. Il en résulte une relation linéaire valable pour une absorption faible et une variation lente de la phase. Une méthode mixte qui étend la validité à la fois aux longues distances et aux objets fortement absorbants (mais variant lentement) a été proposée avec la combinaison de CTF et TIE. Les différents algorithmes ont été quantitativement comparés dans des travaux antérieurs sur des fantômes numériques et expérimentaux.

En ajoutant une hypothèse sur l'homogénéité de l'objet dans le modèle TIE, la méthode de Paganin a été dérivée. Cette méthode s'est avérée populaire car elle est simple à implémenter et ne nécessite l'acquisition que d'une seule image de contraste de phase. Elle est essentiellement basée sur un filtre passe-bas qui peut être appliqué directement sur l'image de projection enregistrée. Toutefois, cette méthode nécessite de définir le rapport δ_n/β du matériau de l'image, qui est le rapport entre la partie réelle et imaginaire de l'indice de réfraction de l'objet, une constante dépendant du matériau et de l'énergie. Pour une composition chimique donnée, ce rapport peut être calculé à partir de valeurs tabulées.

L'objectif de ce chapitre était d'évaluer quantitativement différentes méthodes de reconstruction de phase, à partir d'une ou plusieurs distances de propagation, pour l'imagerie du tissu osseux par nano CT de phase à l'échelle cellulaire.

Acquisition des images

L'acquisition d'images de nano-CT de phase a été réalisée sur la ligne de lumière ID16A à l'ESRF. Elle consiste à enregistrer des ensembles de projections angulaires à différentes positions de l'échantillon entre le focus et le détecteur. Après la focalisation, le faisceau passe du parallèle au divergent, de sorte que les images enregistrées à différentes distances contiennent non seulement du contraste de phase mais aussi des grossissements géométriques. En pratique, la position du détecteur est fixe lorsque l'échantillon est déplacé en aval de la focalisation.

Des échantillons d'os cortical ont été extraits de coupes transversales coupées à partir de la diaphyse moyenne dans les fémurs de cadavres de femmes (50–95 ans). Ensuite, de petits échantillons d'os cortical (0.4×0.4×3 mm^3) ont été préparés à l'aide d'une scie circulaire basse vitesse de haute précision. Chaque échantillon a été positionné dans le support sous vide et tourné autour d'un axe de rotation vertical. Au total, 2000 projections ont été acquises sur un angle de vue de 180° à 4 distances différentes entre l'échantillon et le détecteur. Les tailles de voxel ont été fixées à 120 nm et 30 nm, ce qui correspond à un champ de vision de 245 µm et 61 µm. Le temps d'acquisition d'un ensemble de données complet (avec 4 distances de propagation) était d'environ 4 heures.

Reconstruction de phase

Nous proposons d'étudier d'une part l'intérêt d'utiliser plusieurs distances de propagation au lieu d'une en termes de qualité des images reconstruites, et d'autre part d'évaluer les algorithmes d'extraction de phase pour ce type d'échantillons relativement denses.

Dans un premier temps, nous étendons la méthode de Paganin à des acquisitions à plusieurs distances. Ensuite, à des fins de comparabilité, nous écrivons la méthode CTF multi-distance pour des objets homogènes. De plus, nous examinons les relations entre ces deux méthodes par une analyse dans le domaine de Fourier. Les formules de ces méthodes multi-distance sont présentées ci-dessous:

$$\text{CTF: } \hat{\hat{\varphi}}(\mathbf{f}) = \frac{1}{2}\cdot\frac{\delta_n}{\beta}\cdot\frac{\frac{1}{K}\sum_{k=1}^{K}\left[\cos(\pi\lambda D_k\|\mathbf{f}\|^2)+\frac{\delta_n}{\beta}\sin(\pi\lambda D_k\|\mathbf{f}\|^2)\right]\cdot\left(\tilde{I}_{D_k}(\mathbf{f})-\delta_{Dirac}(\mathbf{f})\right)}{\frac{1}{K}\sum_{k=1}^{K}\left[\cos(\pi\lambda D_k\|\mathbf{f}\|^2)+\frac{\delta_n}{\beta}\sin(\pi\lambda D_k\|\mathbf{f}\|^2)\right]^2+\alpha},$$

$$\text{Paganin: } \hat{\hat{\varphi}}(\mathbf{f}) = \frac{1}{2}\cdot\frac{\delta_n}{\beta}\cdot\frac{\frac{1}{K}\sum_{k=1}^{K}\left(1+\lambda D_k\pi\frac{\delta_n}{\beta}\|\mathbf{f}\|^2\right)\cdot\left(\tilde{I}_{norm,k}(\mathbf{f})-\delta_{Dirac}(\mathbf{f})\right)}{\frac{1}{K}\sum_{k=1}^{K}\left(1+\lambda D_k\pi\frac{\delta_n}{\beta}\|\mathbf{f}\|^2\right)^2+\alpha}.$$

Pour améliorer la qualité de l'image, la solution obtenue avec l'une de ces méthodes est ensuite raffinée itérativement par une méthode de gradient conjugué non linéaire (NLCG) basée sur le modèle de formation d'image non linéaire directe. Ces méthodes sont appliquées à des données sur des échantillons de tissu osseux acquis à la taille du voxel de 120 nm et 30 nm. Les images de phase ainsi obtenues sont ensuite utilisées en entrée à un code de reconstruction tomographique par rétroprojection filtrée (FBP) pour obtenir la carte 3D de phase de l'échantillon (logiciel ESRF PyHST2).

Évaluation quantitative

Pour obtenir une évaluation quantitative des différentes méthodes de reconstruction, nous avons calculé le rapport signal/bruit (SNR) et une estimation de la résolution spatiale. Le SNR a été estimé en calculant le rapport entre la moyenne du signal et l'écart-type du bruit sur une zone homogène du fond. Dans notre cas, le signal a été défini comme les régions occupées par l'os, et le fond comme les régions à l'intérieur des lacunes. La résolution spatiale de l'image a été évaluée expérimentalement à partir de la mesure de la fonction d'étalement du bord (ESF), mesuré sur le bord de lacunes dans des tranches médianes. Après fit de cette courbe par une fonction d'erreur de Gauss, la LSF (fonction d'étalement de ligne) est obtenue par dérivation, ce qui permet de calculer la largeur à demi hauteur (FWHM). La résolution spatiale est définie à partir de la fréquence de coupure à 10% de la fonction de transfert de modulation de Fourier. Les estimations du SNR et de la résolution spatiale ont été répétées à différents endroits pour obtenir une moyenne et un écart-type.

Résultats

Nous avons tracé les filtres des méthodes CTF homogène et Paganin pour les différentes distances de propagation. Nous voyons que ces deux méthodes se comportent de la même façon dans la gamme des basses fréquences lorsqu'on utilise une ou plusieurs distances. Toutefois, le filtre correspondant à la méthode CTF à une seule distance contient de nombreux points de sauts de fortes amplitudes dans les hautes fréquences, par opposition à la méthode de Paganin. Lorsque l'on considère plusieurs distances, ce comportement de réduit, ce qui montre que l'utilisation de plusieurs distances permet de gérer le problème des passages par zéro. Les filtres CTF homogènes et de la méthode de Paganin se superposent dans les basses fréquences. Toutefois, alors que les filtres de la méthode de Paganin sont essentiellement des filtres passe-bas, les filtres de la méthode CTF homogène permet de conserver de l'information haute fréquence.

Nous montrons les images tomographiques reconstruites de 3 échantillons aux tailles de voxel de 120 nm et 30 nm. Nous utilisons des images MIPs (projections d'intensité minimale) des volumes reconstruits en 3D, calculés en sélectionnant la valeur minimale d'intensité sur l'axe Z pour chaque coordonnée XY. Les MIPs permettent de voir des lacunes (structures ellipsoïdales noires de type ellipsoïdales), ainsi que des canalicules. Nous présentons les MIPs obtenus en utilisant la CTF ou la méthode de Paganin étendue à partir de 1, 2 et 4 distances, avec ou sans NLCG (10 itérations).

Tout d'abord, l'impact du raffinement itératif du NLCG est étudié. En général, les coupes reconstruites après NLCG 10 itérations sont plus nettes et mieux contrastées que celles sans raffinement. Toutefois, le gain en qualité d'image est quelque peu différent si l'on considère le CTF ou la méthode de Paganin. Pour la méthode CTF, le raffinement non linéaire n'améliore pas très significativement la qualité de l'image, quel que soit le nombre de distances utilisées. Cependant, le raffinement non linéaire améliore nettement la qualité de l'image pour la méthode étendue de Paganin, qui apparaît flous sans raffinement. Ce comportement est en accord avec la nature passe-bas des filtres correspondants..

Maintenant, nous considérons l'impact de l'utilisation de plusieurs distances plutôt qu'une seule sur la qualité de l'image reconstruite. Pour la méthode CTF homogène, on constate que l'image utilisant une seule distance de propagation est plus floue et que la netteté est améliorée lorsque l'on utilise 4 distances de propagation, indépendamment de l'utilisation du raffinement itératif. Pour la méthode de Paganin étendue sans raffinement, nous observons que la différence entre les reconstructions utilisant une seule distance et des distances multiples est peu visible. Toutefois, après avoir effectué le raffinement NLCG, un meilleur contraste des petites structures de canaux ainsi qu'une diminution du bruit peuvent être observés en utilisant plusieurs distances au lieu d'une seule.

Nous avons présenté le SNR estimé et la résolution spatiale dans les images reconstruites pour le CTF homogène et la méthode de Paganin étendue avec 0 ou 10 itérations, en utilisant 1, 2 ou 4 distances. Pour la méthode CTF homogène, le SNR et la résolution spatiale sont améliorés lorsque le nombre de distances utilisées augmente. Dans le cas d'une seule distance, le raffinement itératif améliore la résolution spatiale mais diminue le SNR. Pour la méthode de Paganin étendue sans raffinement itératif, l'utilisation de distances multiples ne produit pas de différences significatives. Toutefois, si l'on considère le raffinement non linéaire, l'utilisation de distances multiples améliore le SNR et la résolution spatiale. Ces résultats confirment l’observation qualitative. En conclusion, les meilleurs résultats sont obtenus par les méthodes CTF homogène et Paganin étendue utilisant 4 distances avec 10 itérations.

Conclusion

La reconstruction de phase, qui est un problème inverse non linéaire et mal posé, est une étape nécessaire dans la reconstruction de la nano-CT de phase. Les choix de la méthode de reconstruction de phase et des meilleures conditions expérimentales sont restés des questions ouvertes dans le cas de plusieurs distances. C'est ce qui a motivé notre étude détaillée des approches de reconstruction de phase d'un point de vue théorique et expérimental. Dans ce chapitre, nous avons étendu la méthode de Paganin aux acquisitions à plusieurs distances et l'avons comparée à une version homogène de la méthode CTF pour la reconstruction d'échantillons osseux à résolution spatiale nanométrique. Nos résultats ont montré que l'utilisation de 4 distances de propagation améliore généralement la qualité de l'image sauf dans le cas de la méthode de Paganin sans raffinement non linéaire. Lorsque le raffinement itératif a été utilisé, le cas multi-distance a fourni la reconstruction la plus nette avec une résolution spatiale plus haute et un fond plus uniforme. Dans ce cas, le CTF homogène et la méthode de Paganin étendue donnent des résultats comparables. L'avantage d'utiliser plusieurs distances de propagation est qu'il permet une meilleure couverture du domaine de Fourier des projections de phase.

Nos travaux futurs concernent l'analyse quantitative de l'ultra structure osseuse sur laquelle il y a encore très peu de résultats en raison des modalités limitées de l'imagerie 3D disponibles. Dans ce contexte, il était donc important d'optimiser la qualité de l'image car celle-ci peut avoir un impact considérable sur la quantification ultérieure. Bien qu'il soit expérimentalement plus exigeant d'utiliser quatre distances de propagation au lieu d'une seule, nos résultats ont montré qu'un gain net est obtenu en qualité d'image. Dans la suite, nous nous concentrerons sur l'analyse quantitative des données, à partir desquelles nous espérons obtenir des paramètres quantitatifs du réseau lacuno-canaliculaire.

Chapitre 5: Segmentation et quantification du réseau lacuno-canaliculaire par l'imagerie tomographique par rayons X

Dans ce chapitre, nous utilisons la nano-CT de phase en vue de l'analyse de l'ultrastructure osseuse humaine. Des échantillons fémoraux de femmes ont été imagés lors de différentes expériences sur la ligne ID16A de l'ESRF à des tailles de voxel de 120 nm avec des énergies de 17 ou 33.6 keV. Nous décrivons dans ce chapitre la chaine de traitement d'images à mettre en œuvre pour segmenter les lacunes et les canalicules à partir de volumes reconstruits, puis pour en extraire des paramètres quantitatifs du LCN. A partir d'une méthode d'analyse d'image rapide et efficace développée dans notre groupe, nous avons calculé plusieurs descripteurs morphologiques des lacunes tels que le volume, la surface et la longueur de chaque dimension, et quantifié le nombre de canaliculi à différentes distances de la surface de chaque lacune. Nous présentons les résultats obtenus sur 13 échantillons et étudions les relations entre ces paramètres et la porosité osseuse.

Description des échantillons

Tous les spécimens proviennent de cadavres de femmes (âgées de 50 à 90 ans) qui sont fournis par le Centre du Don des Corps (Université Paris 5) et le Département d'anatomie Rockefeller, Université Lyon. Les os extraits de ces sujets cadavériques frais ont été enveloppés dans une gaze imbibée de solution saline pour les hydrater, puis conservés à -20°C jusqu'à la préparation des échantillons. Dans ce travail, nous avons utilisé les diaphyses fémorales, qui ont été découpées en 5 blocs dans la direction longitudinale de l'os avec une scie basse vitesse (Isomet 4000, Buehler, Lyon). La section transversale a été divisée en 4 quadrants différents tels que les quadrants antérieur, postérieur, médian et latéral. Seuls les quadrants latéraux ont été scannés dans nos expériences.

Obtention des images

Les échantillons ont été imagés par nano-CT de phase sur la ligne ID16A de l'ESRF. Les échantillons ont été scannés à 4 distances différentes entre l'échantillon et le détecteur. Pour chaque distance, 2000 projections ont été enregistrées sur un angle de vue de 180° avec une énergie de faisceau de 17 ou 33,6 keV. Le temps d'acquisition pour un ensemble de données complet (avec 4 distances de propagation) était d'environ 4 heures. La reconstruction de phase a été réalisée comme décrit dans le chapitre précédent (méthode de Paganin étendu et raffinement itératif), puis les images 3D ont été reconstruites par l'algorithme standard de rétroprojection filtrée (FBP) (logiciel PyHST2). La taille du volume reconstruit est de 2048 × 2048 × 2048 aux tailles de voxel de 120 nm, 50 nm et 30 nm, correspondant respectivement au champ de vision 245.76 µm, 102.4 µm et 61.44 µm. Dans ce chapitre, nous avons seulement montré les résultats à la taille du voxel de 120 nm, tandis que d'autres résultats à plus haute résolution seront présentés dans le chapitre suivant.

Traitement d'images

<u>Segmentation des lacunes</u>

Tout d'abord, nous utilisons un filtre médian pour retirer les canalicules des volumes reconstruits car parfois ceux-ci étaient au même niveau de gris que les lacunes et reliés aux lacunes voisines ce qui empêchait leur segmentation. Ensuite un seuillage par hystérésis, méthode de segmentation à double seuillage, est réalisé pour segmenter les lacunes Le premier seuil, plus bas, permet d'extraire les voxels des lacunes avec une grande confiance, tandis que le second seuil, plus haut, permet d'améliorer la segmentation. Les voxels avec les valeurs de gris situées entre deux seuils, sont assignés à l'objet s'ils sont connectés aux voxels déjà segmentés. Cette méthode a montré que parfois, des régions appartenant à des canaux de Haversian pouvaient être segmentées en même temps. Comme les canaux de Havers sont beaucoup plus grands que les lacunes, nous éliminons les plus grands objets après une analyse en composantes connexes.

Segmentation des canalicules

La segmentation des canalicules est plus difficile que celle des lacunes en raison de leur taille minuscule. Nous avons d'abord utilisé un filtre pour les rehausser, basé sur une méthode de « vesselness ». Ce filtre est basé sur la matrice Hessienne calculée par les dérivées partielles du second ordre qui reflète les variations d'intensité et contient les informations de forme. Les valeurs propres issues de la décomposition de cette matrice peuvent décrire les propriétés géométriques des structures locales. Après cette étape, nous faisons une première segmentation de l'image, et le résultat binaire sera utilisé comme point de départ à une méthode de croissance de régions. Nous avons utilisé la méthode de croissance par région variationnelle (VRG) pour segmenter les canalicules. Cette méthode permet de formaliser le processus itératif de croissance en minimisant une fonction d’énergie, adaptée à nos images.

Analyse quantitative

Le nombre de lacunes Lc.N a été calculé en comptant le nombre total de labels. La densité de lacunes est calculée par le nombre total de lacunes divisé par le volume osseux (Lc.N/BV). Grâce à la méthode des moments du second ordre, nous approximons chaque lacune à un ellipsoïde, ce qui nous donne la longueur, la largeur et la profondeur de la lacune (Lc.L1, Lc.L2 et Lc.L3), ainsi que l'anisotropie de la lacune détectée par les rapports entre différents axes (Lc.L1/Lc.L2) et (Lc.L2/Lc.L3). Grâce au calcul de volumes intrinsèques, nous calculons la surface moyenne de la lacune (Lc.S) et un paramétre de forme sur la lacune (Lc.SMI). De plus, nous réalisons une tessellation de Voronoi 3D qui permet de partitionner l’image en cellules, chaque cellule contenant une lacune. Ceci nous eprmet de calculer le volume moyen d'une lacune (Lc.V), le volume moyen de chaque cellule (Cell.V) et la porosité lacunaire locale (Lc.V/Cell.V).

En ce qui concerne les canalicules, nous calculons la porosité des canalicules dans l'ensemble du volume, exprimé comme le volume total des canalicules divisé par le volume osseux (Ca.TV/BV), le rapport entre le volume moyen de canalicules par cellule et le volume moyen de chaque cellule (Ca.V/Cell.V). De plus, nous avons évaluons le volume total du LCN (LCN.TV) et la porosité du LCN (LCN.TV/BV) pour l'évaluation du réseau entier. Pour quantifier la ramification des canalicules, nous avons calculé le nombre de canalicules par lacune à différentes distances de la surface de la lacune (Ca.N), et le rapport entre le nombre de canalicules par lacune et le volume de lacune situé dans la même cellule (Ca.N/Lc.V).

Analyse statistique

Nous avons réalisé une analyse statistique des résultats. Pour la corrélation entre les paramètres, nous avons calculé le coefficient de corrélation de Spearman et la valeur p par un test de Fisher. Ces calculs et analyses ont été effectués par Statview® (SAS Institute Inc., Cary, NC, USA). Les valeurs p de moins de 0.05 ont été considérées comme significatives.

Résultats

Pour ce qui est de la segmentation, nous avons comparé plusieurs méthodes de segmentation des canalicules. Nous avons comparé les temps de calcul et les résultats obtenus par la méthode VRG et par vote géodésique. La méthode VRG est beaucoup plus rapide que celle des chemins géodésiques, 829 secondes contre 17697 secondes. Elle permet également de conserver l’épaisseur des canalicules, ce que ne permet pas la méthode des chemins géodésique ce qui signifie que nous aurons besoin d'autres opérations pour récupérer l'information géométrique des canalicules. Par contre, la connection des canalicules est parfois perdue coupée dans d'autres régions après le traitement du vote géodésique. En bref, nous avons choisi la méthode VRG pour segmenter les canalicules dans notre cas en tenant compte de l'efficacité et de l'efficience.

Nous avons reporté les paramètres quantitatifs du LCN calculés sur 8 volumes à la taille de voxel de 120 nm. Le nombre de lacunes moyen était de 256.9 et la densité moyenne de 24000 mm^{-3}. La porosité lacunaire était de (0.78%), canaliculaire de (0.35%) et la porosité totale du LCN, de 1.12%). Le volume moyen d'une lacune est de 315.7 μm^3, ce qui est conforme aux rapports précédents (~50–730 μm^3). De plus, nous avons introduit la porosité locale des lacunes et des canalicules dans leur cellule de Voronoi Le volume moyen de chaque cellule est de 4.2×10^4 μm^3, le volume moyen des canalicules par cellule 139.3 μm^3, le rapport Lc.V/Cell.V 0.88%, Ca.V/Cell.V 0.37% et Ca.V/Lc.V 45.8%. La surface moyenne est de 323.3 μm^2 et l'indice du modèle structurel est de 3.1. La longueur, la largeur et la profondeur moyennes de chaque lacune sont respectivement de 17.1 µm, 9.2 µm et 4.4 µm.

Le calcul du nombre de canalicules par lacune Ca.N a été réalisé à 7 distances physiques différentes de la surface de la lacune: 1.2 µm, 3.0 µm, 4.8 µm, 6.6 µm, 8.4 µm, 10.2 µm and 12.0 µm. Pour évaluer la densité des canalicules, nous avons également calculé le rapport entre le nombre de canalicules par lacune et le volume moyen de lacune. La tendance générale du Ca.N pour tous les échantillons est à la hausse en s'éloignant de la surface de la lacune, de 58.2 à 75.4. Les résultats de Ca.N/Lc.V des échantillons croissent de la même manière, de 0.19 μm^{-3} à 0.25 μm^{-3}. En examinant les échantillons séparément, nous constatons que les valeurs de Ca.N et Ca.N/Lc.V pour la majorité des échantillons augmentent de 1.2 µm à 12.0 µm. Mais il y a plusieurs échantillons qui présentent simplement une fluctuation. C'est parce que les conditions physiologiques et saines des échantillons osseux que nous avons prélevés et les régions d'intérêt que nous avons choisies pour l'observation sont différentes.

Conclusion

En conclusion, nous avons présenté les méthodes utilisées pour segmenter et quantifier le LCN à partir d'images à 120nm, et obtenu des résultats sur 8 échantillons d'os fémoral humain. Pour la segmentation, nous avons utilisé des méthodes classiques de filtrage d'images pour conserver l'efficacité du traitement des grands volumes de données. Nous ont ensuite calculé un certain nombre de paramètres quantitatifs 3D pour la densité, la porosité et la morphologie des lacunes et des canalicules. Nous avons également introduit une notion de porosité locale. Nos résultats sont du même ordre de grandeur que ceux de la littérature, mais leur calcul ici est relativement précis. Le calcul du nombre de canalicules par lacune est lui totalement original. .

Chapitre 6: Quantification du réseau lacuno-canaliculaire à l'échelle nanométrique et comparaison entre différentes résolutions spatiales

Dans ce chapitre, nous présentons l’analyse du LCN sur 13 échantillons d'os fémoral humain imagés en nano CT de phase sur la ligne ID16A de l’ESRF. Ces 13 échantillons ont été scannés à trois tailles de voxel différentes: 120 nm, 50 nm et 30 nm. Les résultats à 120 nm ont été présentés dans le chapitre précédent. Dans ce chapitre, nous présentons les résultats obtenus à plus haute résolution (50 et 30nm) après avoir adapté les méthodes d’analyse. Nous étudions également les différences entre les résultats obtenus à 30 nm et 120 nm sur les mêmes VOIs de différents échantillons. Nous présentons tout d’abord l’approche utilisée pour le recalage, basée sur la méthode de corrélation de phase. Enfin, nous comparons les résultats quantitatifs entre les images coupées à 120 nm et les images correspondantes à 30 nm, afin de vérifier les différences de quantification à différentes tailles de voxel.

Description des échantillons

Au total, 13 échantillons d'os fémoral provenant de femmes (âgées de 56 à 95 ans) ont été analysés. Ils ont été fournis par le Centre du Don des Corps (Université Paris 5) et le Département d'Anatomie Rockefeller, Université Lyon. Des échantillons de taille 0.4×0.4×4 mm^3 ont été découpés à partir de coupes transversales de diaphyses fémorales à l'aide d'une scie de précision diamantée refroidie par eau (Presi Mecatome T210, Struers Diamond Cutoff Wheel EOD15, Liphy, Grenoble). Aucune information complémentaire sur l'état pathologique ou l'historique médicamenteux n'était disponible au regard des dispositions légales du Code d'Ethique de la Santé Publique français.

Technique d'imagerie

Les échantillons ont été imagés en nano-CT de phase sur la ligne de lumière ID16A de l'ESRF. Chaque échantillon a été scanné à 4 distances de propagation différentes et pour chaque distance, 2000 projections ont été enregistrées sur une plage de 180º. Deux énergies spécifiques ont été utilisées pour les expérimentations à ID16A, 17 et 33.6 keV. Le temps total d’acquisition pour un échantillon à 4 distances était d'environ 4 heures. Les reconstructions tomographiques ont été obtenues en suivant la même méthode que précédemment décrit dans le chapitre 5. Les tailles de voxel des volumes reconstruits (2048 × 2048 × 2048) étaient de 120nm, 50 nm et 30 nm, correspondant respectivement au champ de vue de 242.2µm, 102.4 µm et 61.44 µm. Les images à 30nm ont toujours été acquises après avoir déjà acquis une image sur un plus grand champ (à 120nm).

Traitement d'images

Nous rappelons brièvement la chaine de traitement utilisée pour l’analyse.

<u>Segmentation de LCN</u>

La segmentation du LCN a été divisée en deux parties. Pour la segmentation des lacunes, nous avons d'abord utilisé un filtre médian, puis une méthode de seuillage par hystérésis. Nous avons ensuite réalisé une analyse en composante connexe de l’image binaire résultante pour filtrer les composantes de taille anormalement grande (come les canaux de Havers ou Volkman).

Afin de segmenter les canalicules, nous avons d'abord utilisé une méthode de "vesselnesss" pour rehausser les structures cylindriques, puis une méthode de seuillage d'entropie maximale pour obtenir une première image binaire des canalicules. Cette segmentation a été raffinée en utilisant l’algorithme VRG, puis en réalisant analyse des composantes connexes pour filtrer le bruit résiduel.

<u>Recalage des images à 120 et 30nm</u>

Dans notre cas, pour comparer la quantification entre différentes tailles de voxel, nous devons recaler les images à 30 nm avec celles à 120 des mêmes échantillons. Compte tenu de notre protocole d'acquisition, nous savons que entre l'image a 120nm et celle à 30nm, l'échantillon été translaté dans les trois dimensions x, y et z mais n'a pas subi de rotation. Ceci nous a permis d'utiliser une méthode de recalage relativement simple, la méthode de corrélation de phase (PCM). Cette méthode permet d'estimer les translations relatives entre deux images à partir de leurs représentations dans le domaine des fréquences spatiales, 3D dans notre cas.

Analyse quantitative et statistique

Après segmentation, nous avons calculé les mêmes paramètres quantitatifs des lacunes et des canalicules pour les reconstructions aux tailles de voxel de 50 nm et 30 nm, ainsi que les résultats de la méthode de corrélation de phase. Les méthodes de calcul de ces paramètres ont été décrites dans le chapitre précédent. Pour les paramètres calculés à partir des volumes à 30 nm et des volumes recalés, un test de Student a été utilisé pour tester la différence entre ces deux groupes. De plus, nous avons utilisé le coefficient de corrélation de Spearman et la valeur p de la transformation de Fisher pour évaluer les corrélations entre les paramètres mesurés. Les résultats avec des valeurs p de moins de 0.05 ont été considérés comme significatifs.

Résultats

Analyse à 50 nm: l'analyse a porté sur 9 volumes scannés dans 6 échantillons à la taille d'un voxel de 50 nm. Le nombre moyen de lacunes par volume était de 20.8. La porosité lacunaire moyenne est de 0.88% avec une densité moyenne de lacunes de 26000 mm^{-3}. Le volume moyen de chaque lacune est de 338.1 µm^3 et la surface moyenne de 376.4µm^2. Le volume moyen de chaque cellule de Voronoi est de 3400 µm^{3}et le rapport entre le volume moyen d'une lacune et celui de la cellule correspondante de 1.14%. La longueur, la largeur et la profondeur moyennes de chaque lacune sont respectivement de 18.7µm, 9.1µm et 4.5 µm. Pour décrire la planéité des lacunes, nous avons calculé le rapport entre la longueur et la largeur 2.1, le rapport entre la largeur et la profondeur 2.2 et l'indice du modèle structurel 3.1. La porosité moyenne des canalicules est de 0.37%. Le volume moyen de canalicules par cellule est de 141.4 µm^3 avec un rapport de 0.43% entre le volume moyen de canalicules par cellule et sa cellule correspondante. De plus, le rapport moyen entre le volume des canalicules et la lacune dans la même cellule est de 46.4%. La porosité moyenne du LCN est de 1.24%. Aux mêmes 7 distances de la surface de la lacune que pour les données de 120 nm, le nombre moyen de canalicules par lacune est de 72.7, 85.3, 88.3, 89.0, 91.7, 96.5 et 107.3. La densité de canalicules par lacune dans une cellule de Voronoi varie entre 0.23µm^{-3}, et 0.36µm^{-3} aux différentes distances.

Analyse à 30 nm comparée aux résultats sur les mêmes VOIs à 120nm: Les volumes à 30 nm ont le même nombre de lacunes que ceux à 1200nm recalés, 5.3, et la même densité de lacunes 32000 mm^{-3}. La porosité lacunaire à 30 nm 1,10% est plus grande que celle des volumes recalés à 120nm 1.01%. La porosité des canalicules des volumes à 30 nm 0.35% est plus grande que celle des PCM 0.28%. La même observation est faite sur la porosité de l'ensemble du réseau, qui est de 1.45% à 30nm et de 1.28% à 120nm. Le volume moyen des lacunes à 30 nm de 343.3 µm^3 apparait légèrement plus grand que celui des volumes recalés à 120nm, qui est de 314.0 µm^3. La surface moyenne de lacune (Lc.S) à 30 nm 360.8 µm^2 est supérieure aux valeurs des volumes à 120nm 320.9 µm^2. La longueur, la largeur et la profondeur moyennes de la lacune à 30 nm 16.9 µm, 9.2µm et 4.9µm, sont légèrement plus grandes que celles des volumes à 120nm, 16.4µm, 8.9µm et 4.7µm. Les valeurs de Lc.SMI sont presque égales dans les deux groupes: 3.1. Le volume moyen des canalicules par cellule est de 113.0 µm^3 est également plus grand que celui des volumes à 120nm recalés 88.6 µm^3. La porosité locale des lacunes à 30nm, Lc.V/Cell.V 1.73% est comparable à celle à 120nm 1.77%, et celle des canalicules Ca.V/Cell.V 0.51% est également proche de celle à 120nm 0.49%. Le rapport Ca.V.Lc.V à 30 nm 38.6% est un peu plus élevé que celui des volumes à 120nm 31.2%.

Les nombres de canalicules par lacune à 7 distances de la surface (1.2 µm, 3.0 µm, 4.8 µm, 6.6 µm, 8.4 µm, 10.2 µm et 12.0 µm) ont été calculés. Le nombre moyen de canalicules par lacune à 30 nm augmente de 78.5 à 117.9 avec la distance variant de 1.2 µm à 12.0 µm. Les résultats à 120nm ne montrent pas une augmentation constante mais de légères fluctuations. En outre, les valeurs Ca.N/Lc.V à 30 nm continuent à augmenter de 0.24 à 1.2 µm à 0.39à 12.0 µm, tandis que celles des volumes à 120nm fluctuent autour de ~0,18/0.20 µm^{-3}.

Conclusion

En conclusion, nous avons scanné 13 échantillons d'os fémoral humain par nano-CT de phase aux tailles de voxel de 120nm, 50 nm et 30 nm. Grâce à une méthode de corrélation de phase, nous recaler les images à 30nm à leur VOI correspondantes à 120nm. Nous avons ainsi pu comparer les résultats quantitatifs à 30 nm et à 120nm sur les mêmes régions d’analyse. Les résultats montrent des différences significatives essentiellement sur les paramètres des canalicules, qui sont sous-estimés à 120nm. Les paramètres de lacunes sont peu différents et les différences peuvent s’expliquer par plus de détails au niveau de l’interface sur les images à 30nm. La taille de voxel de 50 nm peut être un bon compromis entre précision et champ de vue. Dans ce chapitre, nous avons apporté de nouvelles données quantitatives sur le LCN chez l’humain à partir d’images 3D à 50 et 30 nm qui peuvent servir de référence pour d'autres recherches.

Chapitre 7: Quantification du réseau lacuno-canaliculaire dans une série d'échantillons fémoraux humains par l'imagerie tomographique par rayons X

Dans ce chapitre, nous présentons l’analyse du LCN dans une série de 27 échantillons d’os cortical humain imagés en nano-CT de phase. Pour cette étude sur une plus grande série, nous avons utilisé la nano CT sur la ligne ID16B de l'ESRF. Chaque échantillon a été scanné à quatre distances de propagation différentes pour atteindre la taille finale du voxel de 100 nm avec une énergie de faisceau de 29.6 keV. La reconstruction et l’analyse d’images ont été réalisées come décrit dans les chapitres précédents. Il est à noter que dû à l’utilisation d’une caméra différente, la taille des volumes est de 52.7 Go par volume. Nous reportons les paramètres de porosité et de densité de lacunes et de canalicules, les dimensions des lacunes, ainsi que le nombre de canalicules pour chaque lacune. Cette étude est la première à si grande échelle pour ce genre de quantification.

Description des échantillons

Des échantillons d'os cortical ont été prélevés sur les diaphyses fémorales de 27 cadavres humains fournis par le Centre du Don des Corps (Université Paris 5) et le Département d'anatomie Rockefeller, Université Lyon. Conformément aux dispositions légales prévues par le Code d'Ethique de la Santé Publique, seules les informations relatives au sexe et à l'âge des donneurs sont disponibles. Au total, 15 femmes (50 à 95 ans) et 12 hommes (66 à 89 ans) figurent parmi les donneurs. Des coupes transversales de 0.4 × 0.4 × 4 mm^3 ont été coupées à l'aide d'une scie de précision diamantée (Presi Mecatome T210, Disque à tronçonner diamanté Struers EOD15, Liphy, Grenoble) pour le balayage.

Technique d'imagerie

Nous avons utilisé le nano-CT de phase pour imager les échantillons sur la ligne ID16B de l'ESRF. Pendant le scan, l'échantillon a été placé sur un support équipé de mouvements de rotation et translation. Chaque échantillon a été scanné à 4 distances différentes entre le focus et l'échantillon, et 3400 projections ont été enregistrées à chaque distance sur une plage de 180º. L'énergie du faisceau de rayons X a été fixée à 29.6 keV pour notre expérimentation. Le temps total de balayage pour un échantillon à 4 distances était d'environ 4 heures. La méthode de reconstruction de phase est celle décrite dans le chapitre 5. Après reconstruction tomographique par rétroprojection filtrée (FBP), les volumes 3D ont une taille de 2560 × 2560 × 2160 voxels correspondant à celle de 256 µm × 256 µm × 216 µm.

Segmentation et quantification

Les méthodes d’analyse d’images et statistique sont identiques à celles décrites dans le chapitre 6.

Résultats

Nous avons divisé les résultats en deux groupes selon le sexe (femme et homme) et comparé les mesures entre les groupes. Tout d'abord, nous pouvons voir que le nombre moyen de lacunes dans le groupe des femmes est 231.1 et la densité des lacunes est de 2.2×10^4 mm^{-3}, qui sont légèrement des plus grandes que celles dans le groupe des hommes 216.3 et 2.1×10^4 mm-3. La porosité lacunaire (Lc.TV/BV), la porosité de canaliculi (Ca.TV/BV) et la porosité du LCN (LCN.TV/BV) dans le groupe des femmes 0.79%, 0.44% et 1.23%, sont toutes des plus grandes que celles des hommes 0.66%, 0.36% et 1.02%. Le volume moyen de lacune dans le groupe des femmes est 358.5 μm^3 plus grand que celui du groupe des hommes 323.6 μm^3. Nous avons introduit des paramètres locaux basés sur les cellules de Voronoi autour de chaque lacune. Le volume moyen de chaque cellule du groupe des femmes 4.7×10^4 μm^3 est égal à celui du groupe des hommes, mais le volume moyen des canalicules par cellule est plus grand

198.3 µm^3 contre 173.2 µm^3. Les ratios Lc.V/Cell.V 0.93 %, Ca.V/Cell.V 0.47 % et Ca.V/Lc.V 60.0 % dans le groupe des femmes sont tous de plus haut que ceux des hommes 0.81 %, 0.40 % et 58.7 %, respectivement.

En plus, nous avons calculé quelques paramètres pour décrire la morphologie et l'anisotropie de la lacune. La surface moyenne de lacune dans le groupe de femelles 354.9 µm^2 est plus grande que celle du groupe d'hommes 327.14 µm^2. . De même, les valeurs de Lc.L1 et Lc.L2 dans le groupe des femmes 18.3 µm et 9.6 µm sont plus grandes que celles du groupe des hommes 17.9 µm, 9.4 µm tandis que les valeurs de Lc.L3 de deux groupes sont les mêmes 4.5 µm. Le rapport Lc.L1/Lc.L2, Lc.L2/Lc.L3 et l'indice du modèle de structure Lc.SMI entre les groupes sont proches, 2.0, 2.3 et 3.1 pour les femmes, et 2.0, 2.3 et 3.3 pour les hommes. Par ailleurs, nous avons calculé le nombre de canalicules par lacune à 7 distances de la surface de la lacune. Lorsque la distance passe de 1.2 µm à 12.0 µm, on peut noter que le nombre moyen de canalicules par lacune (Ca.N) dans le groupe des femelles augmentent de 58.4 à 76.6, et de 49.6 à 64.5 pour celui des hommes. Nous avons également obtenu la densité locale des canalicules par le rapport entre le nombre de canalicules par lacune et le volume moyen de lacune (Ca.N/Lc.V). Les valeurs de (Ca.N/Lc.V) dans le groupe des femmes augmentent de 0.17 µm^{-3} à 0.23 µm^{-3}, tandis que celles du groupe des hommes augmentent de 0.16 µm^{-3} à 0.22 µm^{-3}.

Pour vérifier l'association entre les paramètres quantitatifs et l'âge, nous avons divisé les volumes reconstruits en deux autres groupes par âge : le groupe des jeunes et le groupe des vieux. Tout d'abord, on constate que la densité des lacunes et la porosité lacunaire entre deux groupes sont tout à fait comparables, alors que la porosité des canalicules dans le groupe des jeunes 0.45% est plus grande que celle dans le du groupe des vieux 0.37%. Dans chaque cellule de Voronoi, le volume moyen des lacunes et des canalicules dans le groupe des jeunes 348.6 µm3 et 210.2 µm3 est plus grand que ceux du groupe des vieux 339.1 µm3 et 171.3 µm3. Pour les descripteurs morphologiques de la lacune, la longueur moyenne de la lacune Lc.L1 et le rapport (Lc.L1/Lc.L2) dans le groupe des jeunes (18.3 µm et 2.1) sont tous plus grands que ceux du groupe des vieux (17.4 µm et 1.9). D'ailleurs, pour la ramification, on peut aussi voir que le nombre de canaliculi et la densité de canaliculi à 7 distances différentes de la surface de la lacune dans le groupe des jeunes sont tous plus grands que ceux du groupe des vieux.

Conclusion

En conclusion, nous avons utilisé le nano-CT de phase pour l'investigation et l'analyse du LCN dans 27 échantillons fémoraux humains provenant de femmes et d'hommes donneurs. Toutes les données ont été scannées à la taille du voxel de 100 nm dans la lumière ID16B de l'ESRF. Pour vérifier l'association avec le sexe et l'âge, nous avons divisé les volumes reconstitués en différents groupes: femmes et hommes, jeunes et vieux. Après comparaison, nous constatons que le volume moyen et la taille géométrique de la lacune, le volume moyen et la densité des canalicules par cellule de Voronoi dans le groupe des femmes sont tous plus grands que ceux du groupe des hommes. De même, il y a plus de volumes de lacunes et un plus grand nombre de canalicules dans le groupe des jeunes que ceux du groupe des vieux. Nous nous espérons que ces paramètres des lacunes et des canalicules peuvent aider à analyser et à comprendre les microstructures osseuses et fournir des références pour d'autres chercheurs sur les mécanismes de la fragilité osseuse dans les maladies.

Conclusion et perspective

L'objectif de cette thèse était de quantifier le LCN dans une série d'échantillons humains à partir d'images 3D acquises en nano CT synchrotron de phase. Ceci a nécessité d'optimiser les processus d'acquisition et de reconstruction de phase, ainsi que de développer des méthodes efficaces de traitement d'images pour segmenter et quantifier le LCN

La méthode d'imagerie choisie a l'avantage d'avoir une sensibilité plus élevée que les méthodes basées sur l'absorption, de permettre d'accéder à une résolution spatiale très élevée et inégalée pour une méthode grand champ. Elle ne nécessite donc pas de scanner l'objet en le translatant, comme par exemple en ptychographie, ceci conduisant à des temps d'acquisition beaucoup plus longs. Par rapport à l'imagerie confocale, la résolution spatiale est isotrope et ne se dégrade pas avec la profondeur de pénétration. Finalement, le champ de vue est relativement grand par rapport aux techniques microscopiques telles que le FIB/SEM par exemple.

Notre première contribution a porté sur l'optimisation du protocole de formation d'image, en comparant différents algorithmes de reconstruction de phase pour différents distances de propagation. Nous avons étendu la formule de Paganin aux acquisitions à plusieurs distances et l'avons comparé avec la méthode CTF homogène. Les deux méthodes ont été appliquées à des données acquises sur des échantillons de tissus osseux à la taille de voxel de 120 nm et 30 nm. Nous avons démontré l'intérêt d'utiliser plusieurs distances de propagation au lieu d'une seule ainsi que le gain apporté par l'utilisation d'une étape de post-traitement non linéaire pour améliorer la qualité des images de phase 3D. Le SNR et la résolution spatiale ont été calculés pour évaluer la qualité des images reconstruites. D'un point de vue visuel, nous avons trouvé que les images reconstruites à partir de plusieurs distances sont plus nettes que celles reconstruites à partir d'une seule distance de propagation, ce qui a été corroboré par l'analyse quantitative de la résolution spatiale. Cette première étude a permis de fixer les conditions d'acquisition et de reconstruction des images, qui seront utilisées tout au long de cette thèse.

En termes d'acquisition de données, tous nos échantillons de fémurs humains ont été scannés sur deux lignes de lumière ID16A et ID16B de l'ESRF. Typiquement, 2000 projections à ID16A et 3400 projections à ID16B ont été enregistrées sur une plage de 180° à 4 distances différentes entre l'échantillon et le détecteur. Au total, nous avons analysé 13 échantillons de donneuses à ID16A. Parce que le même échantillon a parfois été scanné plus d'une fois à différentes tailles de voxel, nous avons obtenu 8 volumes reconstruits à la taille de voxel de 120 nm, 9 volumes à 50 nm et 14 volumes à 30 nm. Chaque échantillon a été scanné à des tailles de voxels de 120 nm, 50 nm ou 30 nm sous deux énergies spécifiques 17 ou 33.6 keV, et la taille d'un volume reconstruit était 2048 × 2048 × 2048 voxels. À ID16B, nous avons obtenu 27 volumes sur 15 femmes et 12 hommes. La taille du voxel était de 100 nm et l'énergie de 29.6 keV avec une taille de 2560 × 2560 × 2160 voxels par volume. Nous avons mis en œuvre le traitement et l'analyse de ces données.

La chaine de traitement d'image et d'analyse mise en place est décrite dans le chapitre 5. Nous avons dû faire face à plusieurs défile plus important étant la grande taille des données qui a influencé nos choix de méthodes. Par exemple, la taille de chaque volume reconstruit à ID16A était de 32 Go et celle à ID16B de 52.7 Go. Par conséquent, nous avons dû prendre en compte l'utilisation de la mémoire de l'ordinateur et le temps d'exécution des programmes lorsque nous avons choisi des méthodes de traitement. Afin de segmenter les lacunes, nous avons choisi des méthodes classiques et efficaces telles que le filtre médian, le seuillage par hystérésis et l'analyse en composantes connexes. Pour segmenter les canalicules, nous avons utilisé une méthode d'amélioration de la visibilité des structures linéiques, une méthode de croissance de région, le VRG, pour extraire les canalicules et également une analyse en composants connexes pour éliminer le bruit résiduel. L'application de ces méthodes sur les images à 120nm a montré qu'elles permettaient de traiter des données de grande taille et de maintenir la qualité de la segmentation dans des limites de temps d'exécution accessibles.

Nous avons ensuite présenté un certain nombre de paramètres pour quantifier le LCN. Nous avons d'abord calculé quelques paramètres classiques tels que la porosité et la densité des lacunes et des canalicules. Ensuite, nous avons introduits de nouveaux paramètres, par exemple la porosité et la densité locales des lacunes et des canalicules en divisant le volume original en différentes cellules de Voronoi, ainsi que le nombre de canalicules par lacune à différentes distances de la surface de la lacune et le rapport entre le nombre de canalicules par lacune et le volume moyen des lacunes situées dans une seule cellule. Tous les paramètres ont été utilisés pour évaluer les propriétés du LCN et ont été comparés à ceux des études précédentes pour vérifier la fiabilité des mesures. Par ailleurs, nous avons comparé les résultats quantitatifs de reconstructions à différentes tailles de voxel sur la même région d'intérêt. Nous avons constaté que l'utilisation de la taille du voxel de 30 nm permettait une meilleure observation et quantification des canalicules, mais que la taille du voxel de 120 nm était plus appropriée pour étudier et analyser les propriétés 3D de l'ensemble du réseau avec un large champ de vue.

Nous avons finalement pu obtenir résultats quantitatifs sur un grand ensemble d'échantillons (n=27) à partir des images obtenues sur la ligne ID16B à la taille du voxel de 100 nm au chapitre 7. Les lacunes et les canalicules ont été segmentés des volumes selon les méthodes décrites au chapitre 5. Ensuite, des paramètres quantitatifs ont été calculés à partir des images binaires telles que la porosité et la densité des lacunes et des canalicules, certains descripteurs morphologiques des lacunes et la ramification des canalicules. Nous avons divisé les données en deux groupes, selon le sexe, 15 femmes et 12 hommes. Nous avons comparé les paramètres mesurés entre les groupes pour vérifier la différence influencée par le sexe. Tous les résultats ont apporté des caractéristiques du LCN en trois dimensions à l'échelle nanométrique. De plus, nos quantifications sont restées cohérentes avec les résultats des références précédentes après comparaison.

Une grande partie de travail a été centré sur la segmentation des canalicules, qui a une influence directe sur la quantification et l'analyse ultérieures. Contrairement à la segmentation des lacunes, celle des canalicules est difficile pour plusieurs raisons. D'abord, la taille physique des canalicules est à l'échelle nanométrique, par exemple le diamètre des canalicules est de l'ordre de 100-500 nm. Par conséquent, on a besoin de techniques d'imagerie qui peuvent fournir une résolution spatiale très élevée. Ensuite, d'autres microstructures vont influencer la segmentation des canalicules dans nos images, comme les fibres de collagène car elles peuvent avoir le même niveau de gris et des structures géométriques similaires dans une région locale avec celles des canalicules. Cela signifie qu'il faut utiliser plus d'informations sur les caractéristiques des canalicules pour la segmentation. Le dernier problème est de savoir comment conserver la connectivité des canalicules. Il pourrait être intéressant de développer des méthodes de post traitement pour reconnecter des canalicules sans introduire de faux canaux.

Concernant la quantification des lacunes et des canalicules, de nombreux autres descripteurs pourraient être introduits pour quantifier les structures 3D du LCN. Dans cette thèse, en plus des paramètres de porosité et de dimension habituelle, nous avons introduit de nouveaux paramètres comme ceux permettant d'évaluer la densité et la porosité locale des lacunes ou des canalicules dans des cellules de Voronoi, ainsi que la mesure du nombre de canalicules. D'autres paramètres topologiques sur le réseau formé par les lacunes et les canalicules pourraient être intéressants, notamment ceux basés sur des méthodes de graphe.

En conclusion, cette thèse a permis de développer une chaine complète de traitement allant de l'acquisition des données à l'extraction de paramètres pour quantifier le LCN du tissu osseux en trois dimensions. Ces méthodes peuvent par ailleurs servir dans d'autres applications. Bien que la plupart des méthodes de traitement d'images soient classiques, ces méthodes peuvent être utiles dans des applications avec des problèmes analogues de traitement de grands volumes de données ou de quantification de structures tubulaires. Les résultats quantitatifs obtenus sur le LCN dans les chapitres 5, 6 et 7 sont inédits et pourront servir de référence pour des études ultérieures sur le tissu osseux. Ces résultats nous permettent maintenant d'avoir une estimation plus précise de la nano porosité du tissu osseux, ce qui peut être utile pour des études de modélisation biomécanique ou de la simulation e micro mécanique. L'ensemble des travaux de cette thèse contribue donc à une meilleure connaissance de la structure 3D des lacunes et des canalicules et devrait permettre de mieux comprendre les mécanismes de la fragilité osseuse en coopération avec d'autres mesures physiques.

Symbol list

Lacunae:

Lc.N – number of lacunae
Lc.TV – total volume of lacunae (mm^3)
BV – bone volume (mm^3)
Lc.TV/BV – lacunar porosity (%)
Lc.N/BV – density of lacunae (mm^{-3})
Lc.V – average volume of lacuna (μm^3)
Cell.V – average volume of each cell (μm^3)
Lc.V/Cell.V – ratio between the average volume of lacuna and its belonging cell (%)
Lc.S – average surface area of lacuna (μm^2)
Lc.L1, Lc.L2 and Lc.L3 – average length, width and depth of lacuna (µm)
Lc.L1/Lc.L2 and Lc.L2/Lc.L3 – average anisotropy of lacuna
Lc.SMI – average structural model index of lacuna

Canaliculi:

Ca.TV – total volume of canaliculi (mm^3)
LCN.TV – total volume of the LCN (mm^3)
Ca.TV/BV – porosity of canaliculi (%)
LCN.TV/BV – porosity of the LCN (%)
Ca.V – average volume of canaliculi per cell (μm^3)
Ca.V/Cell.V – ratio between the average volume of canaliculi and the average volume of cell
Ca.V/Lc.V – ratio between the average volume of canaliculi and the average volume of lacuna
Ca.N – number of canaliculi per lacuna
Ca.N/Lc.V – ratio between the number of canaliculi per lacuna and the average volume of lacuna

Introduction

Osteoporosis is a bone disease which leads to bone fragility with the abnormalities of bone mass and density. Based on the diagnostic criteria published by the World Health Organization (WHO), about 6% of men and 21% of women aged over 50 years old suffer from osteoporosis [Kanis et al. (2016)]. In the European Union (EU) in 2010, there are 22 million women and 5.5 million men sustaining osteoporosis, and 3.5 million new fragility fractures occurred including major types of hip fractures, vertebral fractures, forearm fractures and some others. All of these fragility fractures have brought an economic burden of € 37 billion to the EU which is estimated to generate a growth of 25% in 2025 [Hernlund et al. (2013)]. Unfortunately, the mechanisms of bone fragility in disease such as osteoporosis are still partially understood.

Bone is a dynamic and living tissue which will regulate its density and strength with age and environmental changes. Recently, osteocytes, which play important roles in bone remodeling, have attracted an increasing number of attentions. Except for maintaining daily metabolic activities such as the transfer of nutrients and wastes, osteocytes also act as mechanosensors for the detection of mechanical pressure by large surface area exposed to interstitial fluid, which changes the bone structural properties to adapt to mechanical stimuli [Fonseca et al. (2014)]. The osteocyte system is deeply embedded inside the bone matrix and also called lacuno-canalicular network (LCN). The network is organized as a complex mesh structure where lacunae serve as nodes housing the cell body of osteocytes connected with each other through processes included in canaliculi. Through the LCN, numerous biochemical signals can be transported between different osteocytes allowing communication among bone cells. Because of the strategic location and spatial arrangement within bone matrix, the osteocyte system integrates biological and environmental information to orchestrate osteoblast and osteoclast activities for bone remodeling [Florencio-Silva et al. (2015)]. However, the mechanisms for stimuli-to-signal conversion inside the osteocytes system still need to be learned more and the quantitative evaluation and analysis of the LCN is also lacking.

Although several imaging techniques have recently been proposed, the 3D observation and analysis of the LCN at high spatial resolution is still challenging. In the past, the LCN was mainly investigated by a lot of 2D imaging modalities which are limited by the observation depth and do not allow to get a full picture of the 3D network. Some 3D imaging techniques have also been used to observe and analyze the LCN with the limited spatial resolution or field of view permitting only to observe few osteocytes. Besides, it is always a problem to achieve the automatic segmentation of canaliculi at the nanoscale and the quantitative data reported on the LCN for human bone samples are still limited.

The objective of this thesis was to quantify the LCN in a large number of human bone samples from magnified X-ray phase nano-CT at the ESRF. This required us to optimize the phase retrieval process and to develop efficient image processing methods to segment and quantify the LCN.

The thesis is divided into five different parts as follows:

(1) Introduction. We briefly introduce some basic knowledge about osteoporosis and the function of the osteocyte system. And we state the objective and the layout of the thesis.

(2) Background. We present the background of our work in 3 chapters.

In Chapter 1, we introduce the hierarchical structure of bone, the functions of bone cells and the main dynamic activities of bone from the embryo to adulthood. We highlight the importance of the LCN, which plays an essential role in regulating bone remodeling and review 2D and 3D imaging techniques to investigate of the LCN.

In Chapter 2, we make a brief review of third generation synchrotron radiation sources around the world, and then described in more details the European Synchrotron Radiation Facility (ESRF) and the ESRF-Extremely Brilliant Source project in the new century. We highlight two beamlines ID16A and ID16B of the ESRF where we scanned the samples in this work, and shortly introduced two main approaches to address the phase retrieval problem when performing the X-ray phase CT.

In Chapter 3, we review the state of art about the quantitative evaluation of the LCN which has raised an increasing interest during the last three years. We also introduced some parameters about the lacunae and canaliculi reported in previous references.

(3) Contribution. This part includes 4 chapters in the thesis.

In Chapter 4 we studied and compare quantitatively different phase retrieval to image the LCN at the nanoscale resolution. We extended Paganin's method from a single distance to multi-distance acquisitions, and compared it to a homogeneous version of the contrast transfer function (CTF) method for the reconstruction of bone samples.

In Chapter 5, we present the segmentation methods, that we will use to extract the lacunae and canaliculi from the reconstructed volumes, and described the parameters calculated for the evaluation of the LCN. We report the quantitative results from the data acquired at the voxel size of 120 nm on beamline ID16A.

In Chapter 6, we present the quantification of the LCN obtained from ID16A images at higher spatial resolution (50 nm and 30 nm). We also compare the quantifications at 30 nm with those of the cropped volumes at 120 nm from the same samples and sharing the same field of view.

In Chapter 7, we report the analysis performed on the beamline ID16B at 100nm on the 27 samples of the MULTIPS project. We divided the data into two groups by the gender and made a comparison between groups.

(4) Conclusion and perspectives. We summarize our contributions in the previous chapters and pointed out the plan for the work in the future.

(5) Annex. In this part, we put some images and tables about our segmentation and quantification as a supplement to the text.

Chapter 1: Bone and osteocyte

Contents

1.1 Introduction

Bone has a very important role in the human body since it acts as a basic framework to support weight, protect the internal organs and store minerals. In order to maintain normal motor function, bone must have complex natural properties. On the one hand, bones must be stiff because they need to carry loads and tolerate the compression. On the other hand, bone must be flexible and elastic to change shape and absorb the energy from deformation. Also, bone must be light to facilitate movement. All of these seemingly contradictory properties are determined by bone's material composition and structural design [Leali et al. (2009)].

1.2 Bone structure

Human bones can be classified into different types such as long bones, short bones, flat bones and irregular bones. A long bone is a good example to illustrate bone structures because it contains all types of bone structures (see Fig. 1.1).

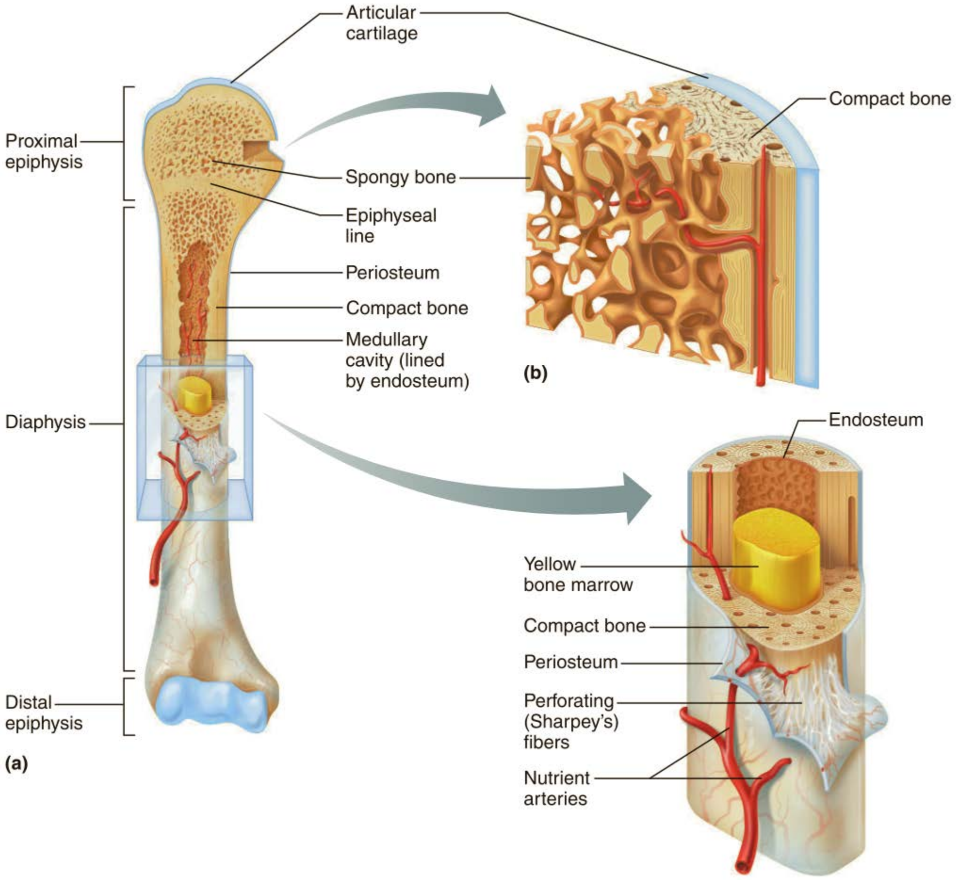

Figure 1.1 Structures of a long bone [Marieb et al. (2013)].

At the macro scale, bone is made up of two major bone tissues (i.e. compact bone and spongy bone), and some other components such as periosteum, endosteum, articular cartilage, marrow, blood vessels and nerves as shown in Fig. 1.2 [Fratzl et al. (2007)]. Compact bone distributes in regions near the outside of the diaphysis and the epiphysis. The lamellae of compact bone such as the outer and inner circumferential lamella are packed more regularly and tightly. There are some perforating canals (i.e. Volkmann canals) traversing circumferential lamellae which serve as the channels of small blood vessels and nerves to supply energy and nutrition [Singh (2015)]. Spongy bone, located in the inside of bone, consists of a large number of bone trabeculae and forms a complex porous network. The cavity of the network, called medullary cavity, is full of red marrow to provide blood cells [Eliaz et al. (2017)]. Besides, the outer surface of compact bone is covered by periosteum while the inner surface of compact bone and the surfaces of trabecula, medullary cavity and perforating canal are covered by endosteum. The function of periosteum and endosteum is mainly for providing protection and nutrition for bone tissue [Colnot (2009)].

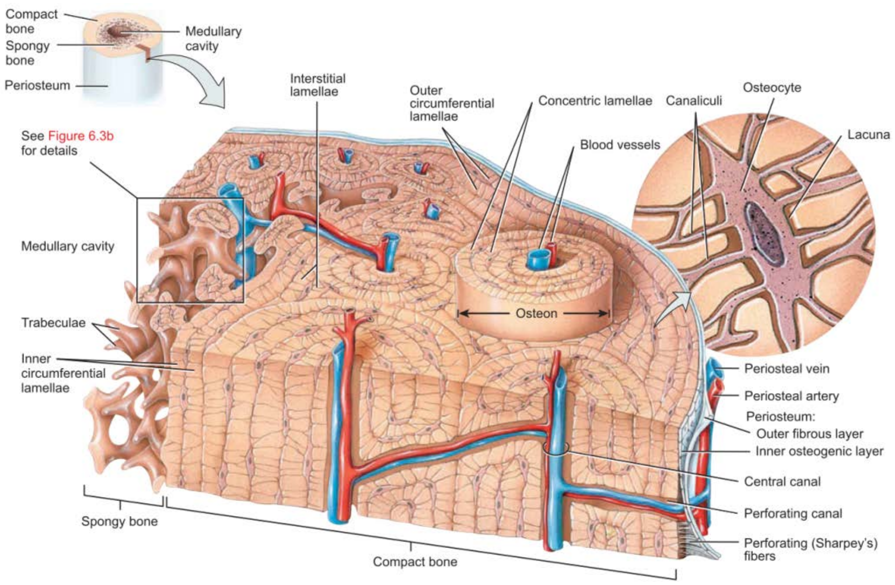

(a) Osteons (haversian systems) in compact bone and trabeculae in spongy bone

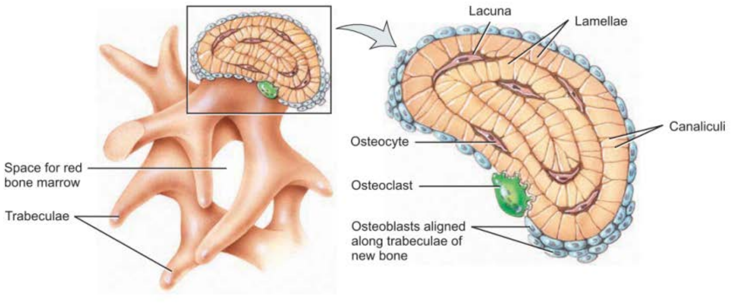

(b) Enlarged aspect of spongy bone trabeculae

(c) Details of a section of a trabecula

Figure 1.2 Histology of compact and spongy bone [Tortora et al. (2012)].

At the micro scale, the anatomical unit of compact bone is called osteon (i.e. Haversian system). Osteons are roughly cylindrical structures and situated in the regions between the outer and inner circumferential lamella. The central canal (or Haversian canal) is in the center of the osteon containing blood vessel and nerves which allow communication with exterior by connecting ones through Volkmann canals. Some lamellae surround the central canal like concentric circles, which are made up of collagen fibers running in a spiral manner and the opposite direction from neighbor layers [Olszta et al. (2007)]. Also, a number of small cavities called lacunae, hosting the osteocytes, can be found at the borders of lamellae.

At the nano scale, tiny canals, called canaliculi, can be observed: they connect adjacent lacunae and form a complex network, the lacuno-canalicular network (LCN). Canaliculi serve as transportation pipelines to permit osteocytes to communicate with each other, to receive nutrient supply and to remove waste through gap junctions [Marieb et al. (2018)]. Besides, some collagen fibrils can be seen at the same time. As the basic building unit of the bone material, the collagen fibrils are made up of collagen molecules secreted by osteoblasts with sizes estimated to be 300 nm long and 1.5 nm thick [Eliaz et al. (2017)]. It is worth mentioning that the arrangement of fibrils and lamellae have an impact on the biomechanical properties of bone and in particular on their toughness [Ke et al. (2014)].

1.3 Bone cells

In bone tissue, bone cells represent a small volume compared with bone matrix, but play crucial roles in adjusting bone structural properties in response to environmental changes [Florencio-Silva et al. (2015)]. There are mainly four types of bone cells: osteoblasts, osteocytes, osteogenic cells and osteoclasts. They are illustrated schematically in Figure 1.3 and with SEM microscopy in Fig. 1.4

Osteoblasts situated on the surface of the growing areas of bone and normally arranged in a layer, are involved in bone formation. Osteoblasts can secret collagen molecules and organic matrix to form unmineralized extracellular matrix, which is also called osteoid [Ralston (2017)]. Meanwhile, osteoblasts also secret matrix vesicles to bone matrix by the way of cell membrane budding, which contain inorganic salt crystals such as hydroxyapatite by the combination of calcium phosphate and magnesium hydroxide. After the rupture of vesicles, these salt crystals are released to bone matrix increasing the deposition of bone salts and finally leading to mineralization [Capulli et al. (2014)]. Also, osteoblasts become osteocytes when they are entrapped in the mineralized matrix.

Osteocytes are the most abundant bone cells and located between or within lamellae. The mature osteocyte looks like a flat ellipsoid, whose cell body lies in the lacuna while the processes are harbored in canaliculi. Osteocytes achieve communication of metabolic activities with adjacent cells by gap junctions which pass through canaliculi connecting corresponding lacunae [Rochefort et al. (2010)]. The interstitial fluid in the lacunae and canaliculi can provide nutrition for osteocytes, maintain calcium balance and remove waste.

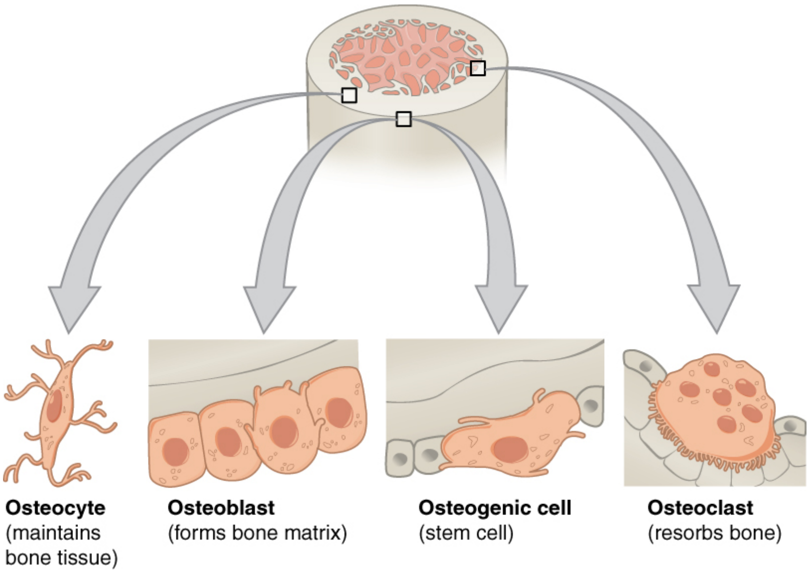

Figure 1.3 Four types of bone cells [Image from: https://opentextbc.ca/anatomyandphysiology/chapter/6-3-bone-structure/].

Osteogenic cells are derived from mesenchymal stem cells (MSC) and located in deep layers of the periosteum and the marrow. The main function of osteogenic cells is that they can differentiate and develop into osteoblasts under the stimulation of some factors such as bone morphogenetic proteins (BMPs), due to the lack of mitotic activity of osteoblasts [Fakhry (2013)].

Osteoclasts which can be found in the resorption bays of the surface (or Howship's lacunae) are involved in bone resorption. Different from osteoblasts and osteocytes, osteoclasts are derived from the granulocyte-macrophage colony forming units (CFU-GM) which are from bone marrow [Menaa et al. (2000)]. Osteoclasts mainly work for the dissolution and resorption of old, injured, or unnecessary bone. In the sealing zone between osteoclasts and bone tissue, osteoclasts release organic acids such as citric acid and lactic acid to dissolve calcium slat crystals, and hydrolytic enzymes such as cathepsins and matrix metalloprotease groups to degrade collagen [Yavropoulou et al. (2008)].

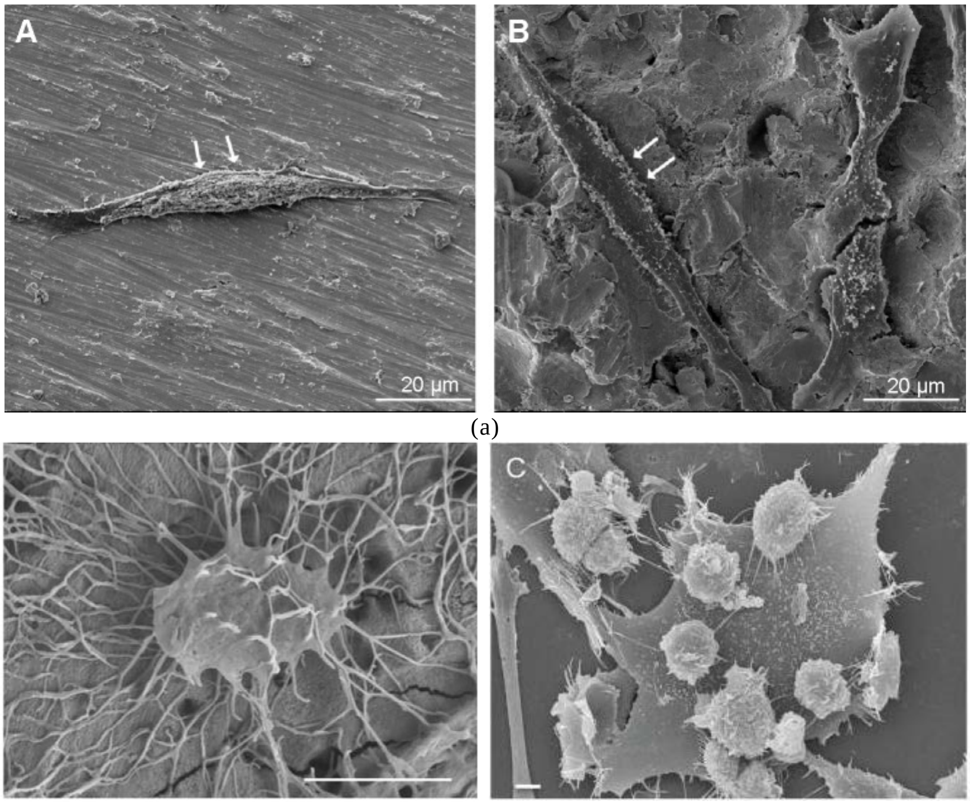

(a)

(b) (c)

Figure 1.4 SEM images of bone cells. (a) Osteoblasts [Thiel et al. (2018)]; (b) Osteocyte. Bar=10 µm [Sasaki et al. (2015)]; (c) Osteoclasts [Narducci et al. (2010)].

1.4 Bone formation, growth and remodeling

Bone starts to form within mesenchyme during the embryo and will keep growing after birth. Normally, bone stops turning longer and wider after reaching adulthood but bone remodeling lasts a lifetime with a rate which will gradually decrease when aging.

1.4.1 Bone formation

There are two patterns for bone formation: intramembranous ossification and endochondral ossification. By intramembranous ossification, only a few bones are formed such as the flat bones of the skull, mandible and clavicle, which start as fibrous membranes in embryonic period. The mechanism of intramembranous ossification illustrated in Fig. 1.5 is simpler than endochondral ossification. In the early region of osteogenesis, mesenchymal cells begin to get together as well as to differentiate into osteogenic cells and then into osteoblasts with the capillary proliferation. This position is called an ossification center from which bone formation will spread to the surrounding. Then, osteoblasts will secret extracellular matrix until they are entrapped within it and turn to osteocytes. Next, mineral salts start to be stored through the canaliculi and the extracellular matrix achieves calcification. With the spreading of bone formation, primary bone trabeculae are formed which will gradually generate a network structure to form spongy bone. Meanwhile, the mesenchyme on the surface of the spongy bone develops into the periosteum. After this, bone will further start to grow and remodel.

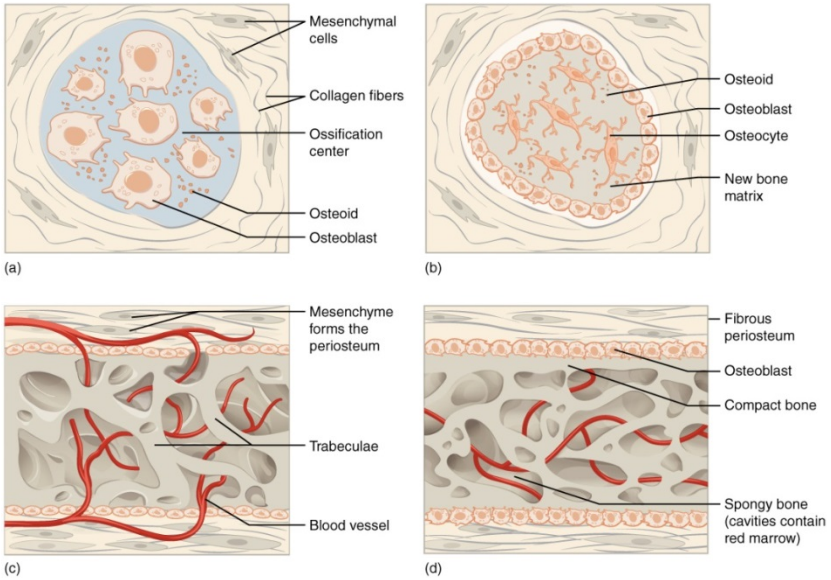

Figure 1.5 Intramembranous Ossification [Image from: https://opentextbc.ca/anatomyandphysiology/chapter/6-4-bone-formation-and-development/].

Endochondral ossification is a relatively complex process which will replace hyaline cartilage by bone and form most bones of a human body. Figure 1.6 shows the process of endochondral ossification in a lone bone from the embryo to childhood. Mesenchymal cells first gather together and differentiate into chondroblasts which secret cartilage extracellular matrix and develop into chondrocytes to generate the cartilage model covered by perichondrium. In the middle region of the cartilage model, osteogenic cells inside the perichondrium differentiate into osteoblasts to form primary spongy bone on the surface of the cartilage, which is also called bone collar. After formation of bone collar, perichondrium is known as periosteum. Meanwhile, near the middle of the cartilage model, the cartilage extracellular matrix starts to calcify leading to death of chondrocytes which leave spaces merged to lacunae. This region becomes the primary ossification center where primary ossification will spread to both ends of the model and most of cartilage will be replaced by bone. With the ossification, osteoclasts dissolve and absorb mixed bone trabeculae and the cavities are enlarged which eventually combine to become the medullary cavity. After birth, secondary ossification center will develop at the center of cartilage in the ends of the long bone, whose bone formation is similar with that in primary ossification center. Finally, the hyaline cartilage on the surface of epiphyses is kept as the articular cartilage, and the hyaline cartilage between the epiphysis and diaphysis as the epiphyseal plate which is related with bone growth later.

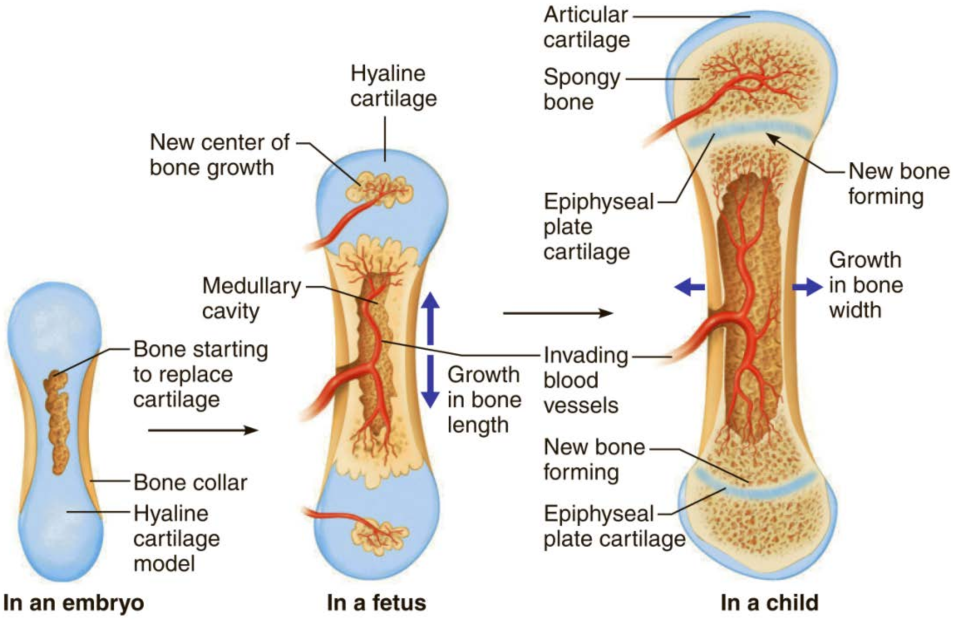

Figure 1.6 Endochondral ossification from the embryo to childhood [Marieb et al. (2018)].

1.4.2 Bone growth

Because osteocytes are not able to differentiate, bone growth cannot process from inside but proceeds by adding new bone on the surface of the previous one to make bone expand outward. Bone growth consists of two different types: growth in thickness and growth in length (see Fig. 1.7).

Bone grows in thickness by the way of appositional growth. Briefly, osteoblasts in the periosteum secret extracellular matrix and develop into osteocytes, which form new bone after calcification and the deposition of mineral salts. In this way, the thickness of bone is increased with the deposition of more circumferential lamellae. Meanwhile, osteoclasts resorb old bone lining the medullary cavity, which increases the diameter of the medullary cavity.

The growth of bone in length is based on the epiphyseal plate, which is made up of two processes, i.e. interstitial growth of cartilage on the epiphyseal plate surface and replacement of cartilage on the diaphyseal side of the plate by bone. The epiphyseal plate has a zone arrangement consisting of 4 parts from the end to the middle of bone: resting zone, where small chondroblasts arrange in a scattering way; proliferating zone, where chondroblasts differentiate fast and secret extracellular matrix; hypertrophic zone, where large chondrocytes arrange in columns; calcified zone, where the extracellular matrix has calcified and most chondrocytes are dead. When bone grows in length, new cartilage is formed on the surface of the articular cartilage and the external side of the epiphyseal plate. Meanwhile, the old cartilage on the internal side towards the diaphyseal side of the plate is replaced by bone through endochondral ossification and the medullary cavity is enlarged by the resorption of osteoclasts. Generally, the epiphyseal plate will close in the end of adolescence and fade to be the epiphyseal line, which means bone stops lengthening.

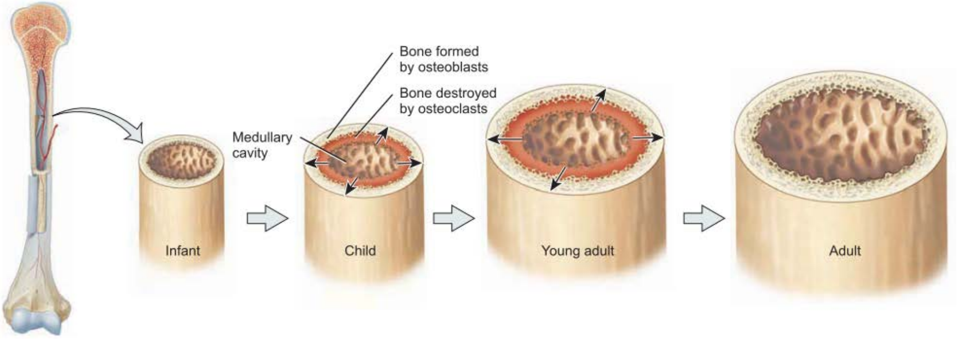

(a)

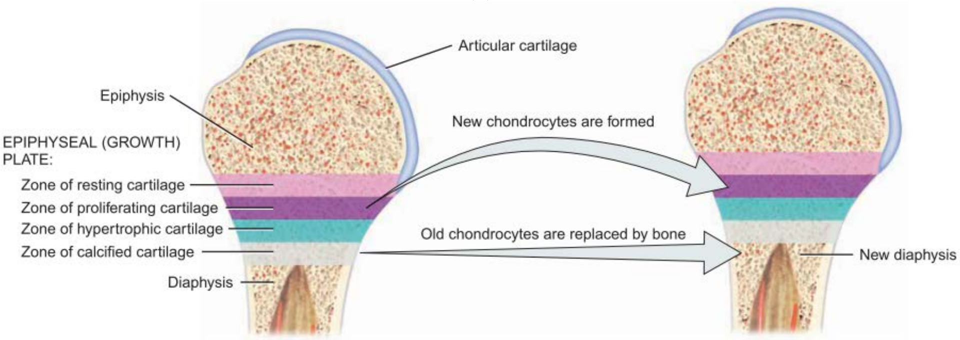

(b)

Figure 1.7 Bone growth in thickness and length, (a) and (b) respectively [Tortora et al. (2012)].

1.4.3 Bone remodeling

Bone is a dynamic and active tissue which will be continually renewed and repaired throughout life by the process of bone remodeling. Bone remodeling is the ongoing replacement of old bone by new bone which involves the action of both osteoclasts and osteoblasts. About 4% of compact bone and 20% of spongy bone of a human body is remodeled each year [Hadjidakis et al. (2006)]. Bone remodeling is very important because it makes bone more adaptive to the environment. For example, bone may turn thicker and stronger after remodeling in order to carry heavy loads, or change its shape being more resistant to the external pressure.

Figure 1.8 illustrates the four different stages of the bone remodeling cycle: resorption, reversal, formation and quiescence [Ralston (2017)]. Bone resorption starts with attraction of mononuclear osteoclast precursors to the remodeling region on the surface of the bone. Then, these mononuclear osteoclast precursors differentiate and fuse together to form multinucleated osteoclasts, which secret hydrolytic enzymes and acids to organic components and minerals of bone. In the reversal stage after resorption, osteoclasts depart and osteogenic cells take the surface preparing for regulators and differentiating into osteoblasts. Next, bone formation is achieved by osteoblasts secreting osteoid which will then be calcified and entrap osteoblasts developing into osteocytes. In this way, old bone is resorbed and gradually replaced by new bone. After replacement is completed, there is a quiescence stage when bone lining cells cover the surface and prepare for a new remodeling cycle.

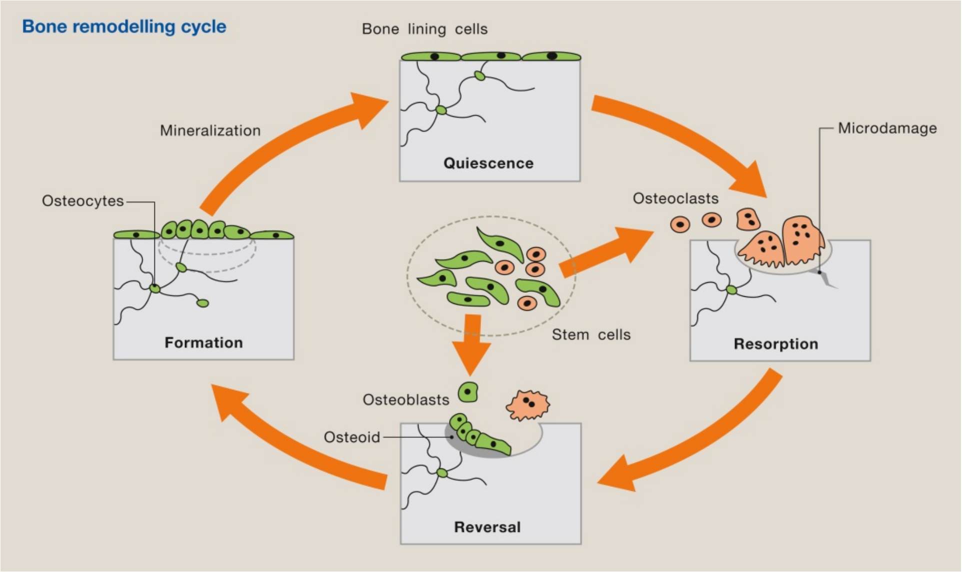

Figure 1.8 Bone remodeling cycle [Ralston (2017)].

1.5 The function of osteocytes

As the most abundant bone cells, osteocytes may act as orchestrators of bone remodeling to regulate the activities of both osteoclasts and osteoblasts [Schaffler et al. (2014)]. It is hypothetized that osteocyte apoptosis could locally function as a recruiting signal of osteoclasts which would increase bone resorption [Plotkin (2014)]. Thus, improving our knowledge about osteocytes could be helpful for targeted bone remodeling. Moreover, osteocytes could release factors which have direct effects on osteoblast activities. For example, osteocyte-derived nitric oxide (NO) in vivo has been shown to promote osteoblast differentiation [Dallas et al. (2013)]. Besides, WNT1 produced by osteocytes plays essential roles in the control of bone formation, since its inactivation leads to low bone mass and spontaneous fractures, and its overexpression increases bone formation resulting in more compact and spongy bone [Joeng et al. (2017)].

The osteocyte system is deeply embedded inside the bone matrix and lie with the so called lacuno-canalicular network (LCN), which is a complex mesh structure where lacunae serve as nodes hosting the osteocytes and are connected with each other by channels called canaliculi (as shown in Fig. 1.9). By gap junctions, the cytoplasmic processes of osteocytes link up with those of their neighboring osteocytes, and of osteoblasts close to the bone surface [Florencio-Silva et al. (2015)]. The LCN permits the communication between numerous biochemical signals to achieve information integration and stimuli interaction. There is an assumption that the LCN could be regarded as a signal amplifier [Wang et al. (2007)]. When detecting some micro-cracks, osteocytes could release biochemical signals which could be triggers for the recruitment of osteoclasts and osteoblasts. It has been suggested that due to osteocytes apoptosis, the LCN could be disrupted and could not maintain the signal transmission, thus hindering the normal bone remodeling and probably leading to bone fragility [Rochefort et al. (2010)].

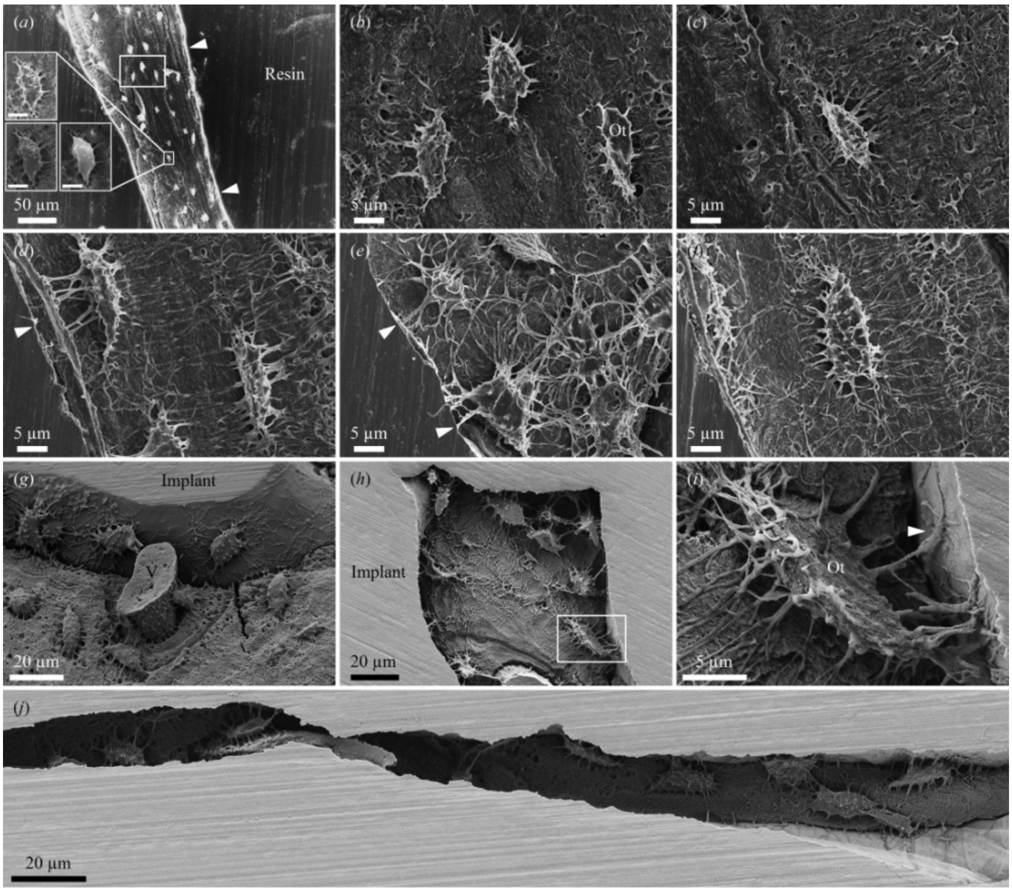

Figure 1.9 SEM images of osteocytes at different resolution [Shah et al. (2016)].

1.6 Imaging osteocytes

Until now, the investigation of LCN is still challenging because of the deeply embedded location and the complexity of the network. The LCN has been mainly investigated by 2D imaging techniques while there have been developments in 3D imaging recently.

1.6.1 2D imaging techniques

1.6.1.1 Light microscopy (LM)

Light microscopy (LM), sometimes called optical microscopy, is a traditional imaging technique to observe the object by visible light. It can realize magnification by utilizing a series of lenses and optimizing their combination. It has been used to investigate LCN for many years [Sissons et al. (1990)], [Marotti et al. (1995)], [Palumbo et al. (2001)], [Bonewald (2011)] (Fig. 1.10). Standard light microscopy does not damage samples but its most common limitation is that the spatial resolution is restricted around 200 nm due to the diffraction limit of visible light. Besides, the preparation of scanned specimens may be time-consuming because it requires the cutting of thin sections and staining processes as alizarin or tetracycline labeling [Sissons et al. (1990)].

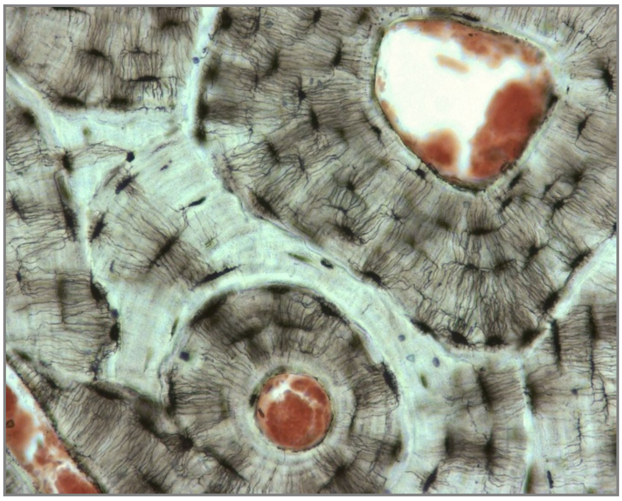

Figure 1.10 Light microscopy. Haversian canals and the osteocyte system from the transverse section of human phalanx [Marenzana et al. (2013)].

1.6.1.2 Electron microscopy

Since Ernst Ruska and Max Knoll constructed the first prototype in 1931, electron microscopes have been widely used in the field of biomedicine. Electron microscopy makes use of the beam of accelerated electrons instead of visible light. Due to shorter wavelength of electrons than visible photons, it achieves higher spatial resolution than light microscopy.

1.6.1.2.1 Transmission electron microscopy (TEM)

The principle of Transmission electron microscopy (TEM) is similar to that of light microscopy. It utilizes a beam of electrons which is emitted by a tungsten filament cathode and focused by a condenser lens to interact with the specimen. By detecting the electrons passing through the object, information reflecting the structure and properties of the specimen can be recorded by a camera. TEM has been used to study the morphology of the LCN [Shah et al. (2015)] (Fig. 1.11).

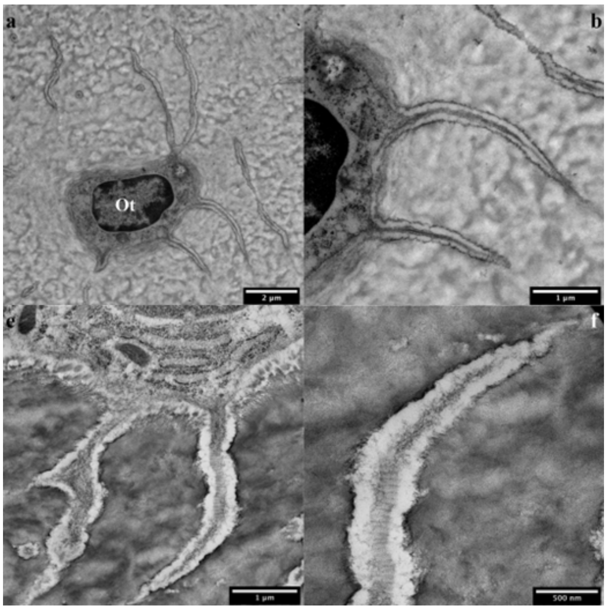

Figure 1.11 Transmission electron microscopy. Well-preserved morphology of an osteocyte and osteocyte processes [Shah et al. (2015)].

1.6.1.2.2 Scanning electron microscopy (SEM)

Scanning electron microscopy (SEM) uses a focused beam of electrons to scan the sample in a raster pattern, which is different from TEM. Because of interaction between the electrons and the specimen, several particles such as secondary electrons, back-scattered electrons, light and X-rays photons are emitted. The SEM image contains information reflecting the topology and the composition of the surface. SEM has been used to investigate the property of the LCN in the 2D mode [Shah et al. (2017)] (Fig. 1.12).

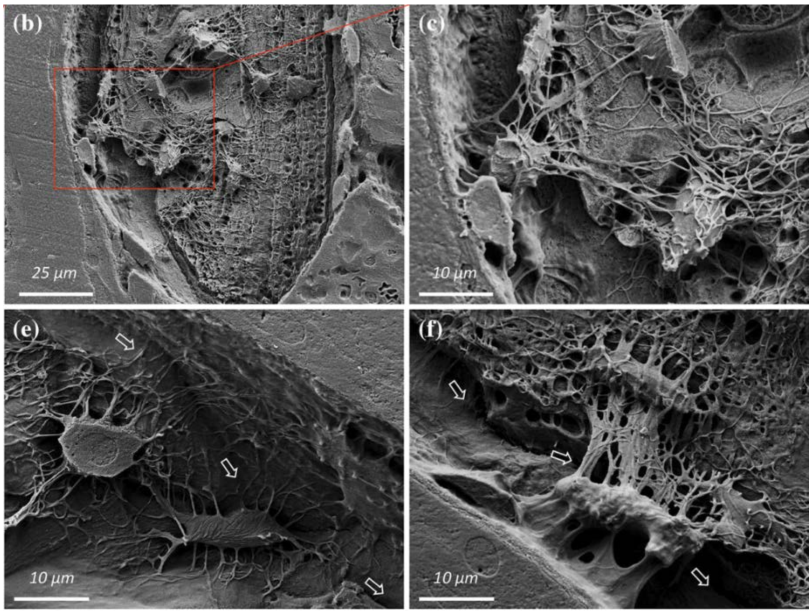

Figure 1.12 Scanning electron microscope. Osteocytes and canaliculi located in a large autogenous bone fragment [Shah et al. (2017)].

1.6.1.2.3 Atomic force microscopy (AFM)

Atomic-force microscopy (AFM) or scanning-force microscopy (SFM) is a type of scanning probe microscopy (SPM). It scans the specimen surface by a cantilever with a sharp probe at its end which can perceive and magnify forces between atoms. Some researchers have used AFM to observe the structure and analyze the distribution of the LCN [Katsamenis et al. (2013)], [Lin et al. (2011)] (Fig. 1.13).

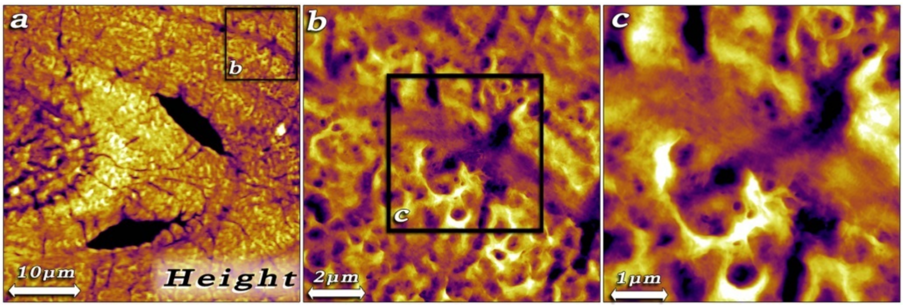

(a)

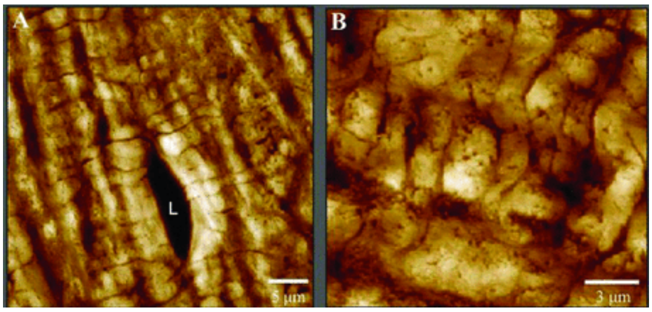

(b)

Figure 1.13 Atomic-force microscopy. (a) The lacuno-canalicular network of the osteon treated with ethylenediaminetetraacetic acid (EDTA) [Katsamenis et al. (2013)]; (b) the distribution of lacunae (L) and canaliculi of demineralized osteons in radial section [Lin et al. (2011)].

1.6.2 3D imaging techniques

1.6.2.1 Confocal laser scanning microscopy (CLSM)

Confocal laser scanning microscopy (CLSM) uses a point light source to illuminate the sample and the reflected fluorescence is collected by the object lenses and sent to the photo detector. There are two identical pinholes in front of the light source and detector, by which only light very close to the focal plane can be detected while the other will be eliminated [Bozal et al. (2011)]. Each 2D image in a focal plane is the optical cross-section of the specimen, also known as an optical slice. By recording a stack of 2D slices, a 3D image can be created and processed with some professional software. For instance this technique has been used in two recent studies to image the LCN in 3D as illustrated in Figure 1.14 [Repp et al. (2017)], [Hemmatian et al. (2017)].

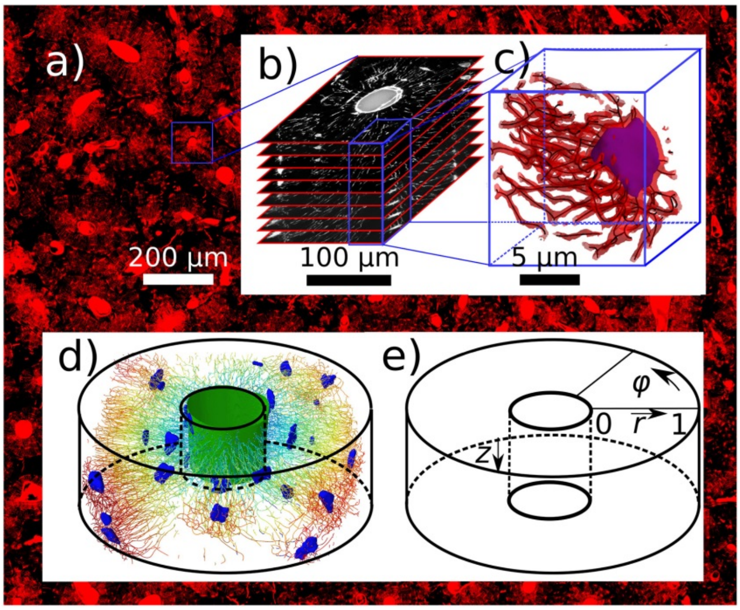

(a)

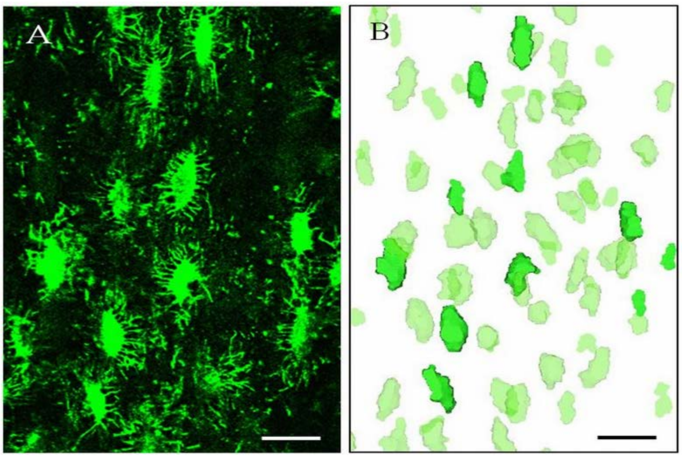

(b)

Figure 1.14 Confocal laser scanning microscopy. (a) Stack of images and 3D rendering results of the LCN from the femoral cross-section [Repp et al. (2017)]; (b) Z-projection and CLSM-based 3D renderings of the lacunae in the mouse cortical bone. Scale bar = 20 μm [Hemmatian et al. (2017)].

1.6.2.2 Electron microscopy

1.6.2.2.1 Ultra-high voltage electron microscopy (UHVEM)

By recording a series of TEM images under different directions, 3D tomographic reconstructions can be applied to obtain the three-dimensional structure of the specimen. Ultra-high voltage electron microscopy (UHVEM) has a basically same principle with traditional TEM, but an acceleration voltage of 3MV which is much higher [Fujita (1986)]This technique was used for instance to reconstruct a single canaliculus from chicken calvariae [Kamioka (2015)] (Fig. 1.15).

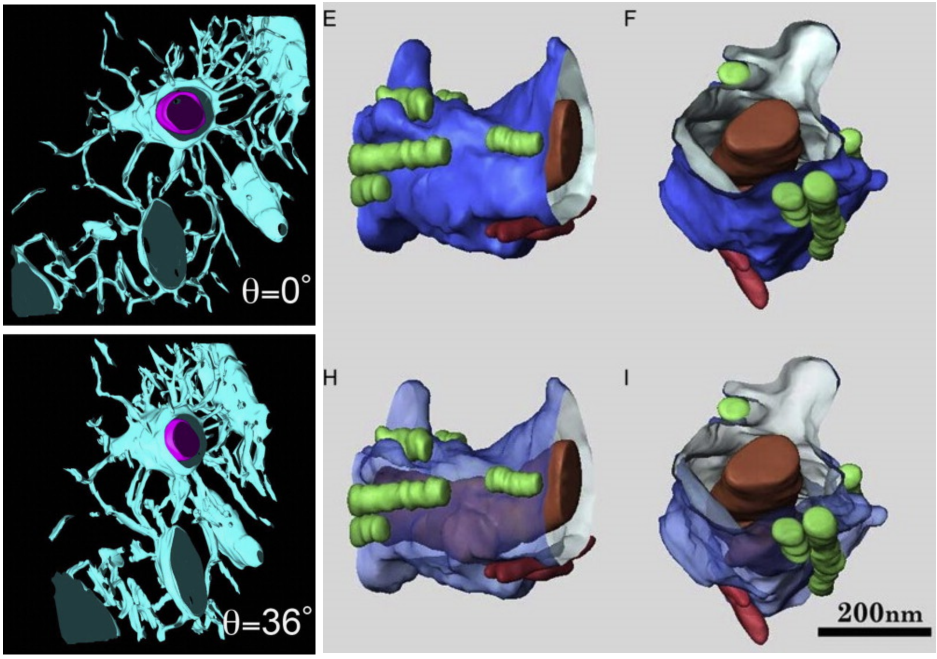

(a) (b)

Figure 1.15 3D reconstruction from UHVEM. (a) Young chick osteoid-osteocytes; (b) Canaliculus containing an osteocyte process, orange: an osteocyte process, blue: a translucent canalicular wall, green and red : perpendicular cell processes for the running of collagen fibrils [Kamioka (2015)].

1.6.2.2.2 Serial block-face SEM (SBF SEM)

Serial block-face SEM (SBF SEM) takes advantage of an ultramicrotome to cut serial sections from the block face after each imaging of the surface. The 3D image can be generated from the stack of 2D SEM images which are acquired by sample imaging and section cutting repeatedly. SBF SEM has been used to image the osteocyte from mouse tibia diaphysis [Goggin et al. (2016)] (Fig. 1.16).

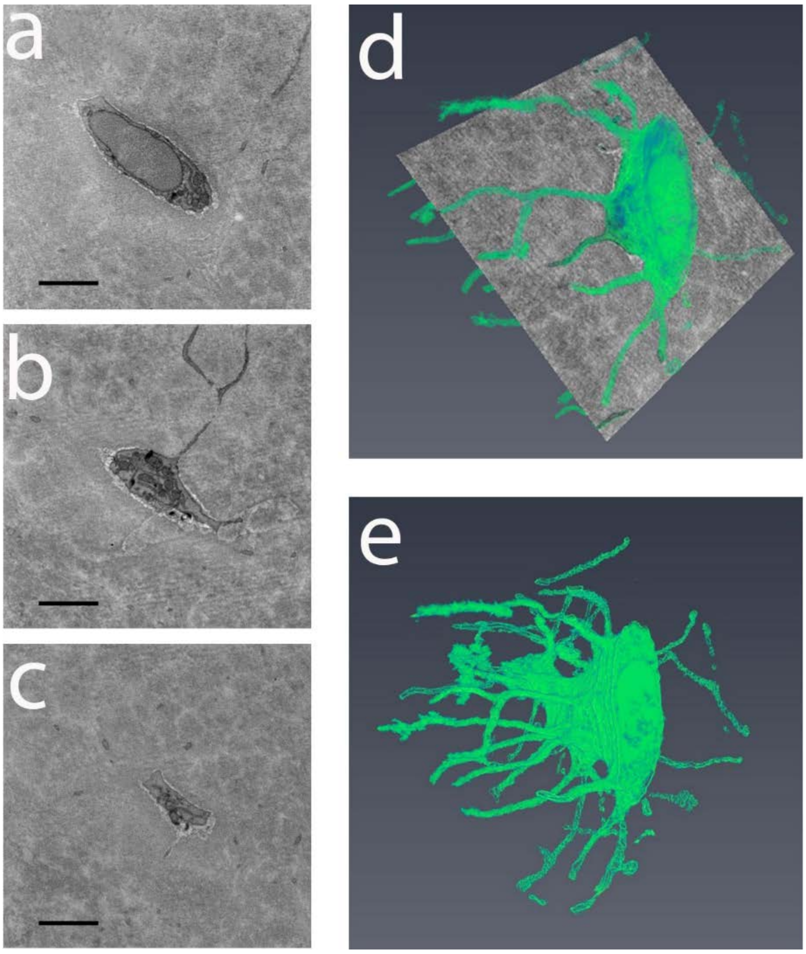

Figure 1.16 Osteocyte from mouse tibia diaphysis imaged by SBF SEM. Scale bar = 2 µm [Goggin et al. (2016)].

1.6.2.2.3 Serial focused ion beam SEM (serial FIB SEM)

Serial focused ion beam SEM (serial FIB SEM) uses a focused beam of ions instead of a focused beam of electrons in conventional SEM. After scanning the surface, the focused beam of ions is used to mill the specimen. Similarly, a sequence of images can be produced through the specimen. Figure 1.17 illustrates serial backscattered images and 3D reconstructions of osteoblasts and osteocytes located in the metaphyseal trabeculae by FIB-SEM observation [Schneider et al. (2011)], [Hasegawa et al. (2018)].

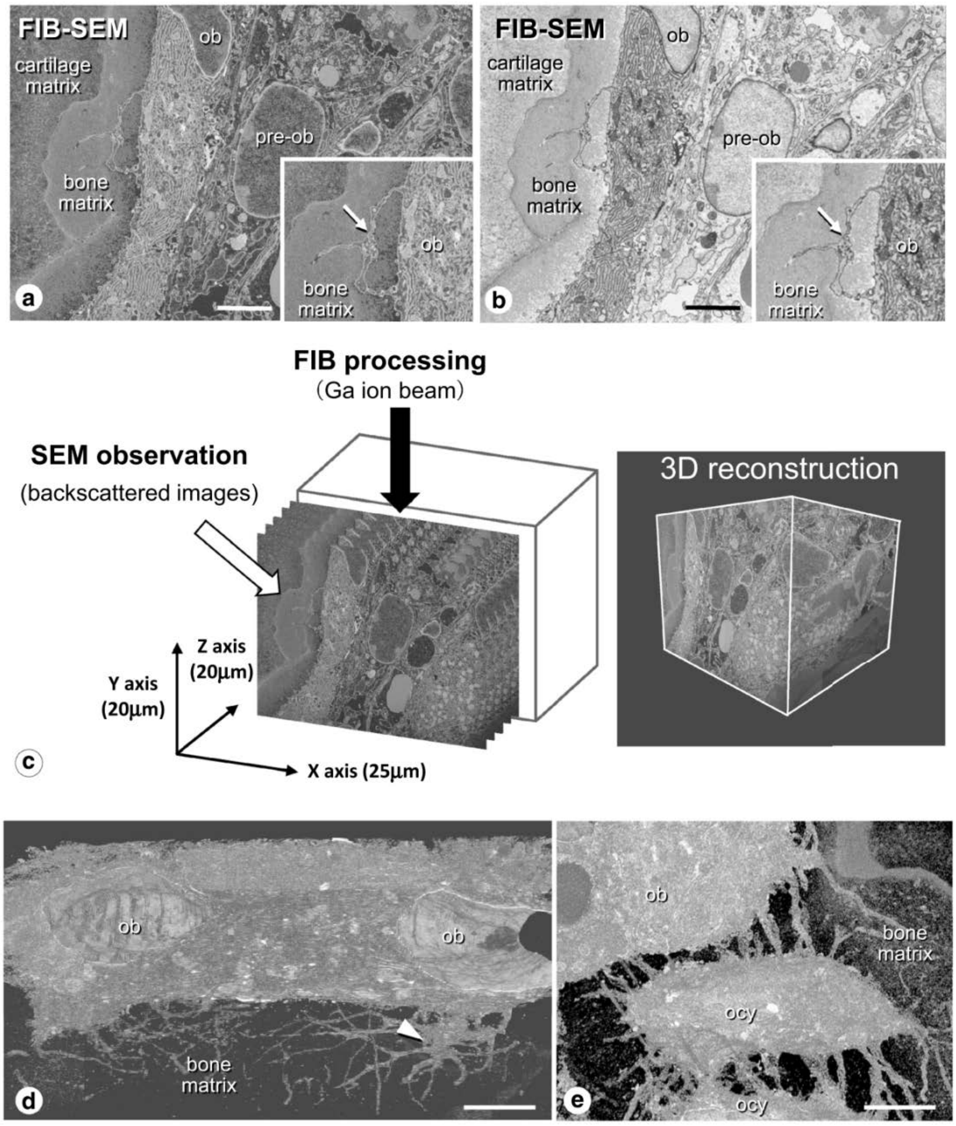

Figure 1.17 Serial backscattered images and 3D reconstructions of osteoblasts and osteocytes located in the metaphyseal trabeculae by FIB-SEM observation [Hasegawa et al. (2018)].

1.6.2.3 X-ray computerized tomography

X-ray computerized tomography (CT) can realize non-destructive visualization of interior structure within the specimen. Based on recording a series of X-ray projection images at different angles of views, 3D maps are generated by means of tomographic reconstruction, which can be used to analyze the three-dimensional geometry and properties of the sample.

1.6.2.3.1 Laboratory based X-ray microscopy

Laboratory based X-ray microscopy combines the principles of X-ray CT and light microscopy by using X-ray projections and magnifying the images by condenser and object lenses [Dalasm et al. (2013)]. It can also exploit the Zernike phase contrast technique to enhance the visibility of edges and boundaries.

ZEISS Xradia 800 Ultra X-ray microscope claims to achieve spatial resolution as fine as 50 nm, the highest among lab-based X-ray imaging systems. The microscope contains absorption and phase contrast imaging modes and X-ray energy of 8 keV. Two osteocyte lacunae with canalicular network have been observed using this microscope (see Fig. 1.18).

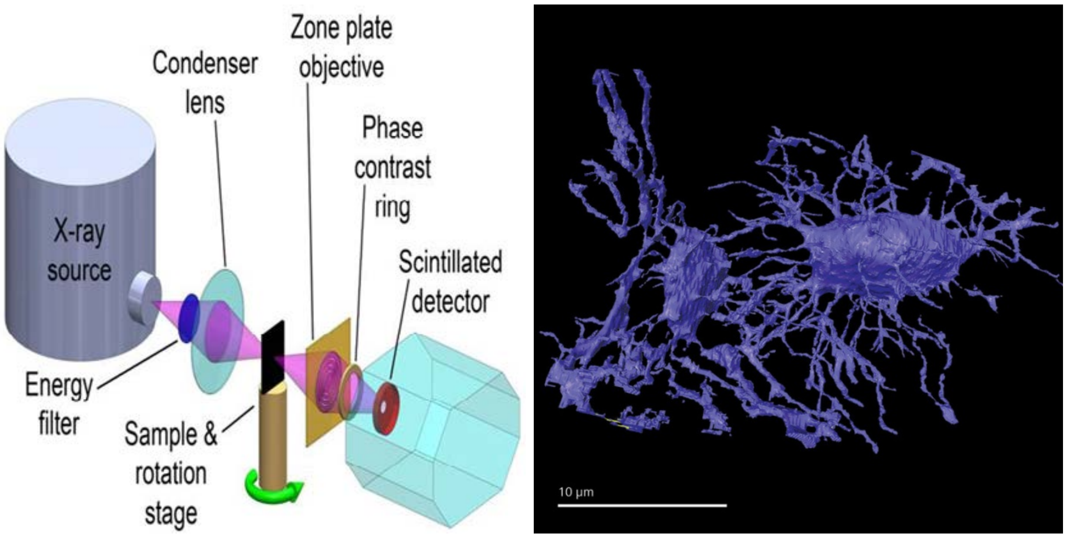

(a) (b)

Figure 1.18 Laboratory based X-ray CT. (a) Schematic illustration of the Ultra X-ray microscope [Image from: http://www.cmu.edu/me/xctf/facility/index.html]; (b) Two osteocyte lacunae with canalicular network, Specimen courtesy of R. Recker, Creighton University [Image from: http://www.zeiss.com/microscopy/en_de/products/x-ray-microscopy/zeiss-xradia-800-ultra.html].

1.6.2.3.2 Synchrotron radiation-based CT (SR CT)

Synchrotron radiation-based CT (SR CT) is based on synchrotron radiation source, which provides high-energy and parallel monochromatic X-rays. Due to the high flux of synchrotron sources, SR CT can acquire scans with low noise and very high special resolution. This technique will be detailed in more details in the next chapter.

(1) Transmission X-ray microscopy (TXM)

Transmission X-ray microscopy (TXM) is a type of X-ray microscopy, which puts a capillary condenser after the source to focus the beam into a pinhole and the specimen is scanned in the focus plane [Andrews et al. (2010)]. Besides, Fresnel zone plate was used as objective lens to re-focus the beam onto the detector in order to produce the magnified image. TXM was recently proposed to investigate bone features such as lacunae and canaliculi in the cortical bone as shown in Fig. 1.19 [Brock et al. (2013)].

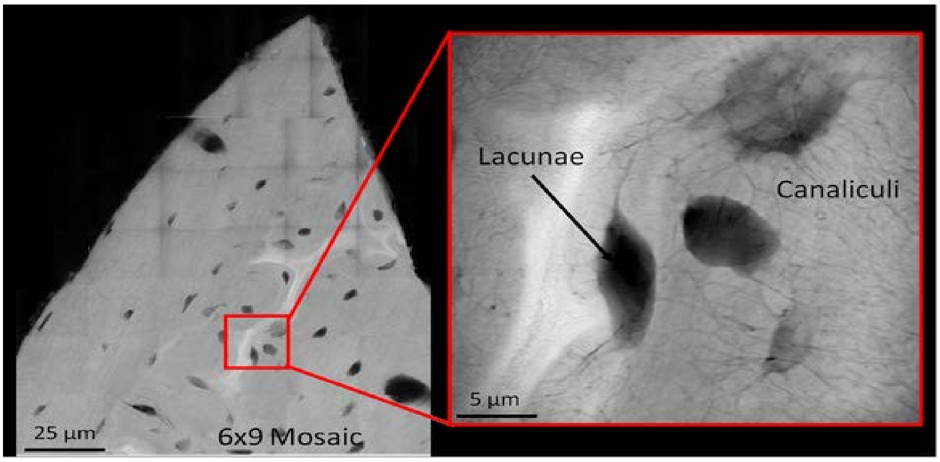

Figure 1.19 Representative TXM absorption contrast image illustrating lacunae and canaliculi present in rat cortical bone [Brock et al. (2013)].

(2) SR micro-CT

The basic principle of SR micro-CT is the same as that of conventional X-ray micro-CT, but the difference is the use of synchrotron radiation sources which brings several benefits. Due to the high brilliance of the X-ray beam, SR micro-CT permits to image the sample with good contrast and high SNR under a relatively short scanning time (Salomé, Peyrin, MedPhys 1999). SR micro-CT has shown good ability to observe microstructures of the bone and even the LCN [Pacureanu et al. (2012)]~~,~~[Andronowski et al. (2017)] (Fig. 1.20).

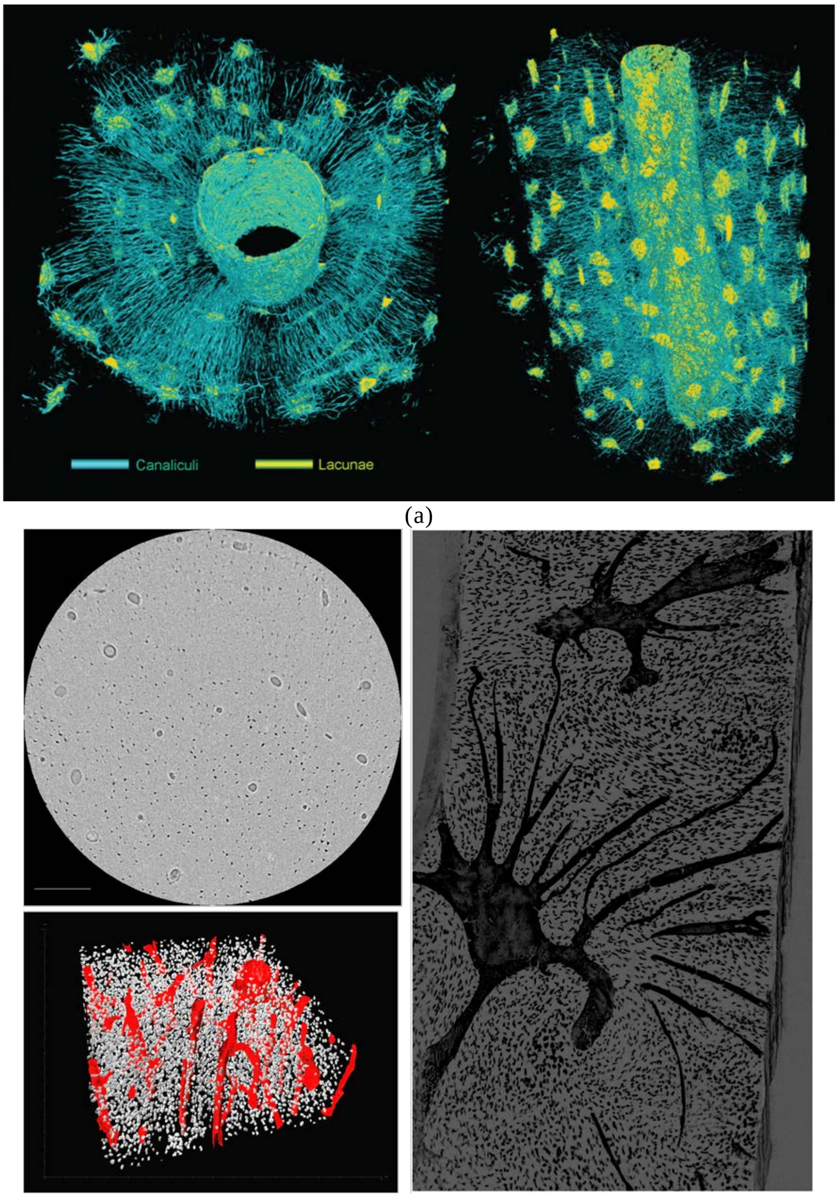

(a)

(b)

Figure 1.20 SR micro-CT. (a) 3D rendering of the osteocyte network organized around a Haversian canal [Pacureanu et al. (2012)]; (b) SR micro-CT single slice, minimum projection re-slice and 3D render of cortical bone [Andronowski et al. (2017)].

(3) X-ray phase tomography

X-ray phase tomography in propagation mode cab easily implemented at synchrotron sources[Cloetens et al. (1997)]. It was used to image the LCN in femoral cortical bone at the European Synchrotron Radiation Facility [Langer et al. (2012)]. A focused monochromatic X-ray beam was used as the illumination source. During the scanning, the specimen was moved downstream of the focus and imaged at 4 different distances. More technical detail will be introduced in later chapters. Figure 1.21 displays one reconstructed slice and segmentation of using X-ray phase tomography.

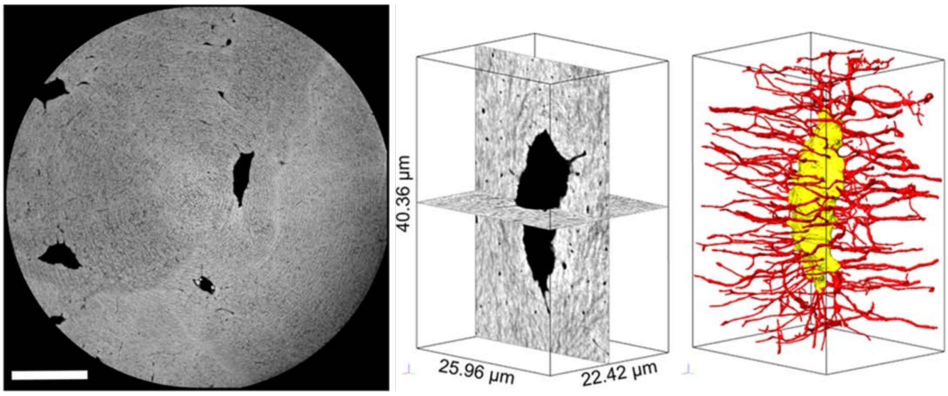

Figure 1.21 One reconstructed slice and segmentation of the LCN in femoral cortical bone of human. Scale bar = 20 µm [Varga et al. (2015)].

(4) Ptychographic X-ray CT

Ptychographic X-ray CT is a lensless imaging technique which can reconstruct the transmission function of the object by recording a series of far-field diffraction patterns [Dierolf et al. (2010)]. After being processed by a ptychographic algorithm, a 3D image reflecting the electron density can be reconstructed. Figure 1.22 gives 3D rendering of the tomographic reconstruction and segmentation of the lacunae and connecting canaliculi using Ptychographic X-ray CT [Dierolf et al. (2010)], [Ciani et al. (2016)].

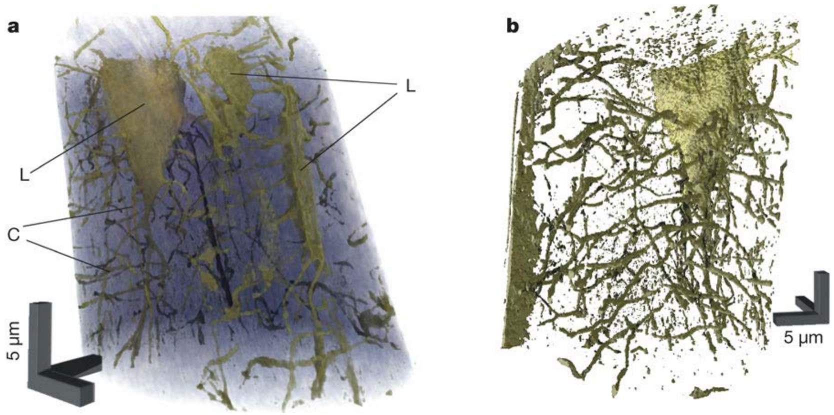

(a)

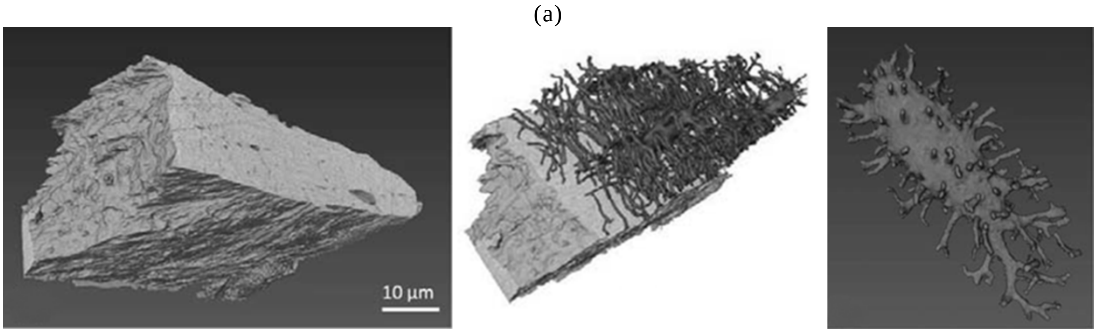

(b)

Figure 1.22 Ptychographic X-ray CT. (a) 3D rendering of the tomographic reconstruction to show osteocyte lacunae [Dierolf et al. (2010)]; (b) 3D reconstruction and segmentation of the LCN of transverse diaphyseal bone sections from rats [Ciani et al. (2016)].

1.7 MULTIPS project

To assess the relationships between human cortical bone effective mechanical properties, the MULTIPS (Multiphysic and multiscale assessment of bone quality) project was designed with financial supports from the Agence Nationale de la Recherche (ANR-13-BS09-0006). The MULTIPS project will be achieved by the collaboration between groups of the Laboratoire d'Imagerie Biomédicale (LIB) (Sorbonne Université), the Inserm research unit Physiopathology, diagnostic and treatment of bone diseases (PDTBD) (Université de Lyon), the Laboratoire Interdisciplinaire de Physique (Université Joseph Fourier, Grenoble) and the Centre de Recherche en Acquisition et Traitement de l'Image pour la Santé (CREATIS) (Université de Lyon).

The main goals of the MULTIPS project were to investigate the properties of cortical bone including stiffness and toughness (by resonant ultrasound spectroscopy and mechanical testing), micro- and nanostructure (by synchrotron radiation computed tomography and quantitative scanning small-angle X-ray scattering imaging), and the characteristics of mineral crystals and of the collagen (by Fourier-transform infrared microspectroscopy). Our work has been concentrated on analyzing micro- and nanostructures of cortical bone in the context of the project.

1.8 Conclusion

In this chapter, we first introduced the hierarchical structure of bone at the macro, micro and nano scales. Then, we provided a brief description of the different types and functions of bone cells such as osteoclasts, osteoblasts, osteocytes and osteogenic cells. Next, we explained the three main dynamic activities of bone from the embryo to adulthood with the action of osteoclasts and osteoblasts, i.e. bone formation, bone growth and bone remodeling. We highlighted the importance of the LCN which plays an essential role in regulating bone resorption as well as formation, and is the subject of this thesis. In the last section of this chapter, we made a review of both 2D and 3D imaging techniques that were previously used to observe the LCN. The 2D techniques do not allow getting a full picture of the 3D network and are limited by the observation depth. Some 3D techniques have either a limited spatial resolution or a limited field of view permitting only to observe few osteocytes. SR phase CT techniques are attractive to image the osteocyte system in 3D since they can achieve high signal-to-noise ratio and spatial resolution and provide high contrast within the object. The principle of this technique that we will use in this work for morphological and quantitative analysis of the LCN will be described in details in the next chapter.

Chapter 2: Synchrotron radiation sources and X-ray phase CT

Contents

2.1 Introduction

Synchrotron radiation (SR) is generated when charged particles accelerated to the velocity of light are bended according to the initial position under the action of the magnetic field [M.-E. Couprie et al. (2008)]. Although synchrotron radiation has nowadays become an important research tool in many study fields, there has been more than 70 years from its first observation to wide applications. In 1947, synchrotron radiation was observed at the General Electric Research Laboratory in Schenectady, New York, despite that it was not immediately recognized as what it was.

Until now, there have been three generations of synchrotron radiation sources. The first generation synchrotron radiation sources were sometimes called parasitic facilities because the experimental devices were primarily designed for high-energy or nuclear physics. Synchrotron Ultraviolet Radiation Facility (SURF I) started experimental measurements to verify feasibility of synchrotron radiation as a source for spectroscopy [Willmott (2011)]. Using synchrotron radiation sources, some researchers tried to measure absorption in thin metal films in Frascati while others obtained soft x-ray absorption spectra of solids in Tokyo.

The experimental conditions required by high-energy physics, such as low beam currents or energies, often limited the possibilities of synchrotron radiation. Therefore, parasitic facilities could not meet the research requirements and dedicated synchrotron radiation facilities were designed. With the development of electron storage rings, the Synchrotron Radiation Source (SRS) at Daresbury, UK became in 1981 the first of the second generation synchrotron radiation sources. with a 2 GeV electron storage ring [Mobilio et al. (2015)]. In the next few years, other new facilities were built in the U.S., Japan, Germany and France. Besides, some first generation facilities upgraded to second generation ones e.g. the Stanford Synchrotron Radiation Laboratory at the SLAC National Accelerator Laboratory.

As more and more experiments with synchrotron radiation are carried out, researchers gradually realized the importance of increased brilliance which cannot be improved by optical techniques but by the proper design of the source decreasing the emittance of the electron beam in the storage ring. This could be achieved with the help of insertion devices such as wigglers and undulators, which were normally set in the straight connections between the curved arcs of storage rings. The first third generation synchrotron radiation facility using insertion devices, was the European Synchrotron Radiation Facility (ESRF) in Grenoble. Following the ESRF, more and more third generation facilities specializing in short-wavelength or long-wavelength X-rays have been built all around the world in the next time (see Fig. 2.1).

Figure 2.1 Synchrotron radiation sources all over the world [M. E. Couprie (2014)].

2.2 Third generation synchrotron radiation sources

Over the past two decades, third generation synchrotron radiation sources have been vigorously developed and applied in a large number of studying fields such as biology, medicine, physics, materials science and some other industrial applications. Since these sources offer a higher brightness than the first and second generation ones, spatial information detected by multiple beams with different wavelengths can be obtained with higher resolution and shorter acquisition time. In this section, we briefly review third generation sources that can be classified into two different types according to the energy of the electron beam in the storage ring, and list some of them as examples.

2.2.1 Large scale sources

As the name suggests, the facilities of large scale sources have large circumferences (> 800 m), high electron energies (> 5 GeV) and a comparable number of beamlines. These facilities specialize in the range of the short-wavelength (or hard) X-rays.

2.2.1.1 Advanced Photon Source

The Advanced Photon Source (APS) is located at Argonne National Laboratory in Argonne, Illinois, USA. APS was established in 1996 funded by the Office of Science-Basic Energy Sciences in the U.S. Department of Energy. The normal energy of the electron beam of APS is 7 GeV and its circumference is 1104 m. It includes 35 user-science sectors and each sector contains one or more beamlines serving for researchers (Fig. 2.2). By spectroscopy, scattering, and imaging techniques, APS targets to perceiving the physical world at the nanoscale such as studying the arrangements of molecules and atoms, probing the interfaces where materials meet, determining the interdependent form and function of biological proteins, and watching nano chemical processes.

Figure 2.2 Research facility and the beamline plan of Advanced Photon Source. [Image from: https://www.aps.anl.gov/About/Welcome; https://www.aps.anl.gov/Beamlines]

2.2.1.2 SPring-8

SPring-8 is another large scale facility developed just after ESRF and APS. It is situated in in Harima Science Park City, Hyogo Prefecture, Japan. Leading by Ministry of Education, Culture, Sports, Science and Technology (MEXT), RIKEN and Japan Atomic Energy Research Institute build SPring-8 between 1991 and 1997. The name

"SPring-8" is derived from “Super Photon ring-8 GeV”, which explains that the electron beam energy is 8 GeV. The circumference of the storage ring is 1436 m and there are 62 beamlines at present (Fig. 2.3). SPring-8 has been used for a number of native or international researchers for many academic research and analysis in the fields of materials, biology and physics.

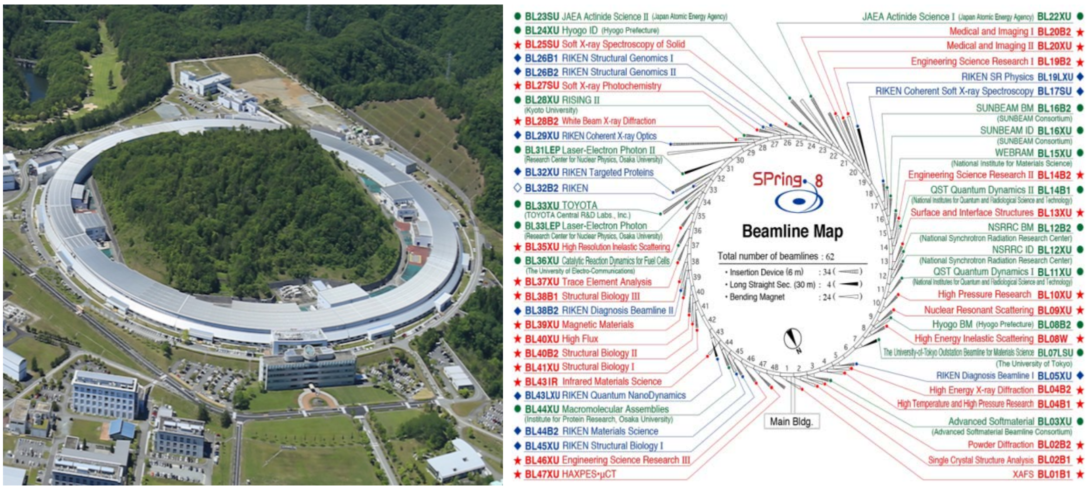

Figure 2.3 Research facility and the distribution of beamlines of Spring-8. [Image from: http://www.spring8.or.jp/en/about_us/whats_sp8/; http://www.spring8.or.jp/en/about_us/whats_sp8/facilities/bl/map/]

2.2.1.3 PETRA III

PETRA III, located in at DESY in Hamburg, Germany, is designed to be one of the most brilliant storage ring light sources in the world. In the beginning, PETRA was built as a particle accelerator for the research of electron-positron collisions from 1978 to 1986. In 1990, it was upgraded with insertion devices to PETRA II serving as a source of high-energy synchrotron radiation and also a pre-accelerator for the HERA which was another particle accelerator at DESY. In 2010, PETRA II began to be converted to PETRA III, a third generation synchrotron radiation source, with many complex rebuilding and expansion tasks. The electron energy is 6 GeV and its circumference is 2304 m. At present, PETRA III is still in upgrade and Fig. 2.4 gives an aerial view and extension project of PETRA III. In 2017, there were 17 beamlines available for users.

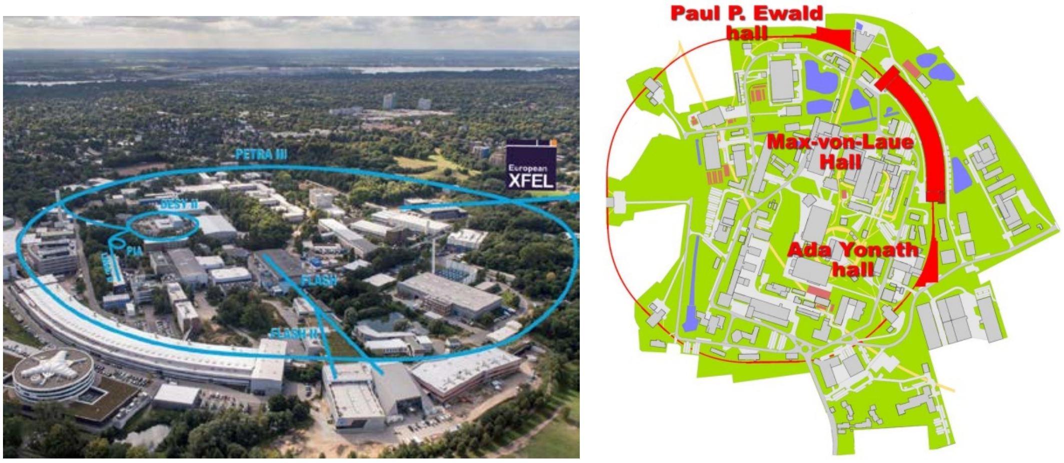

Figure 2.4 Aerial view and extension project of PETRA III [Image from: http://www.kloenschnack.de/magazin/regionales/teilchenbeschleuniger-petra-iii; http://photon-science.desy.de/facilities/petra_iii/petra_iii_extension_project/index_eng.html]

2.2.2 Intermediate scale sources

Compared with the large scale ones, the facilities of intermediate scale sources have smaller circumferences (100~700 m), lower electron energies (~ 3 GeV) and a relatively few beamlines. These facilities mainly use vacuum ultraviolet and long-wavelength (or soft) X-rays.

2.2.2.1 SOLEIL

SOLEIL is a French synchrotron radiation source, whose name means Source Optimisée de Lumière d'énergie intermédiaire du LURE (Laboratoire d'Utilisation du Rayonnement Électromagnétique). It is located in Saint-Aubin, Essonne, southwest of Paris. Funded by the French CNRS and the CEA (Alternative Energies and Atomic Energy Commission), SOLEIL is built to provide a second source selection for experiments using synchrotron radiation, which can meet needs of more scientific organizations. The electron energy of SOLEIL is 2.75 GeV and the circumference is 354 m with 29 beamlines in total (Fig. 2.5).

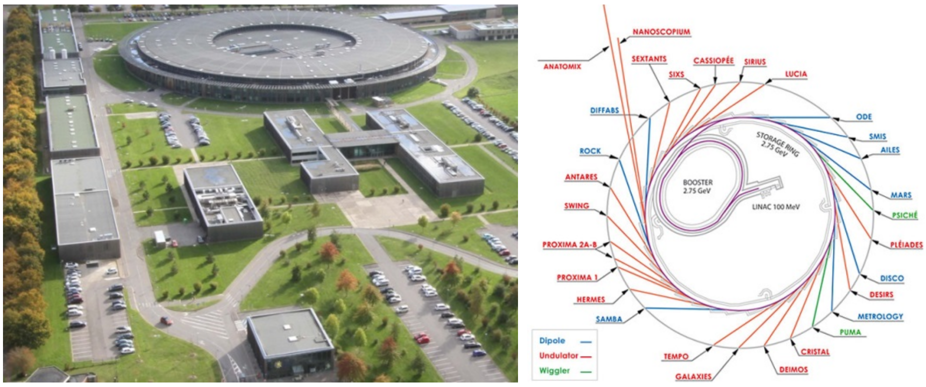

Figure 2.5 Research facility and the beamline map of SOLEIL [Image from: https://www.synchrotron-soleil.fr/en/about-us; https://www.synchrotron-soleil.fr/en/beamlines/position-along-storage-ring]

2.2.2.2 Diamond

Diamond, the national synchrotron radiation source of the UK, is situated on the Harwell Science and Innovation Campus, Oxfordshire. It is a not-for-profit limited company with the funding from the UK Government through the Science & Technology Facilities Council (STFC) and the Wellcome Trust. Diamond began to be built in 2001 and was formally open to users in 2007. Its storage ring has an electron beam energy of 3 GeV and a circumference of 562 m. There are 31 beamlines concentrating on different scientific fields such as macromolecular crystallography, engineering and environment, surfaces and interfaces, soft condensed matter, spectroscopy and materials (Fig. 2.6).

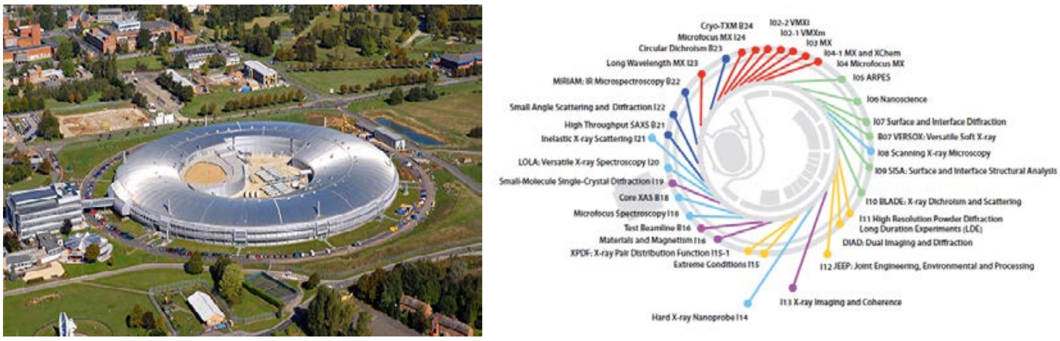

Figure 2.6 Research facility and introduction of beamlines of Diamond [Image from: http://www.diamond.ac.uk/Home/About.html; http://www.diamond.ac.uk/Beamlines.html]

2.2.2.3 NSLS-II

The National Synchrotron Light Source II (NSLS-II) belongs to Brookhaven National Laboratory (BNL), located in Upton, New York with the sponsors of U.S. Department of Energy (DOE), Office of Science, and Office of Basic Energy Sciences. NSLS-II, based on a 3GeV electron storage ring, offers a brilliance, about 10 000 times brighter than the original second generation source, NSLS. The ring circumference is 792 m which is larger than SOLEIL and Diamond. As designed, there will be at least 58 beamlines when NSLS-II is completed but now only 26 beamlines are under operation (see Fig. 2.7). These beamlines are divided into six sections: hard X-ray spectroscopy, imaging & microscopy, soft X-ray scattering & spectroscopy, diffraction & in situ scattering, complex scattering and structural biology.

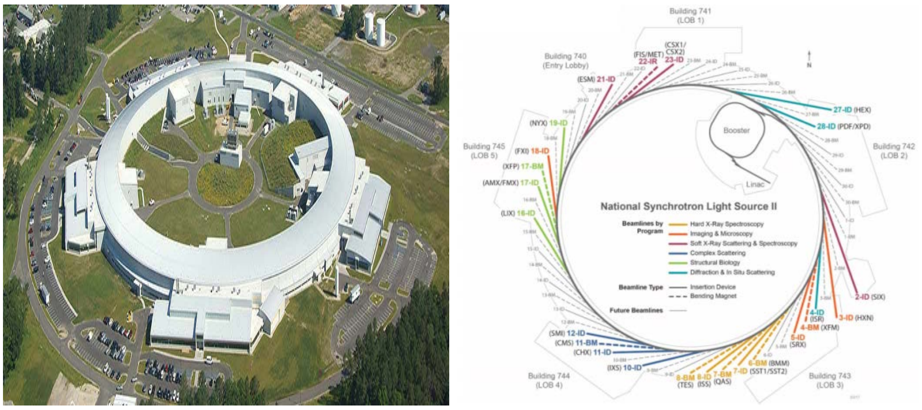

Figure 2.7 Research facility and beamline diagram based on current funding assumptions of NSLS-II [Image from: https://www.bnl.gov/ps/nsls2/about-NSLS-II.php; https://www.bnl.gov/ps/nsls2/beamlines/map.php]

2.2.2.4 MAX IV

MAX IV is a Swedish national synchrotron radiation facility located in Lund. It was inaugurated in 2016 after the experience of three old synchrotron radiation sources MAX I, II and III in the past 30 years. MAX IV is the first light source using the multibend achromat lattice for the production of X-rays. Also, MAX IV has two storage rings which are different from other sources. As shown in Fig. 2.8, one of the rings has energy of 3 GeV and a circumference of 528 m specializing in ultra-bright hard X-rays. The other one has a circumference of 96 m operated at 1.5 GeV, which major in bright soft x-ray and ultraviolet (UV). There are 16 beamlines which are operational at present and 3 new ones are in project.

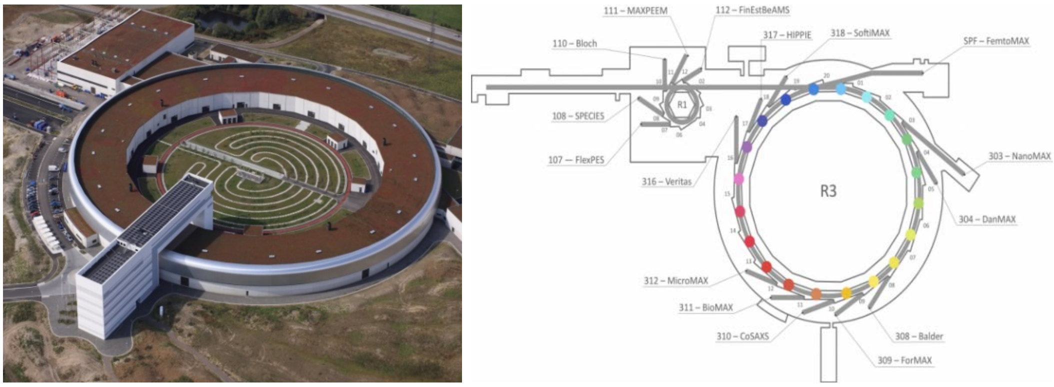

Figure 2.8 Research facility and the beamline map of MAX IV [Image from: https://www.maxiv.lu.se/news/max-iv-paves-the-way-for-ultimate-x-ray-microscope/; https://www.maxiv.lu.se/accelerators-beamlines/beamlines/]

In Table 2.1, we summarize some important characteristics of the different third generation synchrotron radiation sources.

Table 2.1 The important parameters of some third generation synchrotron radiation sources.

Name	Location	Energy (GeV)	Circumference (m)	Current (mA)	Emittance (nmrad)	Beamline Number
APS	U.S.	7	1104	100	2.51	70
Spring-8	Japan	8	1436	100	2.4	62
ESRF	France	6	844	200	3.8	43
PETRA III	Germany	6	2304	100	1.2	17
SOLEIL	France	2.75	354	430	3.9	29
Diamond	UK	3	562	300	3.17	31
NSLS-II	U.S.	3	792	500	0.55	26
MAX-IV	Sweden	3	528	500	0.33	16

2.3 ESRF

As the first third generation synchrotron radiation facility, the ESRF has been successful in promoting technical innovation and generating a very large volume of new and exciting science since the establishment. All the experiments involved in this thesis were performed at the ESRF. We provide more detailed information about the ESRF and the beamlines that were used in this work.

2.3.1 Introduction

In 1988, the ESRF with an electron storage ring of 6 GeV and 844 m began to be built in Grenoble, France, under the investment of 12 European countries. It was considered as the biggest third generation synchrotron radiation light source at that time (Fig. 2.9 (a)). At present, there are 22 partner nations supporting the international facility for academic and industrial research. In the past 30 years, the ESRF has made an outstanding contribution to the development of European science and cultivating a new generation of scientists, with over 4000 researchers visiting each year and resulting in more than 1400 refereed publications. Due to the brilliance and quality of its X-rays, it is possible to observe materials and living matter at high resolution in the fields of chemistry, materials, physics, structural biology and medical applications, environmental and information science.

Synchrotron radiation can be produced when high-energy and high-speed electrons circulating in a storage ring are deflected by magnetic fields. First of all, in the linear accelerator (or linac), the electron gun emits electrons which are then packed into bunches and accelerated to near the velocity of light by electromagnetic waves reaching energy of 200 MeV. After this, the electrons enter the booster synchrotron, which is a ring with a circumference of 300 m and functions as a pre-accelerator. In the booster synchrotron, the electrons continue to be accelerated by travelling round this ring several thousand times and getting more energy gain. When energy in increased to 6 GeV, the electrons are injected into the storage ring by a high-energy bunch every 50 milliseconds. The booster synchrotron does not keep working all the time but when the storage ring needs to be refilled, normally a few times a day for a few minutes. Next, the electrons will continue to circulate at high-speed in the storage ring for hours under ultra-high vacuum conditions. When they pass through certain magnets in the curve and straight sections of the ring, they generate synchrotron radiation and lose energy which will be resupplied by radiofrequency (RF) cavities. There are mainly three types of magnets in the ESRF: bending magnets, undulators and focusing magnets (see Fig. 2.9 (c), (d) and (e)). The bending magnets work for changing the direction of electronic movement and make it match the ring orbit. They can produce synchrotron light with a wide and continuous spectrum ranging from microwaves to hard X-rays. The undulators consist of a series of small magnets with alternating polarity which generate radiation and interfere with each other. The X-ray beams produced by the undulators are a million times more intense than those by the bending magnets, which have higher brilliance and better coherence properties. The focusing magnets, or magnetic lenses, are used to make the electron beam more focused and narrower.

The X-ray beams emitted by the electrons are finally led into the beamlines which are in tangential direction of the orbit and perform concrete experiments. The beamline is normally made up of three parts: the optic cabin, which holds optic devices (slits, filters, monochromators, and mirrors) to give the beam the targeted characteristics; the experimental cabin, where samples are placed and detectors record images; the control cabin, where users control the experiments. At present, there are 43 beamlines in the ESRF equipped dedicated instruments and focusing on different scientific fields (Fig. 2.9 (b)).

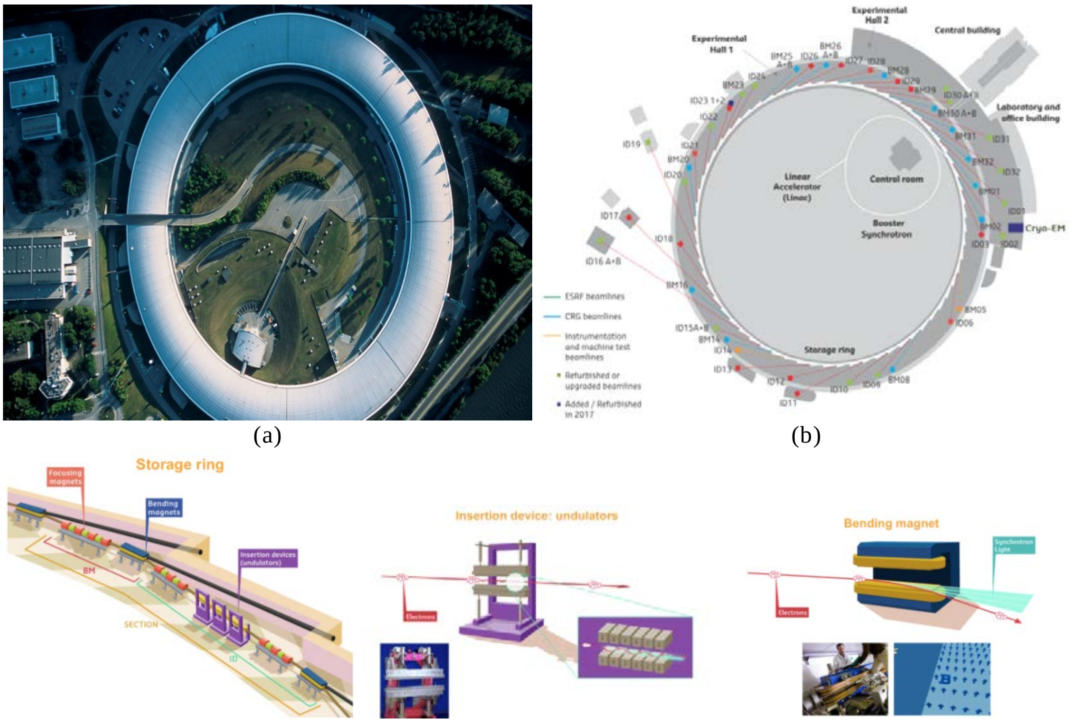

(a) (b)

(c) (d) (e)

Figure 2.9 (a) The European Synchrotron Radiation Facility [http://www.esrf.eu/home/education/what-is-the-esrf.html]; (b) location of the beamlines [Image from: http://www.esrf.eu/Apache_files/Highlights/HL2017.pdf]; (c) magnets in the storage ring; (d) insertion device; (e) bending magnets. [Images from: http://www.esrf.eu/about/synchrotron-science/synchrotron]

2.3.2 ESRF-EBS

The ESRF-Extremely Brilliant Source (ESRF-EBS) project was launched by the ESRF in 2015 in order to consolidate the pioneering role in synchrotron science and prepare for the development of a new generation of synchrotron light source. With the investment and support of 22 partner countries, the ESRF-EBS is estimated to cost € 150 million over the period 2015-2022. Two of the most important tasks of the project are the construction of a new storage ring and the establishment of more new state-of-the-art beamlines. By 2020, the new storage ring is expected to be completed which can generate more intense, coherent and stable X-ray beams, with new adapted beamlines and high performance X-ray detectors.

The new storage ring of the ESRF-EBS is based on the concept of the hybrid multibend achromat (HMBA) or Raimondi lattice which is considered as the design basis of the future fourth generation synchrotron radiation sources [Raimondi (2016)] (Fig. 2.10

(a)). The Raimondi lattice with the seven-bends version will be used as the basis of the new ring, and will permit to substantially decrease the storage ring equilibrium horizontal emittance and generate about 100 times more brilliant and coherent X-ray beams than the present ESRF source [Biasci et al. (2014)]. Thanks to the advancement of the accelerator control technology and better magnet materials, it is possible to maintain almost the same circumference, preserve the time structure operation and keep beamline positions. 90% of the present infrastructure will be reused and there will be a reduction of in the electricity consumption by about 20% after construction. Table 2.2 gives a brief comparison of some parameters between ESRF and ESRF-EBS.

Table 2.2 Comparison of some detailed parameters between ESRF and ESRF-EBS.

	ESRF	ESRF-EBS
Energy (GeV)	6.03	6
Circumference (m)	844.391	843.977
Emittance (nmrad)	3.8	0.134
Beam current (mA)	200	200
Bunch length (mm)	4.28	2.91
Energy spread	1.06×10^{-3}	0.93×10^{-3}

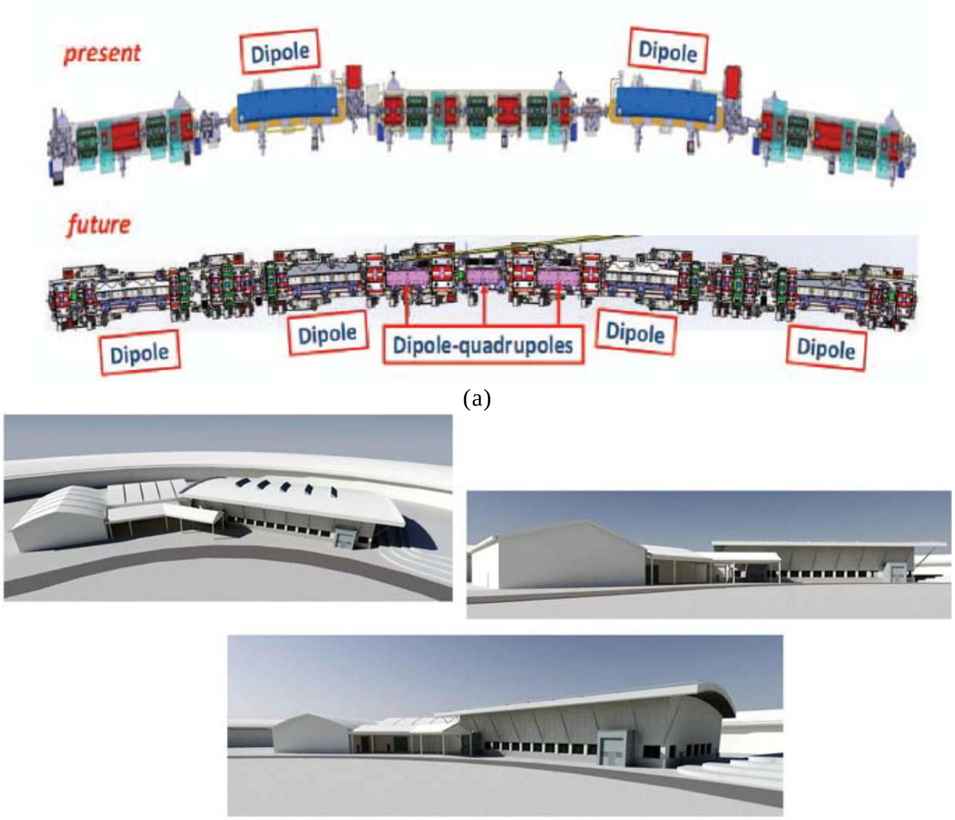

(a)

(b)

Figure 2.10 ESRF-EBS. (a) Layout of the existing DBA (Double Bend Achromat) lattice and the new HMBA (Hybrid Multi-bend Achromat) lattice; (b) Architect's impression of the new ESRF-EBS assembly and storage buildings. [Raimondi (2016)]

In 2018, there will be a relatively long time shut-down (~ 18 months) for installation and commissioning of the new accelerator until 2020 (see Fig. 2.10 (b)). The successful completion of ESRF-EBS will promote the development of European or the world's synchrotron science and provide researchers better chances to observe and perceive materials and living matter from the macroscopic world down to the nano scale.

2.4 NINA Beamlines

The NINA (Nano-imaging and Nano-analysis) project of the ESRF Upgrade Programme UPBL4 has provided two new beamlines, ID16A and ID16B, which can use nano-focused X-ray beams to address scientific challenges in the fields of health, environment, energy and advanced materials. All our experimental data were acquired at these two beamlines at different nanometric voxel size during the first two years of my PhD.

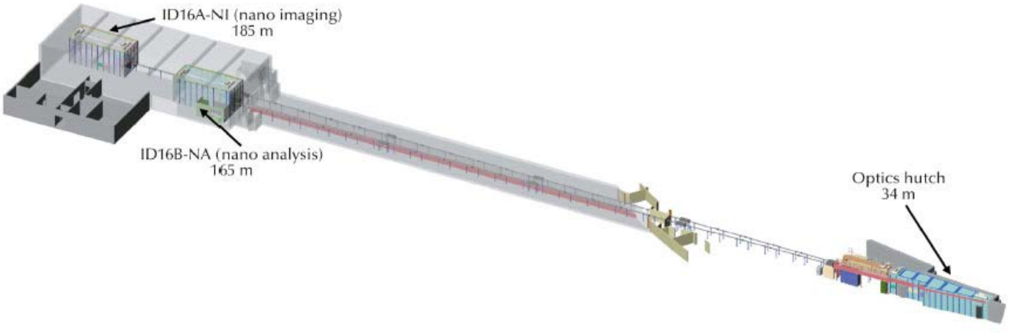

Figure 2.11 Schematics of the general layout of the beamlines ID16A and ID16B. [Image from: http://www.esrf.eu/home/UsersAndScience/Publications/Highlights/highlights-2013/x-ray-imaging.html]

2.4.1 Beamline ID16A

The beamline ID16A combines X-ray imaging techniques at the ultimate spatial resolution, and targets to quantify 3D characterization of the morphology and the elemental composition of specimens in their native state [da Silva et al. (2017)]. This beamline with a length of 185 m is currently the longest beamline at the ESRF. Normally, the beamline works at two specific energies, 17.05 keV and 33.6 keV, with a flux ranging from 6×10^9 to 4×10^{12} photons per second.

It is worth mentioning that ID16A has obtained a sub-13-nm (FWHM) diffraction-limited X-ray focal spot size with 6×10^9 photons per second at the energy of 33.6 keV using graded multilayer coated Kirkpatrick-Baez (KB) mirrors [Cesar da Silva et al. (2017)], which is the smallest focal spot at such a high energy in the world (Fig. 2.11 (c)). The KB focusing optics system can be divided into two independent parts which are perpendicular to each other. As shown in Fig. 2.11 (b), the first part is responsible for the focus in the vertical direction while the second for the horizontal [Morawe et al. (2015)]. The KB mirrors allow focusing the incoming parallel X-ray beam into a focal spot whose size limits the resolution of the image in many cases. There are two independent KB mirror setups which can be adjusted based on the specific energy of the experiment, 17.05 keV or 33.6 keV.

During the scanning, the sample is placed in a piezo-driven short-range hexapod stage which can maintain relative stability and avoid excessive shake during rotation or translation. Generally, the sample will be scanned over a range of 180° at one sample-to-detector distance. The small cabin housing the sample will be evacuated into vacuum keeping room or cryogenic temperature according to the requirement (Fig. 2.11 (a)). The sample is put in and taken out by the mechanical cantilever and pincers which are accurately controlled by the electronic system through software. After passing through the sample, X-ray beam is converted into visible light by the scintillator and is recorded by the detectors which have different types to select in line with applied X-ray imaging techniques. For example, a lens-coupled FReLoN (Fast Readout Low Noise) camera developed by the instrument support group of ESRF with a CCD of size 2048×2048 pixels, was used for X-ray phase nano-CT [Max Langer et al. (2012)].

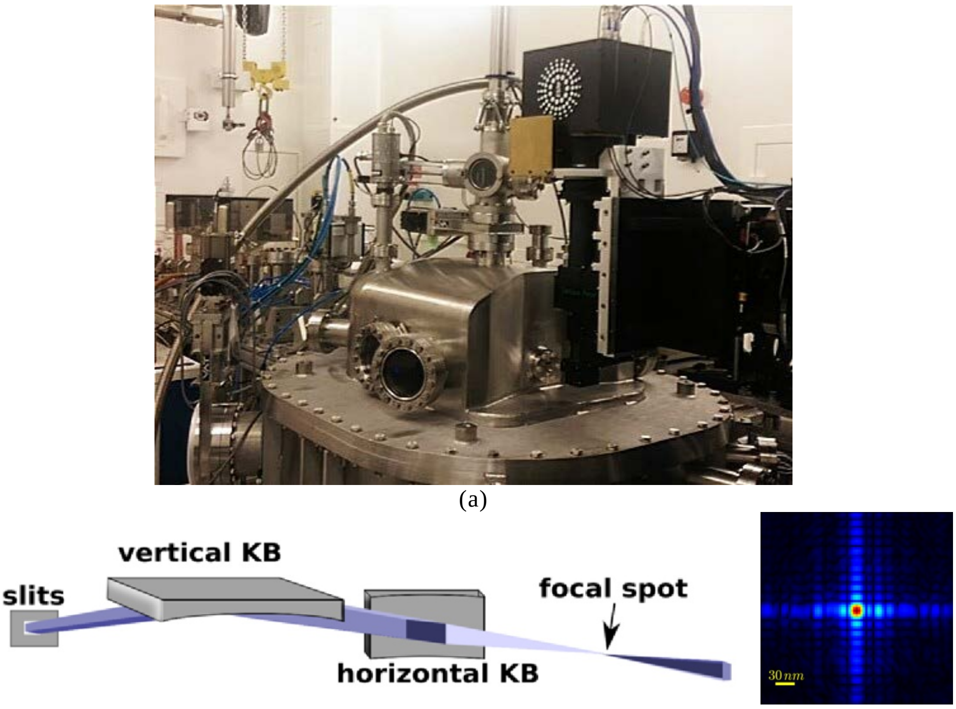

(a)

(b) (c)

Figure 2.11 The beamline ID16A. (a) The end-station; (b) sketch of the KB mirror optics; (c) a zoomed-in view of the beam at the focus position [Cesar da Silva et al. (2017)].

There are mainly three imaging techniques at the ID16A: X-ray fluorescence (XRF), X-ray phase imaging and X-ray ptychography. XRF is a scanning microscopy detecting the secondary emission of the X-rays from the sample which has been bombarded by high-energy rays, to analyze the elemental composition within the focus spot of the source beam. The nanometric size of the spot at the ID16A can yield a very high-resolution fluorescence imaging. For better collection the fluorescence signal, ID16A uses two six elements silicon drift diode detectors which are orthogonal to the incoming beam and placed at both sides of the sample. For example, XRF was used to identity the position of Os from a promising anticancer drug candidate in human ovarian cancer cells, which was finally found in mitochondria and not in the nucleus, accompanied by mobilization of Ca from the endoplasmic reticulum, a signaling event for cell death [Sanchez-Cano et al. (2017)] (Fig. 2.12 (b)).

X-ray phase imaging, which combines with tomography leading to X-ray phase CT, uses phase maps to realize tomographic reconstruction instead of absorption images in conventional X-ray CT. Image acquisition consists in recording several CT scans at different sample positions between the focus and the detector (see Fig. 2.12 (a)). After being focused, the beam turns from parallel to divergent so that the images recorded at different distances contain not only phase contrast but also geometric magnifications. In practice, the position of the detector is fixed while the sample will be moved downstream of the focus [M Langer et al. (2010)]. Images corresponding to different propagation distance between the sample and the detector have a different magnification. After registration, phase shifts can be estimated from these phase contrast images at different distances. Finally, the extracted phase maps are used as inputs to tomographic reconstruction to recover the 3D structure of the sample. For example, it has been used for 3D analysis of a super-flexible resorcinol-formaldehyde aerogel in the sub-micrometer range [Tannert et al. (2017)] (Fig. 2.12 (c)).

X-ray ptychography at the ID16A can be achieved at two incoming energy X-ray beams (17.05 keV or 33.6 keV) with high photon flux and small focal spot size, which offers the potential to realizing imaging with high-resolution. One advantage of the X-ray ptychography is that it does not only retrieve the complex refractive index of the sample but also the illumination [da Silva et al. (2017)]. This can reduce the impact of artifacts on the reconstructed images due to inhomogeneity of the incident X-ray beam. Besides, ID16A can perform X-ray ptychography in both near-field and far-field regimes by adjusting some parameters of the setup before the experiment and the phase retrieval algorithms. For example, it was helpful to observe the different components of the hybrid metal-polymer material in 3D reconstructions [Haubrich et al. (2017)] (Fig. 2.12 (d)).

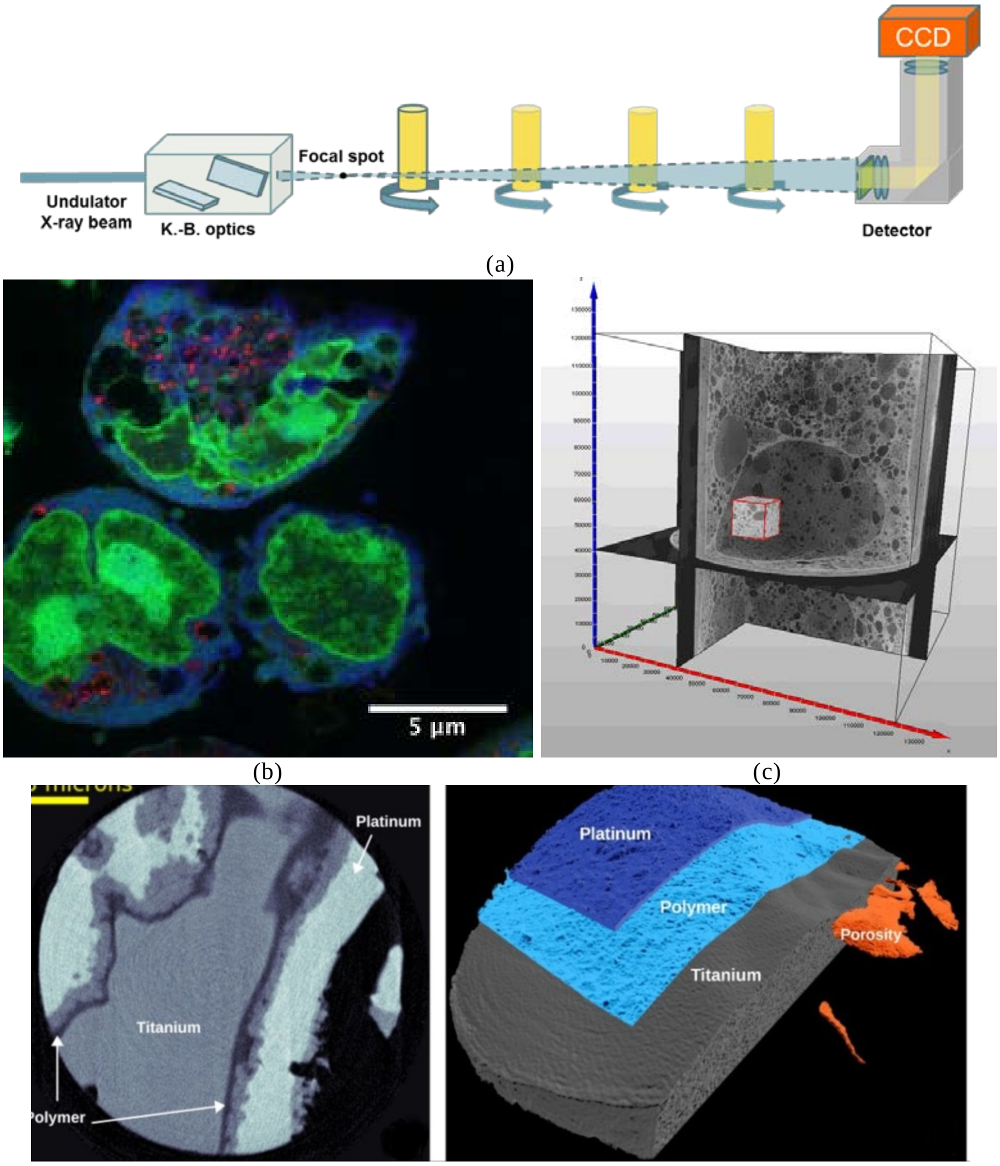

(a)

(b) (c)

(d)

Figure 2.12 Illustration and applications of ID16A. (a) Sheme of magnified X-ray phase nano-CT at the beamline; (b) co-localization XRF map of of the elemental distribution in a 500 nm-thick section of human ovarian carcinoma cells [Sanchez-Cano et al. (2017)]; (c) tomogram of sf-RF (super-flexible resorcinol-formaldehyde) aerogel [Tannert et al. (2017)]; (d) an axial slice and 3D rendering volume of hybrid metal-polymer material obtained by X-ray ptychography [da Silva et al. (2017)].

2.4.2 Beamline ID16B

The beamline ID16B offers a multi-modal approach (spectroscopy - diffraction - imaging) for 2D or 3D analysis of diluted heterogeneous samples at the nanoscale in-situ or in-operando environments. It can allow to investigate spectroscopic characterization of materials and the spatial features of trace elements in relation to the object microstructure and crystallography [Gema Martínez-Criado et al. (2016)]. Compared with ID16A, ID16B has a relatively shorter length of 165 m and can provide monochromatic nanobeams tunable over a wider energy range (5–70 keV) and can be regarded as complementary to ID16A.

The KB system of ID16B uses multilayer coated optics in conjunction with dynamically bent mirrors to give the specified energy covering a continuously variable range (Fig. 2.13 (a) and (b)). The beamline ID16B was designed from the same concepts as the previous beamline ID22. The incident X-ray beam produced from a fully tunable U26 in-vacuum undulator, first passes through a double white beam mirror (DWM) and double-crystal monochromator (DCM) located around 30~35 m from the undulator, which are mainly used to keep the high coherence and stability of the beam [Gema Martínez-Criado et al. (2016)]. The KB mirrors are placed very close to the sample to maintain strong demagnifications [Barrett et al. (2016)].

The sample stage of ID16B consists of a rotation stage and hybrid translation stages as shown in Fig. 2.13 (c). The rotation stage is an air-bearing nano-spindle rotation stage (PIC ISO 3R), which can rotate to different angles mainly for cases of 3D data acquisitions. The hybrid translation stages are made up of three axis stages controlling translations along the axis of X, Y and Z respectively. The X-axis stage is composed of granite block which carries the Y-axis, Z-axis and the rotation stage. The beamline offers many mechanical carrying options according to the characteristic of the sample, e.g. Huber sample carriers for glass and custom Al holders for flat objects [Gema Martínez-Criado et al. (2016)]. Besides, depending on the imaging techniques, there are some choices of detectors such as silicon drift detectors (SDDs), FReLoN camera with fiber optic taper coupling to the scintillator and FReLoN 4M or PCO edge 5.5 using lens coupling.

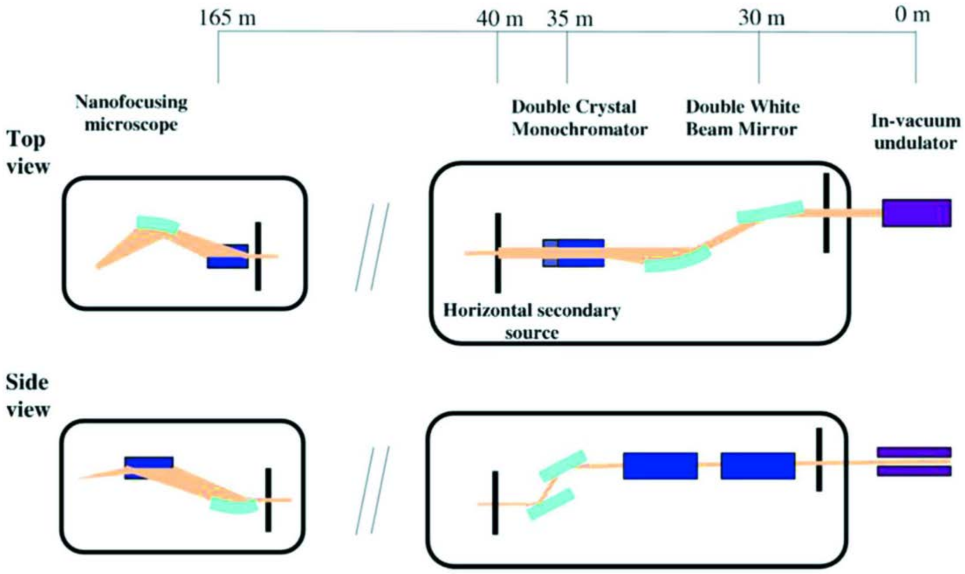

(a)

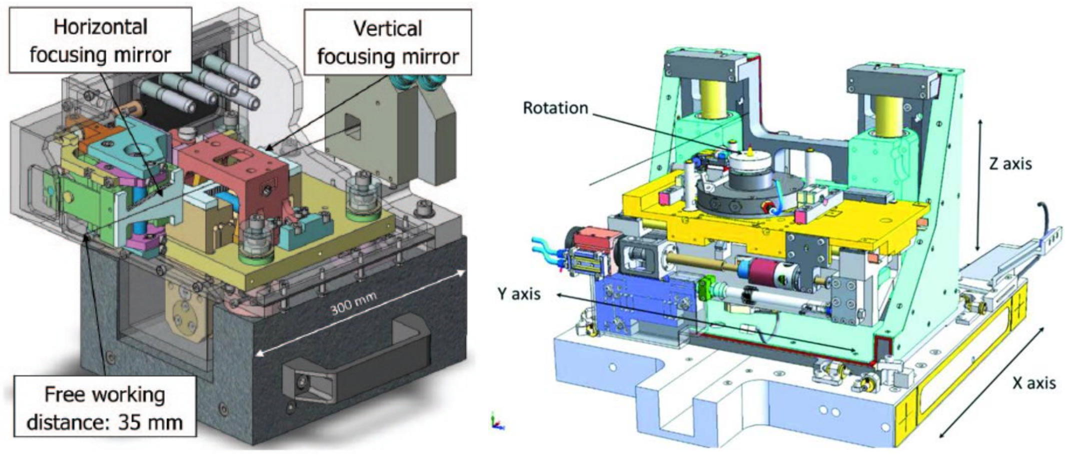

(b) (c)

Figure 2.13 Illustration of Id16B. (a) General optical layout of ID16B with the primary optical elements [Gema Martínez-Criado et al. (2016)]; (b) scheme of the KB system [Barrett et al. (2016)]; (c) the sample stage [Gema Martínez-Criado et al. (2016)]

Different imaging techniques are also implemented at ID16B such as XRF, X-ray absorption spectroscopy (XAS), X-ray diffraction (XRD), X-ray excited optical luminescence (XEOL) and nano-tomography. XRF nano-imaging was used for various applications, for instance to detect fragments of the achronditic meteorite NWA 6693 [Laforce et al. (2014)] (Fig. 2.14 (a)), analyze the composition of Cu(In, Ga)Se2 (CIGS) thin-film solar cells [Schöppe et al. (2015)], and study silver nanoparticles (AgNPs) in sunflower roots [Gema Martínez-Criado et al. (2016)]. XAS is a subclass of absorption spectroscopy which can cooperate with XRF for the determination of a chemical element in the sample and the local geometric structure of materials. XAS includes X-ray absorption near-edge structure (XANES) [Johannes et al. (2017)].and extended X-ray absorption fine structure (EXAFS) [Castillo-Michel et al. (2017)].

XRD is a scattering technique based on the interference of scattered waves when the incident X-ray beam interacts with materials with regular structure (e.g. crystalline). XRD has helped to determine indium content in GaAs/(In, Ga)As/(GaAs) core-shell-(shell) nanowires (NW) [Al Hassan et al. (2018)] (Fig. 2.14 (b)). XEOL is a type of photon in/photon out technique which occurs when energetic electrons are ionized and excited after absorption of the X-ray photons. It was used to elucidate the spatial distribution and constituent elements of nanocrystals in a glass-ceramic [G. Martínez-Criado et al. (2017)] (Fig. 2.14 (c)).

In addition, ID16B can perform phase contrast imaging and further tomography applying the same principle as ID16A. The sample is placed on a rotation stage which controls the angles recording different projections while the X-axis translation stage changes the scanned position to several sample-to-detector distances for phase tomography. The voxel size and X-ray beam energy for experiments at ID16B are different from those at ID16A, and the experimental environment is not in vacuum. As shown in Fig. 2.14 (d), X-ray nano-tomography of ID16B has been used for 3D reconstructions of arsenopyrite and pyrite crystals separated from the orogenic gold deposit in order to observe the 3D distribution of gold inclusions inside the samples at micro and nano scale [Sayab et al. (2016)].

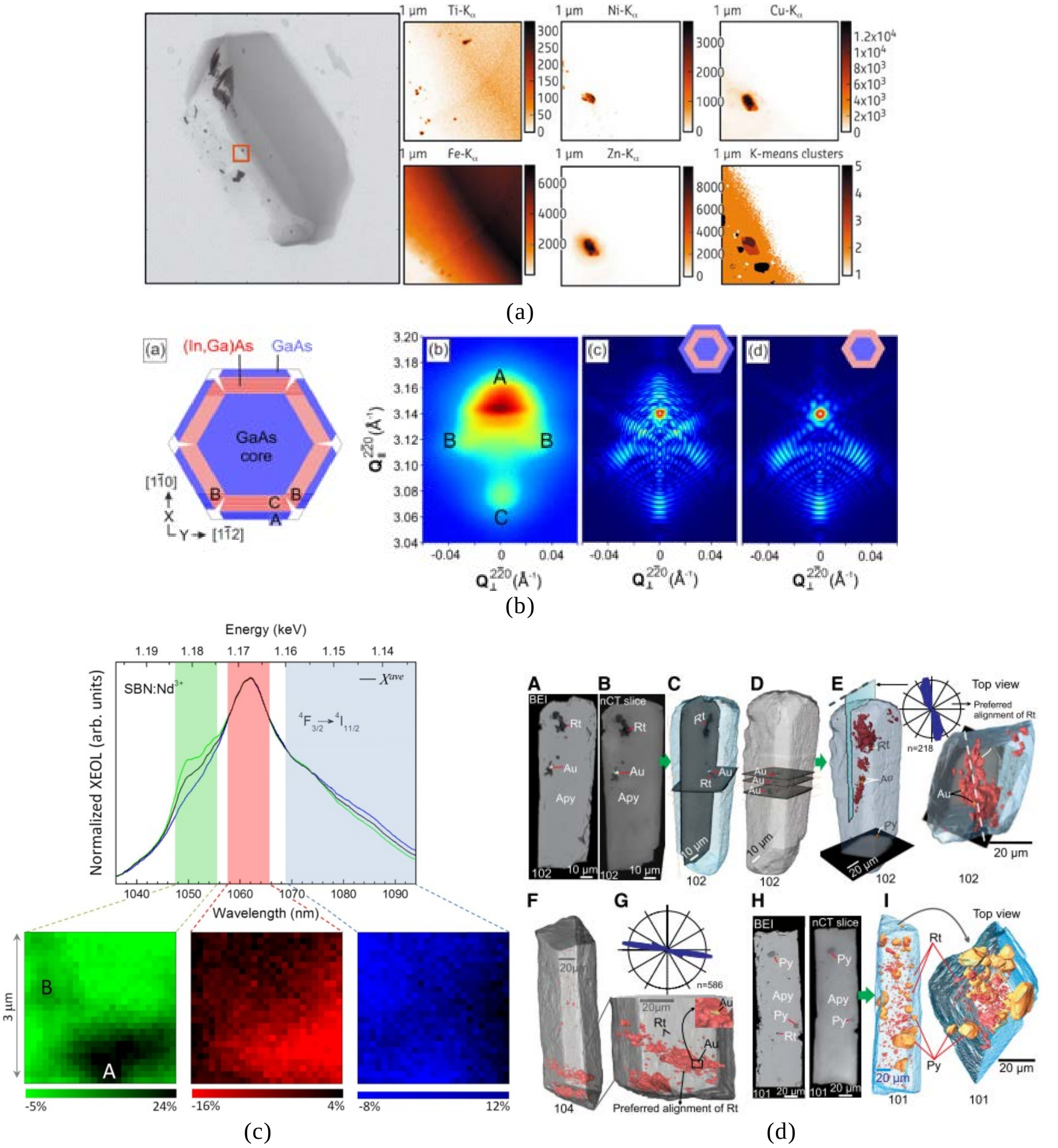

(a)

(b)

(c)

(d)

Figure 2.14 Appications of ID16B. (a) XRF overview map (Fe) of diamond with element distributions of Ti, Fe, Ni, Cu and Zn [Laforce et al. (2014)]; (b) measurement of indium content of the (In,Ga)As shell by high-resolution XRD from NW ensembles [Al Hassan et al. (2018)]; (c) XEOL spectra of an SBN ferroelectric glass-ceramic [G. Martínez-Criado et al. (2017)]; (d) 3D rendering of X-ray nano-CT data from arsenopyrite (Apy) crystals [Sayab et al. (2016)]

2.5 X-ray phase CT

In our work, we used extensively magnified X-ray phase nano-CT at both the ESRF beamlines ID16A and ID16B. Here, we give a brief review of the principle of image formation, as well as the processing necessary to recover the 3D image. We then introduce the basis of phase retrieval and more details will be studied in the next chapter.

2.5.1 Direct image formation

The interaction between X-rays and matter in a 3D object can be modeled by its refractive index distribution [Guigay et al. (2007)]:

$$n(x,y,z) = 1 - \delta_n(x,y,z) + i\beta(x,y,z), \tag{2.1}$$

where δ_n is the refractive index decrement, β the absorption coefficient and (x,y,z) denotes the 3D spatial coordinates.

Let us assume a coherent X-ray beam of wavelength λ, propagating in the z direction through the object. The transmittance function $T(\mathbf{x})$, where $\mathbf{x} = (x, y)$ are the coordinates in the plane perpendicular to z, describes the wave at the output of the object:

$$\begin{gathered} T(\mathbf{x}) = a(\mathbf{x})\exp[i\varphi(\mathbf{x})] = \exp[-B(\mathbf{x}) + i\varphi(\mathbf{x})] \\ B(\mathbf{x}) = (2\pi/\lambda)\int \beta(x, y, z)dz \qquad , \\ \varphi(\mathbf{x}) = -(2\pi/\lambda)\int \delta_n(x, y, z)dz \end{gathered} \tag{2.2}$$

where $B(\mathbf{x})$ is the attenuation caused by the object, $a(\mathbf{x})$ the amplitude and $\varphi(\boldsymbol{x})$ the phase shift of the wave.

If the beam propagates in free space over a distance D_k, where k is the distance index, the recorded intensity can be modeled as the squared modulus of the Fresnel Transform:

$$\begin{gathered} I_{D_k}(\mathbf{x}) = \left|T(\mathbf{x}) * P_{D_k}(\mathbf{x})\right|^2 \\ P_{D_k}(\mathbf{x}) = \frac{1}{i\lambda D_k}\exp\left(i\frac{\pi}{\lambda D_k}|\mathbf{x}|^2\right). \end{gathered} \tag{2.3}$$

The Fourier transform of the intensity $I_{D_k}(\mathbf{x})$, denoted $\tilde{I}_{D_k}(\mathbf{f})$ can be written directly as [Guigay et al. (2007)]:

$$\tilde{I}_{D_k}(\mathbf{f}) = \int T\left(\mathbf{x} - \frac{\lambda D_k \mathbf{f}}{2}\right) T^*\left(\mathbf{x} + \frac{\lambda D_k \mathbf{f}}{2}\right) \exp(-i2\pi\mathbf{x}\cdot\mathbf{f})d\mathbf{x}, \tag{2.4}$$

where $\mathbf{f} = (f_x, f_y)$ represents the 2D coordinates conjugate to $\mathbf{x}$ in Fourier space.

2.5.2 Phase retrieval

The phase modulation present in the recorded intensity images cannot be accessed directly because these images contain contrast both from phase and amplitude modulation induced by the sample. Thus, to reconstruct the phase information one needs to retrieve $\varphi(\mathbf{x})$ from intensity images recorded at one or several propagation distances. This process is also called the phase retrieval.

The phase retrieval is a non-linear inverse problem which has been addressed by various approaches. Most approaches solve a linearized version of the problem. Burvall et al. has reviewed seven linear phase retrieval methods and put them in a general framework. Although the methods are based on different approximations and assumptions, they follow the same pattern and can be numerically implemented using similar methods (see Figure 2.15) [Burvall et al. (2011)]. In this section, we mainly introduce two important and classical approaches to address the phase retrieval, the Transport of intensity equation (TIE) [Teague (1982)], and the Contrast transfer function (CTF) [Cloetens et al. (1999)].

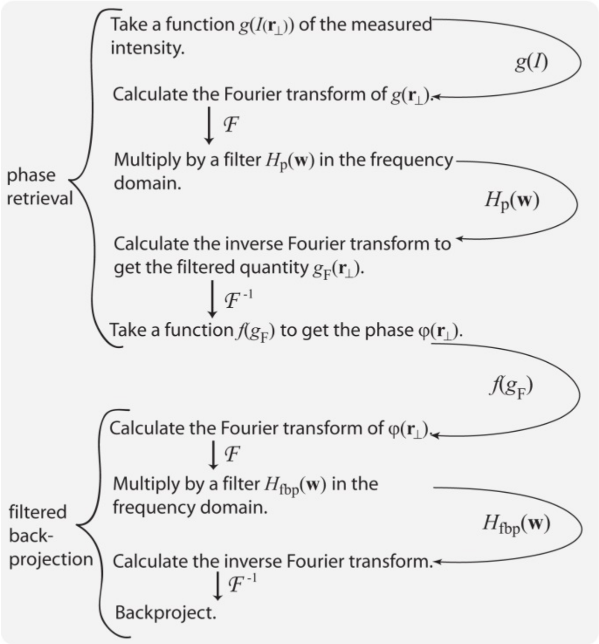

Figure 2.15 The process of phase retrieval followed by tomographic reconstruction. [Burvall et al. (2011)]

2.5.2.1 Transport of intensity equation (TIE)

The transport of intensity equation (TIE) linearizes the intensity by Taylor expansion of the propagator to the first order with respect to the propagation distance [Turner et al. (2004)]:

$$T(\mathbf{x} + \lambda D\,\mathbf{f}/2) = T(\mathbf{x}) + \frac{1}{2}\lambda D\mathbf{f} \cdot \nabla T(\mathbf{x}). \tag{2.5}$$

Substituting Eq. (2.5) to Eq. (2.4) gets:

$$I_D = I_0 - \frac{\lambda D}{2\pi}\nabla \cdot [I_0(\mathbf{x})\nabla\varphi(\mathbf{x})]. \tag{2.6}$$

When considering the cases of short propagation distances, the partial derivative in the propagation direction z can be used to replace the difference $[I_D(\mathbf{x}) - I_0(\mathbf{x})]/D$. Then, the transport of intensity equation is expressed as [Teague (1982)]:

$$\nabla \cdot [I_0(\mathbf{x})\nabla\varphi(\mathbf{x})] = -\frac{2\pi}{\lambda}\frac{\partial}{\partial z}I_0(\mathbf{x}). \tag{2.7}$$

If making the approximation $I_0(\mathbf{x})\nabla\varphi(\mathbf{x}) \approx \nabla\xi(\mathbf{x})$ [Paganin et al. (1998)], then $\xi(\mathbf{x})$ can be solved from Eq. (2.7):

$$\xi(\mathbf{x}) = \nabla^{-2}\left[-\frac{2\pi}{\lambda}\frac{\partial}{\partial z}I_0(\mathbf{x})\right]. \tag{2.8}$$

Finally, the phase can be symbolically expressed as [Max Langer et al. (2008)]:

$$\varphi(\mathbf{x}) = -\frac{2\pi}{\lambda}\nabla^{-2}\left\{\nabla \cdot \left[\frac{1}{I_0(\mathbf{x})}\nabla\left(\nabla^{-2}\frac{\partial}{\partial z}I_0(\mathbf{x})\right)\right]\right\}. \tag{2.9}$$

2.5.2.2 Contrast transfer function (CTF)

The contrast transfer function (CTF) linearizes the intensity by Taylor's expansion at the first order with respect to the wave:

$$T(\mathbf{x}) \approx 1 - B(\mathbf{x}) + i\varphi(\mathbf{x}). \tag{2.10}$$

Substituting it to Eq. (2.4) and keeping the first order terms yields [Cloetens et al. (1999)]:

$$\tilde{I}_{D_k}(\mathbf{f}) = \delta_{Dirac}(\mathbf{f}) - 2\cos(\pi\lambda D_k\|\mathbf{f}\|^2)\tilde{B}(\mathbf{f}) + 2\sin(\pi\lambda D_k\|\mathbf{f}\|^2)\tilde{\varphi}(\mathbf{f}). \tag{2.11}$$

where $\delta_{Dirac}(\mathbf{f})$ is the Dirac function, $\tilde{B}(\mathbf{f})$ the Fourier Transform of $B(\mathbf{x})$ and $\tilde{\varphi}(\mathbf{f})$ the Fourier Transform of $\varphi(\mathbf{x})$.

Because of zero crossings in the Fourier domain in the right hand side of Eq. (2.11), some frequencies cannot be recovered which generates artifacts in the phase-retrieved maps. This problem can be overcome if several propagation distances are used. In this case, the phase retrieval problem can be solved by inducing the least squares method. The solution of the CTF method based on multiple distances can be found by solving an optimization problem:

$$\min \epsilon = \sum_{k=1}^{K} \left| 2\sin(\pi\lambda D_k \|\mathbf{f}\|^2)\tilde{\varphi}(\mathbf{f}) - 2\cos(\pi\lambda D_k \|\mathbf{f}\|^2)\tilde{B}(\mathbf{f}) - \tilde{I}_{D_k}(\mathbf{f}) \right|^2. \qquad (2.12)$$

This yields the following expression of the phase shift in the Fourier domain [Max Langer et al. (2008)]:

$$\tilde{\varphi}(\mathbf{f}) = \frac{1}{2\Delta+\alpha}\left[C\sum_{k=1}^{K}\sin(\pi\lambda D_k\|\mathbf{f}\|^2)\tilde{I}_{D_k}(\mathbf{f}) - A\sum_{k=1}^{K}\cos(\pi\lambda D_k\|\mathbf{f}\|^2)\tilde{I}_{D_k}(\mathbf{f})\right]. \qquad (2.13)$$

where $A = \sum_{k=1}^{K}\sin(\pi\lambda D_k\|\mathbf{f}\|^2)\cos(\pi\lambda D_k\|\mathbf{f}\|^2)$, $B = \sum_{k=1}^{K}\sin^2(\pi\lambda D_k\|\mathbf{f}\|^2)$, $C = \sum_{k=1}^{K}\cos^2(\pi\lambda D_k\|\mathbf{f}\|^2)$, $\Delta = BC - A^2$, and α is a regularizing term.

2.5.2.3 Discussion

Although the TIE can find a unique solution in most cases, it is only valid within a range of small distances and needs to take different images at two sufficiently close planes from the object. The CTF can benefit of the use of several distances to weaken the impact of zero crossings, but is still limited to weak absorption and slowly varying phase. A mixed method which extends the validity to both long distances and strong absorbing (but slowly varying) objects has been proposed with the asymptotical combination of CTF and TIE [Guigay et al. (2007)]. The different algorithms have been quantitatively compared in previous work on numerical and experimental phantoms [Max Langer et al. (2008)]. Besides, a convenient algorithm has been derived from the TIE model by Paganin adding an assumption on the homogeneity of the object [Paganin et al. (2002)]. This method is quite popular since it only requires a single phase contrast image and it is essentially based on a Fourier low-pass filter which can be applied directly on the recorded image. More details about this method will be introduced in the next chapter.

2.5.3 Tomographic reconstruction

In conventional CT, the attenuated intensity of the X-ray beam after passing through the object is recorded by the detector. Thanks to the mathematic support of the Radon Transform defined by Johann Radon in 1917, the projections for each angle θ can be modeled by the integral of a function over lines describing paths of the X-ray beam.

The Fourier slice theorem, also called the central slice theorem, is another crucial result in the theory of image reconstruction [Kak et al. (1988)]. It states that the 1D Fourier transform of the projection of an object at an angle θ is equal to the 1D profile across the origin of the 2D Fourier transform of the object at the same angle. This means that the 2D Fourier transform of the object can be obtained by acquiring projections of the object over a range of 180° (symmetry). Thus, the section can be theoretically reconstructed by 2D inverse Fourier transform.

In practice, the filtered back-projection (FBP) algorithm is commonly used for tomographic reconstruction. It consists in back-projecting each angular projection which has been previously convolved with a 1D filter derived from the ramp filter.

In 3D absorption CT using a parallel beam, this method can be extended to the reconstruction of the 3D linear attenuation coefficient map $\mu(x, y, z)$ by repeating a sequence of 2D FBP algorithm as [Salomé et al. (1999)]:

$$\mu(x, y, z) = \int_0^{\pi} \tilde{p}_\theta(x\cos\theta + y\sin\theta, z)\,d\theta. \qquad (2.14)$$

where $\tilde{p}_\theta$ is the 2D projection at angle θ filtered by a ramp filter.
This algorithm has been implemented at ESRF in the PyHST software (Python High Speed Tomography) and is directly usable on the raw data [Mirone et al. (2014)]

In 3D X-ray phase CT, the same principle can be applied after phase retrieval. In this case, the real part of the refractive index $\delta_n(x, y, z)$ is reconstructed from phase maps retrieved at each projection angle.

2.6 Conclusion

In this chapter, we first introduced the development of synchrotron radiation sources and reviewed a number of third generation synchrotron radiation sources around the world. Then, we described in more details the ESRF and the ESRF-Extremely Brilliant Source project in the new century. Next, we highlighted two beamlines ID16A and ID16B of the ESRF where our experiments were performed, such as the basic condition of the lab, the scanning environment and the imaging techniques. Finally, we shortly introduced the phase retrieval problem in X-ray phase CT as well as the basics of CT reconstruction.

Chapter 3: State of the art on the quantitative analysis of the lacuno-canalicular network

Contents

3.1 Introduction

In order to have a better understanding of the function of the LCN during bone remodeling, it is important to obtain quantitative data about the geometric and structural properties of this complex network. In this chapter, we review a number of studies which achieved the measurement of morphological and topological parameters of the LCN from the 2D and 3D images. According to the imaging method, either, we can see directly the osteocytes, like in optical imaging, or only the osteocyte lacunae, like in X-ray imaging. In this latter case, the osteocyte properties will be indirectly quantified by the lacunar properties.

3.2 Characterization of lacunae or osteocytes

3.2.1 Density of lacunae or osteocytes

The density of lacunae or osteocytes was measured in many experiments using different species. The density of lacunae or osteocytes can be calculated by different ways. For 2D images, the density is defined as the total number of lacunae (osteocytes) divided by the bone area (Lc.N/BA or Ot.N/BA) excluding the areas of Haversian or Volkmann canals[Rolvien et al. (2017)] or by the tissue area (Lc.N/TA or Ot.N/TA). Similarly, in 3D, the density is computed using total the number of lacunae (osteocytes) divided by the bone volume (Lc.N/BV or Ot.N/BV) or the tissue volume (Lc.N/TV or Ot.N/TV). Table 3.1 and Table 3.2 summarize the results found in the literatures about the density of lacunae in 2D and 3D respectively. We can see that the lacunar density in human is about 200–700 mm^{-2} and 10,000–35,000 mm^{-3}, which is smaller than the lacunar density in animals such as rabbits, sheep, rats and mice, about 700–1200 mm^{-2} and 40,000–80,000 mm^{-3}.

Table 3.1 Lacunar density reported in 2D

Reference	Imaging	Species	Location	Group	Samples	Lc/Ot	Values
							Lc.N/BA (#/mm^2)
[Mullender et al. (1996)]	LM	Human	Iliac crest biopsies	Osteoporotic patients	34	Lc	212.1±31.4
				Control	29	Lc	182.6±39.9
[Jordan et al. (2003)]	LM	Human	Femora	Males	3	Lc	433.8±37.7
				Females	8	Lc	447.5±14.8
[Qiu et al. (2006)]	LM	Human	Transiliac biopsies	Black	34	Lc	248±44.0
				White	94	Lc	217±28.6
[Sasaki et al. (2015)]	SEM	Rabbit	Tibial metaphysis	Loading	7	Ot	1191.24±85.24
				Control	7	Ot	835.25±79.64
[Shah et al. (2016)]	SEM	Sheep	Femora	Porous implant	18	Ot	1099±25
				Solid implant	18	Ot	954±28
				Native bone	24	Ot	696±69
[Rolvien et al. (2017)]	LM	Human	Iliac crest biopsies	Vitamin D replete	60	Lc	~ 140±10
				Vitamin D deficient	60	Lc	~ 130±10
[Ashique et al. (2017)]	CLSM	Human	Anterior femora	Young	5	Lc	695±79
				Aged	6	Lc	546±126

Table 3.2 Lacunar density reported in 3D

Reference	Imaging	Species	Location	Group	Samples	Values
						Lc.N/BV (#/mm^3)
[van Hove et al. (2009)]	nCT	Human	Tibia	Osteoarthritis	1	2.18±0.40×10^4
				Osteopenia	1	0.80±0.05×10^4
				Osteopetrosis	1	1.56±0.34×10^4
[Carter, Thomas, Clement, and Cooper (2013)]	SR µCT	Human	Femora		30	2.39±0.25×10^4
[Carter, Thomas, Clement, Peele, et al. (2013)]	SR µCT	Human	Femora		13	3.13±0.30×10^4
[Dong, Haupert, et al. (2014)]	SR µCT	Human	Femora		13	2.05±0.29×10^4
[Bach-Gansmo et al. (2015)]	SR µCT	Rat	Femora	Lamellar	3	4.10±0.80×10^4
				Central	3	7.84±0.97×10^4
[Bach-Gansmo, Brüel, et al. (2016)]	SR µCT	Human	Iliac crest biopsies	Men	42	1.49±0.21×10^4
				Women	46	1.5±0.2×10^4
[Bach-Gansmo, Wittig, et al. (2016)]	SR µCT	Rat	Femora	Botox	5	~ 5±1.1×10^4
				Contralateral	5	~ 4.7±0.6×10^4
				Control	5	~ 4.2±0.8×10^4
[Andronowski et al. (2017)]	SR µCT	Human		Cortical	129	2.27±0.74×10^4
				Cancellous	99	1.05±0.34×10^4
						Lc.N/TV (#/mm^3)
[Sharma et al. (2012)]	CLSM	Rat	Tibia	SHAM	6	6.73±1.4×10^4
				OVX	6	7.70±2.5×10^4
[Palacio-Mancheno et al. (2014)]	µCT	Rat	Tibia	Edge_Det	6	4.28×10^4
				Hist	6	4.07×10^4
[Dong, Haupert, et al. (2014)]	SR µCT	Human	Femora		13	1.86±0.37×10^4
[Hemmatian et al. (2017)]	µCT	Mice	Fibulae	Reproducibility	10	4.22±0.23×10^4
[Sharma et al. (2018)]	µCT	Rat	Tibia	SHAM	6	~ 8.5±1.0×10^4
			Tibia	OVX	6	~ 7.4±1.4×10^4
[Gatti et al. (2018)]	µCT	Rat	Anterior tibia	SHAM	6	6.18±0.75×10^4
			Anterior tibia	OVX	6	3.94±0.78×10^4

3.2.3 Lacunar porosity

Similar to density, the lacunar porosity may have different expressions. In 2D, the porosity is generally calculated by the total surface of lacunae divided by the bone area (Lc.TA/BA) while in 3D it is defined as the total volume of lacunae divided by the bone volume or the tissue volume(Lc.TV/BV or Lc.TV/TV). A recent study reported that the 2D porosity of lacunae is about 3.2% for young women (20–23 years old) and 2.5% for old women (70–86 years old) [Ashique et al. (2017)]. In 3D, the lacunar porosity appears to be lower in human 0.84% [Dong, Haupert, et al. (2014)] or 0.68% [Repp, Kollmannsberger, Roschger, Kerschnitzki, et al. (2017)], and between 1–2% in rats and mice (Table 3.3).

Table 3.3 Porosity of the total lacunae

Reference	Dim	Imaging	Species	Location	Group	Samples	Values
							Lc.TA/BA (%)
[Ashique et al. (2017)]	2D	CLSM	Human	Anterior femora	Young	5	3.2±1.0
					Aged	6	2.5±0.5
							Lc.TV/BV (%)
[Dong, Haupert, et al. (2014)]	3D	SR µCT	Human	Femora		13	0.84±0.17
							Lc.TV/TV (%)
[Palacio-Mancheno et al. (2014)]	3D	µCT	Rat	Tibia	Edge_Det	6	1.24
					Hist	6	1.20
[Dong, Haupert, et al. (2014)]	3D	SR µCT	Human	Femora		13	0.76±0.19
[Repp, Kollmannsberger, Roschger, Kerschnitzki, et al. (2017)]	3D	CLSM	Human	Femora		4	0.68
[Hemmatian et al. (2017)]	3D	µCT	Mice	Fibulae	Reproducibility	10	1.52±0.17
[Sharma et al. (2018)]	3D	µCT	Rat		SHAM	6	~ 1.5±0.5
					OVX	6	~ 1.3±0.2
[Gatti et al. (2018)]	3D	µCT	Rat	Anterior tibia	SHAM	6	1.31±0.18
				Anterior tibia	OVX	6	0.83±0.17

3.2.3 Morphological parameters of lacunae

3.2.3.1 2D morphological parameters

Few morphological parameters can be calculated from 2D images but they are limited by the imaging techniques. Generally, three parameters are considered to describe the lacunae: the average lacunar area (Lc.A), the average lacunar length (Lc.L1) and width (Lc.L2). In addition to these, there are some parameters proposed to evaluate the pericellular space between the osteocyte cell body and the lacunar wall, such as the average lacunar pericellualr area (Lc.PA) and pericellualr thickness (Lc.PT) as shown in Figure 3.1 [X. Lai et al. (2015)]. Table 3.4 reports parameters obtained from 2D imaging techniques. We can see that the average lacunar area for human is about 20–70 µm^2, the average length about 14–25 µm and the average width about 10 µm. Also, the average lacunar pericellualr area is about 7 µm^2 and the pericellualr thickness about 0.45 µm. However, we may note that these parameters are apparent parameters since their values depend on the slicing direction.

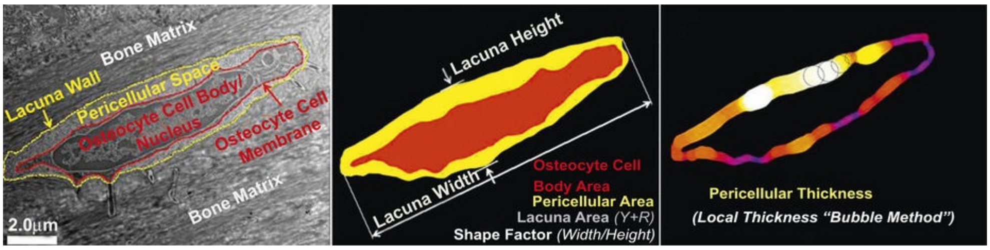

Figure 3.1 The measurements of lacunae by quantifying the pericellular area and the pericellular thickness [X. Lai et al. (2015)]

Table 3.4 2D morphological parameters of lacunae

Reference	Imaging	Species	Location	Group	Samples	Values
						Lc.A (μm^2)
[Mullender et al. (1996)]	LM	Human	Iliac crest biopsies	Osteoporotic patients	34	39.1±4.9
				Control	29	45.5±6.8
[Remaggi et al. (1998)]	LM	Human	Mid-diaphyseal level of long bone	Parallel-fibered bone		~ 26±10
				Woven bone		~ 67±17
[Jordan et al. (2003)]	LM	Human	Femora	Osteoporotic fracture		51±1.1
				Coxarthrosis		49±7
				Control		37±5.4
[Ashique et al. (2017)]	CLSM	Human	Anterior femora	Young	5	45.6±8.7
				Aged	6	46.4±9.3
						Lc.L1 (μm)
[Remaggi et al. (1998)]	LM	Human	Mid-diaphyseal level of long bone	Parallel-fibered bone		~ 25±5
				Woven bone		~ 14±4
[Lin et al. (2011)]	AFM	Bovine	Tibia	Transverse	20	9.66±2.82
				Radial	20	10.88±3.38
						Lc.L2 (μm)
[Remaggi et al. (1998)]	LM	Human	Mid-diaphyseal level of long bone	Parallel-fibered bone		~ 10±2
				Woven bone		~ 12±3
[Lin et al. (2011)]	AFM	Bovine	Tibia	Transverse	20	3.86±1.02
				Radial	20	5.37±1.71
						Lc.PA (μm^2)
[X. Lai et al. (2015)]	TEM	Mice	Femora	C1532Yneo perlecan hypomorph	3	6.85±1.85
				C57BL/6J	3	7.72±1.88
						Lc.PT (μm)
[X. Lai et al. (2015)]	TEM	Mice	Femora	C1532Yneo perlecan hypomorph	3	0.41±0.09
				C57BL/6J	3	0.47±0.09

3.2.3.2 3D morphological parameters

Compared to the 2D, the 3D images can provide unbiased parameters as follows: the average lacunar volume (Lc.V), the average lacunar surface area (Lc.S), the average lacunar length (Lc.L1), width (Lc.L2) and depth (Lc.L3), as well as the average lacunar orientation. The length, width and depth can be defined as the long axis, the medium axis and the short axis of the ellipsoid which fits the targeted lacuna. Carter et al. used the software AMIRA to find the fitting ellipsoid for each lacuna and get three eigenvalues ($Lc.\lambda1 > Lc.\lambda2 > Lc.\lambda3$) of the covariance matrix [Carter, Thomas, Clement, and Cooper (2013)]. Dong et al. used an in-house method based on the calculation of the second order moment matrix [Dong, Haupert, et al. (2014)]. The length of each axis of the ellipsoid can be calculated by scaling the corresponding eigenvalue. Besides, Carter et al. introduced other parameters derived from these three eigenvalues to describe the ellipticity of different lacunae, such as the lacunar stretch

(Lc.St), the lacunar oblateness (Lc.Ob), the lacunar equancy (Lc.Eq), the lacunar elongation (Lc.El) and the lacunar flatness (Lc.Fl), which are expressed as follows:

$$\begin{gathered} Lc.St = \frac{\lambda_1 - \lambda_3}{\lambda_1}, Lc.Ob = 2 * \frac{\lambda_2 - \lambda_3}{\lambda_1 - \lambda_3} - 1 \\ Lc.Eq = \frac{\lambda_3}{\lambda_1}, Lc.El = 1 - \frac{\lambda_2}{\lambda_1}, Lc.Fl = 1 - \frac{\lambda_3}{\lambda_2} \end{gathered} . \tag{3.1}$$

For the lacunar orientation, there are several different calculation methods. Normally, this orientation is defined by computing the angle between the long axis of the lacuna and the longitudinal axis of bone (Lc.θ) [Varga et al. (2015)] [Bach-Gansmo, Wittig, et al. (2016)] [Hemmatian et al. (2017)]. But Carter et al. measured the orientation as the angle between the long axis of the lacuna and the horizontal axis of the sample (Lc.Φ) [Carter, Thomas, Clement, and Cooper (2013)]. In addition, Repp et al. proposed two angles to describe the orientation: the polar angle and the azimuthal angle. Two coordinate systems can be used to calculate these angles: the Haversian coordinate system which defines a central axis in the middle of the Haversian canal and then the radial direction as the shortest direction towards this axis; the lamellar coordinate system which defines the radial direction perpendicular to the bone lamella and then another direction perpendicular to the radial direction and parallel to the Haversian canal. In both coordinate systems, the third coordinate axis is defined by the right-hand rule in the image plane [Repp, Kollmannsberger, Roschger, Berzlanovich, et al. (2017)]. The polar angle is defined as the angle between the small axis of the lacuna and the radial direction while the azimuthal angle as the angle between the long axis of the lacuna and the direction of the Haversian canal. As shown in Figure 3.2, the average polar angle is close to zero which means that the short axis points to the center of the Haversian canal, and the average azimuthal angle in the middle of lamellae is close to 180° which means that the long axis is parallel to the Haversian canal.

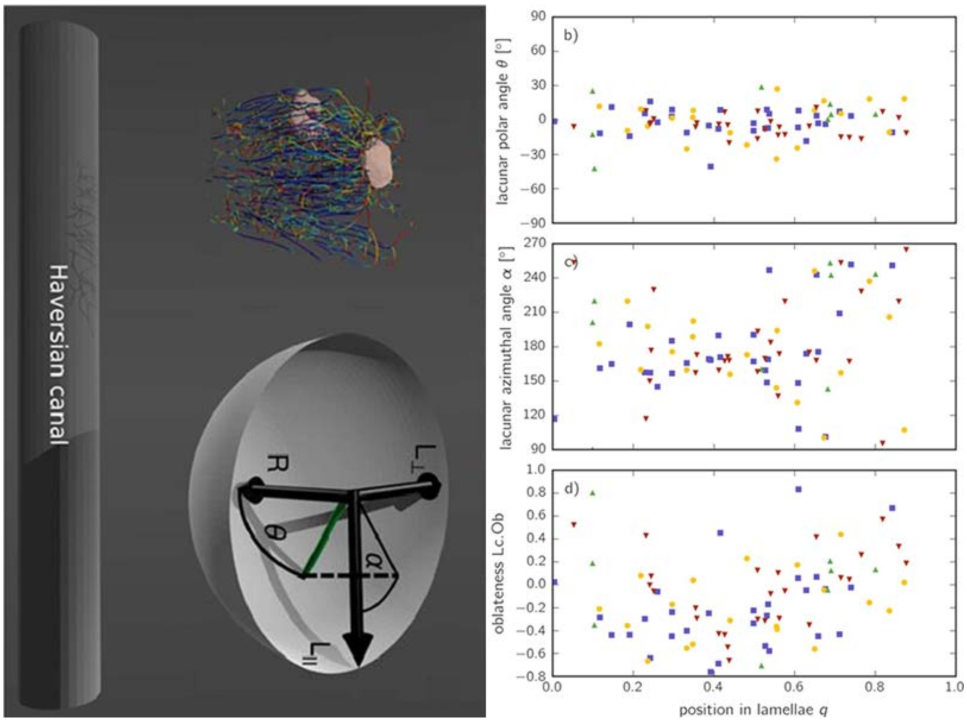

Figure 3.2 The polar angle and the azimuthal angle of lacunae and the statistic results [Repp, Kollmannsberger, Roschger, Berzlanovich, et al. (2017)]

Table 3.5 shows the 3D morphological parameters of lacunae reported in the literatures. The average volume of lacunae for human varies from 50 μm^3 to 730 μm^3 and the average surface from 90 μm^2 to 430 μm^2. The average length, width and depth of lacunae for human is about 15 μm, 12 μm and 6 μm which is bigger than those for rats, about 12 μm, 8 μm and 3 μm respectively. Moreover, the parameters to evaluate the ellipticity are also given in the table: the lacunar stretch (~ 0.73), the lacunar oblateness (~ -0.21), the lacunar equancy (~ 0.18), the lacunar elongation (~ 0.70) and the lacunar flatness (~ 0.50). For the lacunar orientation, the angle between the long axis of the lacuna and the longitudinal axis of bone varies between 7° and 30° while the angle relative to the horizontal axis of the sample is about 55°.

Table 3.5 3D morphological parameters of lacunae

Reference	Imaging	Species	Location	Group	Samples	Values
						Lc.V (μm^3)
[Remaggi et al. (1998)]	LM	Human	Mid-diaphyseal level of long bone	Parallel-fibered bone		~ 570
				Woven bone		~ 730
[van Hove et al. (2009)]	nCT	Human	Tibia	Osteoarthritis	1	51.2±2.2
				Osteopenia	1	179.1±15.6
				Osteopetrosis	1	97.6±4.5
[Sharma et al. (2012)]	CLSM	Rat	Tibia	SHAM	6	352±30
				OVX	6	393±92
[Langer et al. (2012)]	SR nCT	Human	Femora		2	364.1±63.6
[Carter, Thomas, Clement, and Cooper (2013)]	SR μCT	Human	Femora		30	252±63
[Carter, Thomas, Clement, Peele, et al. (2013)]	SR μCT	Human	Femora		13	~ 400±48
[Dong, Haupert, et al. (2014)]	SR μCT	Human	Femora		13	409.5±149.7
[Bach-Gansmo et al. (2015)]	SR μCT	Rat	Femora	Lamellar	3	255±105
				Central	3	187±26
[X. Lai et al. (2015)]	TEM	Mice	Femora	C1532Yneo perlecan hypomorph	3	368.6±168.7
				C57BL/6J	3	447.2±209.4
[Varga et al. (2015)]	SR nCT	Human	Femora		10	511.2±95.54
[Bach-Gansmo, Brüel, et al. (2016)]	SR μCT	Human	Iliac crest biopsies	Men	42	549±40
				Women	46	562±35
[Bach-Gansmo, Wittig, et al. (2016)]	SR μCT	Rat	Femora	Botox	5	~ 260±30
				Contralateral	5	~ 260±35
				Control	5	~ 270±40
[Andronowski et al. (2017)]	SR μCT	Human		Cortical	129	274±28.66
				Cancellous	99	164±40.44
[Dole et al. (2017)]	SR μCT	Mice	Femora	WT	3~4	~ 110±20
[Hemmatian et al. (2017)]	μCT	Mice	Fibulae	Accuracy study	5	235.9±39.83
				Reproducibility study	10	360.49±26.44
	CLSM	Mice	Fibulae	Accuracy study	5	228.4±24.77
[Sharma et al.	μCT	Rat	Tibia	SHAM	6	217.8±18.7

(2018)]						
				OVX	6	210.9 ± 5.0
						Lc.S (µm^2)
[van Hove et al. (2009)]	nCT	Human	Tibia	Osteoarthritis	1	94.6±2.8
				Osteopenia	1	211.9±14.4
				Osteopetrosis	1	142.0±5.0
[Dong, Haupert, et al. (2014)]	SR µCT	Human	Femora		13	336.2±94.5
[X. Lai et al. (2015)]	TEM	Mice	Femora	C1532Yneo perlecan hypomorph	3	347.7±97.4
				C57BL/6J	3	390.8±120.4
[Varga et al. (2015)]	SR nCT	Human	Femora		10	430.4±68.46
						Lc.L1 (µm)
[van Hove et al. (2009)]	nCT	Human	Tibia	Osteoarthritis	1	17.3±0.7
				Osteopenia	1	15.6±0.4
				Osteopetrosis	1	11.1±0.5
[Dong, Haupert, et al. (2014)]	SR µCT	Human	Femora		13	18.9±4.9
[Bach-Gansmo et al. (2015)]	SR µCT	Rat	Femora	Lamellar	3	12.9±3.92
				Central	3	10.57±0.75
[X. Lai et al. (2015)]	TEM	Mice	Femora	C1532Yneo perlecan hypomorph	3	15.4±3.7
				C57BL/6J	3	16.5±3.7
						Lc.L2 (µm)
[van Hove et al. (2009)]	nCT	Human	Tibia	Osteoarthritis	1	12.2±0.6
				Osteopenia	1	13.4±0.6
				Osteopetrosis	1	10.8±0.4
[Dong, Haupert, et al. (2014)]	SR µCT	Human	Femora		13	9.2±2.1
[Bach-Gansmo et al. (2015)]	SR µCT	Rat	Femora	Lamellar	3	8.07±3.13
				Central	3	5.51±0.41
						Lc.L3 (µm)
[van Hove et al. (2009)]	nCT	Human	Tibia	Osteoarthritis	1	8.4±0.4
				Osteopenia	1	8.9±0.4
				Osteopetrosis	1	5.5±0.3
[Dong, Haupert, et al. (2014)]	SR µCT	Human	Femora		13	4.8±1.1
[Bach-Gansmo et al. (2015)]	SR µCT	Rat	Femora	Lamellar	3	2.55±0.45
				Central	3	2.88±0.28
						Lc.λ1
[Carter, Thomas, Clement, and Cooper (2013)]	SR µCT	Human	Femora		30	13.00±2.39
[Carter, Thomas, Clement, Peele, et al. (2013)]	SR µCT	Human	Femora		13	~ 15.44±1.20
						Lc.λ2
[Carter, Thomas, Clement, and Cooper (2013)]	SR µCT	Human	Femora		30	3.33±0.63
[Carter, Thomas, Clement, Peele, et al. (2013)]	SR µCT	Human	Femora		13	~ 4.18±0.60
						Lc.λ3
[Carter, Thomas,	SR µCT	Human	Femora		30	1.55±0.45

Clement, and Cooper (2013)]						
[Carter, Thomas, Clement, Peele, et al. (2013)]	SR µCT	Human	Femora		13	~ 1.75±0.36
						Lc.St
[Bach-Gansmo et al. (2015)]	SR µCT	Rat	Femora		3	0.71±0.00
[Bach-Gansmo, Wittig, et al. (2016)]	SR µCT	Rat	Femora	Botox	5	~ 0.74±0.06
				Contralateral	5	~ 0.72±0.04
				Control	5	~ 0.76±0.05
						Lc.Ob
[Bach-Gansmo et al. (2015)]	SR µCT	Rat	Femora	Central	3	-0.25±0.02
[Bach-Gansmo, Wittig, et al. (2016)]	SR µCT	Rat	Femora	Botox	5	~ -0.18±0.02
				Contralateral	5	~ -0.22±0.02
				Control	5	~ -0.2±0.03
						Lc.Eq
[Carter, Thomas, Clement, and Cooper (2013)]	SR µCT	Human	Femora		30	0.18±0.03
[Carter, Thomas, Clement, Peele, et al. (2013)]	SR µCT	Human	Femora		13	~ 0.19±0.03
						Lc.El
[Carter, Thomas, Clement, and Cooper (2013)]	SR µCT	Human	Femora		30	0.66±0.04
[Carter, Thomas, Clement, Peele, et al. (2013)]	SR µCT	Human	Femora		13	~ 0.73±0.03
						Lc.Fl
[Carter, Thomas, Clement, and Cooper (2013)]	SR µCT	Human	Femora		30	0.41±0.09
[Carter, Thomas, Clement, Peele, et al. (2013)]	SR µCT	Human	Femora		13	~ 0.58±0.01
						Lc.θ (º)
[Bach-Gansmo et al. (2015)]	SR µCT	Rat	Femora		6	30±7
[Varga et al. (2015)]	SR nCT	Human	Femora		10	17.8±10.09
[Bach-Gansmo, Wittig, et al. (2016)]	SR µCT	Rat	Femora	Botox	5	~ 25±6
				Contralateral	5	~ 30±4
				Control	5	~ 28±3
[Hemmatian et al. (2017)]	µCT	Mice	Fibulae	Accuracy study	5	9.52±2.34
				Reproducibility study	10	10.12±1.68
	CLSM	Mice	Fibulae	Accuracy study	5	7.43±0.45
						Lc.Φ (º)
[Carter, Thomas, Clement, and Cooper (2013)]	SR µCT	Human	Femora		30	59.45±3.44
[Carter, Thomas, Clement, Peele, et al. (2013)]	SR µCT	Human	Femora		13	~ 55.90±3.82

3.3 Characterization of canaliculi

3.3.1 Density of canaliculi

In previous researches using 2D imaging techniques, the density of canaliculi was defined as the number of canaliculi per 10 µm length (Ca.N/10 µm) varying between 2.9–3.7 (#/10 µm) [Remaggi et al. (1998)], or the number of canaliculi per unit area (Ca.N/μm^2) which is about 0.85 μm^{-2} for bovine [Lin et al. (2011)]. However, in 3D cases, the density is calculated by the total number of canaliculi divided by the lacunar surface area (Ca.N/Lc.S). It was found to be about 0.20 $\mu m/\mu m^3$ for mice, or the total length of canaliculi per unit volume (Ca.TL/μm^3), about 0.076 $\mu m/\mu m^3$ for human [Repp, Kollmannsberger, Roschger, Berzlanovich, et al. (2017)] (See Table 3.6).

Table 3.6 Density of canaliculi

Reference	Dim	Imaging	Species	Location	Group	Samples	Values
							Ca.N/10 µm (#/10 µm)
[Remaggi et al. (1998)]	2D	LM	Human	Mid-diaphyseal level of long bone	Parallel-fibered bone		~ 2.9±1
					Woven bone		~ 3.7±1
							Ca.N/μm^2 (#/μm^2)
[Lin et al. (2011)]	2D	AFM	Bovine	Tibia	Longitudinal	6	0.85±0.31
							Ca.N/Lc.S (#/μm^2)
[Wang et al. (2005)]	3D	FRAP	Mice	Tibia		5	0.18±0.03
[X. Lai et al. (2015)]	3D	TEM	Mice	Femora	C1532Yneo perlecan hypomorph	3	0.19±0.02
					C57BL/6J	3	0.21±0.05
							Ca.TL/μm^3 ($\mu m/\mu m^3$)
[Repp, Kollmannsberger, Roschger, Kerschnitzki, et al. (2017)]	3D	CLSM	Human	Femoral cortical bone from women		4	0.076±0.008
[Kollmannsberger et al. (2017)]	3D	CLSM	Sheep	Femora		2	0.19±0.01
			Mouse	Femora		2	0.10±0.01

3.3.2 Porosity of canaliculi

Compared with lacunae, there are fewer reports on the porosity of canaliculi. Similar with the definition of porosity of lacunae, the porosity of canaliculi can be expressed as the total area of canaliculi divided by the bone area (Ca.TA/BA) in 2D. It was reported to range from 7.9% to 14.3% in human [Ashique et al. (2017)]. In 3D as shown in Table 3.7, it can be evaluated as the total volume of canaliculi divided by the bone volume (Ca.TV/BV). It was found to be about 0.7% in mouse [Schneider et al. (2011)] and 0.57% in human [Varga et al. (2015)].

Table 3.7 Porosity of canaliculi

Reference	Dim	Imaging	Species	Location	Group	Samples	Values
							Ca.TA/BA (%)
[Lin et al. (2011)]	2D	AFM	Bovine	Tibia	Transverse	20	5.1±1.8
[Ashique et al. (2017)]	2D	CLSM	Human	Femora	Young	5	14.3±1.9

					Aged	6	7.9±2.0
							Ca.TV/BV (%)
[Schneider et al. (2011)]	3D	FIB/SEM	Mouse	Femora			0.70
[Varga et al. (2015)]	3D	SR nCT	Human	Femora		10	0.57±0.13
[Hesse et al. (2015)]	3D	SR nCT	Human	Jaw	Osteonal	1	2.0±0.5
					Interstitial health	4	1.8±0.8
					Interstitial BRONJ	4	2.3±0.8
[Gatti et al. (2018)]	3D	CLSM	Rat	Tibia	SHAM	6	1.90±0.11
					OVX	6	1.70±0.19

3.3.3 Morphological parameters of canaliculi

There are very few works reporting 2D or 3D morphological characteristics of canaliculi. Only with recent development of imaging techniques permitting to visualize canaliculi, some methods have been proposed.

3.3.3.1 2D morphological parameters

In recent studies, some general 2D morphological parameters of canaliculi have been reported, such as the average canalicular diameter (Ca.D), the average canalicular area (Ca.A) and the average canalicular number per each lacuna (Ca.N). Also, with imaging at nano resolution, other parameters inside each canaliculus can be measured like the average pericellular area (Ca.PA) and the average pericellular thickness (Ca.PT) as shown in Figure 3.3 [X. Lai et al. (2015)]. From the results in Table 3.8, it can be seen that the average canalicular diameter is about 259 nm for mice and 443 nm for bovine, and the average canalicular number per each lacuna in 2D is about 16 for human and 32 for sheep. Meanwhile, for mice, the average canalicular area is about 0.074 µm^2 and the average pericellular area is about 0.059 µm^2 [X. Lai et al. (2015)]. Besides, the average pericellular thickness varies between 78–101 µm according to the reports [You et al. (2004)] [X. Lai et al. (2015)].

Table 3.8 2D morphological parameters of canaliculi

Reference	Imaging	Species	Location	Group	Samples	Values
						Ca.D (nm)
[You et al. (2004)]	TEM	Mice	Humeri		3	259±129
[Lin et al. (2011)]	AFM	Bovine	Tibia	Transverse	20	426±118
				Radial	20	459±144
						Ca.N
[Shah et al. (2016)]	SEM	Sheep	Femora	Porous implant	18	~ 35±12
				Solid implant	18	~ 36±13
				Native bone	24	~ 25±11
[Rolvien et al. (2017)]	SEM	Human	Iliac crest biopsies	Vitamin D replete	60	~ 18±1
				Vitamin D deficient	60	~ 14±3
						Ca.A (µm^2)
[X. Lai et al. (2015)]	TEM	Mice	Femora	C1532Yneo perlecan hypomorph	3	0.066±0.031
				C57BL/6J	3	0.081±0.040
						Ca.PA (µm^2)
[X. Lai et al. (2015)]	TEM	Mice	Femora	C1532Yneo perlecan hypomorph	3	0.053±0.026

				C57BL/6J	3	0.065±0.034
						Ca.PT (nm)
[You et al. (2004)]	TEM	Mice	Humeri		3	78±38
[X. Lai et al. (2015)]	TEM	Mice	Femora	C1532Yneo perlecan hypomorph	3	89±27
				C57BL/6J	3	101±32

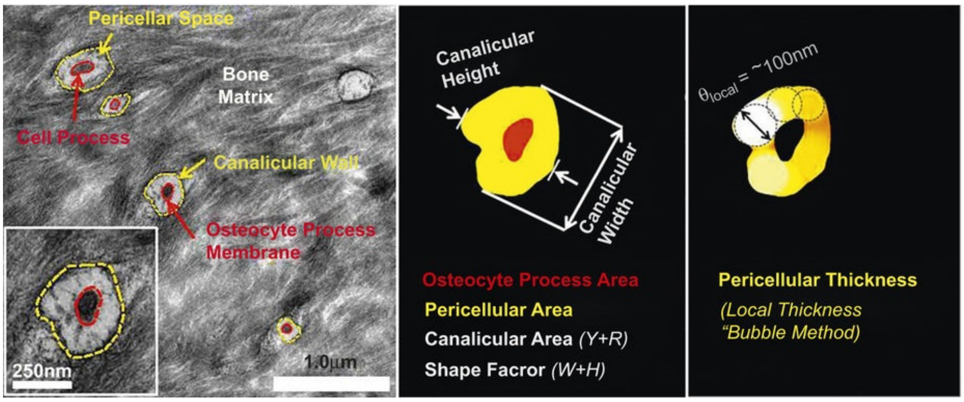

Figure 3.3 The measurements of canaliculi by quantifying the process area, the pericellular area and the pericellular thickness [X. Lai et al. (2015)]

3.3.3.2 3D morphological parameters

Few works reported 3D canaliculi parameters since the emergence of 3D images of the LCN is relatively new and comes mainly from CSLM or SR nCT, such as the average canalicular diameter (Ca.D) and the average canalicular number per each lacuna (Ca.N). Moreover, there are other morphological parameters given in a recent study such as the total canalicular volume (Ca.TV) and the total canalicular surface (Ca.TS) [Varga et al. (2015)]. In Table 3.9, the average canalicular diameter is about 370 nm and the average canalicular number per each lacuna is about 88.5 for human, compared with about 286.6 nm and 86.8 for rats respectively. Also, the canalicular volume is about 144.3 µm^3 and the canalicular surface 1350.6 µm^2 for human, while 123 µm^3 and 461 µm^2 for chick as well as 688 µm3 and 1587 µm^2 for mouse.

Table 3.9 3D morphological parameters of canaliculi

Reference	Imaging	Species	Location	Group	Samples	Values
						Ca.D (nm)
[Varga et al. (2015)]	SR nCT	Human	Femur shaft		10	370±120
[Hesse et al. (2015)]	SR nCT	Human	Jaw	Osteonal	1	~ 360±10
				Interstitial health	4	~ 370±40
				Interstitial BRONJ	4	~ 400±40
[Gatti et al. (2018)]	CLSM	Rat	Tibia	SHAM	6	281.6
				OVX	6	291.6
						Ca.N
[Sharma et al. (2012)]	CLSM	Rat	Tibia	SHAM	6	83.9±14
				OVX	6	89.7±15
[Dong, Pacureanu, et al. (2014)]	SR µCT	Human	Femora		1	~ 90±30
[X. Lai et al. (2015)]	CLSM	Mice	Femora	C1532Yneo perlecan hypomorph	3	65.3±15.2
				C57BL/6J	3	77.5±12.0
[Varga et al. (2015)]	SR nCT	Human	Femur shaft		10	88.5±24.88
						Ca.TV (µm^3)

[Sugawara et al. (2011)]	CLSM	Chick	Parietal bone			123
		Mouse	Parietal bone			688
[Varga et al. (2015)]	SR nCT	Human	Femur shaft		10	144.3±58.51
						Ca.TS (μm^2)
[Sugawara et al. (2011)]	CLSM	Chick	Parietal bone			461
		Mouse	Parietal bone			1587
[Varga et al. (2015)]	SR nCT	Human	Femur shaft		10	1350.6±553.88

3.4 Characterization of the LCN

3.4.1 Porosity of the LCN

Considering lacunae and canaliculi as a whole network, the porosity of the LCN is defined as the total area of the LCN divided by the bone area excluding the area of Haversian canal and vascular (LCN.TA/BA) in 2D, while the total volume of the LCN divided by the tissue volume (LCN.TV/TV) in 3D. From the limited report results (see Table 3.10), we can see that the 2D porosity of the LCN ranges from 10.5% to 17.6% for human depending on ages [Ashique et al. (2017)]. Meanwhile, the 3D porosity of the LCN varies a lot for different species of animals, such as 5% for sheep, 16% for mouse and about 2.88% for rats [Kollmannsberger et al. (2017)], [Gatti et al. (2018)].

Table 3.10 Porosity of the LCN

Reference	Dim	Imaging	Species	Location	Group	Samples	Values
							LCN.BA/BA (%)
[Ashique et al. (2017)]	2D	CLSM	Human	Femora	Young	5	17.6±2.9
					Aged	6	10.5±2.4
							LCN.TV/TV (%)
[Kollmannsberger et al. (2017)]	3D	CLSM	Sheep	Femora		2	5±1
			Mouse	Femora		2	16±5
[Gatti et al. (2018)]	3D	CLSM	Rat	Tibia	SHAM	6	3.22±0.30
					OVX	6	2.53±0.36

3.4.2 Topological parameters of the LCN

To measure the topological parameters, the LCN was converted into a weighted undirected graph by skeletonization, where lacunae serve as nodes connected by edges representing canaliculi [Kollmannsberger et al. (2017)]. To describe the distance between voxels in the graph, several variables need to be defined (see Figure 3.4): the distance from a matrix voxel to its neighboring lacuna (LCN.DL), the distance from a matrix voxel to its neighboring LCN (LCN.DLC) and the distance from any voxel within the canaliculus to the closest lacuna (LCN.DN). Then, there are some topological parameters proposed for the evaluation of the network. The edge density (LCN.ED) is defined as the number of existing edges divided by the number of possible edges in an undirected graph, while the weight of a node (LCN.W) as the number of its connecting edges. To evaluate the local connectivity, the “CC” of a node (LCN.CC) is expressed as the number of existing edges divided by the number of possible edges between all neighbors of this node. Moreover, the average shortest path (LCN.ASP) is calculated by taking the mean of all shortest paths between any two nodes and the betweenness centrality of a node (LCN.BC) by the fraction of all such shortest paths in the network running through this node. Besides, to judge whether the LCN is a small world network, Kollmannsberger et al. defined the small-worldness (LCN.SW) as the ratio of LCN.ASP and LCN.CC divided by the same ratio for an Erdös–Renyi (ER) random graph of the same size and edge density [Kollmannsberger et al. (2017)].

Table 3.11 lists the topological parameters of the LCN which has been reported [Kollmannsberger et al. (2017)]. First, the average distance from a matrix voxel to its neighboring LCN for sheep is about 1.01 µm smaller than 1.75 µm for mouse, which means that the matrix for sheep is closer to the LCN. And the average distance from any voxel within the canaliculus to the closest lacuna for sheep is also smaller than that for mouse, 10.25 µm compared with 16 µm, which may lead to higher transport efficiency. Then, the average edge density is about 0.4×10^{-3} for sheep and 0.7×10^{-3} for mouse, and the average weight of a node is about 3.29 for sheep and 3.27 for mouse which seems no significant difference. Meanwhile, the average CC and the average shortest path for two species are also similar with each other, 0.04 and 47.27 µm for sheep, as well as 0.05 and 49.15 µm for mouse. Besides, the average small-worldness is 44.84 for sheep and 31.91 for mouse. After being compared to other networks, the LCN was found to fit well with the linear relationship between the small-worldness and nodes number of the real small-world network [Kollmannsberger et al. (2017)].

Table 3.11 Topological parameters of the LCN

Reference	Dim	Imaging	Species	Location	Group	Samples	Values
							LCN.DLC (µm)
[Kollmannsberger et al. (2017)]	3D	CLSM	Sheep	Femora		2	1.01±0.04
			Mouse	Femora		2	1.75±0.22
							LCN.DN (µm)
[Kollmannsberger et al. (2017)]	3D	CLSM	Sheep	Femora		2	10.25±1.46
			Mouse	Femora		2	16±5
							LCN.ED
[Kollmannsberger et al. (2017)]	3D	CLSM	Sheep	Femora		2	~ 0.4±0.1×10^{-3}
			Mouse	Femora		2	~ 0.7±0.15×10^{-3}
							LCN.W
[Kollmannsberger et al. (2017)]	3D	CLSM	Sheep	Femora		2	3.29±0.01
			Mouse	Femora		2	3.27±0.01
							LCN.CC
[Kollmannsberger et al. (2017)]	3D	CLSM	Sheep	Femora		2	0.04±0.00
			Mouse	Femora		2	0.05±0.00
							LCN.ASP (µm)
[Kollmannsberger et al. (2017)]	3D	CLSM	Sheep	Femora		2	47.27±4.94
			Mouse	Femora		2	49.15±5.70
							LCN.SW
[Kollmannsberger et al. (2017)]	3D	CLSM	Sheep	Femora		2	44.84±4.97
			Mouse	Femora		2	31.91±4.64

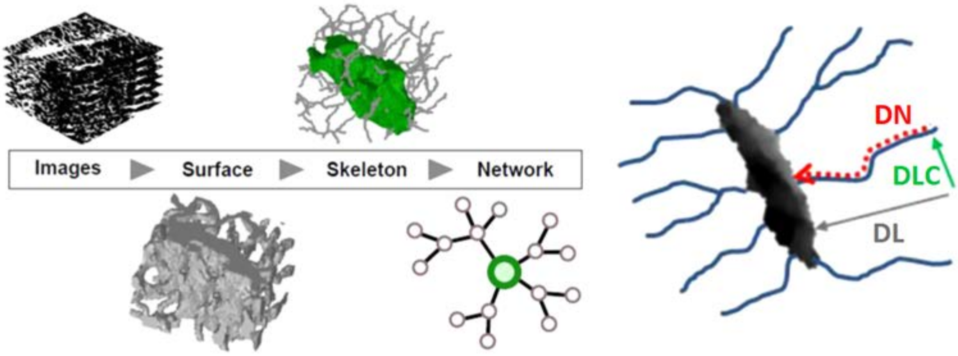

Figure 3.4 Image analysis workflow from image stacks to topological network and the sketch for some distance parameters [Kollmannsberger et al. (2017)]

3.5 Conclusion

In this chapter, we briefly reviewed the state of art about the quantitative evaluation of the LCN. We may note that this topic has raised an increasing interest during the last three years. We first introduced the studies about the lacunae and canaliculi in the field of both 2D and 3D. Then we described some distribution and topological parameters for the whole complex network. In short, there are a number of reports about the characterization of lacunae for porosity, density and morphology, but fewer researches have been done on the quantification of canaliculi and the LCN using 3D imaging techniques. Therefore, it is still crucial to image the LCN at higher resolution and measure relative quantitative parameters to describe the structural properties of the LCN.

Chapter 4: Evaluation of phase retrieval approaches in magnified X-ray phase nano computerized tomography applied to bone tissue

This chapter is a published research paper (B. Yu, L. Weber, A. Pacureanu, M. Langer, C. Olivier, P. Cloetens, and F. Peyrin. "Evaluation of phase retrieval approaches in magnified X-ray phase nano computerized tomography applied to bone tissue," Opt. Express, 26(9), 11110, 2018.). Except the text of the published paper, we described the NLCG method in more details and we added the measured results of the samples at the voxel size of 120 nm as a supplement.

Contents

4.1 Introduction

X-ray is a form of electromagnetic radiation which is emitted when an electron jumps from one energy level to another [Karazija (2013)]. Its wavelength is very short ranging from 0.001 to 10 nm located between visible light and gamma rays in the electromagnetic spectrum. X-ray was discovered by Wilhelm Röntgen in 1895 so that it is also called Röntgen radiation. X-ray has a good ability of penetration which makes it pass through a lot of materials opaque to visible light. Nowadays, X-ray has been widely utilized in all kinds of fields such as medicine, biology, chemistry and material.

X-ray Computerized Tomography (CT) takes advantage of transmission property to record a cross-sectional image of the object. It can distinguish the before and after order among different structures by providing depth information [Zeng (2010)]. The first generation of X-ray CT used a source emitting a pencil beam to measure projections. Source and detector needed to perform both translation and rotation during the scan. Depending on the first, the second generation utilized a narrow fan-beam and a small array of detectors with still two motions, which reduced the scanning time significantly. The third generation included wide fan-beam geometry and a large linear or circular array of detectors. There is no need for translation and the acquisition time is less than 20 s per scan. Compared with the third, the fourth generation had a complete ring detector and the X-ray source rotated inside the ring around the object [Peyrin et al. (2012)].

Imaging the three-dimensional (3D) organization of bone structures has been a pioneering application in micro-computerized tomography (micro-CT) [Rüegsegger et al. (1996)]. Conventional X-ray micro-CT based on laboratory X-ray sources is now routinely used to assess 3D bone micro-architecture. When coupled to synchrotron radiation (SR), with the possibility to use monochromatic or quasi-monochromatic sources, image quality is improved since beam hardening artifacts are avoided, which permits to obtain a quantitative map of the linear attenuation coefficient [Salomé et al. (1999)]. Over the past two decades, a number of third-generation SR sources have been actively developed and most of them have designed SR micro-CT setups.

An additional advantage of SR micro-CT is the facility to implement X-ray phase imaging with the high degree of spatial coherence. This technique is attracting more attention with the progresses in SR sources, detectors and computing facilities. Since its sensitivity can be more than three-orders of magnitude higher than attenuation-based imaging, it enables imaging of weakly absorbing samples such as soft tissue and of materials with small changes in attenuation [Bonse et al. (1965)],[Momose (1995)]. Phase micro-CT has been used in many biomedical areas and has provided valuable images of small animals or biological samples at micrometric scale. For example, it was used to image small animals [Boistel et al. (2013)], brain tissue [Marinescu et al. (2013)] and lung microstructure [Krenkel et al. (2015)].

Phase contrast can be obtained experimentally by various techniques either on synchrotron radiation or laboratory sources (for a review see [Bravin et al. (2013)],[Hagen et al. (2015)]). Here, we will focus on propagation-based phase contrast imaging [Cloetens et al. (1997)] as it provides the highest spatial resolution. This technique can be used with one or several propagation distances. In previous works, the optimization of experimental parameters such as the source size and the detector resolution has been studied using a single propagation distance [Nesterets et al. (2005)],[Balles et al. (2016)].

Phase retrieval can be expressed as solving a non-linear inverse problem. The corresponding direct problem of image formation in X-ray propagation based phase contrast imaging can be modeled by Fourier optics and Fresnel diffraction considering the weak interaction of X-rays with matter inside the object [Goodman (2005)]. Under these circumstances, the intensity recorded by the detector can be expressed as the squared magnitude of the Fresnel transform of the transmittance function of the object.

While the phase retrieval inverse problem is intrinsically non-linear, various approaches have been proposed to linearize it. The first one is the transport of intensity equation (TIE) which linearizes the intensity by Taylor expansion of the propagator to the first order with respect to the propagation distance. The resulting partial derivative in the propagation direction is then approximated by a finite difference, which is only valid for small propagation distances and low spatial frequencies [Teague (1982)]. The other one is the contrast transfer function (CTF) which linearizes the intensity by expanding the transmittance function to the first order with respect to the amplitude and phase. This yields a linear relationship which is valid for weak absorption and slowly varying phase [Cloetens et al. (1999)]. The TIE generally needs to take different images at two sufficiently close planes from the object, while the CTF is still limited to low absorbing objects. A mixed method which extends the validity to both long distances and strongly absorbing (but slowly varying) objects has been proposed with the asymptotical combination of CTF and TIE [Guigay et al. (2007)]. The different algorithms have been quantitatively compared in previous work on numerical and experimental phantoms [Max Langer et al. (2008)]. Generally, phase retrieval in the Fresnel region suffers from sensitivity to noise in the low spatial frequency range yielding cloud-like artefacts due to a slowly varying background. This has prompted the introduction of a priori knowledge on the object in order to regularize the problem [M. Langer et al. (2014)].

By adding an assumption on the homogeneity of the object directly in the TIE model, Paganin's method has been derived [Paganin et al. (2002)]. This method has proven popular since it only requires a single phase contrast image. It is essentially based on a Fourier low-pass filter which can be applied directly on the recorded projection image as a correction for the propagation effect. Recently, the effectiveness of the method for increasing signal-to-noise ratio while preserving spatial resolution was analyzed by modeling the properties of the noise with propagation [Gureyev et al. (2017)]. However, although it has been used in a number of applications, it requires setting the δ_n/β ratio of the imaged material, which is the ratio between the real and imaginary part of the refractive index of the object, a material and energy dependent constant [Paganin et al. (2002)]. For a given chemical composition, this ratio can be calculated from tabulated values, e.g. by the X-ray optics software XOP [del Rio et al. (2004)]. Besides, this method has also been extended to two-materials objects by modifying the filter [Beltran et al. (2010)] or by using 3D filtering based corrections in the object space [Maximilian Ullherr et al. (2015)].

In this chapter, we focus on imaging bone tissue at the cellular scale by using a new magnified phase nano-CT set-up installed on the beamline ID16A at the ESRF. The beamline is capable of focusing the beam to the nanoscale while keeping a high photon flux. This setup permits to record one or several data sets at different propagation distances. However, acquiring data sets at different distances generates long scan time (about 1h per distance), and possibly more radiation-induced damage to the sample. Thus, we propose to investigate the gain of using several propagation distances instead of one in terms of quality of the reconstructed images, on one hand, and to evaluate phase retrieval algorithms for this type of relatively dense samples, on the other hand. To this aim, we first extend Paganin's single distance formula to multiple distance acquisitions. Then, for comparability, we describe the multi-distance CTF method for homogeneous objects with a known δ_n/β ratio. Further, we examine the relationships between these two methods by an analysis in the Fourier domain. The solution obtained with one of these two methods is then refined iteratively by a non-linear conjugate gradient (NLCG) method. The two phase retrieval methods are applied to data sets of bone tissue samples acquired at the voxel size of 120 nm and 30 nm. In order to compare these different phase retrieval approaches, we use qualitative visual assessment and quantitative evaluation based on the SNR (Signal-to-Noise Ratio) and an estimate of spatial resolution. From a visual point of view, we show that the reconstructed images from the two multiple distances methods are sharper than those reconstructed from one propagation distance only. This is corroborated by the quantitative study, which showed an increase in estimated spatial resolution when using images recorded at several propagation distances.

4.2 Single distance phase retrieval methods

We briefly recall the notations of the forward problem and two solutions to the inverse phase retrieval problem using single distance data. An overview of single distance phase retrieval methods can be found in [Burvall et al. (2011)].

4.2.1 Model of image formation

The interaction between the 3D object and X-rays at a given wavelength λ can be modeled by the complex refractive index distribution [Guigay et al. (2007)],

$$n(x,y,z) = 1 - \delta_n(x,y,z) + i\beta(x,y,z), \tag{4.1}$$

where δ_n is the refractive index decrement, β the absorption index and (x,y,z) the 3D spatial coordinates.

If the propagation direction is z, and the illumination considered flat, the wave after passing through the object can be expressed by the transmittance function $T(\mathbf{x})$ which can be written as:

$$\begin{gathered} T(\mathbf{x}) = a(\mathbf{x})\exp[i\varphi(\mathbf{x})] = \exp[-B(\mathbf{x}) + i\varphi(\mathbf{x})] \\ B(\mathbf{x}) = (2\pi/\lambda)\int \beta(x,y,z)dz \qquad , \\ \varphi(\mathbf{x}) = -(2\pi/\lambda)\int \delta_n(x,y,z)dz \end{gathered} \tag{4.2}$$

where $a(\mathbf{x})$ is the amplitude, $B(\mathbf{x})$ the attenuation, $\varphi(\mathbf{x})$ the phase shift of the wave and $\mathbf{x} = (x,y)$ the coordinates in the plane transverse to z.

When this wave is recorded on a detector at a propagation distance D_k from the object, the recorded intensity $I_{D_k}(\mathbf{x})$ can be modeled as the squared modulus of the Fresnel transform of $T(\mathbf{x})$:

$$\begin{gathered} I_{D_k}(\mathbf{x}) = \left|T(\mathbf{x}) * P_{D_k}(\mathbf{x})\right|^2 \\ P_{D_k}(\mathbf{x}) = \frac{1}{i\lambda D_k}\exp\left(i\frac{\pi}{\lambda D_k}|\mathbf{x}|^2\right), \end{gathered} \tag{4.3}$$

with $P_{D_k}(\mathbf{x})$ the Fresnel propagator and k the distance index.

X-ray phase CT reconstructs the refractive index decrement δ_n which is about three-orders of magnitude higher than the absorption index β, thus the technique offers higher sensitivity than conventional X-ray CT. The 3D phase CT images are obtained from phase maps retrieved at each projection angle as inputs of reconstruction instead of absorption images [Cloetens et al. (1999)]. Therefore, it is necessary to estimate the phase shift $\varphi(\mathbf{x})$ from recorded phase contrast images before tomographic reconstruction.

4.2.2 Paganin's method

The single distance Paganin's method can be derived from the TIE model by using an additional homogeneity constraint on the sample [Paganin et al. (2002)]. This is introduced directly in the contrast model. In the case of homogeneous composition, the phase map is proportional to the absorption map. The proportionality constant is given by the ratio between the real and imaginary part of the refractive index δ_n/β and is supposed to be known a priori. Using this constraint, the retrieval formula is obtained:

$$\varphi(\mathbf{x}) = \frac{1}{2}\cdot\frac{\delta_n}{\beta}\cdot\ln\left(\mathcal{F}^{-1}\left\{\frac{\mathcal{F}\left(I_{D_k}/I_{Inc}\right)(\mathbf{f})}{1+\lambda D_k\pi\frac{\delta_n}{\beta}\|\mathbf{f}\|^2}\right\}(\mathbf{x})\right), \tag{4.4}$$

where $I_{Inc}(\mathbf{x})$ is the incident intensity, and $\mathcal{F}$ (resp. $\mathcal{F}^{-1}$) denote the 2D direct (resp. inverse) Fourier transform operator.

4.2.3 Homogeneous CTF method

The CTF method relies on a linearization of the direct problem, based on the first order Taylor expansion of the transmittance function (Eq. (4.2)), which can be written as:

$$T(\mathbf{x}) \approx 1 - B(\mathbf{x}) + i\varphi(\mathbf{x}). \tag{4.5}$$

The CTF model at one distance can be expressed as [Cloetens et al. (1999)]:

$$\tilde{I}_{D_k}(\mathbf{f}) = \delta_{Dirac}(\mathbf{f}) - 2\cos(\pi\lambda D_k\|\mathbf{f}\|^2)\tilde{B}(\mathbf{f}) + 2\sin(\pi\lambda D_k\|\mathbf{f}\|^2)\tilde{\varphi}(\mathbf{f}), \tag{4.6}$$

where $\delta_{Dirac}(\mathbf{f})$ is the Dirac function, $\tilde{B}(\mathbf{f})$ the Fourier transform of $B(\mathbf{x})$ and $\tilde{\varphi}(\mathbf{f})$ the Fourier transform of $\varphi(\mathbf{x})$.

Similarly to Paganin's method, the CTF method can be combined with the homogeneity assumption [Turner et al. (2004)]. With the assumption of a known δ_n/β, the absorption is proportional to the phase:

$$B(\mathbf{x}) = \frac{2\pi}{\lambda}\frac{1}{\delta_n/\beta}\int \delta_n(x,y,z)dz = -\frac{1}{\delta_n/\beta}\varphi(\mathbf{x}). \tag{4.7}$$

Substituting Eq. (4.7) to (4.6), the solution of the CTF method in the Fourier domain can be expressed as:

$$\tilde{\varphi}(\mathbf{f}) = \frac{1}{2}\cdot\frac{\delta_n}{\beta}\cdot\frac{\tilde{I}_{D_k}(\mathbf{f})-\delta_{Dirac}(\mathbf{f})}{\cos(\pi\lambda D_k\|\mathbf{f}\|^2)+\frac{\delta_n}{\beta}\sin(\pi\lambda D_k\|\mathbf{f}\|^2)}. \tag{4.8}$$

Because of zero crossings in the denominator of Eq. (4.8), some frequencies of φ cannot be recovered. This generates artifacts in retrieved phase maps. This problem can be overcome by combining intensity information $\tilde{I}_{D_k}(\mathbf{f})$ at several propagation distances [Zabler et al. (2005)].

4.3 Multi-distance phase retrieval methods

In this section, we derive multiple distance versions of the previous methods: the extended Paganin's method and the homogeneous CTF method. Then we discuss the relationships between the two methods.

4.3.1 Multi-distance Paganin's method

To make the notations more concise, we introduce the three following variables:

$$\begin{gathered} \tilde{I}_{norm,k}(\mathbf{f}) = \mathcal{F}\left(\frac{I_{D_k}}{I_{Inc}}\right)(\mathbf{f}), \quad \widetilde{H}_k(\mathbf{f}) = 1 + \frac{D_k\delta_n\lambda\pi}{\beta}\|\mathbf{f}\|^2 \\ \tilde{T}_1(\mathbf{f}) = \mathcal{F}\left\{\exp\left(\frac{2\beta}{\delta_n}\varphi(\mathbf{x})\right)\right\}(\mathbf{f}) \end{gathered} . \tag{4.9}$$

According to (4.9), Eq. (4.4) becomes:

$$\tilde{I}_{norm,k}(\mathbf{f}) = \tilde{T}_1(\mathbf{f})\widetilde{H}_k(\mathbf{f}). \tag{4.10}$$

When considering different propagation distances, the phase retrieval problem consists in estimating $\tilde{T}_1(\mathbf{f})$ from $\tilde{I}_{norm,k}(\mathbf{f})$ for D_k for $k = 1, \dots, K$. This problem can be solved using an optimization method. We consider a regularized least squares minimization according to:

$$\min \epsilon = \sum_{k=1}^{K}\left|\tilde{T}_1(\mathbf{f})\widetilde{H}_k(\mathbf{f}) - \tilde{I}_{norm,k}(\mathbf{f})\right|^2 + \alpha\left|\tilde{T}_1(\mathbf{f})\right|^2. \tag{4.11}$$

The first term is the data fidelity term and the second is a Tikhonov regularization term, where α is a regularization parameter. The solution can be written as:

$$\hat{\tilde{T}}_1(\mathbf{f}) = \frac{\frac{1}{K}\sum_{k=1}^{K}\widetilde{H}_k(\mathbf{f})\cdot\tilde{I}_{norm,k}(\mathbf{f})}{\left(\frac{1}{K}\sum_{k=1}^{K}\widetilde{H}_k(\mathbf{f})^2\right)+\alpha}. \tag{4.12}$$

The phase map estimated from acquisitions at different distances is finally obtained as:

$$\hat{\varphi}(\mathbf{x}) = \frac{1}{2} \cdot \frac{\delta_n}{\beta} \cdot \ln\left(\mathcal{F}^{-1}\left\{\frac{\frac{1}{K}\sum_{k=1}^{K} \widetilde{H}_k(\mathbf{f}) \cdot \tilde{I}_{norm,k}(\mathbf{f})}{\left(\frac{1}{K}\sum_{k=1}^{K} \widetilde{H}_k(\mathbf{f})^2\right) + \alpha}\right\}(\mathbf{x})\right). \tag{4.13}$$

4.3.2 Multi-distance homogeneous CTF method

Similarly, we introduce a new variable to express the CTF filter,

$$\tilde{G}_k(\mathbf{f}) = \cos(\pi\lambda D_k \|\mathbf{f}\|^2) + \frac{\delta_n}{\beta}\sin(\pi\lambda D_k \|\mathbf{f}\|^2). \tag{4.14}$$

The forward model of the homogeneous CTF can then be expressed as:

$$\tilde{I}_{D_k}(\mathbf{f}) = \delta_{Dirac}(\mathbf{f}) + 2\tilde{G}_k(\mathbf{f})\tilde{\varphi}(\mathbf{f}). \tag{4.15}$$

Then the regularized least-squares solution in the case of homogeneous CTF and multi-distance acquisition can be written as:

$$\hat{\tilde{\varphi}}(\mathbf{f}) = \frac{1}{2} \cdot \frac{\delta_n}{\beta} \cdot \frac{\frac{1}{K}\sum_{k=1}^{K} \tilde{G}_k(\mathbf{f}) \cdot \left(\tilde{I}_{D_k}(\mathbf{f}) - \delta_{Dirac}(\mathbf{f})\right)}{\frac{1}{K}\sum_{k=1}^{K} \tilde{G}_k(\mathbf{f})^2 + \alpha}. \tag{4.16}$$

4.3.3 Relationships between the two approaches

Following Eq. (4.13) and (4.16), both methods can be interpreted as a linear combination of filtering of the recorded intensities in the Fourier domain. It may be noted that the frequency filters involved in both methods are radial.

Let us first examine the single distance situation. The multi-distance expressions (4.13) and (4.16) obviously simplify to the standard methods when $K = 1$. In Paganin's method, the filter is expressed by $1/\widetilde{H}_k(\mathbf{f})$, which can be interpreted as a low-pass Butterworth filter. For the homogeneous CTF method, the filter is given by $1/\tilde{G}_k(\mathbf{f})$ which is a combination of chirp-like functions. The expression of the phase as a function of the filters differs in the two methods due to the natural logarithm term in the Paganin's expression.

If we consider the weak absorption case where $\left|\frac{2}{\delta_n/\beta}\varphi(\mathbf{x})\right| \ll 1$, by the Taylor expansion at the first order, we get:

$$T_1(\mathbf{x}) = \exp\left(\frac{2}{\delta_n/\beta}\varphi(\mathbf{x})\right) \approx 1 + \frac{2}{\delta_n/\beta}\varphi(\mathbf{x}). \tag{4.17}$$

Then calculating the Fourier transform of $T_1(\mathbf{x})$,

$$\tilde{T}_1(\mathbf{f}) \approx \delta_{Dirac}(\mathbf{f}) + \frac{2}{\delta_n/\beta}\tilde{\varphi}(\mathbf{f}). \tag{4.18}$$

Substituting it into Eq. (4.4) yields,

$$\delta_{Dirac}(\mathbf{f}) + \frac{2}{\delta_n/\beta}\tilde{\varphi}(\mathbf{f}) = \frac{\tilde{I}_{norm,k}(\mathbf{f})}{1 + \lambda D_k \pi \frac{\delta_n}{\beta}\|\mathbf{f}\|^2}. \tag{4.19}$$

Finally, we obtain the solution of $\tilde{\varphi}(\mathbf{f})$,

$$\tilde{\varphi}(\mathbf{f}) \approx \frac{1}{2} \cdot \frac{\delta_n}{\beta} \cdot \frac{\tilde{I}_{norm,k}(\mathbf{f}) - \delta_{Dirac}(\mathbf{f})}{1 + \lambda D_k \pi \frac{\delta_n}{\beta}\|\mathbf{f}\|^2}. \tag{4.20}$$

Now, it can be observed that Eq. (4.8) and (4.20) have the same structures except that the involved filters are different. However, if we make use of Taylor expansion at the first order on $\tilde{G}_k(\mathbf{f})$, we obtain,

$$\tilde{G}_k(\mathbf{f}) = \cos(\pi\lambda D_k \|\mathbf{f}\|^2) + \frac{\delta_n}{\beta}\sin(\pi\lambda D_k \|\mathbf{f}\|^2) \approx 1 + \lambda D_k \pi \frac{\delta_n}{\beta}\|\mathbf{f}\|^2. \tag{4.21}$$

Under the assumptions of weak absorption and low spatial frequencies, Paganin's method and the homogeneous CTF method are identical. However, for higher spatial frequencies, the two filters essentially differ at locations corresponding to the zero crossings of the direct CTF model.

Let us now consider the case where information from several distances is used. In this case, we can summarize the homogeneous CTF method as:

$$\hat{\tilde{\varphi}}(\mathbf{f}) = \frac{1}{2} \cdot \frac{\delta_n}{\beta} \cdot \frac{\frac{1}{K}\sum_{k=1}^{K}\left[\cos(\pi\lambda D_k\|\mathbf{f}\|^2)+\frac{\delta_n}{\beta}\sin(\pi\lambda D_k\|\mathbf{f}\|^2)\right]\cdot\left(\tilde{I}_{D_k}(\mathbf{f})-\delta_{Dirac}(\mathbf{f})\right)}{\frac{1}{K}\sum_{k=1}^{K}\left[\cos(\pi\lambda D_k\|\mathbf{f}\|^2)+\frac{\delta_n}{\beta}\sin(\pi\lambda D_k\|\mathbf{f}\|^2)\right]^2+\alpha}, \tag{4.22}$$

and the extended Paganin's method as:

$$\hat{\tilde{\varphi}}(\mathbf{f}) = \frac{1}{2} \cdot \frac{\delta_n}{\beta} \cdot \frac{\frac{1}{K}\sum_{k=1}^{K}\left(1+\lambda D_k\pi\frac{\delta_n}{\beta}\|\mathbf{f}\|^2\right)\cdot\left(\tilde{I}_{norm,k}(\mathbf{f})-\delta_{Dirac}(\mathbf{f})\right)}{\frac{1}{K}\sum_{k=1}^{K}\left(1+\lambda D_k\pi\frac{\delta_n}{\beta}\|\mathbf{f}\|^2\right)^2+\alpha}. \tag{4.23}$$

As previously, the homogeneous CTF method and the extended Paganin's method at multiple distances will be equivalent in the low frequency range when the absorption is weak, but will differ for higher frequencies.

4.4 Non-linear conjugate gradient method

The non-linear conjugate gradient (NLCG) method is usually used to find the minimum of a quadratic function, which generalizes the conjugate gradient (CG) method. In our case, this function $J(\mathbf{x})$ can be written as:

$$J(\mathbf{x}) = \frac{1}{KM}\sum_{k=1}^{K}\sum_{\mathbf{x}}\left|I_{D_{k,reco}}(\mathbf{x}) - I_{D_{k,calc}}(\mathbf{x})\right|^2, \tag{4.24}$$

where K is the total number of propagation distances, M is the total number of pixels in one projection, $I_{D_{k,reco}}(\mathbf{x})$ is the recorded intensity at the distance D_k, $I_{D_{k,calc}}(\mathbf{x})$ is the calculated intensity by Eq. (4.3):

$$I_{D_{k,calc}}(\mathbf{x}) = \left|T(\mathbf{x}) * P_{D_k}(\mathbf{x})\right|^2 * j_0(\mathbf{x}), \tag{4.25}$$

where $j_0(\mathbf{x})$ models the transfer function of the optics (determined experimentally).

The NLCG method contains iterative calculation and recursive update, which needs several iterations to reach convergence to the minimum. If the current iteration number is n, the operation for this iteration of the NLCG method could normally be divided into 5 steps.

(a) Find the steepest descent direction

According to the principle of the steepest descent method, the opposite direction of the gradient direction is where the function decreases fastest. Considering the non-linear function (9), the negative gradient is expressed as:

$$-g(n) = -\frac{dJ(\mathbf{x})}{dT(\mathbf{x})}. \tag{4.26}$$

(b) Calculate β_n depending on the selected formula

In order to calculate the parameter β_n that is the precondition for the conjugate direction s_n, there are several formulas which have been designed based on different starting points. Four of the best known are listed as follows [Hestenes et al. (1952)],[Fletcher (1964)], [Polak et al. (1969)],[Dai et al. (1999)]:

$$\begin{gathered}
\beta_n^{HS} = \frac{g_n^T(g_n-g_{n-1})}{s_{n-1}^T(g_n-g_{n-1})} \\
\beta_n^{FR} = \frac{\|g_n\|^2}{\|g_{n-1}\|^2} \\
\beta_n^{PR} = \frac{g_n^T(g_n-g_{n-1})}{\|g_{n-1}\|^2} \\
\beta_n^{DY} = \frac{\|g_n\|^2}{s_{n-1}^T(g_n-g_{n-1})}
\end{gathered}. \tag{4.27}$$

Besides, P. Cloetens (unpublished) designed a formula that is based on the orthogonality of s_{n-1}:

$$\beta_n^{PC} = \frac{g_n^T \cdot s_{n-1}}{s_{n-1}^T \cdot s_{n-1}}. \tag{4.28}$$

All the calculation programs using these presented formulas are available at ESRF. One should choose the best depending on the experimental data by comparison.

(c) Compute the conjugate direction

After β_n being obtained by a selected formula, the conjugate direction s_n can be computed by the following formula:

$$s_n = \begin{cases} -g_n & if\ k = 0 \\ -g_n + \beta_n s_{n-1} & if\ k \geq 1 \end{cases}. \tag{4.29}$$

(d) Optimize the step length

The step length α_n can be optimized by performing a line search:

$$\alpha_n = \arg\min_{\alpha} J(\mathbf{x}_n + \alpha s_n). \tag{4.30}$$

(e) Update the solution

The solution $\mathbf{x}_n$ is finally updated by:

$$\mathbf{x}_n = \mathbf{x}_n + \alpha_n s_n. \tag{4.31}$$

Normally, we choose 8 to 10 iterations for NLCG.

4.5 Experiment

4.5.1 Data acquisition

Data were acquired at the beamline ID16A, ESRF (Grenoble, France). This beamline combines coherent imaging techniques and X-ray fluorescence microscopy at a spatial resolution down to about 30 nm, enabling quantitative 3D characterization of morphology and elemental composition of specimens in their native state [Cesar da Silva et al. (2017)]. ID16A provides a high-brilliance beam at two specific energies (17 keV or 33.6 keV). The incoming parallel X-ray beam is monochromatized and focused into a focal spot by multilayer coated curved reflective optics (Kirkpatrick-Baez mirrors). After passing through the sample, the X-ray beam is converted into visible light by a scintillator and recorded by a lens-coupled FReLoN (Fast Readout Low Noise) camera developed by the instrument support group of ESRF with a binned CCD size of 2048×2048 pixels.

X-ray phase nano-CT data acquisition consisted in recording sets of angular projections at different sample positions between the focus and the detector. After being focused, the beam turns from parallel to divergent so that the images recorded at different distances contain not only phase contrast but also geometric magnifications. In practice, the position of the detector is fixed while the sample is moved downstream of the focus [Mokso et al. (2007)],[Max Langer et al. (2012)].

The samples were extracted from transverse cross-sections cut from mid-diaphysis in femurs from female cadavers (50–95 years old). Then, small cortical bone samples (0.4×0.4×3 mm^3) were prepared using a high precision low-speed circular saw. Each sample was positioned on the vacuum sample stage and rotated around a vertical rotation axis. In total, 2000 projections were acquired over a range of 180° at 4 different sample-to-detector distances. The voxel sizes were set to 120 nm and 30 nm, corresponding to a field of view 245 µm and 61 µm respectively. The acquisition time for a complete dataset (i.e. with 4 propagation distances) was approximately 4 hours.

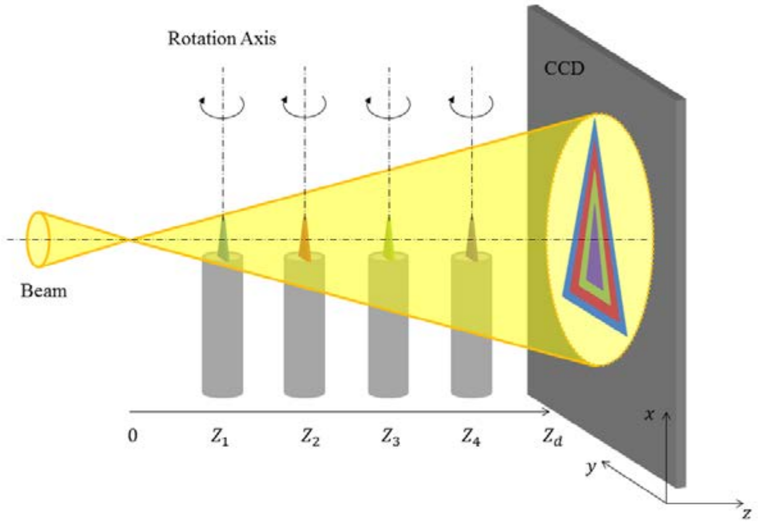

Figure 4.1 Scheme of experimental setup of magnified X-ray phase nano-CT. Z_1, Z_2, Z_3 and Z_4 are 4 different focus-to-sample distances, Z_d the focus-to-detector distance.

4.5.2 Data processing

First, the images are so-called flat-field corrected by the dark-current image $I_{D_{k,dark}}(\mathbf{x})$ and the flat-field image of the beam $I_{D_{k,flat}}(\mathbf{x})$ obtained with the empty beam image recorded without sample:

$$I_{D_{k,corr}}(\mathbf{x}) = \frac{I_{D_{k,acq}}(\mathbf{x}) - I_{D_{k,dark}}(\mathbf{x})}{I_{D_{k,flat}}(\mathbf{x}) - I_{D_{k,dark}}(\mathbf{x})} \tag{4.32}$$

where $I_{D_{k,acq}}(\mathbf{x})$ is the image acquired at the propagation distance D_k, and $I_{D_{k,corr}}(\mathbf{x})$ is the corrected image.

Next, images at different propagation distances must be registered for each rotation angle. This is done after correction of the magnification M_k that depends on the focus-to-sample distance Z_k and the focus-to-detector distance Z_d according to the expression (Fig. 4.1):

$$M_k = Z_d / Z_k. \tag{4.33}$$

The images were rescaled at the highest magnification.

Phase maps were estimated by using different retrieval methods. We used the equivalent propagation distance that can be expressed as:

$$D_k = [Z_k \cdot (Z_d - Z_k)] / Z_d. \tag{4.34}$$

Table 4.1 lists some specific experimental parameters for the datasets of 30 nm such as 4 different focus-to-sample distances, the focus-to-detector distance, the wavelength of the X-ray, the voxel size and Fresnel number F which is calculated by:

$$F_k = A^2 / \lambda D_k, \tag{4.35}$$

where A is the is the characteristic object size, λ the wavelength and D_k the propagation distance. The Fresnel numbers are provided both for the osteocyte lacunae and the canaliculi by setting A as different typical sizes, 10 µm and 200 nm respectively.

The δ_n/β ratio was set to 645 according to the complex refractive index of cortical bone at 33.6 keV, which was calculated from tabulated values by the software XOP. To improve image quality we also considered refining the estimated phase maps by using a non-linear conjugate gradient method (NLCG) based on the direct nonlinear image formation model. Finally, the extracted phase maps were used as the input to tomographic reconstruction to get the 3D structure of the sample. As there are a sufficient number of angular projections, the reconstruction can be performed by the Filtered Back-Projection (FBP) algorithm. We used the ESRF implementation PyHST2 for tomographic reconstruction [Mirone et al. (2014)].

Table 4.1 Specific experimental parameters

Focus-to-sample distances (mm)	Focus-to-detector distance (m)	Wavelength (nm)	Fresnel numbers for lacunae	Fresnel numbers for canaliculi	Voxel size (nm)
50.54; 52.70; 61.37; 79.37	1.2648	0.0369	55.86; 53.66; 46.41; 36.43	0.0223; 0.0215; 0.0186; 0.0146	30.00; 31.29; 36.43; 47.12

4.5.3 Quantitative evaluation of the 3D reconstructions

To get a quantitative assessment of the different reconstruction methods, we computed the Signal-to-Noise Ratio (SNR) and an estimate of the spatial resolution.

The SNR was estimated by calculating the ratio of the average of the signal μ_{sig} to the standard deviation of noise σ_{bkg} of a homogeneous area in the background. In our case, we defined the signal as being the regions occupied by bone in the reconstructed image, and the background as the regions inside osteocyte lacunae.

The spatial resolution of the image was evaluated experimentally from the measurement of the Edge Spread Function (ESF). The border of the lacunae was considered as an edge model, and was fitted with an error function. The analytic first derivative of this function yields the Line Spread Function (LSF). Since the error function is the primitive function of the Gaussian, the Full Width Half Maximum (FWHM) of the LSF can be obtained analytically. The spatial resolution r, defined here from the 10% cut-off frequency of the Fourier Modulation Transfer Function, can be expressed as:

$$r = \frac{\pi w}{4} \cdot \frac{1}{\sqrt{\log 2 \cdot \log(1/a)}}, \tag{4.36}$$

where w is the FWHM and $a = 0.1$ the position of the cut-off frequency.

The estimation of the SNR and the spatial resolution was repeated at different locations to obtain average and standard deviation values. To calculate the spatial resolution, edges are selected in the middle slices of different lacunae from the reconstructed volumes.

4.6 Results

Figure 4.2(a) displays the filters of the CTF and Paganin's methods using a single distance given by Eq. (4.8) and (4.4); (c) (resp. (e)) shows the filters of the homogeneous CTF method given by Eq. (4.22) (resp. the extended Paganin's method given by Eq. (4.23)) using 1 to 4 different propagation distances omitting the image term; (b), (d) and (f) are zooms of the filters shown in (a), (c) and (e), respectively. We can see that the CTF method and Paganin's method behave similarly in the low frequency range when using a single or multiple distances. However, the filter corresponding to the single distance CTF method clearly contains numerous jump points with large amplitudes in the high frequency range, as opposed to Paganin's method which is a simple low-pass filter (Fig. 4.2(a)). When considering multi-distance acquisitions, the amplitudes of the CTF filters are bound in the high frequency range, which shows that the use of multiple distances correctly handles the zero crossings in the direct CTF model. The homogeneous CTF filters again overlap with the extended Paganin's method filters in the low frequency range. However, while the filters in Paganin's method are essentially low-pass filters, the filters involved in the homogeneous CTF method (Fig. 4.2(d)) enable to retrieve the high frequency information during phase retrieval.

We scanned 3 samples cut from human cortical bone in total at the voxel sizes of 120 nm and 30 nm. Figure 4.3 and Figure 4.4 show the Minimum Intensity Projections (MIPs) of the 3D reconstructed volumes for the sample #2 at the voxel size of 30 nm, respectively for the homogeneous CTF and the extended Paganin's method. In our case, the MIPs are calculated by selecting the minimum intensity value along the Z-axis for each XY coordinate. The MIPs permit to see lacunae (ellipsoidal-like black structures), and also to enhance canaliculi which are the very small channels connecting bone lacunae. Figure 4.3(a)–(c) illustrate MIPs retrieved without refinement ("no it.") using 1, 2 and 4 distances respectively; Fig. 4.3(d)–(f) display MIPs retrieved with 10 iterations refinement using 1, 2 and 4 distances respectively. Figure 4.4 shows the same MIPs, when the phase retrieval is performed using the extended Paganin's method.

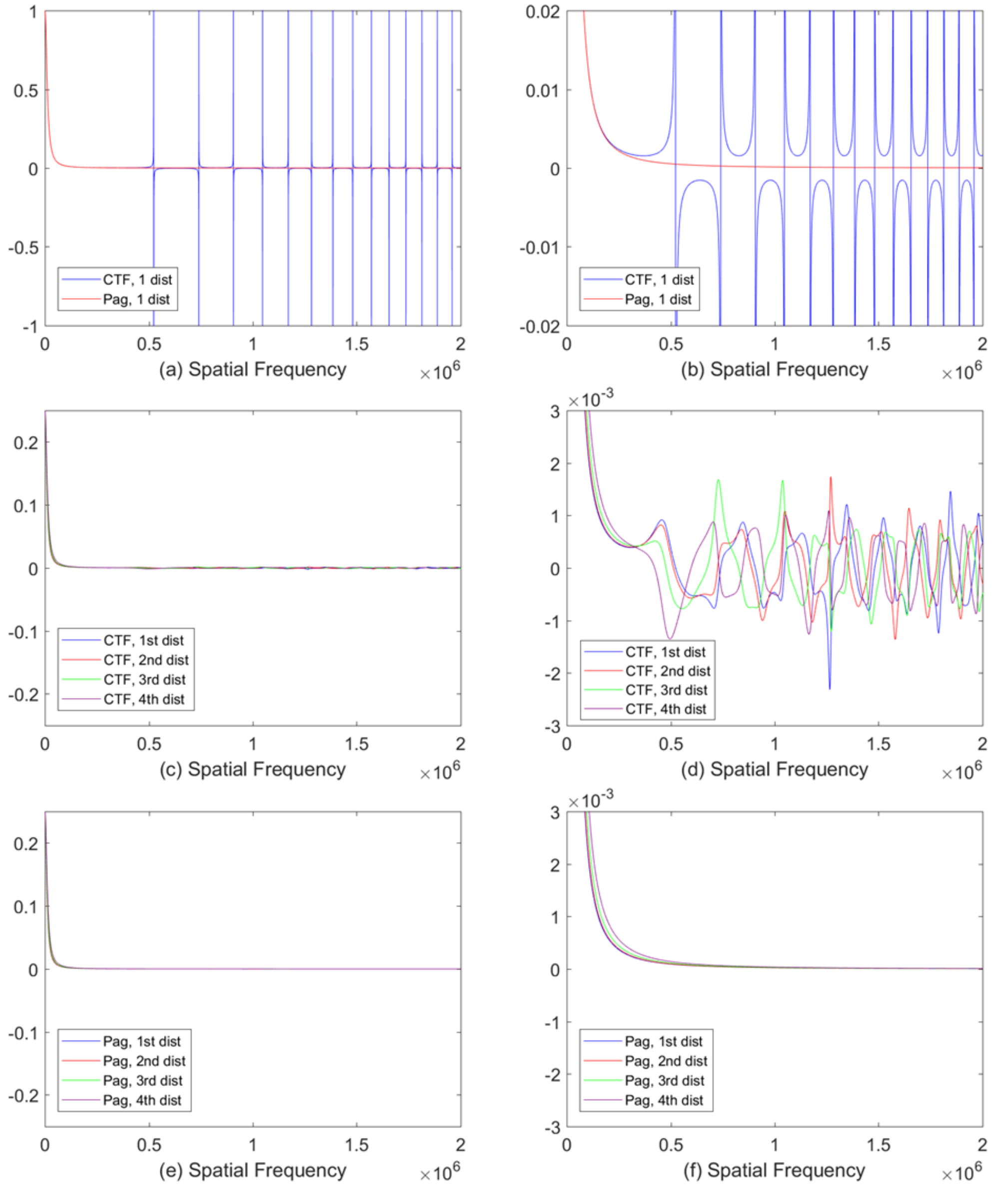

Figure 4.2 Plots of the filters in the Fourier domain. (a) The filters of both the homogeneous CTF method and Paganin's method using a single distance; (c) the filters of the homogeneous CTF method using 4 different propagation distances; (e) the filters of the extended Paganin's method using 4 different propagation distances; (b), (d) and (f) zoom on the filters corresponding to (a), (c) and (e) respectively.

First the impact of the iterative NLCG refinement is studied. Generally, the slices reconstructed and refined with 10 iterations look sharper and better contrasted than ones with no refinement. However, the gain in image quality is somehow different when considering the CTF or Paganin's method. For the CTF method, the non-linear refinement does not improve image quality very significantly, whatever the number of distances used (1, 2, or 4), as shown in Fig. 4.3. However, the non-linear refinement clearly improves the image quality for the extended Paganin's method. In Fig. 4.4(a)–(c) the MIPs retrieved by the extended Paganin's method without iterations look blurred, which is in agreement with the low pass nature of the corresponding filters. It turns sharper with more high frequency information after the NLCG refinement as shown in Fig. 4.4(d)–(f).

Now, we consider the impact of using multiple distances rather than one on the reconstructed image quality. For the homogeneous CTF method, if we compare the single distance case (Fig. 4.3(a) and (d)) with the 4 distances case (Fig. 4.3(c) and (f)), it can be seen that the image using one propagation distance is more blurred and that the sharpness is improved when using 4 propagation distances, regardless the use of iterative refinement. For the extended Paganin's method without refinement, we observe that the difference between reconstructions using a single distance and multiple distances (see Fig. 4.4(a) and (c)) is barely visible. However after performing NLCG refinement, a better contrast of small channel structures as well as a decrease of noise can be observed when using multiple distances instead of one (see Fig. 4.4(d) and (f)).

MIPs of reconstructed volumes at the voxel size of 30 nm retrieved by the homogeneous CTF and extended Paganin's methods both with 10 iterations' refinement using 4 distances for other two samples, #1 and #3, are shown in Fig. 4.6. Similarly, Fig. 4.7 gives MIPs of reconstructed volumes at the voxel size of 120 nm for all three samples, #1, #2 and #3, retrieved by the homogeneous CTF and extended Paganin's methods both with 10 iterations' refinement using 4 distances.

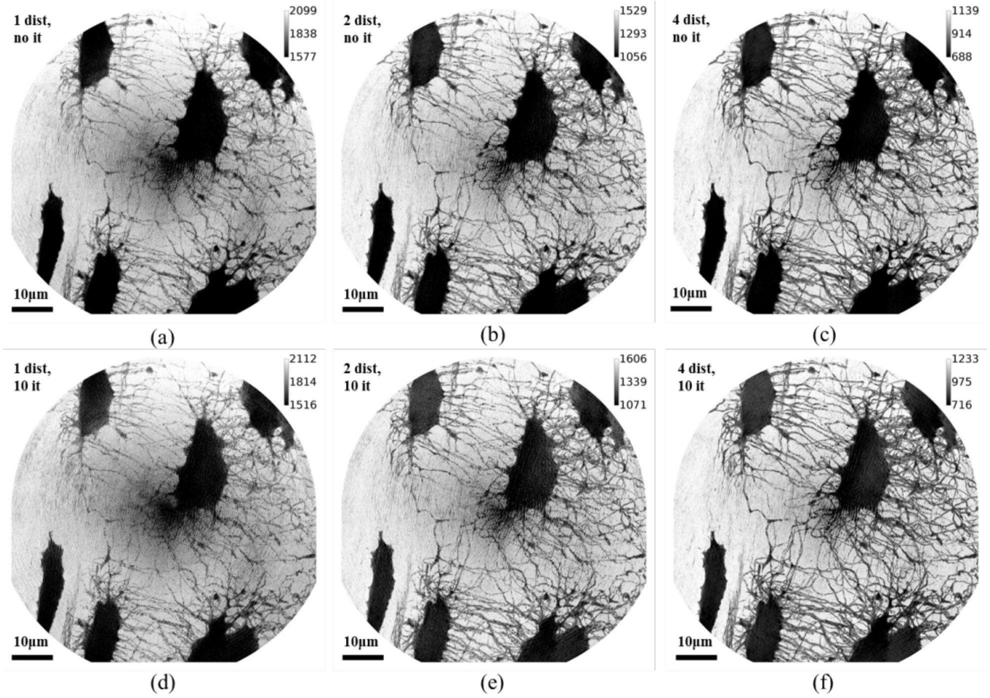

Figure 4.3 Minimum Intensity Projections of reconstructed volumes at 30 nm voxel size for the sample #2 retrieved by the homogeneous CTF method. (a), (b), (c) phase retrieved without iterative refinement using 1, 2 and 4 distances respectively; (d), (e), (f) phase retrieved with 10 iterations' refinement using 1, 2 and 4 distances respectively.

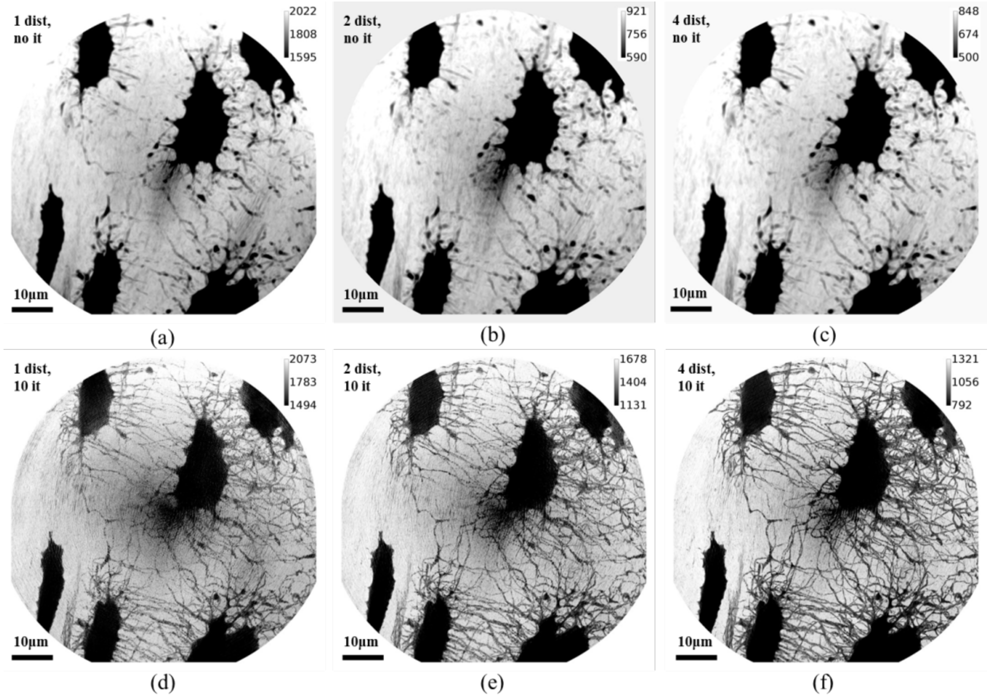

(a) (b) (c)

(d) (e) (f)

Figure 4.4 Minimum Intensity Projections of reconstructed volumes at 30 nm voxel size for the sample #2 retrieved by the extended Paganin's method. (a), (b), (c) phase retrieved without iterative refinement using 1, 2 and 4 distances respectively; (d), (e), (f) phase retrieved with 10 iterations' refinement using 1, 2 and 4 distances respectively.

Table 4.2 presents the estimated SNR and spatial resolution in the reconstructed images of the sample #2 at 30 nm for both the homogeneous CTF and extended Paganin's methods with 0 or 10 iterations, using 1, 2 or 4 distances. Table 4.3 lists similar quantitative parameters for the reconstructions of the samples #1 and #3 at the voxel size of 30 nm, but only using 1 or 4 distances. Also, Table 4.4 gives the quantitative evaluation for the reconstructions of all three samples #1, #2 and #3 at the voxel size of 120 nm retrieved by the homogeneous CTF and extended Paganin's methods with 0 or 10 iterations, using 1 or 4 distances. These quantities are displayed as bar charts in Fig. 4.5, Fig. 4.7 and Fig. 4.9 respectively. For the homogeneous CTF method, both the SNR and the spatial resolution get improved with the number of distances. In the single distance case, the iterative refinement improves the spatial resolution but decreases the SNR. For the extended Paganin's method without iterative refinement, the use of multiple distances does not yield significant differences. However, if we consider the non-linear refinement, the use of multiple distances obviously improves the SNR and to some extent the spatial resolution. Besides, the best results are obtained by the homogeneous CTF and extended Paganin's methods using 4 distances with 10 iterations.

Table 4.2 Measurements of SNR and estimation of the spatial resolution in the reconstructed images of the sample #2 for different phase retrieval methods

Sample ID	Distance number	Iteration	CTF		Paganin	
			SNR	Resolution (nm)	SNR	Resolution (nm)
#2	1	0	5.44 ± 1.00	81.12 ± 4.84	7.89 ± 0.79	108.18 ± 8.14
		10	4.73 ± 0.99	77.66 ± 6.57	5.29 ± 1.06	77.51 ± 4.84
	2	0	6.27 ± 0.77	78.76 ± 3.45	8.29 ± 0.38	120.36 ± 9.60
		10	5.41 ± 0.89	76.35 ± 3.19	6.55 ± 0.97	74.96 ± 4.53
	4	0	7.13 ± 0.84	76.06 ± 6.02	8.32 ± 0.50	115.96 ± 8.39
		10	7.11 ± 1.16	71.71 ± 2.62	8.33 ± 0.94	71.50 ± 3.21

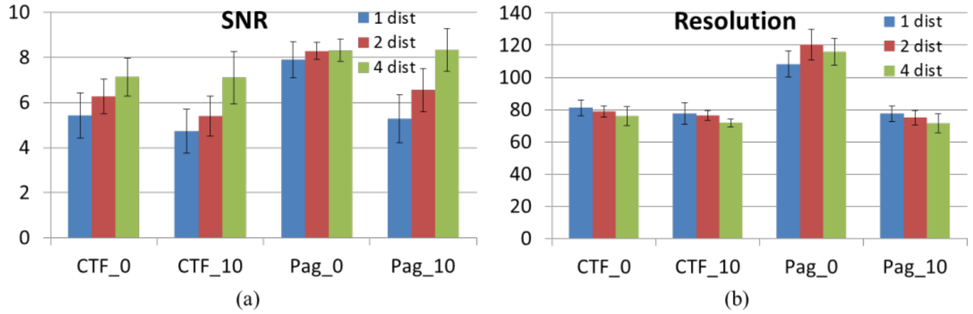

Figure 4.5 Quantitative evaluation of SNR and spatial resolution of the reconstructions of the sample #2 at 30 nm voxel size for both homogeneous CTF and Paganin's methods followed by a refinement with 0 iteration or 10 iterations, using 1, 2 or 4 distances. (a) SNR; (b) spatial resolution. Blue: 1 distance, Red: 2 distances, Green: 4 distances.

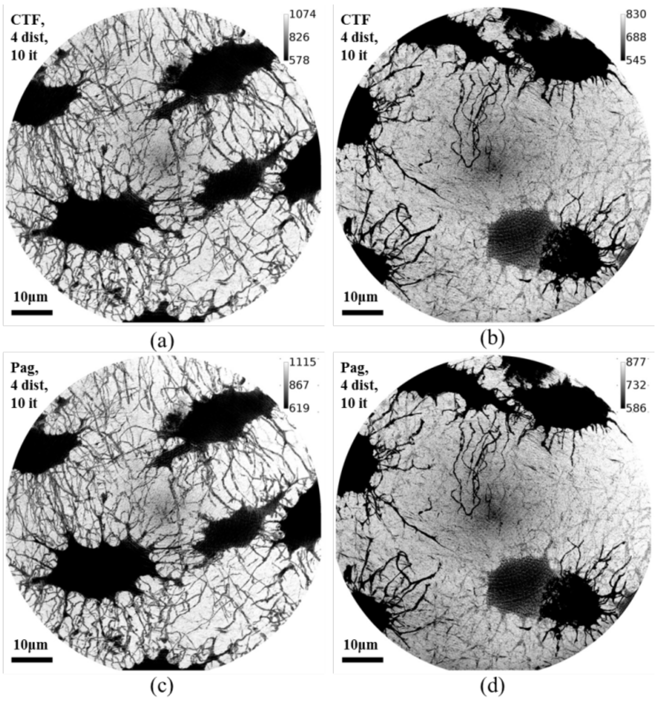

Figure 4.6 Minimum Intensity Projections of reconstructed volumes at 30 nm voxel size for other two samples. (a), (b) MIPs of the reconstructions retrieved by the homogeneous CTF method with 10 iterations' refinement using 4 distances for the sample #1 and #3 respectively; (c), (d) MIPs of the reconstructions retrieved by the extended Paganin's method with 10 iterations' refinement using 4 distances for the sample #1 and #3 respectively.

Table 4.3 Measurements of SNR and estimation of the spatial resolution in the reconstructed images of the samples #1 and #3 for different phase retrieval methods

Sample ID	Distance number	Iteration	CTF		Paganin	
			SNR	Resolution (nm)	SNR	Resolution (nm)
#1	1	0	4.70 ± 0.53	87.98 ± 4.72	7.17 ± 0.60	112.91 ± 7.71
		10	4.07 ± 0.88	79.44 ± 8.07	5.14 ± 0.40	77.54 ± 7.02
	4	0	6.88 ± 0.67	74.94 ± 3.40	8.80 ± 1.07	122.02 ± 9.19
		10	6.82 ± 1.08	72.94 ± 4.09	8.10 ± 1.10	72.27 ± 3.60
#3	1	0	4.66 ± 0.64	90.44 ± 3.80	7.50 ± 1.05	114.20 ± 8.27
		10	4.13 ± 0.74	85.26 ± 7.01	4.58 ± 0.78	81.71 ± 6.09
	4	0	7.22 ± 0.95	79.51 ± 6.92	8.61 ± 0.73	120.92 ± 5.19
		10	7.01 ± 1.06	74.78 ± 3.66	7.53 ± 0.67	74.46 ± 6.42

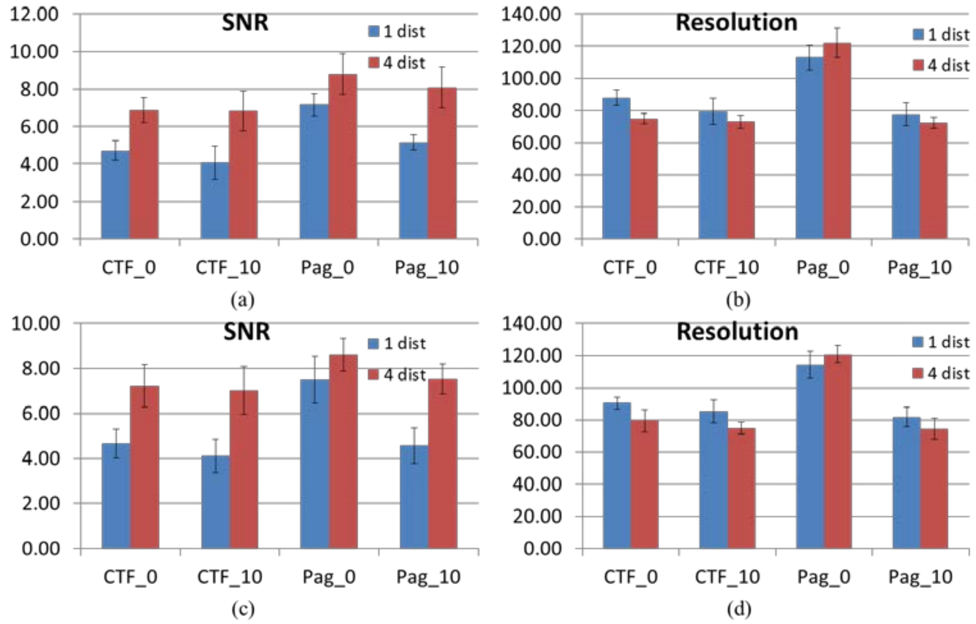

(a) (b) (c) (d)

Figure 4.7 Quantitative evaluation of SNR and spatial resolution of the reconstructions of other two samples at 30 nm for both homogeneous CTF and Paganin's methods followed by a refinement with 0 iteration or 10 iterations, using 1, or 4 distances. (a), (b) SNR and spatial resolution for the sample #1; (c), (d) SNR and spatial resolution for the sample #3. Blue: 1 distance, Red: 4 distances.

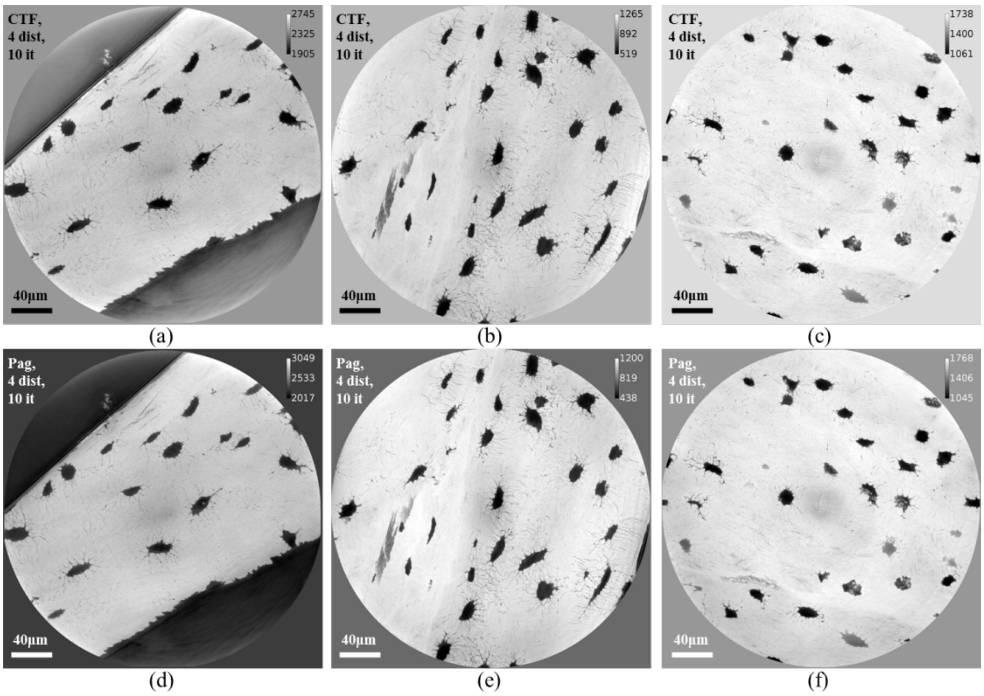

(a) (b) (c) (d) (e) (f)

Figure 4.8 Minimum Intensity Projections of reconstructed volumes at 120 nm voxel size for three samples. (a), (b), (c) MIPs of the reconstructions retrieved by the homogeneous CTF method with 10 iterations' refinement using 4 distances for the sample #1, #2 and #3 respectively; (d), (e), (f) MIPs of the reconstructions retrieved by the extended Paganin's method with 10 iterations' refinement using 4 distances for the sample #1, #2 and #3 respectively.

Table 4.4 Measurements of SNR and estimation of the spatial resolution in the reconstructed images of the samples #1, #2 and #3 for different phase retrieval methods

Sample ID	Distance number	Iteration	CTF		Paganin	
			SNR	Resolution (nm)	SNR	Resolution (nm)
#1	1	10	5.88 ± 0.70	274.26 ± 5.37	6.16 ± 0.62	281.08 ± 5.00
	4		9.97 ± 0.93	250.11 ± 3.86	10.78 ± 1.41	244.52 ± 4.93
#2	1	10	5.86 ± 0.90	262.49 ± 5.61	5.93 ± 0.91	268.82 ± 7.85
	4		9.82 ± 0.82	255.06 ± 4.13	10.46 ± 1.16	252.05 ± 4.94
#3	1	10	5.93 ± 0.65	268.36 ± 8.55	7.02 ± 0.64	277.25 ± 5.12
	4		9.45 ± 0.91	249.22 ± 3.73	10.51 ± 0.99	245.98 ± 5.85

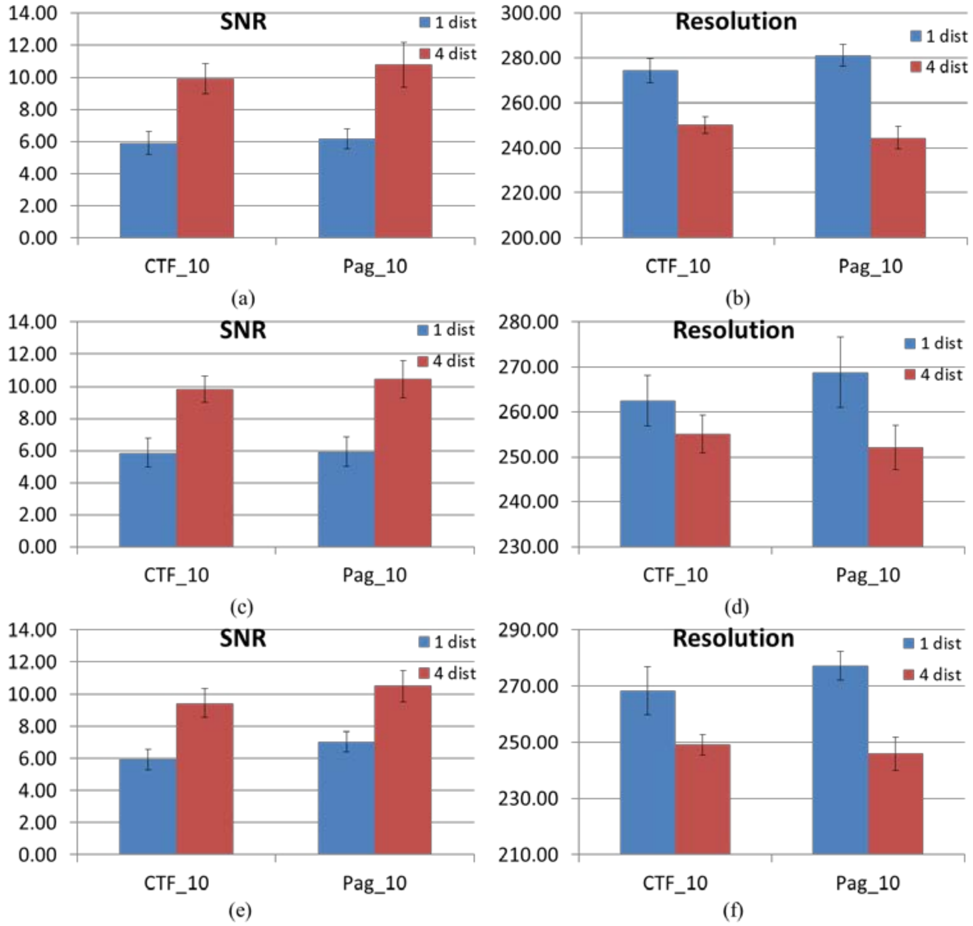

Figure 4.9 Quantitative evaluation of SNR and spatial resolution of the reconstructions of three samples at 120 nm for both homogeneous CTF and Paganin's methods followed by a refinement with 10 iterations using 1 or 4 distances. (a), (b) SNR and spatial resolution for the sample #1; (c), (d) SNR and spatial resolution for the sample #2; (e), (f) SNR and spatial resolution for the sample #3. Blue: 1 distance, Red: 4 distances.

4.7 Discussion

In this study, we compared and evaluated two phase retrieval methods for homogeneous objects based on the CTF and TIE approaches. We studied an extension of the single distance Paganin's method to multi-distance acquisitions and provided a similar formula for the multi-distance CTF method using a homogeneity assumption on the sample. Moreover, assuming weak absorption, we derived relationships between the extended Paganin's and the homogeneous CTF methods. Considering the case of a single propagation distance, the homogeneous CTF and Paganin's filters are almost identical when restricted to low spatial frequencies and low absorption. Nevertheless, the filters differ at higher spatial frequency and particularly around the zero crossings of the direct CTF model where the homogeneous CTF filter reaches large values. When it comes to multi-distance acquisitions, the filters of both methods are still similar in the low frequency range. However, the amplitudes of the CTF filters are bound and different from zero which permits to retrieve the high frequency information while Paganin's method always acts as a low-pass filter.

These findings were confirmed by reconstructions performed on experimental bone data sets with the voxel sizes of 120 nm and 30 nm. From those reconstructions, we observed that the structures such as lacunae and canaliculi are similarly reconstructed in the images from the extended Paganin's and homogeneous CTF methods using 4 distances. The quantitative criteria, such as the SNR and the spatial resolution corroborate the visual observation. In this chapter, we calculate the standard SNR which is used in the very large majority of studies and comparable to the literature. Other quality measures such as the recently proposed spatial SNR could be investigated to evaluate the quality of X-ray images [M. Ullherr et al. (2018)].

The phase retrieval and tomographic reconstruction were performed sequentially. This has many practical advantages as only a large number of 2D problems have to be solved. Recently some methods have been proposed to combine the two steps together [Bronnikov (2002)],[Kostenko et al. (2013)],[Kongskov et al. (2016)]. However, 3D approaches require extensive computer resources both in terms of computing time and memory. Therefore they are not practical for standard use on large data sets today, but they will be increasingly important in the future.

In previous works, Paganin's method was compared with the modified Bronnikov algorithm and was shown to provide better reconstructions on low-attenuating samples [Boone et al. (2012)], but only one propagation distance was considered. Similarly, a good agreement was shown between the TIE and the CTF method in the low-spatial frequency range [Turner et al. (2004)]. However, the work was limited to one propagation distance and not applied to CT reconstruction. Burvall et al. detailed the processing involved in seven phase retrieval methods found in the literature and made a comprehensive analysis of these methods [Burvall et al. (2011)]. The Paganin's and CTF methods considered here corresponding to their "single material" and "Fourier-Born" methods have the expected behavior. But again their analysis was performed for a single propagation distance and results were provided on 2D phase maps but not on 3D reconstructed images. Besides, Krenkel et al. proposed a Holo-TIE algorithm to address the phase retrieval in hard x-ray in-line holography and extended it from single-distance recordings to multiple-distance cases for achieving single-cell imaging [Krenkel et al. (2017)].

In our experimental conditions, the best reconstructed images (i.e. with a sharper display of edge information and a better detection of small structures) were obtained after applying a non-linear conjugate gradient method to refine the results of the filtering based phase retrieval methods. Actually, iterative near-field methods have been recently developed a lot in phase contrast imaging. However, they are mostly based on a single distance and generally use iterative algorithms, such as Fienup's error reduction (ER) [Carroll et al. (2016)]or the Gerchberg-Saxton (GS) algorithms [Ruhlandt et al. (2014)]. In this work, we used a NLCG algorithm, taking as initialization, the phase maps retrieved from the extended Paganin's or homogeneous CTF method. Our results indicate that this refinement critically improves the spatial resolution if the extended Paganin's method is used, while the homogeneous CTF alone is already close to the optimal result. Both initial linear estimates converge in the end to similar solutions. However, it is worth underlining that the improvement obtained with the non-linear refinement is marginal in the case of the homogeneous CTF method which is probably due to the fact that our samples approximately satisfy the weak absorption assumption.

Thus, it would also be possible to use the multi-distance homogeneous CTF method without iterative refinement if computing time is an issue.

4.8 Conclusion

Phase retrieval which is a non-linear ill-posed inverse problem is a necessary step in the reconstruction of propagation-based SR X-ray phase nano-CT. The choice of the phase retrieval method and the best experimental conditions remained open questions in the multiple distance case. This has motivated our detailed study of two phase retrieval approaches in the case of multiple propagation distances from a theoretical and experimental point of view. Paganin's method using a single distance is one popular phase retrieval method due to its simple implementation. In this chapter, we extended Paganin's method to multi-distance acquisitions, and compared it to a homogeneous version of the CTF method for the reconstruction of bone samples at nanoscale spatial resolution. Our results showed that using 4 propagation distances generally improves image quality except in the case of the Paganin's method without non-linear refinement. When iterative refinement was used, the multi-distance case provided the sharpest reconstruction with a higher spatial resolution and flatter background. In this case, the homogeneous CTF and the extended Paganin's method give comparable results. The advantage of using several propagation distances is that it provides a better coverage of the Fourier domain of the phase projections.

Our perspectives concern the quantitative analysis of the bone ultra-structure on which there are still very few data due to the limited 3D imaging modalities available for this purpose. In this respect, it is important to optimize image quality since the latter may have a considerable impact on the further quantification. While it is experimentally more demanding to use four propagation distances than one, our results showed that a clear gain is obtained in image quality. Future works will focus on the quantitative analysis of the data, from which we expect to obtain quantitative parameters, of the lacuno-canalicular network such as porosity and connectivity but also information about the extra cellular matrix.

Chapter 5: Segmentation and quantification of the lacuno-canalicular network for X-ray phase nano-CT images

This chapter is a research article prepared for submission to a journal.

Contents

5.1 Introduction

Osteoporosis is a bone disease which is characterized by a decrease of bone mass and density. It affects the strength and the mechanical structure of bones which leads to a higher risk of fractures even by minor injury or little knock in some serious cases [Subashi et al. (2017)]. Moreover, osteoporosis is not only a health problem, but also a social and economic issue. According to the investigation in the European Union (EU), 22 million women and 5.5 million men suffered from osteoporosis in 2010 and there were 3.5 million fragility fractures occurring mainly in the areas of hips, spines and wrists, which represented an economic burden of € 37 billion to the EU [Kanis et al. (2016)]. Since the cortical porosity has a strong impact on bone strength, it is important to have a better knowledge about the microarchitecture of cortical bone to have a better understanding of bone mechanical properties and figure out the mechanisms of bone fragility in disease [Hemmatian et al. (2017)].

Bone has a hierarchical structure with different levels of organization and it is known that all scales are involved in bone strength [Rho et al. (1998)]. At the cellular scale, bone micro porosity is due to the lacuno-canalicular network (LCN), which is a complex mesh structure deeply embedded inside the bone matrix [Knothe Tate et al. (2004)]. Osteocytes which are the most abundant bone cells are located within lacunae. Osteocytes have been identified as important regulators in bone remodeling acting as the activator of NFkB ligand (RANKL) for the recruitment of osteoclasts [Jilka et al. (2016)] and produce WNT1 to control bone formation through inactivation and overexpression [Joeng et al. (2017)]. In the LCN, lacunae function as nodes connected with each other by the canaliculi channels which hold the cytoplasmic processes of osteocytes linking up with those of their neighboring bone cells [Florencio-Silva et al. (2015)]. Through gap junctions, the LCN permits communication among osteocytes and osteoblasts close to the bone surface to transport nutrient supplements and release waste products [Bonewald (2011)]. The LCN has been thought to be able to sense local mechanical deformation and interstitial fluid flow on bone matrix, and to produce and exchange stimuli signals for the control of bone cell activities [Buenzli et al. (2015)]. Hence, it is crucial to have a better knowledge of the LCN in order to understand more clearly the specific role of the LCN in bone remodeling and bone strength.

Because of its complex structure and tiny size, it is still challenging to achieve the 3D observation and analysis of the LCN and especially of the canaliculi whose diameter are below the micrometer. 2D imaging techniques were usually used to observe the LCN, such as light microscopy (LM) [Marotti et al. (1995)], [Jordan et al. (2003)], [Qiu et al. (2006)], transmission electron microscope (TEM) [Rubin et al. (2005)] and scanning electron microscope (SEM) [Shah et al. (2017)]. Since these techniques do not allow imaging the complete picture of the LCN, there has recently, been new interest in developing 3D imaging techniques. Confocal laser scanning microscopy (CLSM) [Repp et al. (2017)] and serial focused ion beam SEM (serial FIB SEM) [Schneider et al. (2011)], [Hasegawa et al. (2018)] have been used in recent studies, however, the spatial resolution of optical microscopy is diffraction-limited and electron microscopy usually has a limited field of view. Using synchrotron radiation (SR) nano-CT, it has been proved to be possible to image the 3D structures of the LCN with a relatively large field of view permitting to realize statistical analysis [Pacureanu et al. (2012)], [Langer et al. (2012)]. The feasibility of ptychographic X-ray CT was demonstrated earlier [Dierolf et al. (2010)] and recently used in a preliminary study to analyze the LCN in rats [Ciani et al. (2016)] but also limited to very small field of view. Still, there have been very few studies reporting quantitative data on the LCN in human.

The aim of this work is to present a workflow including image acquisition and data processing to extract 3D quantitative parameters of the LCN in human bones. Imaging was performed using magnified X-ray phase nano-CT at the beamline ID16A of the European Synchrotron Radiation Facility (ESRF), Grenoble, France [Yu et al. (2018)].

Femoral samples from female donors have been imaged at voxel sizes of 120 nm. We first present an image analysis procedure to segment lacunae and canaliculi from the reconstructed volumes. Then, quantitative parameters for the assessment and analysis of the LCN were calculated based on fast image analysis methods previously developed by our group. We computed the density of lacunae, the porosity of lacunae and canaliculi, and several morphological descriptors for lacunae such as the volume, the surface and the length of each dimension. Additional parameters are introduced to quantify the number and the density of canaliculi at different distances from the surface of each lacuna.

5.2 Materials and methods

5.2.1 Sample description

All the specimens were taken from female cadavers (aging 50–90 years old) provided by the Centre du Don des Corps (University Paris 5) and the Dept. of Anatomy Rockefeller, University Lyon. Except the sex and the age, no other information regarding disease status or medication history was available in accordance with legal clauses stated in the French Code of Public Health Ethical [Cai et al. (2017)]. Femoral diaphyses were extracted from different parts of these fresh cadaveric subjects and wrapped in gauze soaked with saline to keep hydrated, and then stored at -20°C until sample preparation.

The samples were then cut into 5 blocks along the longitudinal axis of bone using a low speed saw with a diamond coated blade (Isomet 4000, Buehler, Lyon). The block #1 corresponded to the location of proximal metaphysis (see Figure 5.1), from which the transverse cross-section was divided into 4 different quadrants such as anterior, posterior, medial and lateral quadrants as shown in Figure 5.2. Only the lateral quadrants were scanned in our experiments. First, all the lateral quadrants were dehydrated in 70% ethanol and stored at 4°C. Then, they were cut with a water-cooled diamond precision saw (Presi Mecatome T210, Struers Diamond Cut-off Wheel EOD15, Liphy, Grenoble) in several steps to produce parallelepiped samples of approximate cross sections 0.4 mm × 0.4 mm (length ~ 4 mm) in the endosteal-periosteal direction. Samples were also conserved in 70% ethanol at 4°C until imaging.

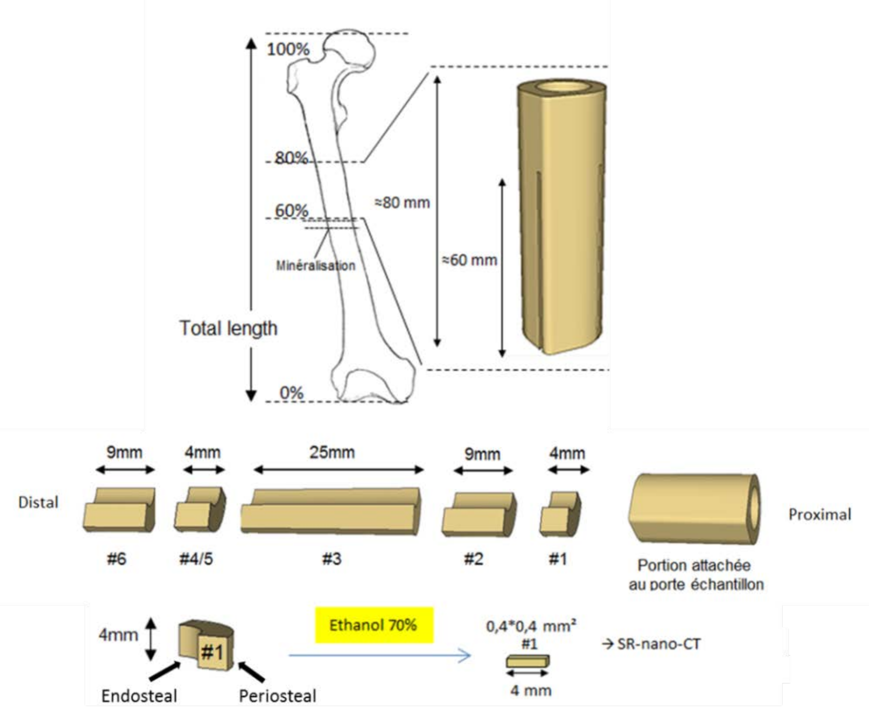

Figure 5.1 Scheme of sample preparation

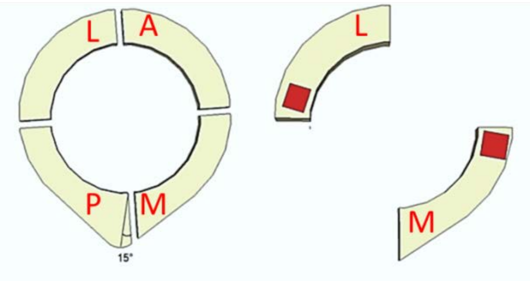

Figure 5.2 Different quadrants of each block. L: lateral; A: anterior; P: posterior; M: medial.

5.2.2 Synchrotron radiation nano-CT

All the samples were imaged by magnified X-ray phase nano-CT at the beamline ID16A of the ESRF. During the scan, the sample was placed on a piezo-driven short-range hexapod stage in a small vacuum cabin. Because we used the extended Paganin's method to address the phase retrieval, the sample needed to be scanned at 4 different sample-to-detector distances [Yu et al. (2018)]. For each distance, 2000 projections were recorded for one sample over a range of 180° with the beam energy of 17 or 33.6 keV. After data acquisition and the phase retrieval, we used the standard Filtered Back-Projection (FBP) algorithm for the tomographic reconstruction performed by the ESRF implementation PyHST2 [Mirone et al. (2014)]. The size of the reconstructed volume is 2048 × 2048 × 2048 at the voxel sizes of 120 nm, 50 nm and 30 nm, corresponding to the field of view 245.76 µm, 102.4 µm and 61.44 µm respectively. Acquisition time for a complete dataset (i.e. with 4 propagation distances) was approximately 4 hours.

We scanned 13 samples in total at ID16A denoted by the number #1–#13 according to the increasing order of ages. The samples respectively scanned at voxel sizes 120 nm, 50 nm and 30 nm were respectively denoted by the alphabet A, B and C. The samples were generally first scanned a at the voxel size of 120 nm and then with a smaller voxel size (50 or 30nm) in a region of interest (ROI). In short, we got 8 reconstructed volumes at the voxel size of 120 nm, denoted by A2, A3, A6, A8, A9, A11, A12 and A13; 9 volumes at 50 nm denoted by B1, B4-1, B4-2, B4-3, B4-4, B5, B7, B10 and B11; 7 volumes at 30 nm denoted by C2, C3, C6, C8, C9, C12, and C13. In this chapter, we just consider the analysis of the images at the voxel size of 120 nm, while other results at higher resolution will be given in the next chapter.

5.2.3 Image processing

The segmentation of the LCN requires to segment both the lacunae and the canaliculi and to identify each structure. Since these structures have different characteristics, different segmentation methods were used according to the target. It has to be noted that the choice of the segmentation methods is constrained by the data size, i.e. 32 GB per volume. Due to the very high spatial resolution (120 nm), the field of view is limited to about 250µm in each dimension, and then we expect to process the entire 3D volume and not only a volume of interest (VOI). The workflow of the whole segmentation procedures is shown in Fig. 5.3.

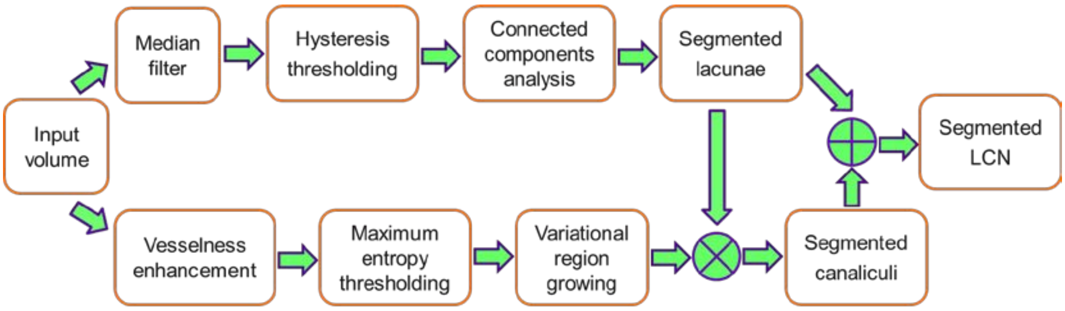

Figure 5.3 Workflow of the segmentation of the LCN.

5.2.3.1 Segmentation of lacunae

The aim of this step is to obtain a binary volume of the lacunae only. First of all, we used a median filter to remove canaliculi from the reconstructed volumes because sometimes canaliculi were at the same gray level as lacunae and connected with their neighboring lacunae, which would hinder the segmentation. We chose a median filter of size 10 voxels for the data at 120 nm, which was chosen from the same size with the previous work of our group [Dong, Haupert, et al. (2014)]. It has been proved to be enough to remove canaliculi and keep the structure of lacunae as shown in Fig. 5.4 (b). After median filtering, hysteresis thresholding was used to segment the lacunae from the images (see Fig. 5.4 (c)). This method involves two thresholds: the first lower threshold is the so-called "hard" threshold which extracts the voxels of lacunae with high confidence; the second one is a higher threshold, the "weak" one, which is used to refine the regions and return the segmented result. The voxels having gray values between two thresholds will be assigned into the object if they are connected to the high confidence voxels. Fig. 5.5 gives the histograms of two reconstructed volumes with the positions of the low and high thresholds. We notice that there are two peaks in each histogram although one of them could be very small. The low threshold is probably located in the middle of two peaks and the high threshold is at the edge of the second peak close to the side of the first peak. The hysteresis thresholding method is a simple case of region growing method. The application of this method performed well but showed that regions of the Haversian canals could be segmented at the same time if they were in the field of view. Because the size of Haversian canal is much larger than that of lacuna, these structures were eliminated after connected component analysis by removing the components which contained a number of voxels larger than 1,157,407, i.e. ~ 2000 μm^3 at the voxel size of 120 nm. This threshold could keep the components thought to be lacunae and remove huge regions of the Haversian canals.

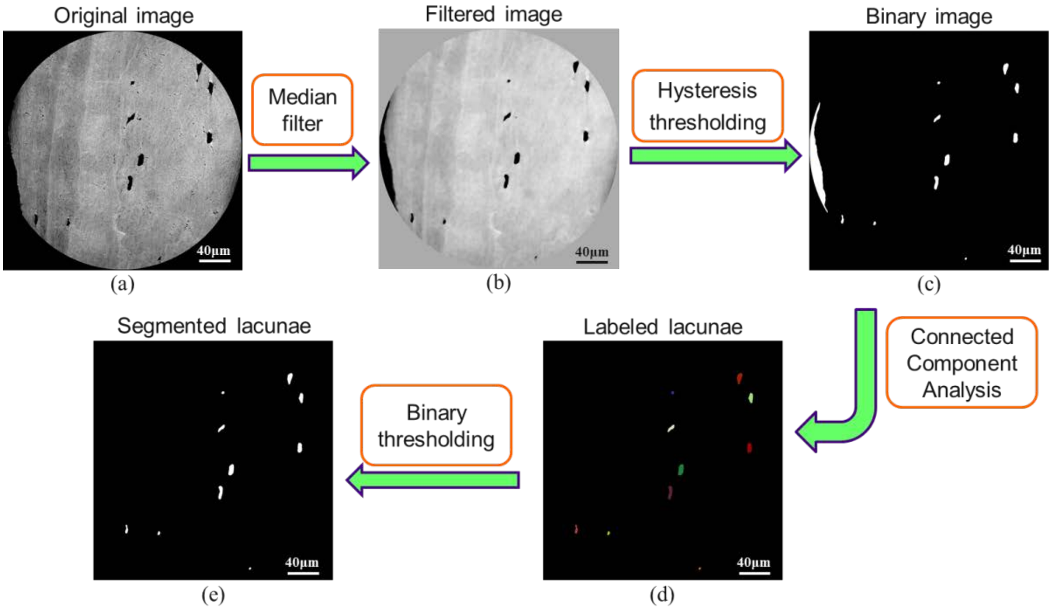

Figure 5.4 Slice images for the segmentation of lacunae. (a) One middle slice from the reconstructed volumes at 120 nm; (b) The slice after median filtering; (c) The first segmented slice by the hysteresis thresholding; (d) The labeled slice of lacunae after segmentation and refinement;(e) the segmented slice of lacunae.

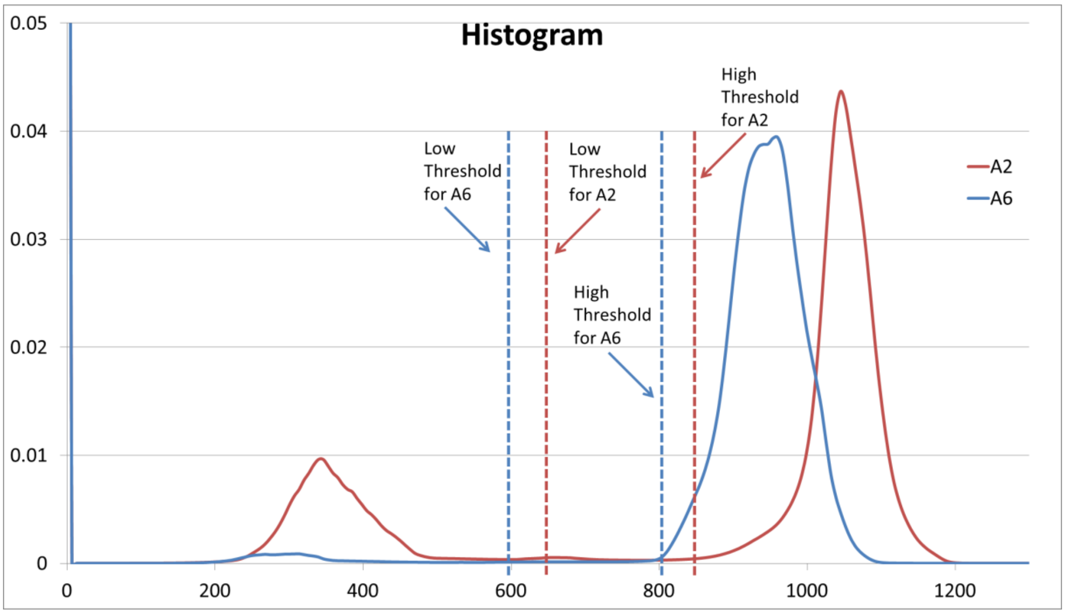

Figure 5.5 Histograms of two reconstructed volumes for A2 and A6 showing the low and high thresholds when performing the hysteresis thresholding.

5.2.3.2 Segmentation of canaliculi

Compared with lacunae, the segmentation of canaliculi is more difficult because of their tiny sizes, the diameter of canaliculi being about 200–500 nm [Varga et al. (2015)]. In previous work, a segmentation method based on minimal path and geodesic voting was proposed to segment micro-CT images acquired at 300nm [Zuluaga et al. (2014)]. However, this method was found less adapted in the present case due to its extensive computing time and since the canaliculi were better resolved. In this work, we used a workflow including different steps. The first step consists in a vesselness enhancement filtering to enhance the line structures and improve the visibility of canaliculi based on calculating Hessian matrix and eigenvalue decomposition [Pacureanu (2012)]. We then apply a maximum entropy thresholding method followed by a variational region growing approach to segment the canaliculi. Finally a filtering step by connected components analysis was performed to remove noise.

5.2.3.2.1 Vesselness enhancement

The vesselness enhancement filter is based on the calculation of the local Hessian matrix involving the second-order partial derivatives of the image, which reflects the intensity variations and encodes local shape information (see Fig. 5.5 (b)). The eigenvalues of this matrix can describe the geometrical properties of the local structures.

To decrease the noise sensitivity of the second-order derivatives, the original image is first convolved with a Gaussian function whose standard deviation can also tune the filter to the specific widths of line structures. If we define the 3D image as $f(\mathbf{x})$ with $\mathbf{x} = (x, y, z)$, the second derivatives of the smoothed image $f_{ab}(\mathbf{x};\sigma)$ can be expressed as:

$$f_{ab}(\mathbf{x};\sigma) = \left\{\frac{\partial^2}{\partial a \partial b} g_\sigma(\mathbf{x})\right\} * f(\mathbf{x}), \tag{5.1}$$

where $g_\sigma(\mathbf{x})$ is a 3D Gaussian function of standard deviation σ, a and b represent direction of derivation (either x, y or z).

We arrange the eigenvalues in ascending order of the magnitude and note the three eigenvalues as λ_1, λ_2 and λ_3 ($|\lambda_1| \leq |\lambda_2| \leq |\lambda_3|$). For the bright tubular structures which we want to segment as canaliculi from the image, the eigenvalues should meet the conditions: $|\lambda_1| \approx 0$; $|\lambda_1| \ll |\lambda_2|$; $\lambda_2 \approx \lambda_3$ and both of them are negative.

Sato et al. proposed a generalized measurement of similarity to a line by taking advantage of two eigenvalues [Sato et al. (1998)]. If we define $\lambda_c = \min(-\lambda_2, -\lambda_3)$, the line-filter image can be expressed as:

$$l(\mathbf{x}) = \begin{cases} \lambda_c \exp(-\lambda_1^2/2(\alpha_1\lambda_c)^2), & \lambda_1 \leq 0, \lambda_c > 0 \\ \lambda_c \exp(-\lambda_1^2/2(\alpha_2\lambda_c)^2), & \lambda_1 > 0, \lambda_c > 0, \\ 0, & \text{otherwise} \end{cases} \tag{5.2}$$

where α_1 and α_2 are two constant parameters. In our case, $\alpha_1 = 0.5$ and $\alpha_2 = 2$ based on a previous report in our group [Pacureanu et al. (2010)].

The vesselness filter is expected to enhance the visibility of canaliculi.

5.2.3.2.2 Maximum entropy thresholding

Before region growing, we need to make an initial segmentation of the 3D line-filter image, and the binary result will be used as the seed map whose bright voxels function as the starting points of growing. The initialization process should be automatic and efficient to segment as many target voxels as possible but avoid other objects having similar features like collagen fibers and speckle noise in our case. Hence, we decided to use a global single threshold segmentation algorithm. After several tests, we found that the maximum entropy thresholding method met all the requests and was used as the initial step of a region growing segmentation.

5.2.3.2.3 Variational region growing

(1) Discrete region function

Variational region growing permits to build a theoretical framework to formalize the iterative growing process by minimizing a region-based energy function [Rose et al. (2010)]. If the 3D image $f(\mathbf{x})$ is defined in the domain Ω, a subset of $\mathbb{R}^3$, the evolving function can be expressed based on a characteristic function $\varphi_{\mathbf{x}}$:

$$\varphi_{\mathbf{x}} = \varphi(\mathbf{x}) = \begin{cases} 1, & if\ \mathbf{x} \in \Omega_{in} \\ 0, & if\ \mathbf{x} \in \Omega_{out} \end{cases}, \tag{5.3}$$

where Ω_{in} is the segmented region in Ω, and $\Omega_{out} = \Omega \backslash \Omega_{in}$ the background region.

The candidate voxels at the iteration n are noted by the set of voxels C^n:

$$C^n(\Omega_{in}, \varepsilon) = \{\mathbf{u} \in \Omega_{out}, \mathbf{v} \in \Omega_{in} | d(\mathbf{u}, \mathbf{v}) \leq \varepsilon\}, \tag{5.4}$$

where $d(\mathbf{u}, \mathbf{v})$ is the Euler distance between two voxels and ε, the distance threshold.

At each iterative step, we check the candidate voxels belonging to the background Ω_{out} and connected to the segmented region Ω_{in}. If the new energy function decreases, these voxels are accepted as objects and we update the characteristic function.

If the region-based energy function is noted by $J(\varphi)$, the optimal solution φ^* of the energy minimization can be expressed as:

$$\varphi^* = \underset{\varphi_{\mathbf{x}}}{\operatorname{argmin}} J(\varphi_{\mathbf{x}}). \tag{5.5}$$

To compute the solution, we define the time-dependent variation of $\varphi_{\mathbf{x}}$ as $\Delta_t\varphi$ and estimate the energy variation $\Delta J(\tilde{\varphi})$ for a small variation $\tilde{\varphi}$ as follows:

$$\Delta_t\varphi - c(\varphi) \cdot H\big(-\Delta J(\tilde{\varphi})\big) = 0, \tag{5.6}$$

where $c(\varphi) = 1 - 2\varphi_{\mathbf{x}}$ is the switch function, and H the one-dimensional Heaviside function defined by:

$$H(z) = \begin{cases} 0, & if\ z < 0 \\ 1, & if\ z \geq 0 \end{cases}. \tag{5.7}$$

Then, the value of the function $\varphi_{\mathbf{x}}$ at the iteration $n+1$ can be given by:

$$\varphi_{\mathbf{x}}^{n+1} = \varphi_{\mathbf{x}}^n + c(\varphi_{\mathbf{x}}^n) \cdot H\big(-\Delta J(\tilde{\varphi}_{\mathbf{x}}^n)\big). \tag{5.8}$$

(2) Evolution of the energy function

Based on the given “region-independent” descriptor $k_{\mathbf{x}}$, Jehan-Besson et al. has defined a general expression for the region-based energy function [Jehan-Besson et al. (2003)]:

$$J(\Omega_{in}) = \int_{\Omega_{in}} k_{\mathbf{x}} d\mathbf{x}. \tag{5.9}$$

In our discrete case, we rewrite the energy function as:

$$J(\varphi^n) = \sum_{\mathbf{x}\in\Omega} k_{\mathbf{x}} \cdot \varphi_{\mathbf{x}}^n. \tag{5.10}$$

Here, we calculate the energy $J(\tilde{\varphi}^n)$ when the state of a voxel $\mathbf{v}$ is switched to the opposite side. The characteristic function of this voxel turns:

$$\tilde{\varphi}_{\mathbf{v}}^n = 1 - \varphi_{\mathbf{v}}^n. \tag{5.11}$$

The other voxels keep the previous states, so we have:

$$\tilde{\varphi}_{\mathbf{x}}^n = \varphi_{\mathbf{x}}^n, \quad if\ \mathbf{x} \neq \mathbf{v}. \tag{5.12}$$

Then, the energy function after switching can be expressed as:

$$J(\tilde{\varphi}^n) = k_{\mathbf{v}} \cdot \tilde{\varphi}_{\mathbf{v}}^n + \sum_{\mathbf{x}\in\Omega,\mathbf{x}\neq\mathbf{v}} k_{\mathbf{x}} \cdot \varphi_{\mathbf{x}}^n. \tag{5.13}$$

We make an equivalent transformation of this function,

$$J(\tilde{\varphi}^n) = k_{\mathbf{v}} \cdot (1 - \varphi_{\mathbf{v}}^n) - k_{\mathbf{v}} \cdot \varphi_{\mathbf{v}}^n + \underbrace{k_{\mathbf{v}} \cdot \varphi_{\mathbf{v}}^n + \sum_{\mathbf{x}\in\Omega,\mathbf{x}\neq\mathbf{v}} k_{\mathbf{x}} \cdot \varphi_{\mathbf{x}}^n}_{J(\varphi^n)}. \tag{5.14}$$

Finally, we can obtain the variation of the energy function $\Delta J(\tilde{\varphi}^n)$:

$$\Delta J(\tilde{\varphi}^n) = (1 - 2\varphi_{\mathbf{v}}^n) \cdot k_{\mathbf{v}}. \tag{5.15}$$

Note that this expression is valid for any region-independent descriptor $k_{\mathbf{v}}$.

(3) Energy function for the LCN

The variational formalism described above can be used by using different region-based functions such as the average of gray level [Chan et al. (2001)] or the estimation of probability distributions [Song Chun Zhu et al. (1996)], for instance. Besides, our group has proposed a method before to cope with the complex structure of the LCN, especially with the slender size of canaliculi [Pacureanu et al. (2009)]. This method is based on a Gaussian distribution model and the 3D line-filter image $l(\mathbf{x})$ is also used to test the candidate voxels during iterations.

We define the region-based energy function as:

$$J(f,l) = g(\mathbf{x}) J_f(f) + [1 - g(\mathbf{x})] J_{fl}(f,l), \tag{5.16}$$

where,

$$J_f(f) = \int_{\Omega_{in}} \left| f(\mathbf{x}) - \mu_{f_{in}} \right|^2 d\mathbf{x} + \int_{\Omega_{out}} \left| f(\mathbf{x}) - \mu_{f_{out}} \right|^2 d\mathbf{x}, \tag{5.17}$$

and

$$\begin{gathered} J_{fl}(f,l) = \int_{\Omega_{in}} G_{in}(f,l) d\mathbf{x} + \int_{\Omega_{out}} G_{out}(f,l) d\mathbf{x} \\ G_{in}(f,l) = \frac{1}{\sqrt{2\pi\sigma_{f_{in}}}} \exp\left(-\frac{\left| f(\mathbf{x}) - \mu_{f_{in}} \right|^2}{2\sigma_{f_{in}}^2 l(\mathbf{x})} \right) \quad , \\ G_{out}(f,l) = \frac{1}{\sqrt{2\pi\sigma_{f_{out}}}} \exp\left(-\frac{\left| f(\mathbf{x}) - \mu_{f_{out}} \right|^2}{2\sigma_{f_{out}}^2 (1 - l(\mathbf{x}))} \right) \end{gathered} \tag{5.18}$$

with:

$$g(\mathbf{x}) = \begin{cases} 0, & if\ f(\mathbf{x}) < \delta \\ 1, & if\ f(\mathbf{x}) \geq \delta \end{cases}, \tag{5.19}$$

where $\mu_{f_{in}}$ and $\mu_{f_{out}}$ are the average gray values in the domain Ω_{in} and Ω_{out} of the original image $f(\mathbf{x})$, $\sigma_{f_{in}}$ and $\sigma_{f_{out}}$ the corresponding standard deviations, δ is a threshold value.

Then, the variation of the energy function can be calculated by:

$$\Delta J(\varphi^{n+1}) = (1 - 2\varphi^{n})\left(\Delta J_{f}(f) + \Delta J_{fl}(f,l)\right), \tag{5.20}$$

where we have

$$\Delta J_{f}(f) = \left|f(\mathbf{x}) - \mu_{f_{in}}\right|^{2} - \left|f(\mathbf{x}) - \mu_{f_{out}}\right|^{2}, \tag{5.21}$$

and

$$\Delta J_{fl}(f,l) = \frac{1}{\sqrt{2\pi\sigma_{f_{in}}}}\exp\left(-\frac{\left|f(\mathbf{x})-\mu_{f_{in}}\right|^{2}}{2\sigma_{f_{in}}^{2}\, l(\mathbf{x})}\right) - \frac{1}{\sqrt{2\pi\sigma_{f_{out}}}}\exp\left(-\frac{\left|f(\mathbf{x})-\mu_{f_{out}}\right|^{2}}{2\sigma_{f_{out}}^{2}(1-l(\mathbf{x}))}\right). \tag{5.22}$$

5.2.3.2.4 Image post-processing

Although we tried to avoid segmenting false voxels in the initialization, there are still some of them left and their number may increase after region growing. To avoid this problem, we used a connected components analysis with a threshold of 100 voxels which was also from the previous work of our group [Pacureanu (2012)]. It removed the independent components which could be collagen fibers or noise. Finally, since the segmented image contains both canaliculi and parts of lacunae as shown in Fig. 5.6 (d), we subtracted the segmented lacunae from the result to obtain the binary image of canaliculi only (see Fig. 5.6 (e)).

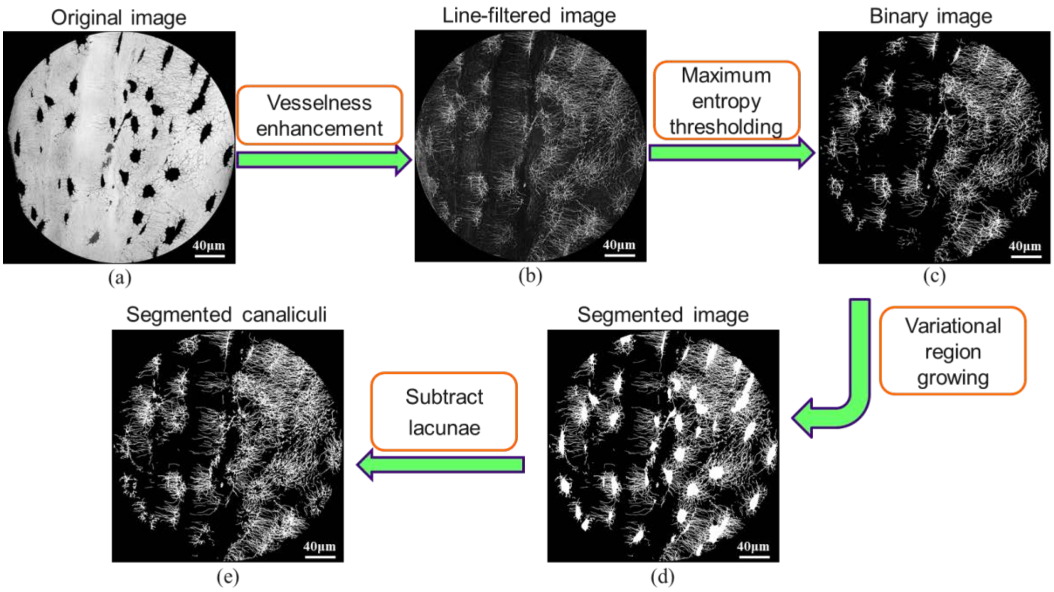

Figure 5.6 Minimum Intensity Projections (MIPs) of 256 slices from the reconstructed volume at 120 nm for the segmentation of canaliculi. (a) MIPs from the original volume; (b) MIPs of the result after vesselness enhancement; (c) The seed map after maximum entropy thresholding; (d) MIPs of the result of VRG including lacunae and canaliculi; (e) MIPs of the segmented result of canaliculi.

5.2.4 Quantitative analysis

In this section, we describe the parameters that were extracted both from the binary lacunae and canaliculi images.

5.2.4.1 Quantification of lacunae

5.2.4.1.1 Number of lacunae

First, each object in the binary lacunae image was labeled by using a connected component analysis. The labels were consecutive integer values starting at one, after sorting the objects by decreasing size. We used the 26 connectivity in 3D. The number of lacunae $Lc.N$ was calculated by counting the total number of labels.

5.2.4.1.2 Volume of lacuna

Let us denote the labeled lacunae image as $L(\mathbf{x})$. An osteocyte lacuna L_n with the label value n can be expressed by:

$$L_n = \{\, \mathbf{x} = (x, y, z) \in \Omega \mid L(\mathbf{x}) = n\}. \tag{5.23}$$

Then, the volume of one specific lacuna $Lc.V(L_n)$ could be simply computed by summing all the voxels with the label value n.

5.2.4.1.3 Moment based descriptors

Our group previously proposed a method based on the second-order central moments, to estimate the lengths of three axes of each lacuna by fitting it to an ellipsoid [Dong, Haupert, et al. (2014)]. The second-order central moments μ_{pqr} of one lacuna L_n can be calculated by:

$$\mu_{pqr} = \sum\nolimits_{(x,y,z)\in L_n} (x - \bar{x}_n)^p \cdot (y - \bar{y}_n)^q (z - \bar{z}_n)^r, \tag{5.24}$$

where $(\bar{x}_n, \bar{y}_n, \bar{z}_n)$ is the center coordinates of L_n.

Then, the second-order central moment matrix $M(L_n)$ can be expressed as follows [Flusser et al. (2009)]:

$$M(L_n) = \begin{pmatrix} \mu_{200} & \mu_{110} & \mu_{101} \\ \mu_{110} & \mu_{020} & \mu_{011} \\ \mu_{101} & \mu_{011} & \mu_{002} \end{pmatrix}. \tag{5.25}$$

Depending on the three eigenvalues $\lambda_1 \geq \lambda_2 \geq \lambda_3$ of this matrix, the half-lengths of axes of the best fitting ellipsoid can be computed by:

$$a_k = \sqrt{5\lambda_k / Lc.V(L_n)}, \quad k = 1,2,3. \tag{5.26}$$

After doubling, we obtain the final length, width and depth of the ellipsoid:

$$Lc.L_1(L_n) = 2a_1, \quad Lc.L_2(L_n) = 2a_2, \quad Lc.L_3(L_n) = 2a_3. \tag{5.27}$$

The ratio between the volumes of the real lacuna and the ellipsoid can be expressed by:

$$\tau = 3Lc.V(L_n)^{5/2} / \left(20\pi\sqrt{5\lambda_1\lambda_2\lambda_3}\right). \tag{5.28}$$

Also, we calculate the ratios between different axes such as $Lc.L_1/Lc.L_2$ and $Lc.L_1/Lc.L_3$ to describe the anisotropy of the lacunae.

5.2.4.1.4 Intrinsic volumes

We also calculated the intrinsic volumes of lacunae providing interesting characteristics of shapes, such as the surface area $Lc.S(L_n)$, the integral of the mean curvature $Lc.M(L_n)$ and the Euler number $Lc.\chi(L_n)$ of the lacuna L_n. These quantities can be efficiently computed by using the Crofton formula [Ohser and Schladitz (2009)]. If the discrete image is defined on the cubic primitive lattice $\mathbb{L}^n = a\mathbb{Z}^n$, where $\mathbb{Z}$ denotes the set of integers and a the lattice spacing, the estimation of the intrinsic volumes $\hat{V}_{3-k}(L_n)$ for of each lacuna can be expressed by:

$$\hat{V}_{3-k}(L_n) = 2a^{3-k} \sum\nolimits_{l=0}^{v} v_l^{(k)} h_l(L_n), \tag{5.29}$$

where l is an index spanning local configurations of voxels, $h_l(L_n)$ the number of the configuration l in the set L_n, $v_l^{(k)}$ the weight coefficient of the configuration and $v = 22$ the congruence classes of the local pixel configurations for the 3D images.

For each lacuna, the surface area $Lc.S(L_n)$, the integral of the mean curvature $Lc.M(L_n)$ and the Euler number $Lc.\chi(L_n)$ of the lacuna L_n can be obtained as:

$$\begin{gathered} Lc.S(L_n) = 2\hat{V}_2(L_n) = 4a^2 v_l^{(1)} h \\ Lc.M(L_n) = \pi \hat{V}_1(L_n) = 2\pi a v_l^{(2)} h, \\ Lc.\chi(L_n) = \hat{V}_0(L_n) = v_l^{(3)} h \end{gathered} \tag{5.30}$$

where the weights $4a^2 v_l^{(1)}$, $2\pi a v_l^{(2)}$ and $v_l^{(3)}$ for each configuration have been given in the previous publication [Ohser, Nagel, et al. (2009)].

Besides, we computed the structure model index $Lc.SMI(L_n)$ of each lacuna, from these intrinsic volumes [Dong, Pacureanu, et al. (2014)]:

$$Lc.SMI(L_n) = 12 Lc.V(L_n) Lc.M(L_n) / Lc.S(L_n)^2, \tag{5.31}$$

The SMI characterizes the lacunar shape with values of 0 for a pure plate, 3 for a rod and 4 for a sphere [Hildebrand et al. (1997)].

5.2.4.1.5 Density and porosity of lacunae

To calculate the density and porosity of lacunae, we first define that the bone volume (BV) is equal to the tissue volume (TV) minus the volume of Haversian and Volkmann canals. Because the volume of canals is much larger than that of lacunae, we can segment canals from the original volumes based on thresholding and a connected component filter. Then, we obtain a mask for the bone volume which contains the bone matrix and the LCN by subtracting canals. Hence, we can compute BV by counting the number of voxels contained in the mask image.

Then, the density of lacunae is computed by the number of total lacunae dividing by the bone volume ($Lc.N/BV$) while the porosity is equal to the total volume of lacunae in the reconstructed image divided by the bone volume or the tissue volume ($Lc.TV/BV$).

In order to compute parameters in the neighborhood of each lacuna, we used a 3D Voronoi tessellation of the images after connected components analysis (see Fig. 5.7). The Voronoi diagram was calculated based on the centroids of each lacuna. After this step, we obtain a partition of the 3D volume into small regions, that we call $Cell$, each of them containing only one lacuna and its canaliculi. Then, we computed the average volume of each cell ($Cell.V$) and the ratio between the average volume of lacuna and the average volume of each cell ($Lc.V/Cell.V$).

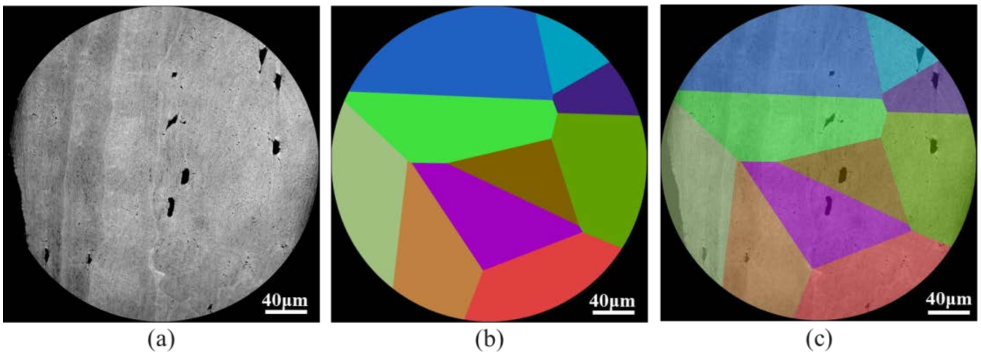

Figure 5.7 3D Voronoi tessellation. (a) A slice from the original volume; (b) A slice of tessellation image; (c) A overlay of (a) and (b).

5.2.4.2 Quantification of canaliculi

5.2.4.2.1 Porosity of canaliculi

Similarly to the case of lacunae, we calculated the 3D porosity of canaliculi in the whole volume expressed as the total volume of canaliculi divided by the bone volume ($Ca.TV/BV$). To obtain a local measure, we also computed the ratio between the average volume of canaliculi per cell and the average volume of each cell ($Ca.V/Cell.V$). Besides, we calculated the total volume of the LCN ($LCN.TV$) and the porosity of the LCN ($LCN.TV/BV$) for the evaluation of the whole network.

5.2.4.2.3 Number and ramification of canaliculi

To quantify the number of canaliculi and its ramification, we calculated the number of canaliculi per lacuna at different distances from the surface of the lacuna [Dong, Pacureanu, et al. (2014)]. The entire calculation process is achieved by using the 3D Euler number, which can be computed by the Betti numbers:

$$\chi = \beta_0 - \beta_1 + \beta_2, \tag{5.32}$$

where β_0 denotes the number of connected components, β_1 the number of tunnels and β_2 the number of cavities [Odgaard (1997)].
Actually, if each voxel of the 3D object is regarded as a cube and the 3D object is decomposed into a set of 1-voxels, the 3D Euler number can be also calculated by:

$$\chi = n_0 - n_1 + n_2 - n_3, \tag{5.33}$$

where n_0 is the number of vertexes of 1-voxels, n_1 the number of edges of 1-voxels, n_2 the number of faces of 1-voxels, n_3 the number of 1-voxels [Toriwaki et al. (2002)].

Before calculating the number of canaliculi per lacuna, we first need to obtain the bounding surface of the lacuna by using the dilation operation in mathematical morphology. We begin with the binary segmentation of the lacuna L_n and perform r times dilated operations $\oplus_r L_n$, where $\oplus$ denotes the dilation operation. The bounding surface $\partial_r L_n$ at the distance r can be expressed as:

$$\partial_r L_n = \oplus_r L_n - \oplus_{r-1} L_n. \tag{5.34}$$

Then, if we denote the segmentation of canaliculi surrounding the lacuna L_n as C_n, we can get a bounding surface with holes which represent the number of canaliculi:

$$\mathcal{H}_r L_n = \partial_r L_n - (\partial_r L_n \cap C_n). \tag{5.35}$$

Moreover, the Euler number of $\mathcal{H}_r L_n$ can be calculated by:

$$\chi(\mathcal{H}_r L_n) = \beta_0(\mathcal{H}_r L_n) - \beta_1(\mathcal{H}_r L_n) + \beta_2(\mathcal{H}_r L_n). \tag{5.36}$$

where $\beta_0(\mathcal{H}_r L_n) = 1$ (one connected component for one lacuna), $\beta_1(\mathcal{H}_r L_n)$ is the number of holes on the surface $\mathcal{H}_r L_n$, $\beta_2(\mathcal{H}_r L_n) = 1$ (one cavity inside one lacuna).

Finally, we compute the number of canaliculi per lacuna at the distance r by:

$$Ca.N(L_n)(r) = \beta_1(\mathcal{H}_r L_n) = 2 - \chi(\mathcal{H}_r L_n). \tag{5.37}$$

By changing the dilated times, we can thus obtain a set of numbers of canaliculi for each lacuna $\{Ca.N(L_n)(r) | r \in [r_0, r_{max}]\}$ which describes the distribution of canaliculi around the lacuna within the distance region $[r_0, r_{max}]$.

To quantify the density of canaliculi, we computed the ratio between the number of canaliculi per lacuna and the volume of lacuna located in the same cell ($Ca.N/Lc.V$).

5.2.5 Statistics analysis

We provide the average and standard deviation of all parameters. The correlation between parameters were studied by using the Spearman correlation coefficient (R^2) and the p-value by the Fisher's r to z transformation. These calculations and analysis were performed by Statview® (SAS Institute Inc., Cary, NC, USA). P-values under 0.05 were considered as significant.

5.3 Results

5.3.1 Segmentation method

5.3.1.1 Variational region growing

Figure 5.8 illustrates the Minimum Intensity Projections (MIPs) of an image segmented from the VRG method for a cropped VOI in one reconstructed volume at the voxel size of 120 nm. The size of the VOI is 256 × 256 × 128 voxels, corresponding to a physical size of 30.72 µm × 30.72 µm × 15.36 µm. Fig. 5.8 shows the MIPs: (a) of the original reconstructed volume; (b) of the segmented image by the maximum entropy thresholding; (c) of the result of the VRG. It can be seen that the VRG method detect the lacunae and canaliculi voxels at the same time. The red circle regions in Fig. 5.8 (b) and (c), show that the connectivity between some canaliculi is restored after the VRG process.

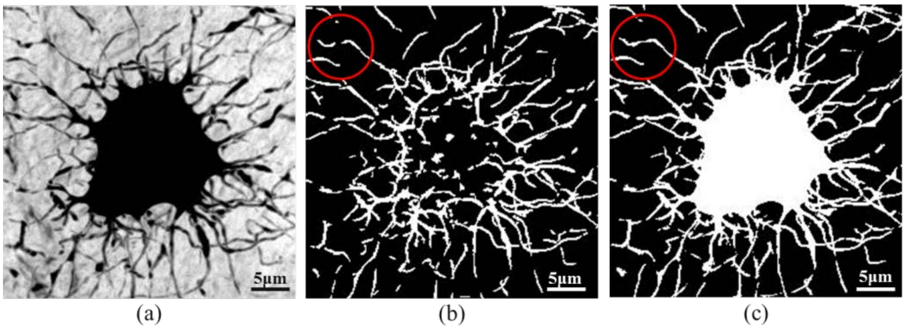

Figure 5.8 Minimum Intensity Projections (MIPs) along the Z-axis of the results after implementing VRG. (a) MIPs of the original volume at 120 nm; (b) MIPs of the segmented image by the maximum entropy thresholding; (c) MIPs of the results of VRG.

5.3.1.2 VRG and geodesic voting

We also compare the result of the VRG segmentation on our volumes at the voxel size of 120 nm to another method developed in our group to segment the LCN at lowest resolution: the geodesic voting method [Zuluaga et al. (2014)]. We consider the running time of these two methods to segment canaliculi from one reconstructed volume, excluding the pre and post processing before and after the segmentation, and we check the segmented results visually. All the programs were run in the Networked Interactive Computing Environment (NICE) which is the ESRF computing infrastructure implemented to store, manipulate, and process large data sets. The CPU of the nodes of the cluster was an Intel(R) Xeon(R) CPU E5-2670 v2 @ 2.50GHz. There were 20 cores (10 per socket) in total to run the programs.

Table 5.1 reports the running time of these two canaliculi segmentation methods. The VRG method needed 829 seconds to finish the process, while the geodesic voting took 17697 seconds, which is 21.3 times longer. In Fig. 5.9, we present the segmented results based on VRG and geodesic voting. To have a better observation of the segmented images, we added the segmentation of lacunae, which was obtained by the method mentioned in the section 5.2.3 of this chapter. The display is presented on a region of 2048 × 2048 × 128 voxels. Fig. 5.9 gives (a) the MIPs in the original volume, (b) the MIPs of the LCN segmented by using VRG, (c) the MIPs of the LCN segmented based on the geodesic voting; (d), (e), (f) are zooms of the MIPs shown in (a), (b) and (c), respectively. We can see that both of methods can achieve the extraction of canaliculi from the reconstructed volumes. However, by using the geodesic voting, the connectivity between canaliculi in some region is broken after the segmentation, and the thickness of the extracted canaliculi is just one voxel which is smaller than that of VRG (see Fig. 5.9 (e) and (f)) and not representative of the truth at this scale. These results confirm that the VRG method is better suited to segment the canaliculi in the present study.

Table 5.1 Record of time cost by two segmented methods

Segmented methods	Time cost (seconds)
VRG	829
Geodesic voting	17697

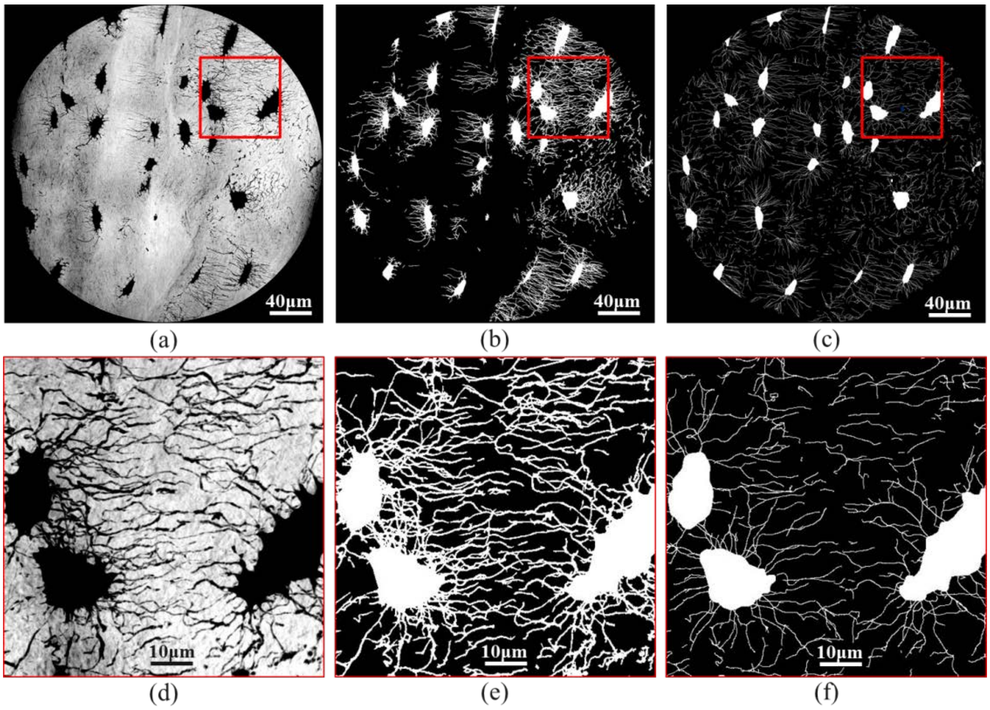

(a) (b) (c)

(d) (e) (f)

Figure 5.9 Minimum Intensity Projections (MIPs) of 128 slices along the Z-axis showing the segmentation of VRG and geodesic voting. (a) MIPs of the original volume at 120 nm; (b) MIPs of the segmented LCN by VRG; (c) MIPs of the segmented LCN of geodesic voting; (d), (e) and (f) zoom on the MIPs corresponding to (a), (c) and (e) respectively.

5.3.1.3 3D rendering

In Fig. 5.10 (a), we show the MIPs along the Y-axis of 100 middle slices from the reconstructed volume of the sample A3 in order to observe the distribution of lacunae surrounding the osteon. The 3D display of the segmented lacunae and canaliculi rendered by VGStudioMax® is given in Fig. 5.10 (b).

5.3.2 Quantitative analysis of the LCN at 120 nm

After segmentation, we calculated a number of parameters described in the section 5.2.4. Here, we report the quantitative results in terms of tables and figures.

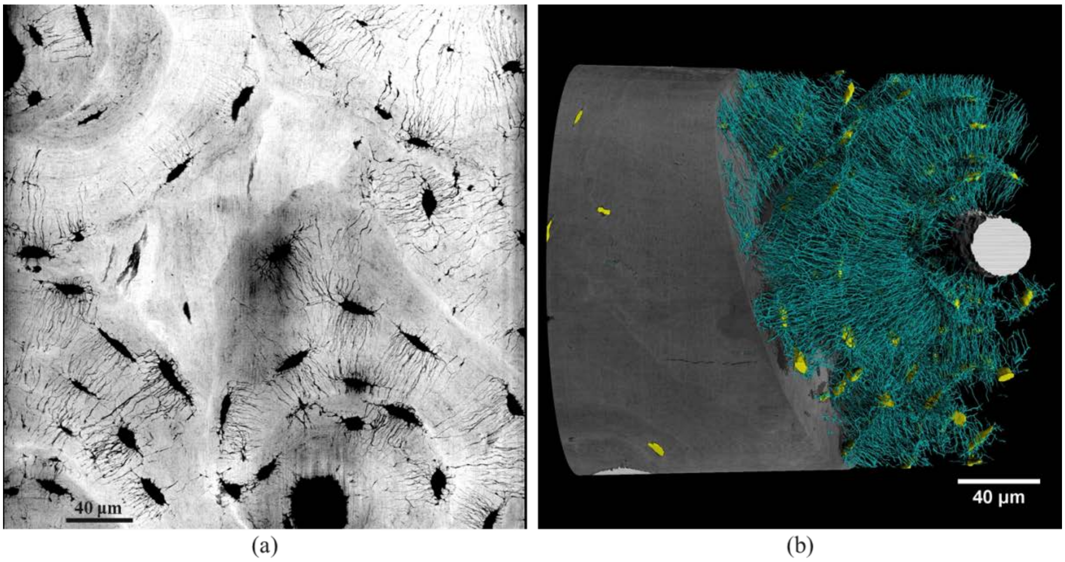

Figure 5.10 Segmentation results for the sample A3 at 120 nm. (a) MIPs along the Y-axis of 100 middle slices from the reconstructed volume; (b) 3D rendering of the segmented lacunae and canaliculi.

5.3.1.1 Morphometric parameters of lacunae

Table 5.2 presents quantitative statistical features of lacunae for the data at the voxel size of 120 nm. For all the 8 samples, the average number of lacunae per volume is 259.6 and the average total volume of lacunae is 8.2×10^{-5}mm^3. The average bone volume is 10.6×10^{-3} mm^3 with the average lacunar porosity 0.78% and the average density of lacunae 24000 mm^{-3}. The average volume of each lacuna is 315.7 µm^3 and the average surface is 323.3 µm^2. The average volume of each Voronoi cell is 42000 µm^3 and the ratio between the average volume of each lacuna and its belonging cell is 0.88 %. The average length, width and depth of each lacuna are 17.1 µm, 9.2 µm and 4.4 µm, respectively. The anisotropy of the lacunae is described by the ratio between the length and the width found to be 2.0, the ratio between the width and the depth found to be 2.2 and the structural model index found to be 3.1.

Figure 5.11 displays plots of some morphological lacunar parameters averaged on each reconstructed volume, such as the average length, width and depth, as well as the descriptors of the flatness ($Lc.L1/Lc.L2$, $Lc.L1/Lc.L2$ and $Lc.SMI$).

Table 5.2 Morphometric parameters of lacunae at the voxel size of 120 nm

Sample ID	Lc.N	Lc.TV ($\times10^{-5}$ mm^3)	BV ($\times10^{-3}$ mm^3)	Lc.TV/BV (%)	Lc.N/BV ($\times10^4$ mm^{-3})	Lc.V (µm^3)	Cell.V ($\times10^4$ µm^3)	Lc.V/Cell.V (%)
A2	194	7.6	8.6	0.88	2.2	393.4±172.6	5.1±2.8	0.92±0.55
A3	298	9.3	11.4	0.81	2.6	311.1±116.6	3.6±1.3	0.98±0.59
A6	347	10.1	11.3	0.9	3.1	291.5±108.1	3.1±1.1	1.02±0.49
A8	255	7.2	11.3	0.64	2.3	284.1±99.9	4.3±1.6	0.75±0.39
A9	278	8.3	10.7	0.77	2.6	298.8±96.4	3.8±1.3	0.86±0.38
A11	229	7.6	9.2	0.83	2.5	333.4±132.6	5.1±2.7	0.84±0.53
A12	222	7.6	11	0.69	2	341.0±168.5	4.6±1.8	0.83±0.47
A13	254	7.8	11.3	0.69	2.3	307.0±161.3	4.3±1.5	0.77±0.36
Mean All	259.6	8.2	10.6	0.78	2.4	315.7	4.2	0.88
Std. All	44.9	0.9	1	0.09	0.3	134.8	2.3	0.48

Sample ID	Lc.S (µm^2)	Lc.L1 (µm)	Lc.L2 (µm)	Lc.L3 (µm)	Lc.L1 /Lc.L2	Lc.L2 /Lc.L3	Lc.SMI
A2	365.8±110.7	19.3±4.7	9.1±2.2	4.7±1.2	2.2±0.8	2.0±0.6	3.1±0.3

A3	334.7±92.8	16.8±4.0	10.0±2.1	4.1±1.0	1.8±0.6	2.6±0.8	3.0±0.4
A6	298.3±77.2	16.9±4.3	8.2±1.8	4.7±1.0	2.2±0.8	1.8±0.5	3.2±0.4
A8	301.9±81.7	15.7±3.6	9.3±2.1	4.3±1.0	1.8±0.6	2.3±0.8	3.0±0.4
A9	317.4±70.0	16.4±3.8	9.3±1.8	4.5±1.0	1.8±0.6	2.2±0.7	3.0±0.4
A11	329.3±91.4	17.2±4.2	9.2±1.9	4.5±1.1	2.0±0.7	2.1±0.6	3.1±0.3
A12	335.6±110.5	17.7±4.8	9.1±2.4	4.6±1.3	2.1±0.8	2.1±0.8	3.1±0.4
A13	323.4±106.5	17.5±5.0	9.1±2.2	4.3±1.0	2.1±0.9	2.2±0.7	3.1±0.4
Mean All	323.3	17.1	9.2	4.4	2	2.2	3.1
Std. All	93.8	4.4	2.1	1.1	0.8	0.7	0.4

Lc.N – number of lacunae
Lc.TV – total volume of lacunae (mm^3)
BV – bone volume (mm^3)
Lc.TV/BV – lacunar porosity (%)
Lc.N/BV – density of lacunae (mm^{-3})
Lc.V – average volume of lacuna (µm^3)
Cell.V – average volume of each cell (µm^3)
Lc.V/Cell.V – ratio between the average volume of lacuna and its belonging cell (%)
Lc.S – average surface area of lacuna (µm^2)
Lc.L1, Lc.L2 and Lc.L3 – average length, width and depth of lacuna (µm)
Lc.L1/Lc.L2 and Lc.L2/Lc.L3 – average anisotropy of lacuna
Lc.SMI – average structural model index of lacuna

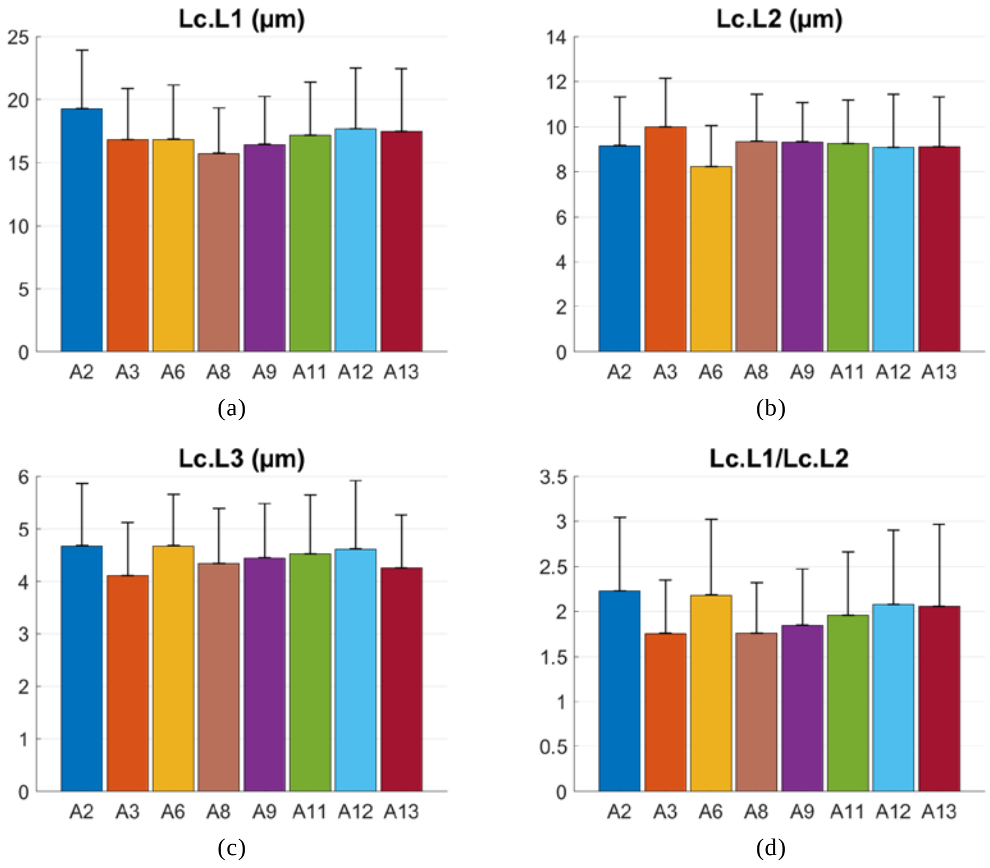

(a) (b)

(c) (d)

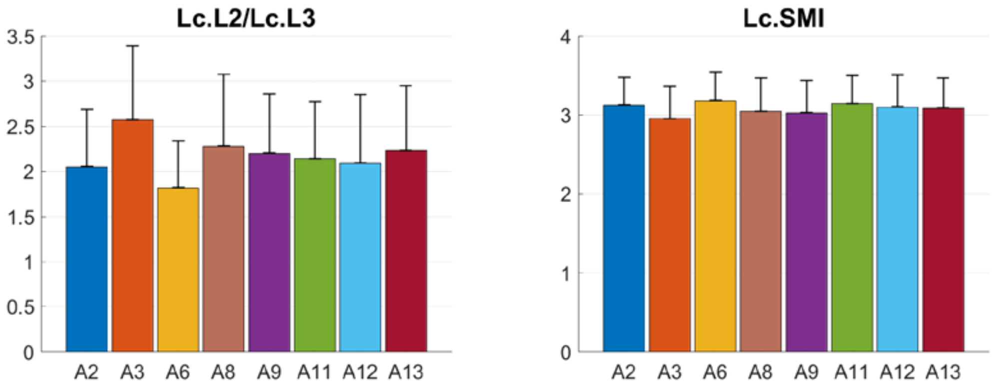

(e) (f)

Figure 5.11 Some descriptors for the morphology of lacuna at the voxel size of 120 nm.

5.3.1.2 Morphometric parameters of canaliculi

Table 5.3 reports the morphometric parameters of canaliculi for the 8 samples at the voxel size of 120 nm. From the results, the average total volume of canaliculi is 3.6×10^{-5} mm^3 and the average porosity of canaliculi is 0.35%. The average volume of canaliculi per cell is 139.3 µm^3 with the ratio of 0.37% between the average volume of canaliculi per cell and its belonging cell. Also, the average ratio between the volume of canaliculi and the lacuna in the same cell is 45.8%. The average total volume of the LCN is 11.8×10^{-5} mm^3 and the average porosity of the LCN is 1.12%.

Figure 5.12 presents the average porosity of lacunae and canaliculi within their belonging cells for different samples at the voxel size of 120 nm. We show the average volume of lacuna, canaliculi and the cell, as well as the ratios between these values of volumes ($Lc.V/Cell.V$, $Ca.V/Cell.V$ and $Ca.V/Lc.V$).

Table 5.4 and Figure 5.13 give the quantitative results of the ramification of canaliculi at the voxel size of 120 nm. At 7 different distances ranging from 1.2 µm to 12.0 µm from the surface of lacuna, the average number of canaliculi per lacuna is 58.2, 57.9, 61.8, 63.3, 65.0, 68.6 and 75.4. The corresponding ratio between the number of canaliculi per lacuna and the volume of lacuna in the same cell is 0.19 µm^{-3}, 0.18 µm^{-3}, 0.20 µm^{-3}, 0.20 µm^{-3}, 0.21 µm^{-3}, 0.22 µm^{-3} and 0.25 µm^{-3}, respectively.

Table 5.3 Morphometric parameters of canaliculi at the voxel size of 120 nm

Sample ID	Ca.TV (10^{-5} mm^3)	LCN.TV (10^{-5} mm^3)	Ca.TV/BV (%)	LCN.TV/BV (%)	Ca.V (µm^3)	Ca.V/Cell.V (%)	Ca.V/Lc.V (%)
A2	3.2	10.9	0.37	1.26	166.9±93.9	0.36±0.21	45.1±22.9
A3	5.2	14.5	0.46	1.27	175.4±89.8	0.52±0.25	58.4±28.8
A6	2.8	12.9	0.25	1.14	80.2±42.1	0.27±0.13	29.4±16.7
A8	3	10.2	0.26	0.9	116.8±78.4	0.29±0.18	42.6±28.5
A9	4.2	12.5	0.39	1.16	149.8±103.6	0.42±0.30	50.4±32.4
A11	5.2	12.9	0.57	1.4	228.0±147.5	0.52±0.34	71.7±49.4
A12	3.3	10.9	0.3	0.99	148.2±79.7	0.36±0.19	47.0±25.9
A13	2	9.8	0.18	0.87	79.8±43.5	0.20±0.11	27.9±15.2
Mean All	3.6	11.8	0.35	1.12	139.3	0.37	45.8
Std. All	1.1	1.5	0.12	0.18	99.9	0.25	31.7

Ca.TV – total volume of canaliculi (mm^3)
LCN.TV – total volume of the LCN (mm^3)
Ca.TV/BV – the porosity of canaliculi (%)
LCN.TV/BV – the porosity of the LCN (%)
Ca.V – average volume of canaliculi per cell (µm^3)
Ca.V/Cell.V – ratio between the average volume of canaliculi and the average volume of cell
Ca.V/Lc.V – ratio between the average volume of canaliculi and the average volume of lacuna

Table 5.4 Number of canaliculi per lacuna at 7 different distances from the surface of the lacuna and the ratio between the number and the average volume of lacuna at the voxel size of 120 nm

Sample ID	Ca.N (r=1.2 µm)	Ca.N (r=3.0 µm)	Ca.N (r=4.8 µm)	Ca.N (r=6.6 µm)	Ca.N (r=8.4 µm)	Ca.N (r=10.2 µm)	Ca.N (r=12.0 µm)
A2	67.8±30.1	63.7±39.2	70.8±44.0	77.6±48.0	82.6±50.3	87.6±53.4	95.8±58.9
A3	71.8±28.9	80.8±38.2	85.5±41.7	85.9±43.7	87.2±47.2	91.7±52.0	101.0±58.9
A6	49.8±20.3	41.1±21.8	42.7±23.6	42.2±25.0	42.0±25.2	44.2±27.4	48.7±29.9
A8	51.4±24.2	51.6±31.8	52.5±34.2	51.2±34.4	51.0±35.3	53.4±39.0	58.9±41.9
A9	62.0±28.1	59.6±36.6	65.3±42.6	67.7±46.6	71.2±52.1	76.2±57.2	85.2±64.8
A11	59.0±32.7	71.2±37.7	79.9±42.5	85.7±47.3	91.3±52.5	100.1±58.9	112.7±68.8
A12	60.4±27.9	63.5±35.0	70.1±39.5	71.9±41.1	73.6±43.6	75.6±46.7	79.8±50.4
A13	46.4±24.0	37.4±23.7	35.7±24.5	34.3±25.3	32.6±25.0	32.7±25.0	34.3±26.3
Mean All	58.2	57.9	61.8	63.3	65	68.6	75.4
Std. All	28.1	36	40.4	43.4	46.7	51.1	57.3
Sample ID	Ca.N/Lc.V (μm^{-3}, r=1.2 µm)	Ca.N/Lc.V (μm^{-3}, r=3.0 µm)	Ca.N/Lc.V (μm^{-3}, r=4.8 µm)	Ca.N/Lc.V (μm^{-3}, r=6.6 µm)	Ca.N/Lc.V (μm^{-3}, r=8.4 µm)	Ca.N/Lc.V (μm^{-3}, r=10.2 µm)	Ca.N/Lc.V (μm^{-3}, r=12.0 µm)
A2	0.18±0.06	0.16±0.08	0.18±0.10	0.20±0.11	0.22±0.13	0.23±0.14	0.26±0.15
A3	0.24±0.09	0.26±0.10	0.28±0.11	0.28±0.13	0.29±0.15	0.31±0.18	0.34±0.22
A6	0.18±0.08	0.15±0.08	0.15±0.09	0.15±0.09	0.15±0.09	0.16±0.10	0.18±0.11
A8	0.18±0.07	0.18±0.09	0.18±0.10	0.18±0.11	0.18±0.12	0.19±0.14	0.22±0.16
A9	0.21±0.11	0.19±0.10	0.21±0.12	0.22±0.14	0.23±0.16	0.25±0.18	0.28±0.21
A11	0.18±0.08	0.21±0.09	0.24±0.11	0.26±0.13	0.28±0.15	0.30±0.17	0.34±0.19
A12	0.19±0.07	0.19±0.08	0.21±0.10	0.22±0.12	0.23±0.13	0.23±0.14	0.25±0.16
A13	0.16±0.08	0.12±0.07	0.12±0.08	0.12±0.08	0.11±0.08	0.11±0.09	0.12±0.10
Mean All	0.19	0.18	0.2	0.2	0.21	0.22	0.25
Std. All	0.09	0.1	0.11	0.13	0.14	0.16	0.18

Ca.N – number of canaliculi per lacuna
Ca.N/Lc.V – ratio between the number of canaliculi per lacuna and the average volume of lacuna

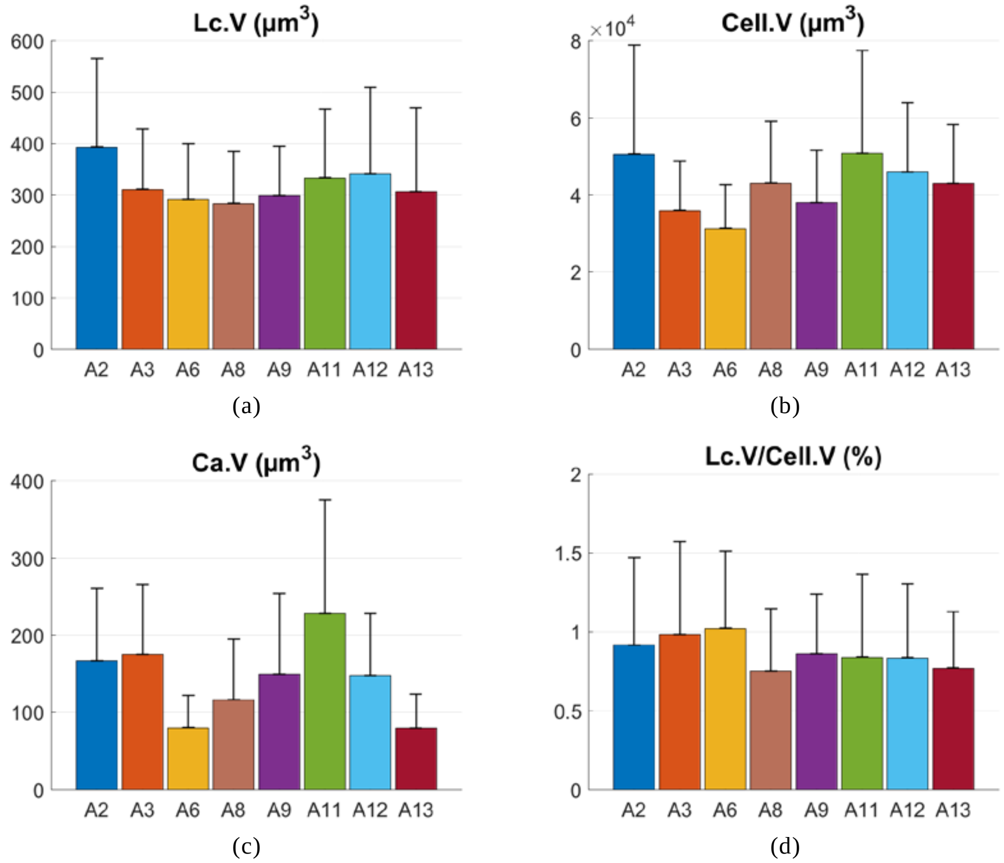

(a) (b)

(c) (d)

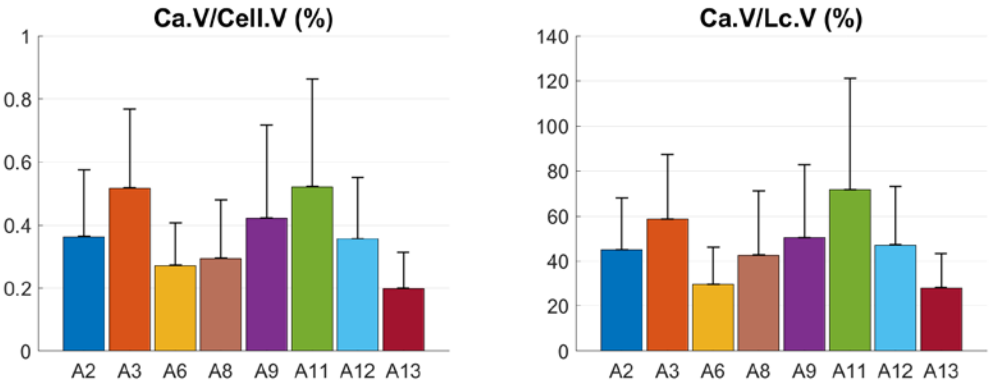

(e) (f)

Figure 5.12 Average porosity of lacunae and canaliculi within different cells at the voxel size of 120 nm.

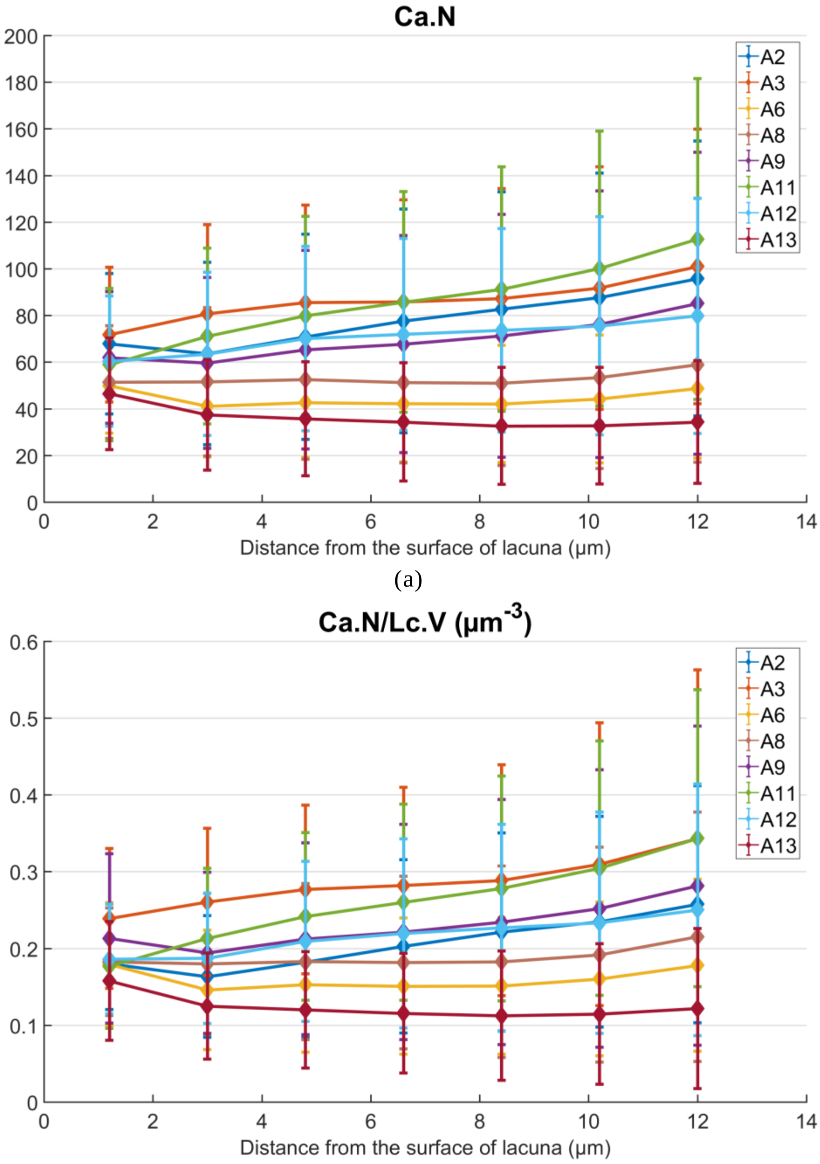

(a)

(b)

Figure 5.13 Number of canaliculi per lacuna at 7 distances from the surface of lacuna and the ratio between the number of canaliculi and the average volume of lacuna at the voxel size of 120 nm.

5.3.4 Statistical analysis

We computed correlation coefficients and p-values between all the quantitative parameters. In Table 5.5, we just gave the results with good correlation ($R^2 > 0.5$ and $p < 0.05$), and we show the regression plots of these parameters from different voxel sizes in Fig. 5.14.

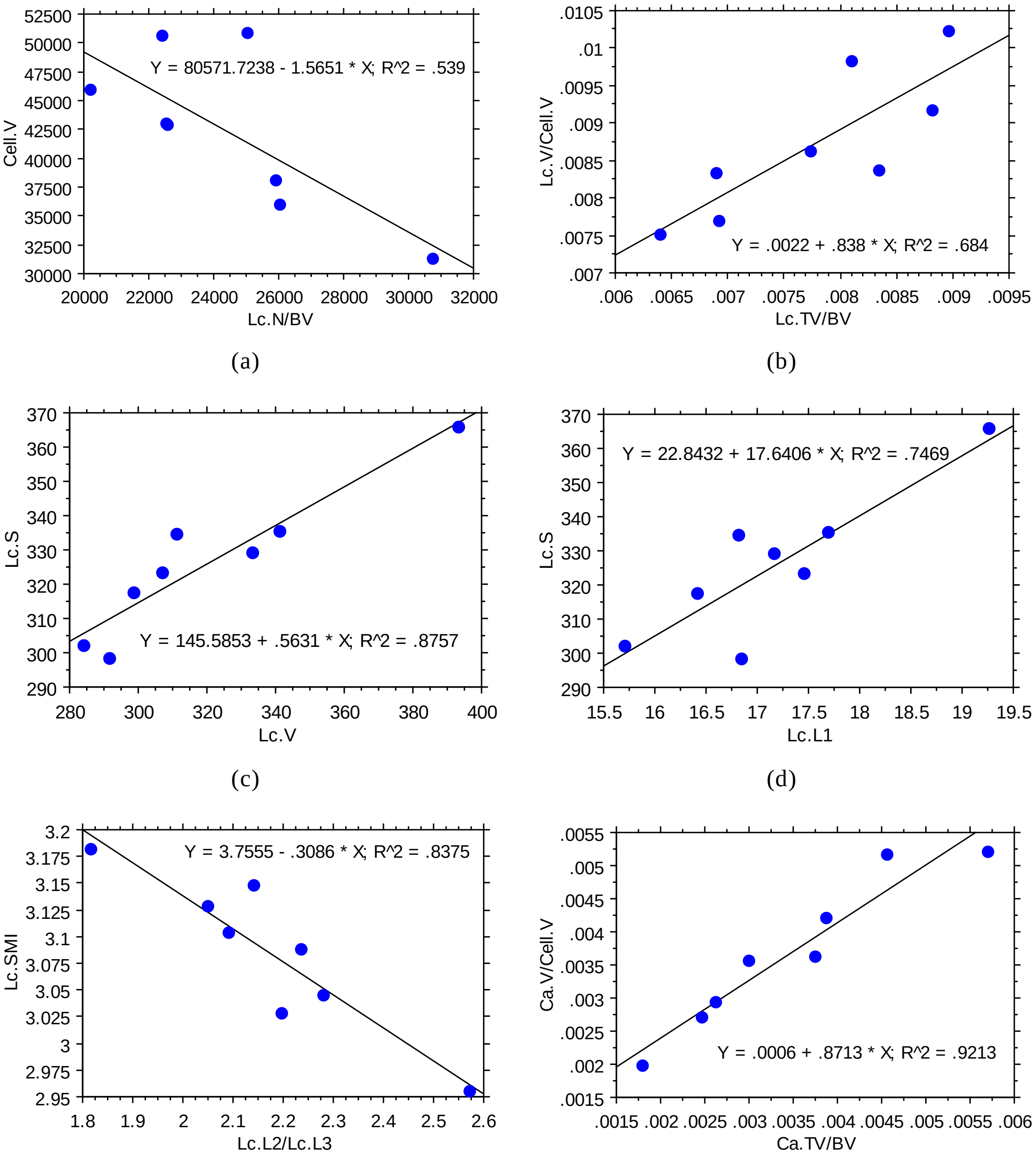

(a) (b)

(c) (d)

(e) (f)

Figure 5.14 Regression of parameters for the results of the voxel size of 120 nm. (a) correlation between $Cell.V$ (μm^3) and $Lc.N/BV$ (mm^{-3}); (b) correlation between $Lc.V/Cell.V$ and $Lc.TV/BV$;(c) correlation between $Lc.S$ (μm^2) and $Lc.V$ (μm^3); (d) correlation between $Lc.S$ (μm^2) and $Lc.L1$ (μm); (e) correlation between $Lc.SMI$ and $Lc.L1/Lc.L2$; (f) correlation between $Ca.V/Cell.V$ and $Ca.TV/BV$.

Table 5.5 Spearman correlation detection between some parameters in the three groups

Parameter 1	Parameter 2	120 nm	
		R^2	p-value
Lc.N/BV	Cell.V	0.5390	0.0381
Lc.TV/BV	Lc.V/Cell.V	0.6840	0.0113
Lc.V	Lc.S	0.8757	0.0006
Lc.L1	Lc.S	0.7469	0.0056
Lc.L2/Lc.L3	Lc.SMI	0.8375	0.0014
Ca.TV/BV	Ca.V/Cell.V	0.9213	0.0002

5.4 Discussion

In this chapter, we presented a method to segment and quantify the LCN from 3D phase nano CT images at the voxel size of 120nm, and reported results on 8 femoral human bone samples. The segmentation of lacunae is quite straightforward due to the size of lacunae (several µm) compared to the voxel size (0.12 µm). For the segmentation of canaliculi, two methods were compared: VRG and geodesic voting. The results of both methods were assessed qualitatively. We can observe that the VRG method succeeds in keeping the connectivity of canaliculi and extract canaliculi with some thickness. On the other hand, when using the geodesic voting method, the connections within canaliculi break in more regions and the thickness of the segmented canaliculi is generally one voxel. This results from the design of the geodesic voting method, which was developed to extract thin connected canaliculi path from CT images obtained at a lower spatial resolution (voxel size 300 nm) [Zuluaga et al. (2014)]. Conversely to this previous situation, the canaliculi may be spread on more than one voxels in the present case. Thus, we would need other operations to recover the geometric information of canaliculi, such as morphological dilation to increase the thickness. In addition, the running time of the geodesic voting is much larger than that of the VRG method and could even become prohibitive in some volumes. In conclusion, we selected the VRG method to segment canaliculi in our case considering the efficiency and efficacy.

Actually, we have tried to segment canaliculi from the reconstructed volumes manually by VGStudioMax®. However, we thought that the result of manual segmentation was not reliable and could not be used as the ground truth image. Due to the limitation of the spatial resolution of the reconstructions (voxel size of 120 nm), the gradual change of gray values was not obvious in the boundary region of canaliculi and bone mass. Hence, it was difficult to determine the attribution of voxels in these regions just relying on visual judgment. Besides, we needed to consider the 3D structure information of canaliculi to maintain their connectivity instead of checking 2D images slice by slice. This manual segmentation was highly dependent on the experience and the knowledge of the operator. Different people could obtain different segmentations and experienced researcher would achieve better results. Therefore, we did not use the manual segmentation as a reference for analysis in this chapter.

After segmentation, we calculated a number of quantitative parameters for the LCN in 8 human femoral cortical bone samples imaged at the voxel sizes of 120 nm. The quantification was performed from an average number of lacunae of 256.9 per volume and the average density of lacunae was found to be 24000 mm^{-3}. The result of the density of lacunae is in the range of previous works 15000–35000 mm^{-3} [van Hove et al. (2009)], [Bach-Gansmo et al. (2016)], [Andronowski et al. (2017)]. Our study permitted an estimation of the porosity of the LCN ($LCN.TV/BV$) 1.12% including both the lacunar porosity ($Lc.TV/BV$) and the canaliculi porosity ($Ca.TV/BV$). The 3D lacunar porosity $Lc.TV/BV$ (0.78%) is in agreement with that of previous research in our group using SR-µCT 0.84% [Dong, Haupert, et al. (2014)], and that obtained from CSLM 0.68 % [Repp et al. (2017)]. The canaliculi porosity $Ca.TV/BV$ in human is found here to be 0.37%, which is slightly smaller compared to 0.57% in [Varga et al. (2015)]. The other values from the literature were found to be 0.7% in mice using FIB/SEM [Schneider et al. (2011)], and (1.7–1.9)% in rat tibias using CSLM [Gatti et al. (2018)].

We also obtained parameters describing the morphology and anisotropy of lacuna. Our result of $Lc.V$ at the voxel size of 120 nm (315.7 μm^3) is consistent with previous reports (~50–730 μm^3) [Remaggi et al. (1998)], [Carter et al. (2013)]. Considering each lacuna as an ellipsoid, we got the average length of three axes. All the calculated values of the length, the width and the depth are comparable with previous works (~ 17 μm, 9 μm and 4 μm) and the ratio between them is about 4:2:1 [van Hove et al. (2009)], [Dong, Haupert, et al. (2014)]. The average surface area $Lc.S$ is 323.3 μm^2 at 120 nm, which is consistent with that found in Dong 336.2 μm^2 [Dong, Haupert, et al. (2014)], but higher than that of van Hove 211.9 μm^2 [van Hove et al. (2009)] and lower than that of Varga 430.4 μm^2 [Varga et al. (2015)]. The average structure model index of the samples is 3.1 comparable with the report of Dong 3.3 meaning that the 3D structure of the lacuna is close to an object between a cylinder and a sphere [Dong, Haupert, et al. (2014)].

Moreover, we introduced some new parameters. The local porosity of the lacuna and canaliculi were assessed by calculating the volume of their corresponding Voronoi cells. The average volume of each cell ($Cell.V$) was found to be 42000 μm^3, and represents in a way the area of influence of an osteocyte and its processes. The average volume of canaliculi per cell ($Ca.V$) was 139.3 μm^3, and the ratio $Lc.V/Cell.V$ (0.88%), $Ca.V/Cell.V$ (0.37%). It may be noted that the relative volume ratio of canaliculi to lacunae $Ca.V/Lc.V$ is 45.8%. These new parameters could help to evaluate the properties of lacunae and canaliculi not just in the whole volume but in a local region within their environment.

In addition, we quantified the ramification of the canaliculi for all the reconstructions. According to Dong [Dong, Pacureanu, et al. (2014)], the average distance between two nearest lacunae is about 23.2 μm. Therefore, we chose 7 different physical distances from the surface of each lacuna to count the number of canaliculi ($Ca.N$): 1.2 μm, 3.0 μm, 4.8 μm, 6.6 μm, 8.4 μm, 10.2 μm and 12.0 μm. To evaluate the density of the canaliculi, we also calculated the ratio between the number of canaliculi per lacuna and the average volume of lacuna ($Ca.N/Lc.V$). From the results, it can be seen that the overall trend of $Ca.N$ for all the samples is on the rise when getting away from the surface of lacuna, from 58.2 to 75.4 at the voxel size of 120 nm. Our calculations are all consistent with previous works, e.g. 89.7±15 for rat tibia samples [Sharma et al. (2012)], 77.5±12.0 for mice femoral samples [Lai et al. (2015)] and 88.5±24.9 for human femoral samples [Varga et al. (2015)], but these works only counted the number of canaliculi per lacuna in one fixed distance. The results of $Ca.N/Lc.V$ of the samples grow in the similar way, from 0.19 μm^{-3} to 0.25 μm^{-3}. Checking the samples separately, we found that the values of $Ca.N$ and $Ca.N/Lc.V$ for most of samples increased from the distance 1.2 μm to 12.0 μm. But there are several samples just showing a fluctuation and few of them indicating a slightly decreasing trend. The reason is that the physiological and healthy conditions of the bone samples we cut and the regions of interest we chose for observation are different. The quantification of canaliculi could be affected by the mineralization or some bone diseases.

For the statistical analysis, we listed the calculated coefficients and p-values to show the correlation between pairs of parameters. The good correlation between $Cell.V$ and $Lc.N/BV$ can be explained by the dependency between the division of Voronoi cells to the number of lacunae. Since the total imaged volume in each sample is the same, the average volume of each cell is smaller when including more lacunae. We found that the values of $Lc.S$ was highly related to $Lc.V$ and $Lc.L1$. This is because the ellipsoid is well-defined for the 3D shape of lacunae and the length of the long axis took the major proportion when determining the geometry of the ellipsoid. The correlation between

$Lc.L2/Lc.L3$ and $Lc.SMI$ illustrates that these two parameters function similarly to show the anisotropy of the lacunae. Besides, there were good linear regressions between $Lc.V/Cell.V$ and $Lc.TV/BV$, as well as $Ca.V/Cell.V$ and $Ca.TV/BV$. This proves that the results of our local porosity of lacunae and canaliculi per cell maintain consistent with the porosity for the whole image.

In conclusion, we achieved the quantification and analysis for 8 human femoral bone samples at the voxel size of 120 nm. We used magnified X-ray phase nano-CT for the scan and reconstruction of the samples to offer enough resolution for the observation of the LCN and keep a relative large field of view. For segmentation, we used some classical image filtering methods to keep the efficiency of processing for the large datasets. Also, we calculated a number of 3D quantitative parameters for the density, the porosity and the morphology of the lacunae and canaliculi. After being compared with previous works, we verified the reliability our measurements by checking the consistency. This scale is interesting to obtain detailed information on canaliculi in 3D while keeping a sufficient field of view. We hope that these results will bring reference values on the LCN morphology in 3D and contribute to a better understanding of the mechanisms of bone fragility.

Chapter 6: Quantification of the lacuno-canalicular network at the nanoscale and comparison between different spatial resolutions

This chapter is a research article prepared for submission to a journal.

Contents

6.1 Introduction

Osteocytes, which occupy the largest percentage of bone cells, have attracted the increasing attention of scientists in the past decades. If their role has been undervalued for a long time, various recent works have evidenced its major role in bone remodeling and reparation and even as endocrine cells that could have an impact on many organs [Dallas et al. (2013)]. For example, osteocytes could be regulators of bone resorption by secreting Receptor activator of NFkB ligand (RANKL) [Nakashima et al. (2011)] and play crucial roles in the control of bone formation by producing WNT1 [Rauch (2017)]. Except for the function in bone homeostasis, osteocytes may also contribute to fat metabolism by secreting sclerostin leading to the increase of beige adipogenesis [Fulzele et al. (2017)] and influence hematopoiesis by the adjustment of endosteal microenvironment through the release of soluble factors [Asada et al. (2015)]. After being entrapped in the bone matrix, the mature osteocyte is housed within lacuna and is connected to other osteocytes by cytoplasmic processes hosted within canaliculi channels. The porous network embedding the osteocyte system is called the lacuna-canalicular network (LCN). Through the LCN, the osteocytes can transport nutrients, biochemical signals and hormonal stimuli to achieve information integration and interaction with other bone cells [Bonewald (2011)].

The assessment of the LCN is still difficult due to the deeply embedded location and the complexity of the network. Conventional 2D imaging techniques have been used to investigate the LCN, for instance using light microscopy (LM) [Marotti et al. (1995)], [Qiu et al. (2006)], transmission electron microscope (TEM) [Rubin et al. (2005)], scanning electron microscope (SEM) [Sasaki et al. (2015)], and Atomic force microscopy (AFM) [Katsamenis et al. (2013)]. The lacunae are typically described as flattened ellipsoids with an average area of about 20–70 μm2, an average length about 14–25 μm and an average width about 5–10 μm [Remaggi et al. (1998)], [Ashique et al. (2017)]. Similarly, the canaliculi are described as channels with the average diameter of about 100–600 nm [You et al. (2004)], [Lin et al. (2011)]. However, these parameters have some uncertainty because the slicing direction influences the results with missing the information of the third dimension.

To avoid this problem, various 3D imaging techniques are explored [Schneider et al. (2010)]. Confocal laser scanning microscopy (CLSM) has been used to image the LCN by recording a series of 2D optical slices and then forming the 3D image [Kamioka et al. (2001)], [Genthial et al. (2017)]. Meanwhile, Serial focused ion beam SEM (serial FIB SEM) is another imaging technique to generate 3D reconstructions of the osteocytes by scanning a sequence of 2D images using a focused beam of ions [Schneider et al. (2011)], [Hasegawa et al. (2018)]. Besides, it is possible to image the 3D structures of the LCN with Synchrotron Radiation absorption or phase nano-CT (SR nCT) providing an isotropic spatial resolution and a relatively large field of view [Pacureanu et al. (2012)], [Langer et al. (2012)]. The feasibility of ptychographic X-ray CT with synchrotron radiation was also demonstrated in [Dierolf et al. (2010)] and recently used to visualize the LCN in rats [Ciani et al. (2016)].

After imaging, various 3D parameters have so far been proposed to quantify the LCN. For the lacunae, the computed parameters include the lacunar density and porosity, the lacunar volume and surface, the lacunar length, width and depth, the anisotropy and the angle between their long axis and the longitudinal axis of bone [Mader et al. (2013)], [Carter et al. (2013)], [Dong, Haupert, et al. (2014)], [Bach-Gansmo et al. (2015)]. There are only a few parameters, which have been computed on canaliculi. The first parameter is the canalicular porosity which was reported for instance in rodents [Schneider et al. (2011)], [Gatti et al. 2018] and human [Hesse et al. (2011)]. The 3D diameter of canaliculi has also been reported from SR nCT images [Varga et al. (2015)], [Hesse et al. (2015)]. Another parameter of interest is the number of canaliculi per lacuna [Lai et al. (2015)], [Varga et al. (2015)]. Besides, most of the time, the lacunae and canaliculi were evaluated separately, while they were quantified as a whole network in a recent study [Kollmannsberger et al. (2017)].

Although there is an increasing number of quantitative data in the literature, there are only few data on humans and they are generally limited to a very small number of samples. In addition, these data come from different imaging techniques at different spatial resolution. Since each given modality can generally be used to acquire images at different voxel sizes, the question arises to know which spatial resolution should be used. One straightforward observation is that the higher the spatial resolution is, the smaller the field of view is. But no study has been dedicated to the comparison of the effect of spatial resolution on the quantification of the LCN.

The objective of this work is twofold. First we expect to provide quantitative data on the LCN from images at unequaled isotropic voxels sizes (50 nm and 30 nm), and second we wish to study the impact of spatial resolution on the properties of the LCN assessed in 3D at very high spatial resolution. To this aim, we use X-ray phase nano-CT to scan bone samples at 120 nm, 50 nm and 30nm, and we propose a methodology to quantify and compare the results at the various spatial resolutions. We briefly recall the image analysis techniques used to extract quantitative parameters at 120nm and present the new developments required to handle the images at 30nm. We then propose an image registration approach to compare the quantitative results between the registered cropped images at 120 nm and their corresponding images at 30 nm, in order to check the differences of quantifications at distinct voxel sizes.

6.2 Materials and methods

6.2.1 Sample description

There were 13 samples in total from female donators (aging 56–95 years old) scanned in this study. They were provided by the Centre du Don des Corps (University Paris 5) and the Dept. of Anatomy Rockefeller, University Lyon. All these samples were cut from transverse cross-sections of the femoral diaphysis with the size of 0.4×0.4×4 mm^3 using a water-cooled diamond precision saw (Presi Mecatome T210, Struers Diamond Cut-off Wheel EOD15, Liphy, Grenoble). No additional information regarding disease status or medication history was available following the legal clauses stated in the French Code of Public Health Ethical.

As described in Chapter 6, we denoted the samples by the number #1–#13 according to the increasing order of ages. We divided the images in three groups based on the different voxel sizes 120 nm, 50 nm and 30 nm, denoted by the alphabet letters A, B and C respectively. In this chapter, we show the results for: 9 volumes at 50 nm denoted by B1, B4-1, B4-2, B4-3, B4-4, B5, B7, B10 and B11; 7 volumes at 30 nm denoted by C2, C3, C6, C8, C9, C12, and C13.

6.2.2 Synchrotron radiation nano-CT

Data acquisition was performed using the magnified X-ray phase nano-CT at the beamline ID16A of the ESRF. Experiments were performed during the LTP MD830 at different periods. Each sample was scanned at 4 different propagation distances and for each distance, 2000 projections were recorded over a range of 180° (see Chapter 5). There were two specific energies used for the experiments at ID16A, 17 and 33.6 keV. The total scanning time for one sample at 4 distances was about 4 hours. Tomographic reconstructions were achieved by the standard Filtered Back-Projection (FBP) algorithm [Mirone et al. (2014)]. The voxel sizes of the reconstructed volumes (2048 × 2048 × 2048) were 50 nm and 30 nm, corresponding to the field of view 102.4 µm and 61.44 µm, respectively.

For each sample, we generally performed a scan at 120 nm providing a larger field of view (~ 246 µm) and recorded one or several scans within the first one at 50 nm or 30 nm to zoom in for different volumes of interest (VOIs).

6.2.3 Image processing

6.2.3.1 Segmentation of the LCN

The segmentation of the LCN was divided into two parts as described in Chapter 6. We briefly recall the process.

For the segmentation of lacunae, we first used a median filter to eliminate some speckles which could be canaliculi or noise but their physical size was smaller than lacunae. The filter sizes were 18 voxels for 50 nm and 33 voxels for 30 nm, which were chosen from a previous report of our group [Dong, Haupert, et al. (2014)]. Then a hysteresis thresholding method was applied to segment the lacunae from reconstructed volumes and obtain the binary images. The low threshold was used to achieve a high-confidence segmentation but with less objects, and the high threshold helped to refine the results by checking the voxels in the ambiguous region between two thresholds. The method of selecting the two thresholds has been described in Chapter 5. Finally, we took advantage of connected components analysis to filter out abnormal components with huge size, and they were Haversian canals actually. The thresholds were 16,000,000 voxels for 50 nm and 74,074,074 voxels for 30 nm, i.e. the physical size of 2000 µm^3.

In order to segment canaliculi, we first used a vesselness enhancement method [Sato et al. (1998)] by computing the eigenvalues of the Hessian matrix to improve the visibility of line structures in the images. After this, we used a maximum entropy thresholding method to process the 3D line-filter image and get the binary seed map of canaliculi. Next, we applied a variational region growing (VRG) algorithm [Pacureanu et al. (2010)] which was based on an energy functional combining gray level information from the original image and shape information from the 3D line-filter image to segment canaliculi. Finally, we used a connected components analysis to filter out residual noise. The thresholds were 150 voxels for 50 nm and 250 voxels for 30 nm based on the previous work of our group [Pacureanu (2012)].

6.2.3.2 Image Registration

Image registration is usually used in the analysis and fusion of images acquired on different devices. In our case, to compare the quantification between different voxel sizes, we need to register the images at the voxel size of 30 nm with those of 120 nm from the same samples (see Fig. 6.1). Due to the acquisition protocol at different voxel sizes, we know that the samples did not rotate but were just translated to different positions in the three dimensions, x, y and z. Therefore, the registration process is simplified and we selected a phase correlation method (PCM) to address it.

For a given sample, let us denote $I_1(\mathbf{x})$ and $I_2(\mathbf{x})$ the reconstructed images at the voxel sizes of 120 nm and 30 nm respectively, where $\mathbf{x} = (x, y, z)$ are the 3D coordinates. First, we downsampled the original image (2048 × 2048 × 2048) at the voxel size of 30 nm twice to reach the voxel size 120 nm, yielding an image (512 × 512 × 512) denoted by $I_{2_D}(\mathbf{x})$. Then, we padded this downsampling image with the zeros to the same size of that at 120 nm, 2048 × 2048 × 2048, denoted by $I_{2_{DP}}(\mathbf{x})$. The result of the phase correlation $p(\mathbf{x})$ can be written as follows [Foroosh et al. (2002)]:

$$p(\mathbf{x}) = \mathcal{F}^{-1}\left[\frac{\tilde{I}^*_{2_{DP}}(\mathbf{f})\tilde{I}_1(\mathbf{f})}{\left|\tilde{I}^*_{2_{DP}}(\mathbf{f})\tilde{I}_1(\mathbf{f})\right|}\right], \tag{6.1}$$

where $\tilde{I}_1(\mathbf{f})$ is the 3D Fourier transform of $I_1(\mathbf{x})$, $\tilde{I}^*_{2_{DP}}(\mathbf{f})$ the complex conjugate of the Fourier transform of $I_{2_{DP}}(\mathbf{x})$ and $\mathcal{F}^{-1}$ the inverse 3D Fourier transform.

By finding the peak intensity of $p(\mathbf{x})$, we can calculate the translation offsets along the three axes. Using these offsets, we cut a small volume from the image $I_1(\mathbf{x})$ with the size of 512 × 512 × 512. The cropped result was denoted by $I_{2_{PCM}}(\mathbf{x})$ which corresponded to the same region with $I_2(\mathbf{x})$ in the sample and had the same field of view 61.44 µm.

By applying this process to 7 volumes at the voxel size of 120 nm, we obtained 7 cropped volumes corresponding to those at 30 nm, denoted by P2, P3, P6, P8, P9, P12, and P13. We called these cropped results "the PCM images" denoted by "P".

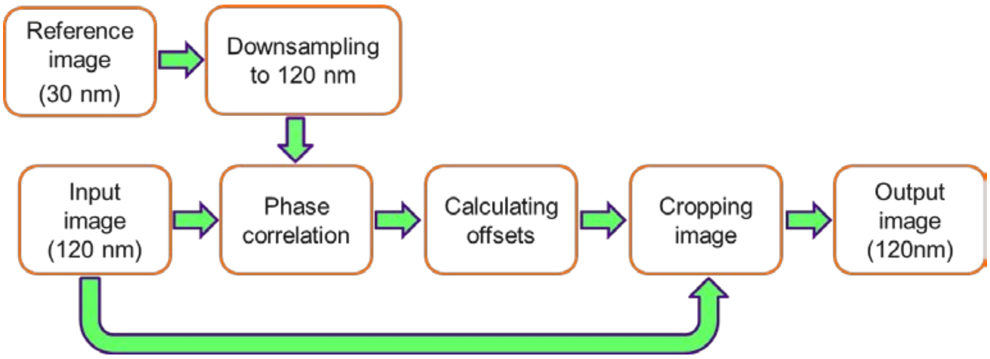

Figure 6.1 Sketch of the image registration using the phase correlation method.

6.2.4 Quantitative analysis

After segmentation, we calculated the same quantitative parameters of the lacunae and canaliculi for the reconstructions at the voxel sizes of 50 nm and 30 nm, as well as the cropped results of the phase correlation method.

6.2.4.1 Quantification of lacunae

For the quantification of lacunae, we first computed the number of lacunae ($Lc.N$), the total volume of lacunae ($Lc.TV$), the bone volume (BV), the density of lacunae ($Lc.N/BV$) and the lacunar porosity ($Lc.TV/BV$). Then, based on the labeled images of lacunae and 3D Voronoi tessellation which divided the images into different cells and each cell contained only one lacuna, we obtained the average volume of one lacuna ($Lc.V$), the average volume of each cell ($Cell.V$) and the local lacunar porosity ($Lc.V/Cell.V$). Different from the case at the voxel size of 120 nm, each Voronoi cell contains more voxels at 30 nm. This means that it will take longer time to achieve the tessellation. To solve this problem, we tried first to downsample the initial binary volumes of lacunae at 30 nm, and then to divide the Voronoi cells, and finally to upsample the volumes to the original size (see Fig. 6.2).

Moreover, we calculated some morphological descriptors of each lacuna by regarding it as an ellipsoid through the second-order central moments [Flusser et al. (2009)], such as the length, width and depth of lacuna ($Lc.L_1$, $Lc.L_2$, and $Lc.L_3$), as well as the anisotropy of lacuna detected by the ratios between different axes ($Lc.L_1/Lc.L_2$ and $Lc.L_2/Lc.L_3$). Besides, according to Ohser's method [Ohser et al. (2009)], we got the average surface area of lacuna ($Lc.S$) and the structure model index of lacuna ($Lc.SMI$).

Figure 6.2 Sketch of the image resampling and Voronoi tessellation.

6.2.4.2 Quantification of canaliculi

The quantification of canaliculi was similar with the case of lacunae. First, we calculated the total volume of canaliculi ($Ca.TV$), the porosity of canaliculi ($Ca.TV/BV$), the average volume of canaliculi per cell ($Ca.V$), the local porosity of canaliculi ($Ca.V/Cell.V$) and the ratio between the average volume of canaliculi and lacunae per cell ($Ca.V/Lc.V$). Then, we computed the total volume of the LCN ($LCN.TV$) and the porosity of the LCN ($LCN.TV/BV$) for the evaluation of the whole network. Moreover, to quantify the ramification of canaliculi, we calculated the number of canaliculi per lacuna at different distances from the surface of the lacuna ($Ca.N(r)$, where r is the distance) [Dong, Pacureanu, et al. (2014)]. As described in Chapter 6, we calculated the number of canaliculi based on the number of holes on the bounding surface. In the original process, this surface was generated by the dilation of the surface of the segmented lacuna. However, the surface of lacuna at 30 nm contains too many voxels so the 3D dilation becomes very time-consuming. Here, we propose another way to obtain the bounding surface based on the equation of the ellipsoid. Generally, an ellipsoid after rotation can be expressed by a matrix equation:

$$(\mathbf{x}-\mathbf{c})^T\mathbf{R}^T\mathbf{A}\mathbf{R}(\mathbf{x}-\mathbf{c}) = 1, \tag{6.2}$$

where $\mathbf{x} = (x, y, z)$ denotes the coordinates of the ellipsoid points, $\mathbf{c} = (xc, yc, zc)$ the center of the ellipsoid, **A** a square, symmetric matrix and **R** the rotation matrix.

In our case, **A** is a diagonal matrix which can be written as:

$$\mathbf{A} = \begin{pmatrix} 1/(L_1/2+r)^2 & 0 & 0 \\ 0 & 1/(L_2/2+r)^2 & 0 \\ 0 & 0 & 1/(L_3/2+r)^2 \end{pmatrix}, \tag{6.3}$$

where L_1, L_2, L_3 are the length, width and depth of the ellipsoid, and r the distance from the surface of lacuna.

In Chapter 6, we computed three eigenvalues of the second-order central moment matrix to estimate the length, width and depth of the ellipsoid. Meanwhile, we got three eigenvectors corresponding to different eigenvalues. Actually, each column vector of the rotation matrix **R** is composed of one eigenvector of the second-order central moment matrix. Therefore, we obtained the bounding surface by finding the points on the surface of the ellipsoid.

In addition, we computed the ratio between the number of canaliculi per lacuna and the average volume of lacuna located in the same cell ($Ca.N/Lc.V$) in order to quantify the density of canaliculi.

6.2.5 Statistics analysis

We used the software Statview® (SAS Institute Inc., Cary, NC, USA) for the statistics analysis. For parameters calculated from the volumes at 30 nm and the PCM ones, the Kolmogorov-Smirnov (K-S) test was used to assess the normality and F-test to determine the homogeneity of variances. If these conditions were verified, the paired t-test was used to test the difference between these two groups. If not, the results were statistically tested by the Wilcoxon signed rank test. Besides, we used the Spearman correlation coefficient (R^2) and the p-value by the Fisher's r to z transformation to evaluate correlations between the measured parameters. Results with p-values under 0.05 were considered as significant.

6.3 Results

6.3.1 Image Processing

6.3.1.1 Image Registration

To illustrate the results of image registration, Fig. 6.3 (a) and (c) show slices from the original input images with the size of 2048 × 2048 × 2048 voxels at 120 nm and 30 nm, respectively. Fig. 6.3 (b) presents the position where we cropped the slice from the input image at 120 nm. Based on the Fig. 6.3 (b), we crop the Fig. 6.3 (d) at 120 nm with the size of 512 × 512 × 512 voxels, which is the output of the image registration and called the "PCM" image. Compared Fig. 6.3 (d) with (c), we can see that the phase correlation method can find the basically accurate position of the region of interest (ROI) in the image at 120 nm, corresponding to that in the image at 30 nm.

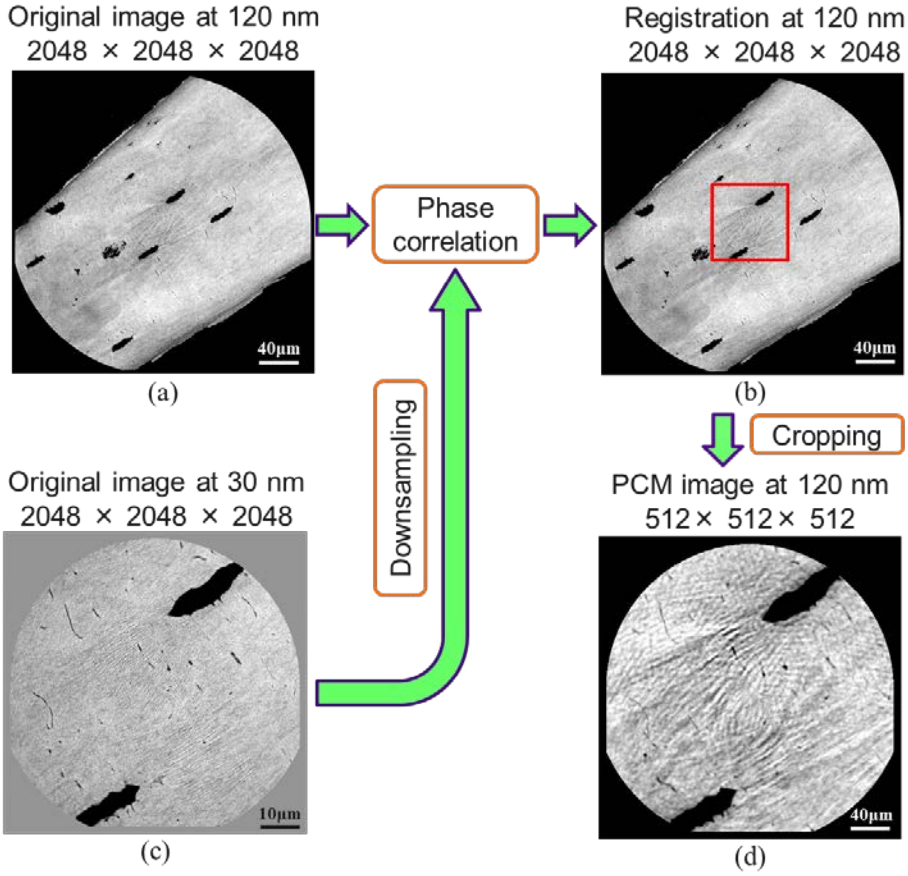

Figure 6.3 Slices of image registration using the phase correlation method. (a) One slice from the original image at 120 nm with the size of 2048 × 2048 × 2048 voxels; (b) The same slice as (a) showing the cropping position after registration; (c) One slice from the original image at 30 nm with the size of 2048 × 2048 × 2048 voxels; (d) One slice from the PCM image at 120 nm with the size of 512 × 512 × 512 voxels.

6.3.1.2 Downsampling for tessellation

Figure 6.4 gives the results when we used two different methods to calculate the Voronoi image. Fig. 6.4 (a) shows the original slice of the segmentation of lacunae at 30 nm and (c) is the downsampled image of (a) at 60 nm; (b) and (d) display the slices from the tessellation images corresponding to (a) and (c); (e) is the difference image between (b) and (d). From the results, it can be seen that there are only few differences in the border region between Voronoi cells. We recorded the running time of two methods on the work station "jupiteros3" (Intel(R) Xeon(R) CPU E5-2697 v2 @

2.70GHz, 48 CPUs in total). If we calculated the tessellation from the original image at 30 nm, it took 6904 secs; if we used downsampling, tessellation and Upsampling, it took 1041 secs. Therefore, the use of resampling and tessellation can divide the binary image into Voronoi cells keeping accuracy and saving running time. However, we did not use this method in our case but it should be a better choice if we need to process similar large datasets in future.

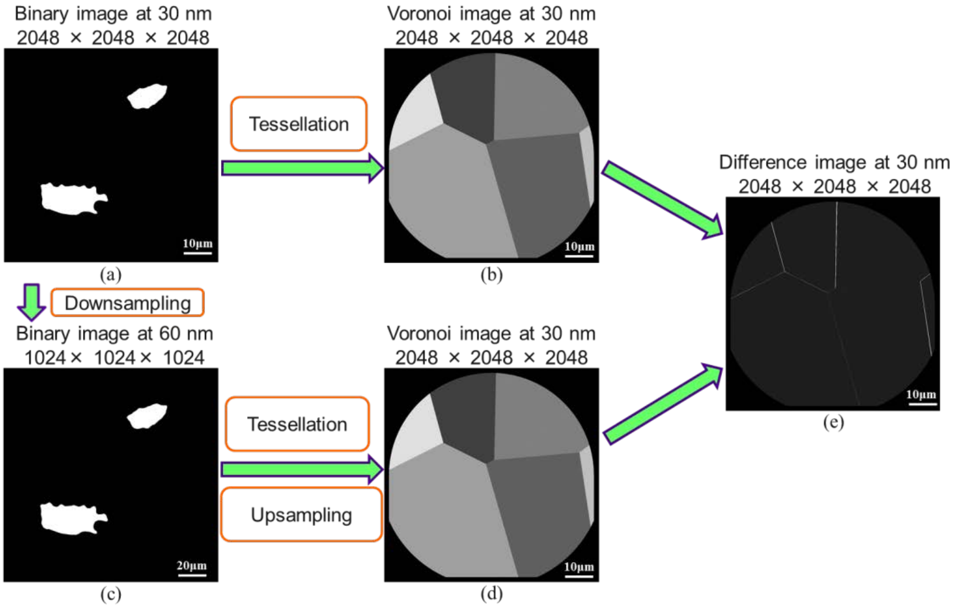

Figure 6.4 Slices of image resampling and Voronoi tessellation. (a) One slice from the original binary image at 30 nm with the size of 2048 × 2048 × 2048 voxels; (b) One slice from the image after tessellation at 30 nm with the size of 2048 × 2048 × 2048 voxels; (c) One slice from the binary image after downsampling at 60 nm with the size of 1024 × 1024 × 1024 voxels; (d) One slice from the image after tessellation and upsampling to 30 nm with the size of 2048 × 2048 × 2048 voxels; (e) One slice from difference image between (b) and (d) at 30 nm with the size of 2048 × 2048 × 2048 voxels.

6.3.1.3 Ellipsoid for counting canaliculi

Figure 6.5 shows the slice of one segmented lacuna and the bounding surface calculated by the dilation or solving the equation of the ellipsoid. Similarly, we also recorded the running time of two methods on the work station "jupiteros3". Generating the bounding surface at the distance 1.2 µm (40 voxels at 30 nm) from the original surface of lacuna, it took 17008 secs to perform the 3D dilation while only cost 182 secs to solve the equation of the ellipsoid. Therefore, although the bounding surface from the ellipsoid is not totally the same as that from the dilation, it could save a lot of time on image processing. To cope with our large datasets, we finally used the equation of the ellipsoid to count the number of canaliculi in our reconstructions.

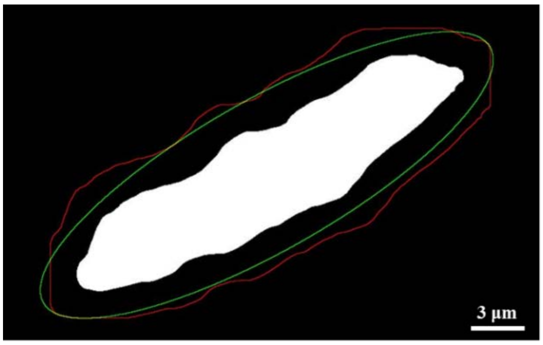

Figure 6.5 Slice of one lacuna and the bounding surface of two methods.

6.3.1.4 3D rendering

In Fig. 6.6 (a), (c) and (e), we show the MIPs along the Y-axis of all the slices from the reconstructed volumes of the samples B4-1 at 50 nm, C2 at 30 nm and P2 cropped at 120 nm. And the 3D displays of the segmented lacunae and canaliculi rendered by VGStudioMax® are also given in Fig. 6.6 (b), (d) and (e), respectively. If we check the difference between Fig. 6.6 (c) and (e), (d) and (f), it can be seen that for the same VOI, we have a better observation and segmentation of canaliculi at the voxel size of 30 nm compared with that cropped at 120 nm.

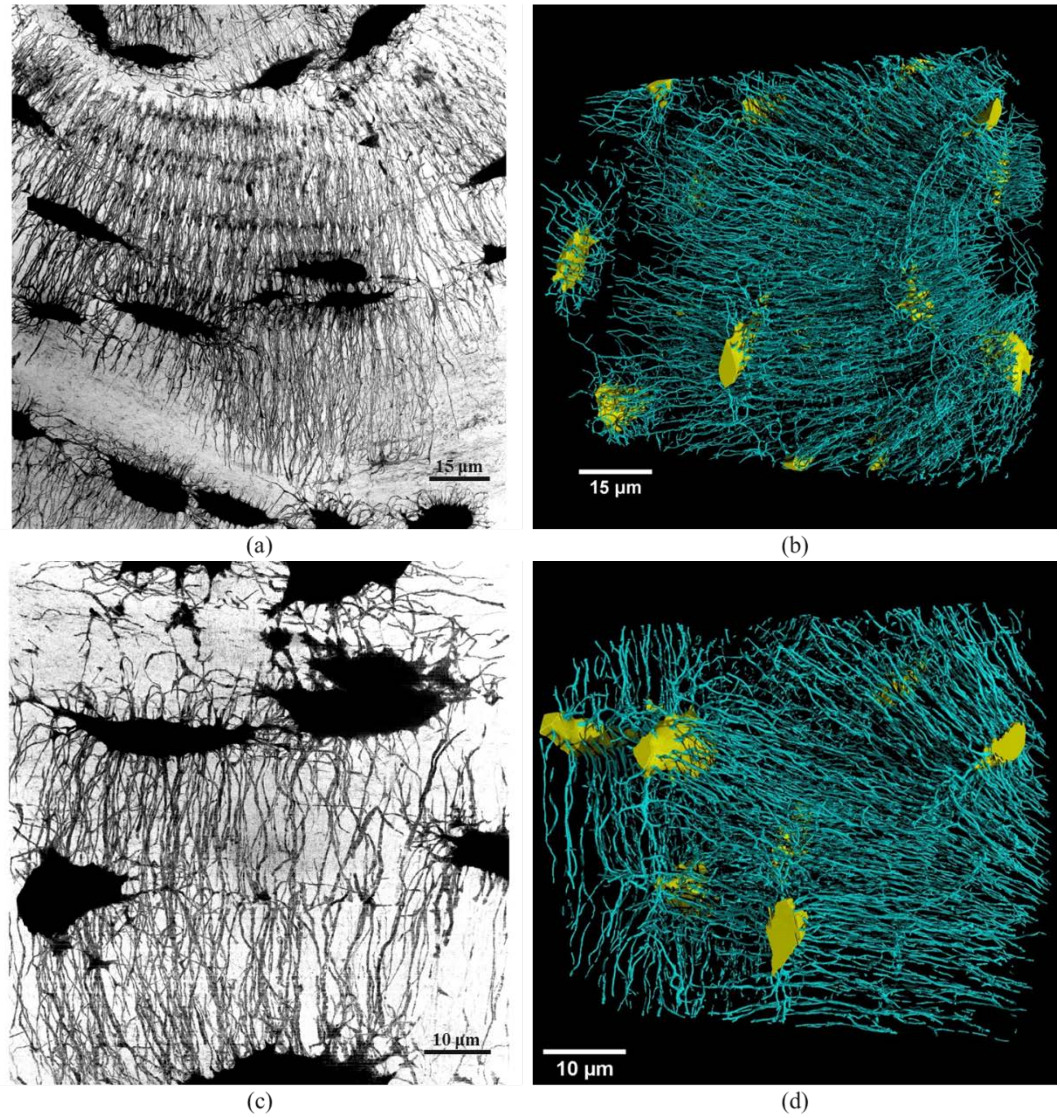

(a) (b)

(c) (d)

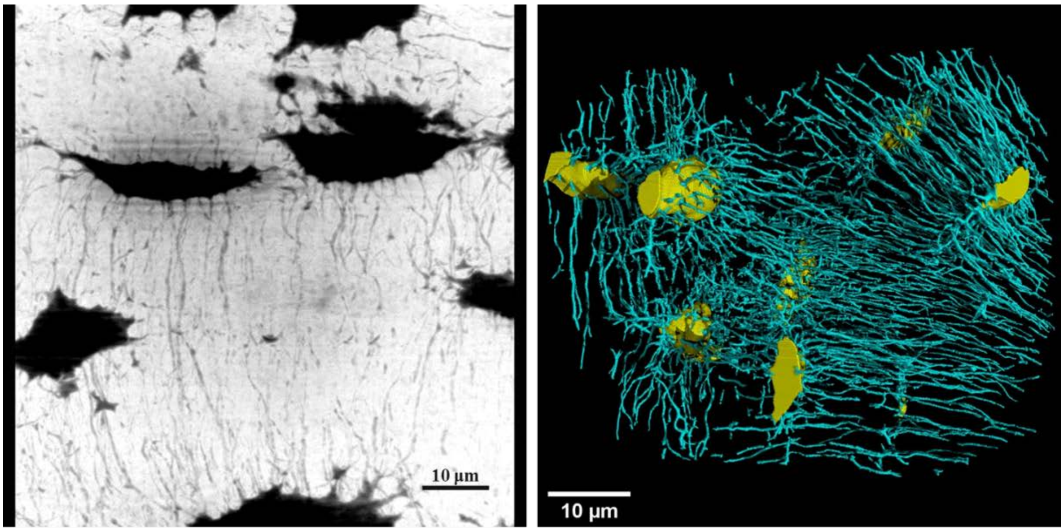

(e) (f)

Figure 6.6 Segmentation results for the volumes B4-1 at 50 nm, C2 at 30nm and P2 cropped at 120 nm. (a), (c) and (e) MIPs along the Y-axis of all the slices from the reconstructed volumes B4-1, C2 and P2; (b), (d) and (f) 3D rendering of the segmented lacunae and canaliculi corresponding to (a), (c) and (e).

6.3.2 Quantification of 50 nm

6.3.2.1 Morphometric parameters of lacunae

There are 9 reconstructed volumes from 6 samples scanned at the voxel size of 50 nm. Table 6.1 presents quantitative parameters of lacunae for these samples. The average number of lacunae is 20.8 and the average total volume of lacunae is 0.70×10^{-5} mm^3. The average bone volume is 0.80×10^{-3} mm^3 with the average lacunar porosity 0.88 and the average density of lacunae 2.6×10^4 mm^{-3}. The average volume of each lacuna is 338.1 μm^3 and the average surface area is 376.4 μm^2. The average volume of each cell is 3.4×10^4 μm^3 and the ratio between the average volume of each lacuna and its belonging cell is 1.14%. The average length, width and depth of each lacuna are 18.7 µm, 9.1 µm and 4.5 µm, respectively. To describe the flatness of the lacunae, we calculated the ratio between the length and the width 2.1, the ratio between the width and the depth 2.2 and the structural model index 3.1.

Figure 6.7 shows some parameters of the morphology of lacuna for different samples at the voxel size of 50 nm, such as the average length, width and depth, as well as the descriptors of the flatness ($Lc.L1/Lc.L2$, $Lc.L1/Lc.L2$ and $Lc.SMI$).

Table 6.1 Morphometric parameters of lacunae at the voxel size of 50 nm

Sample ID	Lc.N	Lc.TV (×10^{-5} mm^3)	BV (×10^{-3} mm^3)	Lc.TV/BV (%)	Lc.N/BV (×10^4 mm^{-3})	Lc.V (μm^3)	Cell.V (×10^4 μm^3)	Lc.V/Cell.V (%)
B1	16	0.55	0.78	0.70	2	341.4±77.9	4.4±1.5	0.85±0.27
B4-1	14	0.55	0.81	0.69	1.7	395.8±174.8	4.9±1.6	0.87±0.43
B4-2	21	0.70	0.70	0.99	3	332.1±103.9	2.7±0.9	1.33±0.56
B4-3	25	0.77	0.84	0.91	3	306.5±91.0	3.1±1.1	1.09±0.57
B4-4	26	0.78	0.82	0.95	3.2	299.5±151.8	2.7±1.2	1.32±0.90
B5	20	0.59	0.81	0.74	2.5	297.0±94.3	3.5±1.6	0.97±0.38
B7	18	0.9	0.82	1.10	2.2	501.4±301.0	4.3±1.8	1.25±0.65
B10	22	0.63	0.83	0.76	2.7	284.6±86.0	3.5±0.9	0.84±0.28
B11	25	0.86	0.82	1.04	3	342.7±140.3	2.7±1.2	1.47±0.78
Mean All	20.8	0.70	0.80	0.88	2.6	338.1	3.4	1.14
Std. All	4	0.12	0.04	0.15	0.5	155.6	1.5	0.63

Sample ID	Lc.S (μm^2)	Lc.L1 (μm)	Lc.L2 (μm)	Lc.L3 (μm)	Lc.L1 /Lc.L2	Lc.L2 /Lc.L3	Lc.SMI
B1	407.2±121.2	20.7±6.0	8.8±1.4	4.5±1.0	2.4±0.9	2.1±0.6	3.0±0.4
B4-1	433.7±138.9	19.6±5.3	10.7±2.4	4.2±1.0	1.9±0.7	2.6±0.7	3.1±0.4
B4-2	356.4±83.0	18.0±4.7	9.1±1.6	4.6±1.0	2.1±0.8	2.1±0.7	3.2±0.3
B4-3	391.2±107.8	20.6±4.8	8.5±1.6	4.0±0.8	2.5±0.8	2.3±0.7	2.8±0.4
B4-4	341.2±138.6	17.8±5.6	8.6±2.0	4.6±1.2	2.2±0.9	2.0±0.6	3.1±0.3
B5	349.4±89.0	18.5±4.6	9.4±1.7	3.8±0.6	2.0±0.6	2.6±0.7	2.8±0.3
B7	514.7±267.5	21.8±7.8	11.3±3.4	4.5±1.2	2.0±0.8	2.7±1.0	2.9±0.4
B10	304.1±67.4	16.2±4.1	8.6±1.6	4.6±1.0	2.0±0.8	2.0±0.7	3.3±0.4
B11	348.9±115.5	16.4±4.9	8.4±1.6	5.7±1.2	2.0±0.6	1.5±0.4	3.5±0.3
Mean All	376.4	18.7	9.1	4.5	2.1	2.2	3.1
Std. All	142	5.5	2.1	1.1	0.8	0.7	0.4

Lc.N – number of lacunae
Lc.TV – total volume of lacunae (mm^3)
BV – bone volume (mm^3)
Lc.TV/BV – lacunar porosity (%)
Lc.N/BV – density of lacunae (mm^{-3})
Lc.V – average volume of lacuna (μm^3)
Cell.V – average volume of each cell (μm^3)
Lc.V/Cell.V – ratio between the average volume of lacuna and its belonging cell (%)
Lc.S – average surface area of lacuna (μm^2)
Lc.L1, Lc.L2 and Lc.L3 – average length, width and depth of lacuna (μm)
Lc.L1/Lc.L2 and Lc.L2/Lc.L3 – average anisotropy of lacuna
Lc.SMI – average structural model index of lacuna

6.3.2.2 Morphometric parameters of canaliculi

Table 6.2 shows the morphometric parameters of canaliculi. It can be seen that the average total volume of canaliculi is 0.29×10^{-5} mm^3 and the average porosity of canaliculi is 0.37%. The average volume of canaliculi per cell is 141.4 μm^3 with the ratio of 0.43% between the average volume of canaliculi per cell and its belonging cell. Also, the average ratio between the volume of canaliculi and the lacuna in the same cell is 46.4%. The average total volume of the LCN is 1.00×10^{-5} mm^3 and the average porosity of the LCN is 1.24%.

Figure 6.8 presents the average porosity of lacunae and canaliculi within their belonging cells for different samples at the voxel size of 50 nm. We show the average volume of lacuna, canaliculi and the cell, as well as the ratios between these values of volumes ($Lc.V/Cell.V$, $Ca.V/Cell.V$ and $Ca.V/Lc.V$).

Table 6.3 and Figure 6.9 display the quantitative results of the ramification of canaliculi. At the same 7 distances from the surface of lacuna with those for the data of 120 nm, the average number of canaliculi per lacuna is 72.7, 85.3, 88.3, 89.0, 91.7, 96.5 and 107.3. The corresponding ratio between the number of canaliculi per lacuna and the volume of lacuna in the same cell is 0.23 μm^{-3}, 0.27 μm^{-3}, 0.28 μm^{-3}, 0.29 μm^{-3}, 0.30 μm^{-3}, 0.32 μm^{-3} and 0.36 μm^{-3}, respectively.

Table 6.2 Morphometric parameters of canaliculi at the voxel size of 50 nm

Sample ID	Ca.TV (10^{-5} mm^3)	LCN.TV (10^{-5} mm^3)	Ca.TV/BV (%)	LCN.TV/BV (%)	Ca.V (μm^3)	Ca.V/Cell.V (%)	Ca.V/Lc.V (%)
B1	0.31	0.86	0.40	1.10	194.9±60.2	0.46±0.13	58.0±17.2
B4-1	0.40	0.95	0.49	1.18	282.6±144.0	0.56±0.17	83.3±52.9
B4-2	0.26	0.96	0.37	1.37	124.4±62.5	0.49±0.20	42.2±27.1
B4-3	0.23	1.00	0.28	1.19	94.0±59.9	0.31±0.17	31.8±19.7
B4-4	0.32	1.10	0.39	1.35	122.7±66.1	0.48±0.19	46.9±25.0
B5	0.31	0.90	0.38	1.12	152.7±70.4	0.46±0.11	52.5±17.4
B7	0.27	1.18	0.33	1.43	152.6±64.6	0.38±0.12	36.0±16.0
B10	0.32	0.95	0.39	1.15	145.7±50.9	0.41±0.11	57.7±36.5
B11	0.22	1.08	0.27	1.31	88.5±41.6	0.35±0.14	28.4±13.1

Mean All	0.29	1.00	0.37	1.24	141.4	0.43	46.4
Std. All	0.05	0.1	0.06	0.11	84.5	0.17	29.6

Ca.TV – total volume of canaliculi (mm^3)
LCN.TV – total volume of the LCN (mm^3)
Ca.TV/BV – the porosity of canaliculi (%)
LCN.TV/BV – the porosity of the LCN (%)
Ca.V – average volume of canaliculi per cell (μm^3)
Ca.V/Cell.V – ratio between the average volume of canaliculi and the average volume of cell
Ca.V/Lc.V – ratio between the average volume of canaliculi and the average volume of lacuna

Table 6.3 Number of canaliculi per lacuna at 7 different distances from the surface of the lacuna and the ratio between the number and the average volume of lacuna at the voxel size of 50 nm

Sample ID	Ca.N (r=1.2 μm)	Ca.N (r=3.0 μm)	Ca.N (r=4.8 μm)	Ca.N (r=6.6 μm)	Ca.N (r=8.4 μm)	Ca.N (r=10.2 μm)	Ca.N (r=12.0 μm)
B1	81.7±20.3	96.4±24.8	102.4±24.1	110.8±25.3	120.6±28.7	130.0±28.9	140.3±33.7
B4-1	84.8±36.2	112.6±42.5	110.4±43.7	110.1±52.2	117.4±58.7	117.2±63.4	127.5±73.8
B4-2	69.3±25.4	81.4±32.5	86.1±33.7	85.1±37.4	86.4±43.6	90.5±48.9	106.5±56.4
B4-3	54.4±30.1	65.8±36.0	70.4±38.2	73.4±43.3	72.9±44.1	75.9±44.1	84.3±52.1
B4-4	74.4±38.5	89.0±43.8	93.7±43.1	91.0±40.9	96.2±46.9	106.8±48.9	122.1±54.2
B5	79.2±30.8	88.2±32.0	91.7±30.6	95.9±34.0	102.4±39.7	111.1±50.7	126.8±56.9
B7	108.1±59.0	114.8±57.4	106.0±45.3	97.8±52.7	92.8±51.5	90.9±49.5	97.7±53.8
B10	64.5±17.9	76.5±25.1	87.8±32.0	98.4±39.4	101.0±49.2	101.1±49.8	111.0±57.5
B11	56.5±28.1	65.9±31.9	65.9±35.2	60.2±30.4	59.8±32.6	66.6±34.3	71.2±38.4
Mean All	72.7	85.3	88.3	89	91.7	96.5	107.3
Std. All	36	39.9	38.7	42.1	47	49.5	56.3

Sample ID	Ca.N/Lc.V (μm^{-3}, r=1.2 μm)	Ca.N/Lc.V (μm^{-3}, r=3.0 μm)	Ca.N/Lc.V (μm^{-3}, r=4.8 μm)	Ca.N/Lc.V (μm^{-3}, r=6.6 μm)	Ca.N/Lc.V (μm^{-3}, r=8.4 μm)	Ca.N/Lc.V (μm^{-3}, r=10.2 μm)	Ca.N/Lc.V (μm^{-3}, r=12.0 μm)
B1	0.25±0.10	0.30±0.10	0.31±0.07	0.34±0.08	0.36±0.08	0.39±0.07	0.42±0.08
B4-1	0.22±0.05	0.30±0.09	0.30±0.11	0.31±0.15	0.34±0.19	0.34±0.21	0.38±0.25
B4-2	0.22±0.07	0.26±0.09	0.28±0.10	0.29±0.15	0.28±0.15	0.31±0.20	0.36±0.21
B4-3	0.17±0.08	0.21±0.10	0.23±0.11	0.24±0.14	0.24±0.14	0.26±0.15	0.29±0.20
B4-4	0.26±0.09	0.32±0.15	0.34±0.13	0.33±0.11	0.35±0.14	0.40±0.16	0.46±0.20
B5	0.27±0.09	0.30±0.07	0.32±0.08	0.34±0.11	0.36±0.12	0.39±0.14	0.45±0.21
B7	0.23±0.06	0.26±0.10	0.25±0.13	0.22±0.11	0.21±0.12	0.21±0.13	0.22±0.13
B10	0.24±0.07	0.28±0.07	0.32±0.09	0.37±0.17	0.37±0.19	0.37±0.19	0.41±0.23
B11	0.17±0.08	0.20±0.08	0.19±0.08	0.18±0.07	0.18±0.08	0.20±0.09	0.22±0.11
Mean All	0.23	0.27	0.28	0.29	0.3	0.32	0.36
Std. All	0.09	0.1	0.11	0.14	0.15	0.17	0.21

Ca.N – number of canaliculi per lacuna
Ca.N/Lc.V – ratio between the number of canaliculi per lacuna and the average volume of lacuna

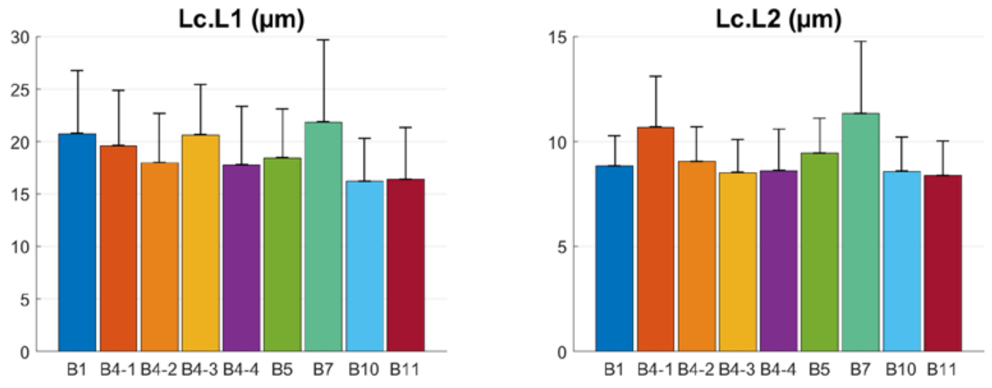

(a) (b)

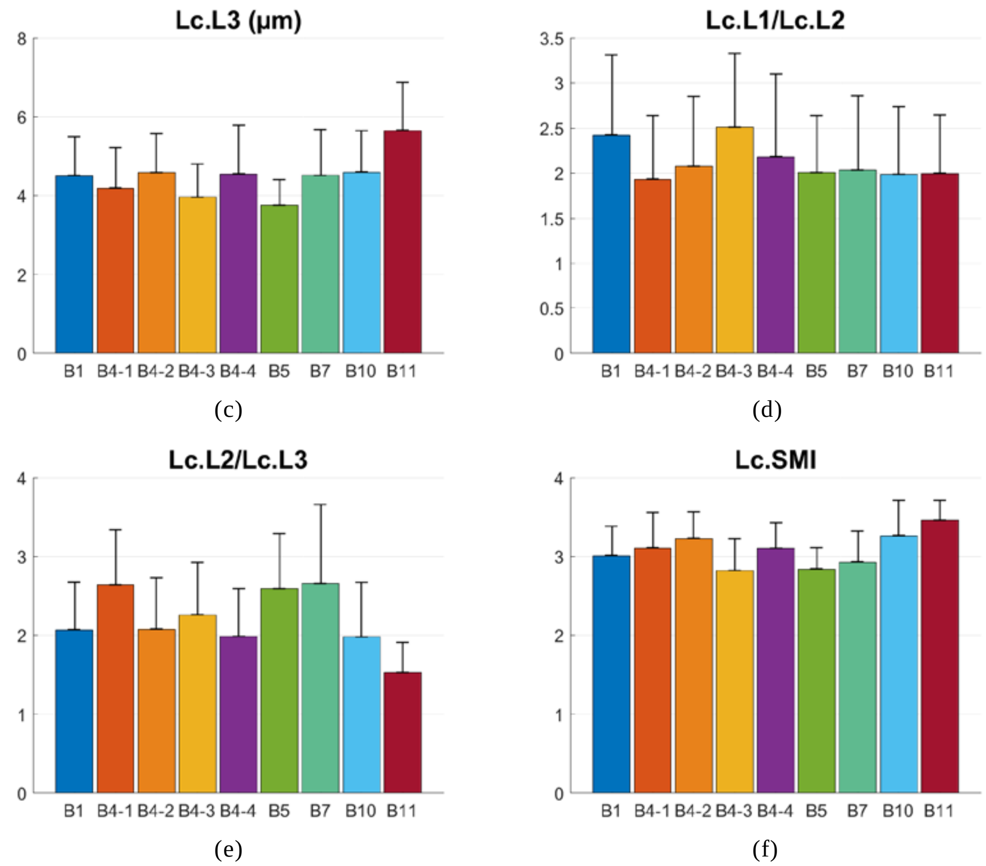

(c) (d)

(e) (f)

Figure 6.7 Some descriptors for the morphology of lacuna at the voxel size of 50 nm.

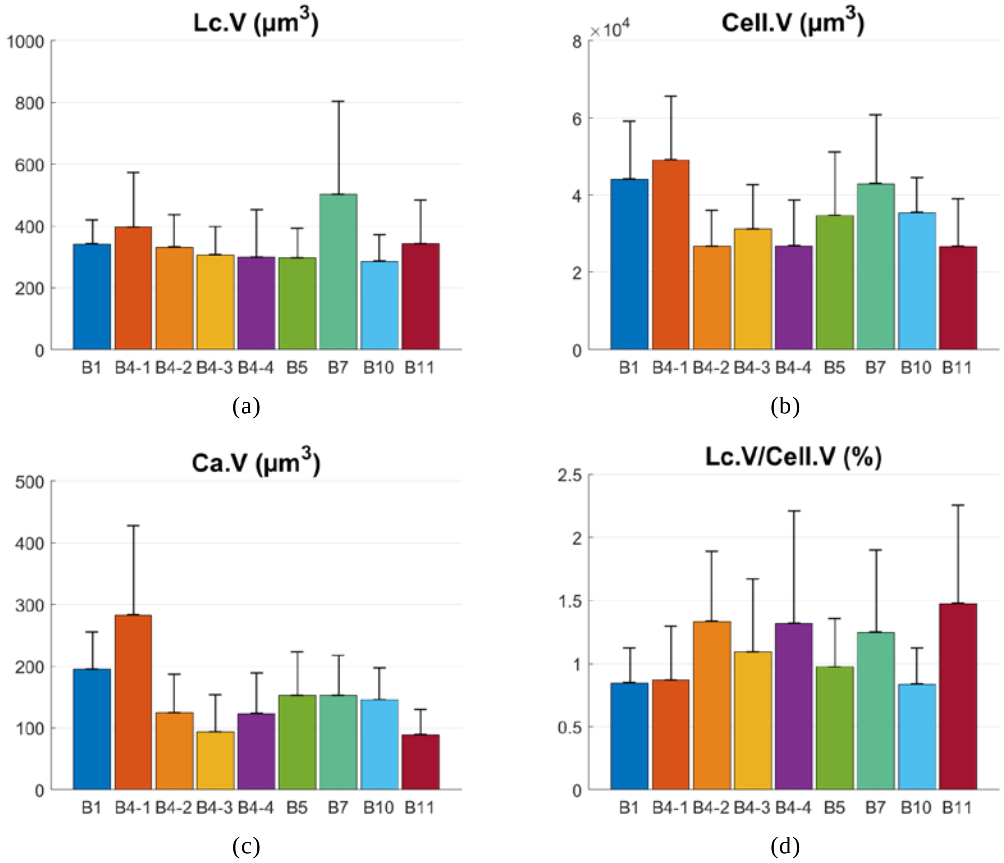

(a) (b)

(c) (d)

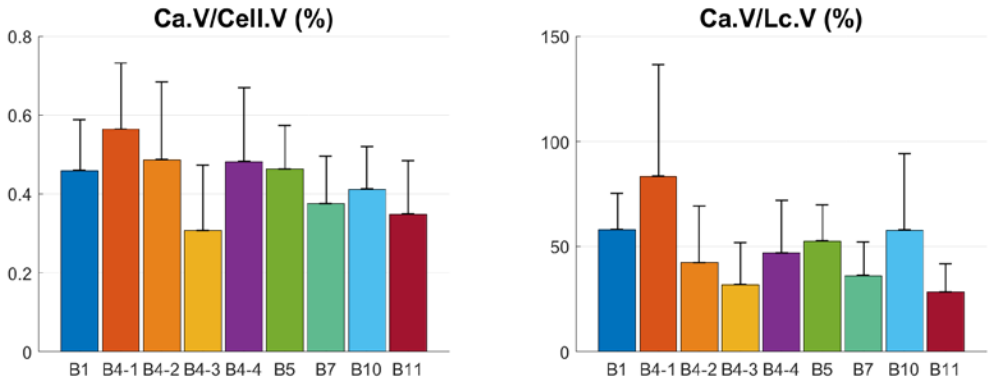

(e) (f)

Figure 6.8 Average porosity of lacunae and canaliculi within different cells at the voxel size of 50 nm.

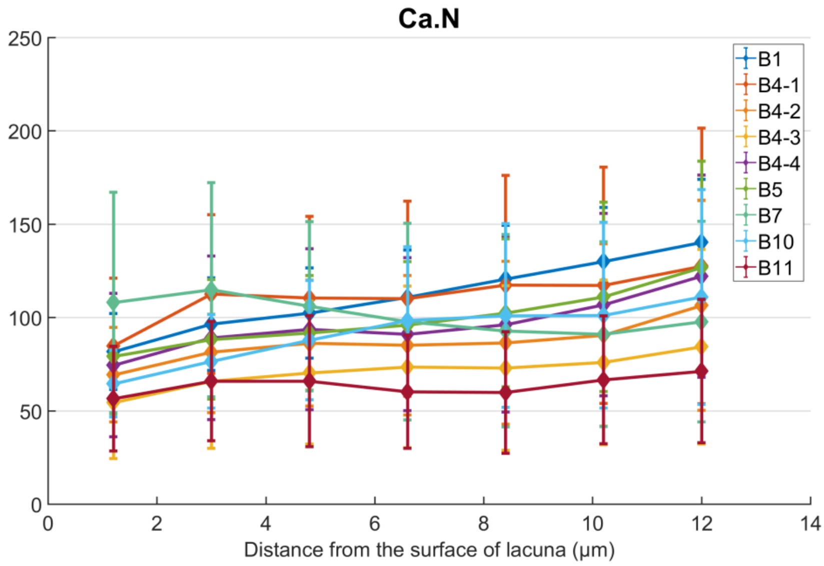

(a)

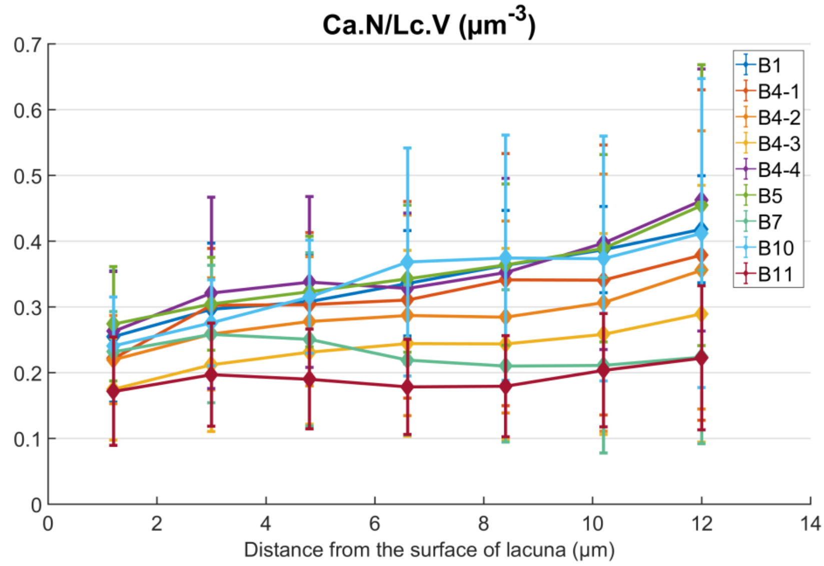

(b)

Figure 6.9 Number of canaliculi per lacuna at 7 distances from the surface of lacuna and the ratio between the number of canaliculi and the average volume of lacuna at the voxel size of 50 nm.

6.3.3 Comparison between 30 nm and 120 nm

6.3.3.1 Quantification of 30 nm

6.3.3.1.1 Morphometric parameters of lacunae

The quantification was performed on 7 samples at the voxel size of 30 nm. Table 6.4 reports the morphometric parameters of lacunae for all samples. The average number of lacuna is 5.3 and the average total volume of lacunae is 0.18×10^{-5} mm^3. The average bone volume is 0.17×10^{-3} mm3 with the average lacunar porosity 1.10% and the average density of lacunae 3.2×10^{4} mm^{-3}. The average volume of each lacuna is 343.3 μm^3 and the average surface area is 360.8 μm^2. The average volume of each cell is 2.4×10^{4} μm^3 and the ratio between the average volume of each lacuna and its belonging cell is 1.73%. The average length, width and depth of each lacuna are 16.9 μm, 9.2 μm and 4.9 μm, respectively. To describe the flatness of the lacunae, we calculated the ratio between the length and the width 1.9, the ratio between the width and the depth 2.0 and the structural model index 3.1.

Table 6.4 Morphometric parameters of lacunae at the voxel size of 30 nm

Sample ID	Lc.N	Lc.TV ($\times10^{-5}$ mm^3)	BV ($\times10^{-3}$ mm^3)	Lc.TV/BV (%)	Lc.N/BV ($\times10^{4}$ mm^{-3})	Lc.V (μm^3)	Cell.V ($\times10^{4}$ μm^3)	Lc.V/Cell.V (%)
C2	7	0.19	0.18	1.10	4	276.5±129.7	2.2±1.1	1.32±1.13
C3	7	0.19	0.18	1.08	4	269.9±122.6	2.3±1.1	1.20±0.37
C6	3	0.11	0.18	0.62	1.7	371.3±180.0	3.1±1.9	1.41±0.84
C8	3	0.1	0.13	0.77	2.2	343.1±25.3	3.5±1.7	1.10±0.40
C9	8	0.34	0.16	2.10	4.9	426.0±206.9	1.6±0.6	2.61±0.83
C12	4	0.17	0.18	0.91	2.2	415.1±216.4	3.0±1.9	1.56±0.82
C13	5	0.17	0.15	1.13	3.4	332.7±202.1	2.6±0.6	1.35±0.90
Mean All	5.3	0.18	0.17	1.10	3.2	343.3	2.4	1.73
Std. All	1.9	0.07	0.02	0.45	1.1	167.3	1.2	1.19

Sample ID	Lc.S (μm^2)	Lc.L1 (μm)	Lc.L2 (μm)	Lc.L3 (μm)	Lc.L1 /Lc.L2	Lc.L2 /Lc.L3	Lc.SMI
C2	345.9±93.1	18.0±4.3	8.1±2.2	4.3±1.0	2.4±0.9	1.9±0.6	3.1±0.5
C3	279.2±102.1	13.9±3.5	8.6±2.3	4.7±1.0	1.7±0.5	1.9±0.6	3.3±0.2
C6	368.4±91.2	17.2±2.8	9.2±2.1	5.4±1.3	2.0±0.8	1.7±0.4	3.3±0.3
C8	386.7±65.5	19.7±5.6	9.3±1.6	4.3±1.0	2.2±0.8	2.3±0.8	3.0±0.5
C9	380.9±123.2	16.3±3.3	9.3±2.2	6.0±1.6	1.8±0.5	1.6±0.3	3.4±0.4
C12	471.2±220.7	17.9±4.7	11.6±3.4	4.4±1.7	1.6±0.6	3.0±1.4	2.8±0.4
C13	355.5±149.4	17.6±4.4	9.5±2.4	4.5±0.8	1.9±0.6	2.1±0.4	2.8±0.5
Mean All	360.8	16.9	9.2	4.9	1.9	2.0	3.1
Std. All	127.3	4.0	2.4	1.3	0.7	0.7	0.5

6.3.3.1.2 Morphometric parameters of canaliculi

Table 6.5 shows the morphometric parameters of canaliculi at the voxel size of 30 nm. We can see that the average total volume of canaliculi is 0.06×10^{-5} mm^3 and the average porosity of canaliculi is 0.35%. The average volume of canaliculi per cell is 113.0 μm^3 with the local porosity of canaliculi 0.51%. Also, the average ratio between the volume of canaliculi and the lacuna in the same cell is 38.6%. The average total volume of the LCN is 0.24×10^{-5} mm^3 and the average porosity of the LCN is 1.45%.

Table 6.6 displays the quantitative results of the ramification of canaliculi. At the same 7 distances from the surface of lacuna with those for the data of 50 nm, the average number of canaliculi per lacuna is 78.5, 83.8, 87.7, 88.0, 92.5, 103.1 and 117.9. The corresponding ratio between the number of canaliculi per lacuna and the volume of lacuna in the same cell is 0.24 μm^{-3}, 0.26 μm^{-3}, 0.28 μm^{-3}, 0.28 μm^{-3}, 0.30 μm^{-3}, 0.34 μm^{-3} and 0.39 μm^{-3}, respectively.

Table 6.5 Morphometric parameters of canaliculi at the voxel size of 30 nm

Sample ID	Ca.TV (10^{-5} mm^{3})	LCN.TV (10^{-5} mm^{3})	Ca.TV/BV (%)	LCN.TV/BV (%)	Ca.V (μm^{3})	Ca.V/Cell.V (%)	Ca.V/Lc.V (%)
C2	0.09	0.29	0.53	1.63	134.2±68.7	0.63±0.10	54.2±28.5
C3	0.08	0.27	0.48	1.56	119.7±70.8	0.55±0.25	54.2±37.6
C6	0.04	0.15	0.2	0.82	121.7±58.6	0.42±0.07	36.9±18.8
C8	0.03	0.14	0.26	1.03	113.5±56.4	0.32±0.04	32.8±15.4
C9	0.08	0.42	0.49	2.59	98.4±31.0	0.64±0.18	26.6±8.8
C12	0.07	0.24	0.41	1.32	186.4±102.6	0.65±0.13	49.0±21.4
C13	0.02	0.18	0.11	1.24	32.8±19.1	0.13±0.08	10.1±3.0
Mean All	0.06	0.24	0.35	1.45	113.0	0.51	38.6
Std. All	0.03	0.09	0.15	0.53	68.8	0.23	26.7

Table 6.6 Number of canaliculi per lacuna at 7 different distances from the surface of the lacuna and the ratio between the number and the average volume of lacuna at the voxel size of 30 nm

Sample ID	Ca.N (r=1.2 μm)	Ca.N (r=3.0 μm)	Ca.N (r=4.8 μm)	Ca.N (r=6.6 μm)	Ca.N (r=8.4 μm)	Ca.N (r=10.2 μm)	Ca.N (r=12.0 μm)
C2	88.0±32.9	88.6±38.7	101.1±40.5	118.0±57.4	127.6±51.4	150.1±50.9	162.0±42.8
C3	71.1±42.0	83.0±56.1	85.0±54.3	80.3±59.7	78.1±55.6	83.4±64.9	83.9±61.3
C6	80.7±18.5	90.3±22.0	86.3±23.7	81.0±21.5	88.0±30.3	92.7±47.5	122.3±60.7
C8	93.7±20.6	67.7±26.9	79.0±40.1	72.0±38.6	67.3±37.9	75.7±39.8	71.3±18.7
C9	82.6±36.2	98.1±44.7	102.8±41.8	98.5±36.3	104.5±35.6	114.5±35.0	149.8±57.4
C12	100.0±72.9	116.3±70.0	122.3±63.9	134.5±90.5	148.0±97.5	160.8±95.3	186.0±93.5
C13	41.6±42.2	35.2±42.4	27.2±32.0	16.8±14.3	17.6±16.9	22.8±30.5	23.8±32.3
Mean All	78.5	83.8	87.7	88.0	92.5	103.1	117.9
Std. All	41.3	48.5	49.1	58.3	60.4	65.7	73.5

Sample ID	Ca.N/Lc.V (μm^{-3}, r=1.2 μm)	Ca.N/Lc.V (μm^{-3}, r=3.0 μm)	Ca.N/Lc.V (μm^{-3}, r=4.8 μm)	Ca.N/Lc.V (μm^{-3}, r=6.6 μm)	Ca.N/Lc.V (μm^{-3}, r=8.4 μm)	Ca.N/Lc.V (μm^{-3}, r=10.2 μm)	Ca.N/Lc.V (μm^{-3}, r=12.0 μm)
C2	0.34±0.11	0.33±0.08	0.39±0.11	0.45±0.14	0.49±0.16	0.58±0.14	0.64±0.18
C3	0.29±0.12	0.33±0.16	0.36±0.20	0.33±0.20	0.33±0.18	0.35±0.22	0.36±0.24
C6	0.24±0.08	0.26±0.07	0.25±0.07	0.24±0.09	0.27±0.13	0.28±0.15	0.37±0.19
C8	0.27±0.04	0.19±0.07	0.23±0.10	0.21±0.10	0.19±0.10	0.22±0.10	0.21±0.04
C9	0.21±0.06	0.24±0.05	0.26±0.05	0.25±0.06	0.29±0.12	0.32±0.14	0.41±0.18
C12	0.23±0.06	0.27±0.04	0.30±0.06	0.34±0.15	0.37±0.13	0.42±0.20	0.52±0.28
C13	0.10±0.05	0.08±0.07	0.06±0.05	0.05±0.04	0.05±0.05	0.07±0.09	0.07±0.10
Mean All	0.24	0.26	0.28	0.28	0.30	0.34	0.39
Std. All	0.11	0.12	0.14	0.17	0.18	0.21	0.25

6.3.3.2 Quantification of cropped volumes at 120 nm

6.3.3.2.1 Morphometric parameters of lacunae

After registration using the phase correlation method, the 7 volumes at the voxel size of 120 nm were cropped to get the same field of view as those of 30 nm. Table 6.7 presents the lacunae parameters calculated on the cropped regions at 120 nm. The average number of lacunae is 5.3 and the average total volume of lacunae is 0.17×10^{-5} mm^{3}. The average bone volume is 0.17×10^{-3} mm3 with the average lacunar porosity 1.01% and the average density of lacunae 3.2×10^{4} mm^{-3}. The average volume of each lacuna is 314.0 μm^{3} and the average surface is 320.9 μm^{2}. The average volume of each cell is 2.0×10^{4} μm^{3} and the local lacunar porosity 1.77%. The average length, width and depth of each lacuna are 16.4 μm, 8.9 μm and 4.7 μm, respectively. To describe the flatness of the lacunae, we calculated the ratio between the length and the width 1.9, the ratio between the width and the depth 2.0 and the structural model index 3.1.

Table 6.7 Morphometric parameters of lacunae for the cropped volumes at 120 nm

Sample ID	Lc.N	Lc.TV ($\times10^{-5}$ mm^3)	BV ($\times10^{-3}$ mm^3)	Lc.TV/BV (%)	Lc.N/BV ($\times10^4$ mm^{-3})	Lc.V (μm^3)	Cell.V ($\times10^4$ μm^3)	Lc.V/Cell.V (%)
P2	7	0.19	0.18	1.06	4.0	265.9±129.2	2.0±0.7	1.52±0.93
P3	7	0.18	0.18	1.01	4.0	254.2±118.9	2.0±1.4	1.43±0.43
P6	3	0.10	0.18	0.55	1.7	329.8±160.6	2.2±1.2	1.68±0.97
P8	3	0.09	0.13	0.67	2.2	296.2±40.4	2.5±1.0	1.27±0.34
P9	8	0.31	0.16	1.91	4.9	387.0±176.9	1.5±0.6	2.52±0.59
P12	4	0.15	0.18	0.83	2.2	377.5±198.8	2.5±2.0	1.28±0.02
P13	5	0.15	0.15	1.01	3.4	298.9±195.5	2.2±0.5	1.41±0.99
Mean All	5.3	0.17	0.17	1.01	3.2	314.0	2.0	1.77
Std. All	1.9	0.07	0.02	0.41	1.1	152.1	1.0	0.95

Sample ID	Lc.S (μm^2)	Lc.L1 (μm)	Lc.L2 (μm)	Lc.L3 (μm)	Lc.L1 /Lc.L2	Lc.L2 /Lc.L3	Lc.SMI
P2	289.6±80.8	17.4±4.0	7.8±2.1	4.3±1.0	2.4±0.9	1.9±0.5	3.2±0.4
P3	250.9±91.7	13.3±3.5	8.4±2.3	4.6±1.0	1.7±0.5	1.9±0.6	3.3±0.2
P6	307.1±75.8	16.0±2.2	8.7±2.2	5.2±1.2	2.0±0.8	1.7±0.4	3.2±0.3
P8	332.5±69.5	18.9±5.1	8.9±1.8	4.0±0.7	2.2±0.7	2.3±0.7	3.0±0.2
P9	356.1±118.5	16.4±4.1	9.0±1.8	5.9±1.4	1.9±0.5	1.6±0.3	3.4±0.6
P12	406.8±187.9	17.3±4.3	11.0±3.2	4.3±1.7	1.7±0.6	2.9±1.4	2.8±0.6
P13	339.3±157.6	17.5±4.5	9.3±2.6	4.1±1.0	1.9±0.5	2.3±0.6	2.7±0.4
Mean All	320.9	16.4	8.9	4.7	1.9	2.0	3.1
Std. All	117.6	4.0	2.3	1.3	0.6	0.7	0.5

6.3.3.2.2 Morphometric parameters of canaliculi

Table 6.8 shows the morphometric parameters of canaliculi for the cropped volumes at the voxel size of 120 nm. It can be seen that the average total volume of canaliculi is 0.05×10^{-5} mm^3 and the average porosity of canaliculi is 0.28%. The average volume of canaliculi per cell is 88.6 μm^3 with the local porosity of canaliculi 0.49%. Also, the average ratio between the volume of canaliculi and the lacuna in the same cell is 31.2%. The average total volume of the LCN is 0.21×10^{-5} mm^3 and the average porosity of the LCN is 1.18%.

Table 6.9 displays the quantitative results of the ramification of canaliculi. At the same 7 distances from the surface of lacuna with those for the data of 50 nm, and 30 nm, the average number of canaliculi per lacuna is 49.6, 50.2, 52.7, 51.3, 49.6, 50.9 and 53.7. The corresponding ratio between the number of canaliculi per lacuna and the volume of lacuna in the same cell is 0.17 μm^{-3}, 0.17 μm^{-3}, 0.18 μm^{-3}, 0.19 μm^{-3}, 0.18 μm^{-3}, 0.18 μm^{-3} and 0.20 μm^{-3}, respectively.

Table 6.8 Morphometric parameters of canaliculi for the cropped volumes at 120 nm

Sample ID	Ca.TV (10^{-5} mm^3)	LCN.TV (10^{-5} mm^3)	Ca.TV/BV (%)	LCN.TV/BV (%)	Ca.V (μm^3)	Ca.V/Cell.V (%)	Ca.V/Lc.V (%)
P2	0.07	0.26	0.41	1.46	102.4±40.9	0.53±0.14	42.7±17.7
P3	0.07	0.24	0.38	1.39	95.2±62.6	0.57±0.29	43.0±25.3
P6	0.02	0.12	0.10	0.65	60.1±11.6	0.33±0.17	20.9±9.5
P8	0.02	0.11	0.18	0.85	81.0±19.9	0.34±0.09	27.1±3.5
P9	0.07	0.38	0.45	2.36	91.9±44.3	0.64±0.27	24.9±10.1
P12	0.06	0.21	0.34	1.17	155.3±109.1	0.66±0.11	42.0±20.3
P13	0.01	0.16	0.08	1.09	23.3±9.9	0.11±0.05	8.6±1.7
Mean All	0.05	0.21	0.28	1.28	88.6	0.49	31.2
Std. All	0.03	0.09	0.14	0.52	59.6	0.26	19.4

Table 6.9 Number of canaliculi per lacuna at 7 different distances from the surface of the lacuna and the ratio between the number and the average volume of lacuna for the cropped volumes at the voxel size of 120 nm

Sample ID	Ca.N (r=1.2 μm)	Ca.N (r=3.0 μm)	Ca.N (r=4.8 μm)	Ca.N (r=6.6 μm)	Ca.N (r=8.4 μm)	Ca.N (r=10.2 μm)	Ca.N (r=12.0 μm)
P2	49.0±14.1	58.0±22.1	62.4±31.6	65.1±32.8	64.4±32.6	64.7±25.9	72.1±34.6
P3	50.0±24.5	54.4±33.8	57.0±36.5	57.1±38.0	50.1±36.0	49.0±34.7	46.0±34.1
P6	49.7±24.8	36.0±18.2	40.3±14.6	32.7±6.5	31.7±3.1	31.3±2.1	21.3±6.5
P8	58.3±5.5	46.3±11.4	38.0±18.1	43.3±22.1	37.0±13.1	32.7±19.5	26.3±12.9
P9	59.5±30.6	63.5±34.5	67.6±36.8	60.5±27.6	59.6±28.8	67.0±34.3	75.5±31.4
P12	63.3±41.9	67.3±39.7	78.5±41.3	80.0±50.6	84.8±40.7	86.5±50.3	98.3±48.9
P13	18.0±15.3	9.6±10.2	5.0±3.8	1.8±2.2	2.6±2.7	3.0±2.1	4.0±6.4
Mean All	49.6	50.2	52.7	51.3	49.6	50.9	53.7
Std. All	26.7	31.7	36.3	36.6	35.4	37.3	41.2
Sample ID	Ca.N/Lc.V (μm^{-3}, r=1.2 μm)	Ca.N/Lc.V (μm^{-3}, r=3.0 μm)	Ca.N/Lc.V (μm^{-3}, r=4.8 μm)	Ca.N/Lc.V (μm^{-3}, r=6.6 μm)	Ca.N/Lc.V (μm^{-3}, r=8.4 μm)	Ca.N/Lc.V (μm^{-3}, r=10.2 μm)	Ca.N/Lc.V (μm^{-3}, r=12.0 μm)
P2	0.22±0.09	0.24±0.08	0.24±0.09	0.26±0.11	0.26±0.10	0.26±0.10	0.29±0.11
P3	0.22±0.10	0.24±0.14	0.26±0.15	0.27±0.19	0.23±0.16	0.24±0.17	0.23±0.20
P6	0.16±0.06	0.11±0.04	0.13±0.02	0.12±0.06	0.12±0.07	0.11±0.06	0.08±0.07
P8	0.20±0.03	0.16±0.03	0.12±0.05	0.14±0.06	0.12±0.03	0.11±0.06	0.09±0.05
P9	0.16±0.08	0.16±0.07	0.17±0.08	0.17±0.08	0.18±0.09	0.19±0.10	0.23±0.14
P12	0.16±0.03	0.18±0.04	0.22±0.07	0.23±0.12	0.25±0.10	0.25±0.13	0.31±0.18
P13	0.06±0.02	0.03±0.02	0.02±0.02	0.01±0.01	0.01±0.02	0.01±0.01	0.01±0.02
Mean All	0.17	0.17	0.18	0.19	0.18	0.18	0.20
Std. All	0.09	0.10	0.11	0.14	0.12	0.13	0.16

6.3.3.3 Correlation between parameters on matched VOIs at 30nm and 120nm

In this section, we show the results of the Spearman correlation coefficients and the corresponding p-values between the same measured parameters from the same VOIs at the voxel sizes of 30 nm and 120 nm. We want to check whether there are good correlations between these quantitative parameters from different groups. We list the results with good correlation ($R^2 > 0.5$ and $p < 0.05$) in Table 6.10 and some regression plots of these parameters are shown in Fig. 6.10, Fig.6.11, and Fig. 6.12.

Table 6.10 Spearman correlation detection between parameters from the volumes at the voxel size of 30 nm and the cropped ones at 120 nm

Parameter		R^2	p-value
Lc.N/BV		1.0000	<0.0001
Lc.TV/BV		0.9951	<0.0001
Lc.V		0.9710	<0.0001
Lc.S		0.8849	0.0016
Lc.L1		0.9470	0.0002
Lc.L2		0.9885	<0.0001
Lc.L3		0.9713	<0.0001
Lc.L1/Lc.L2		0.9933	<0.0001
Lc.L2/Lc.L3		0.9767	<0.0001
Lc.SMI		0.9269	0.0005
Ca.TV/BV		0.9534	0.0002
LCN.TV/BV		0.9989	<0.0001
Ca.V		0.8430	0.0035
Ca.V/Lc.V		0.9080	0.0009
Ca.N	r=1.2 μm	0.8772	0.0019
	r=3.0 μm	0.7816	0.0082
	r=4.8 μm	0.9382	0.0003

	r=6.6 µm	0.9084	0.0009
	r=8.4 µm	0.9123	0.0008
	r=10.2 µm	0.8849	0.0016
	r=12.0 µm	0.8007	0.0065
Ca.N/Lc.V	r=1.2 µm	0.9217	0.0006
	r=3.0 µm	0.8374	0.0039
	r=4.8 µm	0.9422	0.0003
	r=6.6 µm	0.8796	0.0018
	r=8.4 µm	0.8741	0.0020
	r=10.2 µm	0.8495	0.0032
	r=12.0 µm	0.7895	0.0075

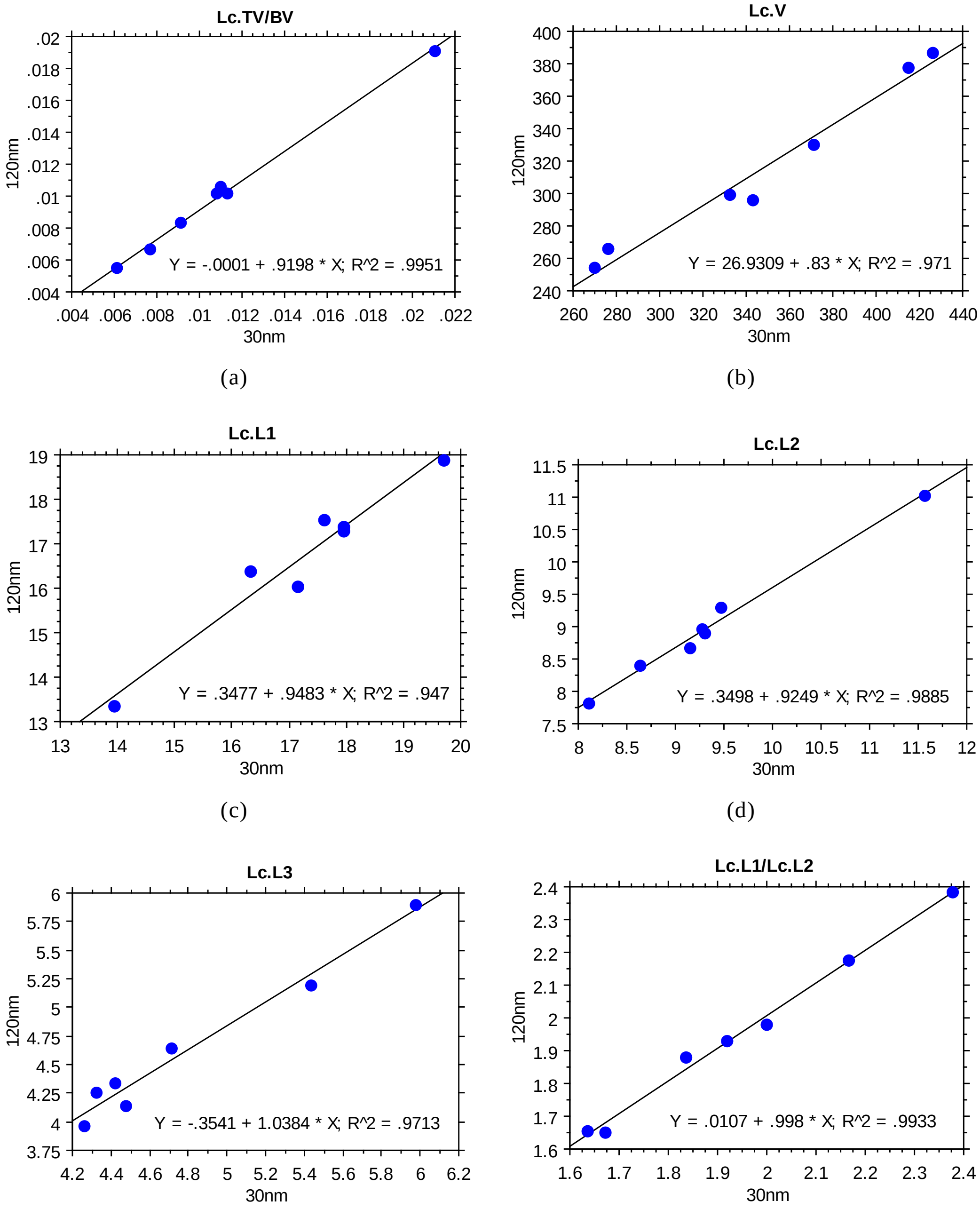

(a) (b)

(c) (d)

(e) (f)

Figure 6.10 Regression of morphological parameters of lacunae from the volumes at 30 nm and the cropped ones at120 nm. (a) $Lc.TV/BV$; (b) $Lc.V$ (µm^3); (c) $Lc.L1$ (µm); (d) $Lc.L2$ (µm); (e) $Lc.L3$ (µm); (f) the ratio $Lc.L1/Lc.L2$.

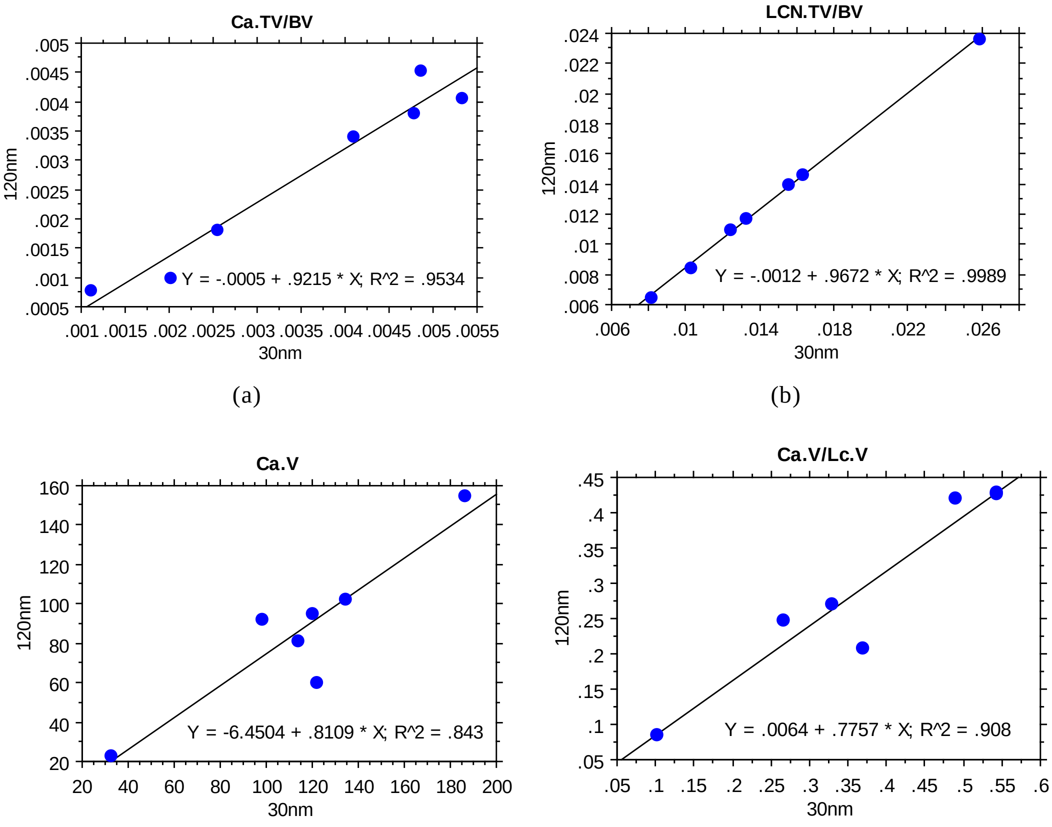

(a) (b)

(c) (d)

Figure 6.11 Regression of parameters of lacunae and canaliculi within the belonging Voronoi cell from the volumes at 30 nm and the cropped ones at120 nm. (a) $Ca.TV/BV$; (b) $LCN.TV/BV$; (c) $Ca.V$ (μm^3); (d) the ratio $Ca.V/Cell.V$.

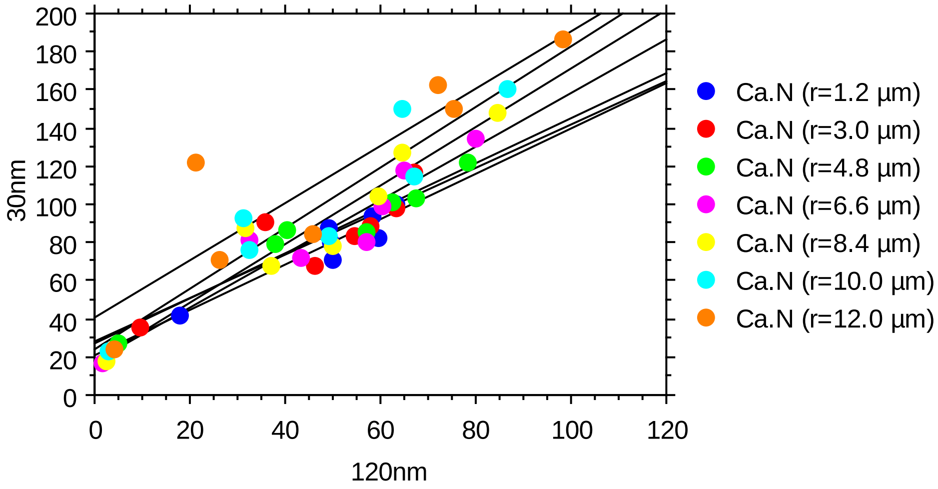

(a)

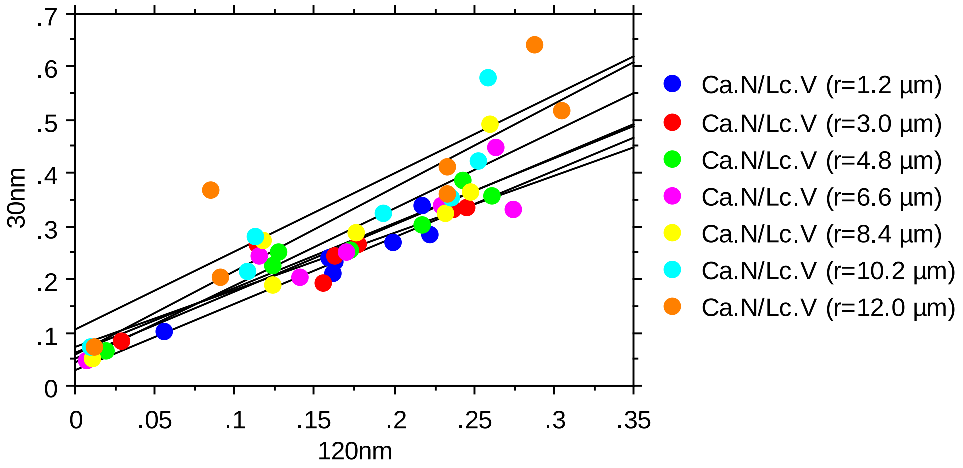

(b)

Figure 6.12 Regression of parameters for the ramification of canaliculi at 7 different distances from the volumes at 30 nm and the cropped ones at120 nm. (a) $Ca.N$; (b) $Ca.N/Lc.V$ (μm^{-3}).

6.3.3.4 Statistical analysis

For the parameters quantified from the volumes at 30 nm and the PCM ones, all the parameters passed the test of the homogeneity of variances. Therefore, we used the paired t-test for the evaluation of parameters as shown in Table 6.10. Between the two groups, there were not significant differences for the $Lc.N/BV$, $Lc.L_1/Lc.L_2$, $Lc.L_2/Lc.L_3$, $Lc.SMI$. But the results of $Lc.TV/BV$, $Lc.V$, $Lc.S$, $Lc.L1$, $Lc.L_2$, $Lc.L_3$, $LCN.TV/BV$, $Ca.TV/BV$, $Ca.V$, $Ca.N$, $Ca.N/Lc.V$ and $Ca.V/Lc.V$ at 30 nm are significantly different from those of the PCM volumes.

Table 6.10 P-values of the F-test and paired t-test for the two groups

		P-values	
		F-test	Paired t-test
Lc.N/BV		0.9995	0.9534
Lc.TV/BV		0.8489	0.0022
Lc.V		0.6875	0.0008
Lc.S		0.7489	0.0011
Lc.L1		0.9515	0.0126
Lc.L2		0.8651	0.0005
Lc.L3		0.9023	0.0093
Lc.L1/Lc.L2		0.9975	0.4416
Lc.L2/Lc.L3		0.9842	0.9404
Lc.SMI		0.9984	0.4239
Ca.TV/BV		0.8919	0.0013
LCN.TV/BV		0.9386	<0.0001
Ca.V		0.7707	0.0063
Ca.V/Lc.V		0.6299	0.0089
Ca.N	r=1.2 μm	0.5698	<0.0001
	r=3.0 μm	0.5537	0.0003
	r=4.8 μm	0.6429	<0.0001
	r=6.6 μm	0.3674	0.0007
	r=8.4 μm	0.2719	0.0010
	r=10.2 μm	0.2277	0.0009
	r=12.0 μm	0.2321	0.0014
Ca.N/Lc.V	r=1.2 μm	0.5338	0.0003
	r=3.0 μm	0.7105	0.0007
	r=4.8 μm	0.5963	0.0002
	r=6.6 μm	0.495	0.0024
	r=8.4 μm	0.3109	0.0028
	r=10.2 μm	0.2155	0.0026
	r=12.0 μm	0.2474	0.0026

6.4 Discussion

In this chapter, we quantified the LCN from phase nano CT images at voxel sizes of 50 nm and 30 nm. In addition, we assessed the effect of the voxel size by comparing results obtained from registered images acquired at 30 and 120 nm. We used a phase correlation method to register the volumes at 30 nm with those of 120 from the same samples, which provided the translations between the images. Due to the acquisition protocol ensuring a rigid transformation without rotation between the two images, the phase correlation method was found quite suitable.

Results at 50nm

We first provided the quantitative results for the reconstructed volumes at the voxel size of 50 nm. The average number of lacunae per volume was 20.8 and the density of lacunae ($Lc.N/BV$) was 2.6×10^4, which is in the range of 1.5×10^4–3.5×10^4 mm^{-3} reported in the work of Carter [Carter et al. (2013)]. The lacunar porosity ($Lc.TV/BV$) was 0.88% which is comparable with that of previous research in our group 0.84% [Dong, Haupert, et al. (2014)]. The canalicular porosity ($Ca.TV/BV$) was 0.37% which is slightly smaller compared to 0.57% in [Varga et al. (2015)], and the porosity of the whole network ($LCN.TV/BV$) was in average 1.24%. Moreover, we introduced a notion of local porosity for lacuna and canaliculi within their belonging Voronoi cells. The average cell volume $Cell.V$ was 3.4×10^4 μm^3 with a ratio $Lc.V/Cell.V$ being 1.14%. The total canalicular volume within one cell $Ca.V$ was 141.4 μm^3 with a ratio $Ca.V/Cell.V$ equal to 0.43%. This permits to quantify the space occupied by lacunae and canaliculi within their neighborhood. Also, the ratio $Ca.V/Lc.V$ was found to be 46.4%, which shows that the total volume of canaliculi within one cell is approximately the half of the lacunar volume. To our knowledge, there is no equivalent data in the literature.

The value of $Lc.V$ 338.1 μm^3 is in agreement with previous reports (50–730 μm^3) [Remaggi et al. (1998)], [Carter et al. (2013)]. The average length (18.7 µm), width (9.1 µm) and depth (4.5 µm) of lacuna at 50 nm are consistent with previous reports (~ 17 µm, 9 µm and 4 µm) and the ratio between them is about 4:2:1 [van Hove et al. (2009)], [Dong, Haupert, et al. (2014)]. The surface area $Lc.S$ (376.4 μm^2) and the structure model index $Lc.SMI$ (3.1) are also both comparable with previous works [Dong, Haupert, et al. (2014)], [Varga et al. (2015)].

We also quantified the number of canaliculi per lacuna on the images at 50 nm. This number $Ca.N$ which was computed at 7 different physical distances from the surface of each lacuna from 1.2 µm to 12.0 µm was found to increase from 72.7 to 107.3, and the density of canaliculi $Ca.N/Lc.V$ from 0.23 μm^{-3} to 0.36 μm^{-3}. The value of $Ca.N$ is comparable with previous works, e.g. 89.7±15 for rat tibia samples [Sharma et al. (2012)], 77.5±12.0 for mice femoral samples [Lai et al. (2015)] and 88.5±24.9 for human femoral samples [Varga et al. (2015)], but these works only counted the number of canaliculi per lacuna in one fixed distance.

Results at 30nm

Then, we reported the results at 30 nm and compared them to the site-matched registered volumes at 120 nm. Firstly, the lacunar porosity ($Lc.TV/BV$) calculated at 30 nm found to be 1.10% was larger than that of the PCM volumes 1.01% while sharing the same number of lacunae 5.3 and the same density of lacunae 3.2×10^4 mm^{-3}. The results are in the range of previous studies for the density (10,000–35,000 mm^{-3}) and the porosity (0.5–2%) [Carter et al. (2013)], [Dong, Haupert, et al. (2014)], [Andronowski et al. (2017)], [Gatti et al. (2018)].

Concerning the properties of lacunae, the average volume ($Lc.V$) and surface ($Lc.S$) of lacuna at 30 nm was respectively 343.3 μm^3 and 360.8 μm^2, which was bigger than those of the PCM volumes found to be 314.0 μm^3 and 320.9 μm^2. The values of $Lc.V$ are in the range of previous researches (50–730 μm^3) [Remaggi et al. (1998)], [Carter et al. (2013)]. The calculations of $Lc.S$ is close to the reports of Dong 336.2±94.5 [Dong, Haupert, et al. (2014)] but less than that of Varga 430.4±68.46 [Varga et al. (2015)]. The average length, width and depth of lacuna ($Lc.L1$, $Lc.L2$, and $Lc.L3$) at 30 nm were 16.9 µm, 9.2 µm, 4.9 µm, and were slightly larger (<0.5µm) than those of the PCM volumes 16.4 µm, 8.9 µm and 4.7 µm. These values are consistent with previous works [van Hove et al. (2009)], [Dong, Haupert, et al. (2014)].

According to the calculated p-values by the paired t-test of the results at 30 nm and the PCM ones, there are indeed significant differences between the quantitative parameters of lacunae such as the porosity ($Lc.TV/BV$) and morphological descriptors ($Lc.V$, $Lc.S$, $Lc.L_1$, $Lc.L_2$ and $Lc.L_3$). After checking the plots in Fig. 6.10, we can also find that the values of $Lc.V$, $Lc.L_1$, $Lc.L_2$ and $Lc.L_3$ from the reconstructed volumes at 30 nm are a little higher than those of the PCM ones at 120 nm. However, the parameters of the average anisotropy of lacunae ($Lc.L_1/Lc.L_2$, $Lc.L_2/Lc.L_3$ and $Lc.SMI$) are comparable between the results at 30 nm and the PCM ones. The average ratios between the length, the width and the depth are the same 3.8:2:1 for two groups. Also, we find that the values of $Lc.SMI$ are nearly equal in the two groups: 3.1. These values illustrate that the 3D structure of the lacuna is close to an object between a cylinder and a sphere [Dong, Haupert, et al. (2014)]. Considering the quantitative and statistical results together, we can see that the segmented lacunae from the volumes at 30 nm maintain the similar 3D shape structure but their geometrical sizes are a little enlarged compared with those from the PCM volumes. This is probably due to the influence of image processing methods when performing segmentation of lacunae. For example, we used the median filter to remove canaliculi and some speckle noise before segmentation. Because the canaliculi are actually connected with lacunae, it was difficult to judge whether the voxels in adjacent areas belonged to lacunae or canaliculi. After filtering, some border region of lacunae might be removed at the same time. At the voxel size of 120 nm, the size of canaliculi was just several voxels so that the segmentation of lacunae was more affected than that at 30 nm. Besides, the thresholds had impact on the segmented results although we have used the hysteresis thresholding to refine the segmentation. It was difficult to keep the consistency of segmentation between different voxel sizes using different thresholds.

Concerning the quantification of canaliculi, their porosity ($Ca.TV/BV$) at 30 nm was 0.35%, which is higher than that of the PCM ones (0.28%). Compared with porosity of previous works (0.5–2.0%) [Sharma et al. (2012)], [Varga et al. (2015)], our values of $Ca.TV/BV$ are lower. The average volume of canaliculi per cell ($Ca.V$) at 30 nm was 113.0 µm^3, which was found bigger than that of the PCM volumes (88.6 µm^3). The local porosity of canaliculi, $Ca.V/Cell.V$ at 30 nm was 0.51% and also higher than that of the PCM volumes (0.49%). The ratio $Ca.V/Lc.V$ at 30 nm was estimated to 38.6% also higher than that of the PCM volumes (31.2%). These differences are probably related to a better segmentation of canaliculi at 30 nm.

To number of canaliculi per lacuna was also computed at 7 distances from the surface of lacuna: (1.2 µm, 3.0 µm, 4.8 µm, 6.6 µm, 8.4 µm, 10.2 µm and 12.0 µm). The results show that the average number of canaliculi per lacuna ($Ca.N$) at 30 nm increases from 78.5 to 117.9 with the distance changing from 1.2 µm to 12.0 µm. This increase is not clearly seen on the PCM volumes sine there is just a slight fluctuation, first an increase from 49.6 at 1.2 µm to 52.7 at 4.8 µm, then a decrease to 49.6 at 8.4 µm, and finally a growing to 53.7 at 12.0 µm. Varga et al. has reported the number of canaliculi per lacuna ranging 53–126 but using only a fixed distance [Varga et al. (2015)]. Dong et al. has also shown that the average number of canaliculi per lacuna increased from 41.5 to 139.1 with the distance changing from 1.4 µm to 11.2 µm [Dong, Pacureanu, et al. (2014)]. Our results are consistent with the study of Dong but our growth rate of $Ca.N$ seems to be lower, however in the work of Dong the analysis was performed on a single sample (to be checked) from images at 300nm. The ratio between the number of canaliculi per lacuna and the average volume of lacuna ($Ca.N/Lc.V$) describing a local density of canaliculi keep increasing from 0.24 µm^{-3} at 1.2 µm to 0.39 µm^{-3} at 12.0 µm at 30nm, while they just fluctuate around ~0.18 µm^{-3} from the distance 1.2 µm to 10.2 µm, and then increases to 0.20 µm^{-3} at 12.0 µm on the PCM volumes.

Based on the statistical analysis, the average number and density of canaliculi at all 7 distances ($Ca.N$ and $Ca.N/Lc.V$) from the volumes at the voxel size of 30 nm are significantly different from those of PCM volumes. Also, based on Table 6.6 and Table 6.9, we can see that the values of $Ca.N$ and $Ca.N/Lc.V$ of volumes at 30 nm are much higher than those of the PCM ones which are cropped from volumes at 120 nm. This means that we achieved better segmentation and quantification of canaliculi using the reconstructed volumes at the voxel size of 30 nm. In other words, a relatively high spatial resolution of reconstructions could improve the investigation and analysis of canaliculi to cope with their tiny physical diameter (~ 200–500 nm) [Varga et al. (2015)], [Gatti et al. (2018)]. Although we can better observe and quantify the 3D structures of canaliculi and some specific lacunae using the voxel size of 30 nm, this case may be not appropriate for statistical analysis of lacunae and global investigation of the whole network. If we check each single sample separately, we find that there are some volumes at 30 nm having larger values of some parameters than the average level, e.g. $Lc.TV/BV$ (2.10%, C9), $Lc.V$ (415.1 µm^3, C12) and $Lc.L1$ (19.7 µm, C8). This can be explained by the fact that there are only a few lacunae (5.3) kept in the field of view when using the voxel size of 30 nm to observe the sample. Therefore, these quantitative measurements are limited in the local region instead of the whole volume.

In addition, we calculated the Spearman correlation coefficients and the p-values between the same parameters from the volumes at the voxel size of 30 nm and the cropped ones at 120 nm. We notice that there were good correlations between the same parameters measured in the same VOIs at different voxel sizes. This explains that the observations and quantifications maintain the consistency at the voxel sizes of 30 nm ad 120 nm. Especially, the Spearman correlation coefficients of some parameters are quite high ($R^2 > 0.9$), such as the porosity of lacunae and canaliculi ($Lc.TV/BV$, $Ca.TV/BV$ and $LCN.TV/BV$), the morphology of lacunae ($Lc.V$, $Lc.L1$, $Lc.L2$ and $Lc.L3$), and the anisotropy of lacunae ($Lc.L_1/Lc.L_2$, $Lc.L_2/Lc.L_3$ and $Lc.SMI$).

There are some limitations of this study. First, the quantitative results on the LCN have been obtained from 7 samples, which remains a limited number of samples although there is not comparable study in the literature. In future, we expect to quantify a larger number of samples to increase the statistical representativity of the population. Second, although a complete image processing has been used, it is likely that more research should be done to improve the segmentation of canaliculi. The latter is still challenging because they have small physical size and it is difficult to keep their connectivity after segmentation. Therefore, a perspective could be to further develop segmentation methods dedicated to canaliculi by trying to preserve the connectivity of canaliculi without introducing false channels. Third, we should find or design some descriptors to evaluate the properties of the whole network instead of lacunae and canaliculi separately. We calculated the volume and porosity of the 3D network in this work, but some new parameters are necessary to figure out the spatial distribution and the topological structure of the LCN.

In conclusion, we scanned 13 samples from female femoral bone using magnified X-ray magnified X-ray phase nano-CT at the voxel sizes of 50 nm and 30 nm. Based on the phase correlation method, we obtained the translative offsets and cropped the small pieces in the volumes at 120 nm with the same field of view corresponding to the volumes at 30 nm. We compared the quantitative results of volumes at 30 nm with those of the PCM volumes after cropping. And we found that using the voxel size of 30 nm can have a better effect on the observation and quantification of the morphological structures of canaliculi. But the voxel sizes of 50 nm or 120 nm seem more suitable to investigate and analyze the 3D properties of the whole network with a large field of view. We also compared our results with those in previous studies to verify the reliability of the measurements. Furthermore, all our quantitative parameters of lacunae and canaliculi at the voxel sizes of 50 nm and 30 nm are expected to improve our knowledge on bone microarchitectures and provide reference for other relative researches.

Chapter 7: Quantification of the lacuno-canalicular network in a series of human femoral samples by the magnified X-ray phase nano-CT

This chapter is a research article prepared for submission but not yet submitted at the time of writing this thesis.

Contents

7.1 Introduction

Bone fragility can be caused by both physiological and environmental factors, which will increase the risk of fracture and be enhanced by some bone diseases such as osteoporosis [Pignolo et al. (2018)]. Hence, it is important to have a better understanding of the processes involved in bone strength. The relative contributions of cortical versus trabecular bone to bone strength have been revisited recently. In the femoral neck, the cortical shell contributes 40-90% of the bending rigidity [Holzer et al. (2009)]. In addition, cortical porosity is a major determinant of bone fragility [Zebaze et al. (2010)]. Cortical porosity includes the Haversian-Volkmann system which represents the largest porosity, and at the cellular scale, the osteocyte system which is also called the lacuno-canalicular network (LCN).

Osteocytes, which play important roles in bone remodeling is attracting a growing attention. Osteocytes are considered to function as orchestrators to regulate the activities of both osteoclasts and osteoblasts during bone remodeling [Schaffler et al. (2014)]. For example, recent researches demonstrated that osteocytes participated in the control of bone formation by expressing Klotho [Komaba et al. (2017)] and producing WNT1 [Joeng et al. (2017)]. Also, osteocytes within the autogenous fragments were observed to be able to repair the disrupted canalicular networks and connect with other osteocytes in the bone formed on the surface of fragments [Shah et al. (2017)].

In this context, it is important to get a better knowledge about the structure and function of the LCN. Basic information has been obtained from the earlier work of Marotti [Marotti et al. (1995)]. In the past twenty years, an increasing number of researches have concentrated on the characterization of lacunae in different species e.g. human, rat, mice, rabbit, sheep and bovine. 2D images were used to assess the porosity and density of lacunae [Mullender et al. (1996)], [Jordan et al. (2003)], [Ashique et al. (2017)]. Meanwhile, a few parameters were calculated to quantify the morphology of lacuna. They include the lacunar area [Remaggi et al. (1998)], the length and width of lacuna [Lin et al. (2011)] as well as the average lacunar pericellular area and pericellualr thickness [Lai et al. (2015)]. Additional parameters were assessed by using 3D images avoiding the effect of slicing [van Hove et al. (2009)], [Dong, Haupert, et al. (2014)], [Bach-Gansmo et al. (2016)]. and van Hove presented the surface area of lacuna [van Hove et al. (2009)]. The length, width and depth of lacuna can be defined as the long axis, the medium axis and the short axis of the ellipsoid which fits the targeted lacuna. Carter et al. used the software AMIRA to find the fitting ellipsoid for each lacuna and get three eigenvalues of the covariance matrix [Carter et al. (2013)]. Dong et al. used an in-house method based on the calculation of the second order moment matrix [Dong, Haupert, et al. (2014)]. The lacunar orientation can also be defined by computing the angle between the long axis of the lacuna and the longitudinal axis of bone [Mader et al. (2013)], [Varga et al. (2015)] or the angle between the long axis of the lacuna and the horizontal axis of the sample [Carter et al. (2013)]. Repp et al. also proposed two angles based on two coordinate systems to describe the orientation: the polar angle and the azimuthal angle [Repp, Kollmannsberger, Roschger, Berzlanovich, et al. (2017)].

There are fewer methods and studies for the characterization of canaliculi in bone samples. 2D imaging techniques have been used to report the porosity of canaliculi in bovine [Lin et al. (2011)] and human [Ashique et al. (2017)]. The density of canaliculi was also presented as the number of canaliculi per 10 µm length [Remaggi et al. (1998)], or the number of canaliculi per unit area [Lin et al. (2011)]. Meanwhile, a few 2D morphological parameters of canaliculi have been reported, such as the canalicular diameter [You et al. (2004)], the number of canaliculi per each lacuna [Shapiro (1988)], as well as the canalicular area, the pericellular area and the pericellular thickness [Lai et al. (2015)]. The emergence of 3D imaging permitted the assessment of the same parameters in 3D as well as the computation of additional parameters. The porosity of canaliculi is the most straightforward parameter [Schneider et al. (2011)], [Hesse et al.

(2015)], the total volume and the total surface area of canaliculi could also be evaluated [Sugawara et al. (2011)], [Varga et al. (2015)]. The density of canaliculi was presented by the total number of canaliculi divided by the lacunar surface area [Wang et al. (2005)] or the total length of canaliculi per unit volume [Repp, Kollmannsberger, Roschger, Kerschnitzki, et al. (2017)]. The canalicular diameter can also be measured [Varga et al. (2015)], Hesse, 2015, as well as the number of canaliculi per lacuna were also presented [Sharma et al. (2012)], [Dong, Pacureanu, et al. (2014)], [Hesse et al. (2015)]. Besides, it may also be of interest to quantify simultaneously the lacunae and canaliculi as a whole network to evaluate its topological properties [Kollmannsberger et al. (2017)].

Despite such improvements, the properties of the LCN on large data sets are still missing. Data on the LCN in human bone samples were mainly achieved by using 2D imaging techniques or SR µCT in 3D, while most of researches using CLSM were performed for animal bone samples (mice, rats). Due to the anisotropy of the LCN, the lack of information in one dimension when using 2D imaging techniques makes it difficult to get a reliable estimation of parameters. As seen before, the lacunae can be satisfyingly quantified on large fields of view using SR µCT at spatial resolution about one micrometer. Nevertheless, the quantification of the canaliculi requires a higher spatial resolution not to miss the small channels. To this aim, SR nCT has been successfully used in previous works [Varga et al. (2015)], [Hesse et al. (2015)].

The purpose of this study is to report quantitative parameters of the LCN in 27 human femoral samples from female and male donators. This work is based on magnified X-ray phase nCT at 100nm performed at the beamline ID16B of the European Synchrotron Radiation Facility (ESRF), Grenoble, France. After phase retrieval and tomographic reconstruction, the LCN are segmented with efficient methods to cope with the large datasets (52.7 GB per volume). Based on the segmented volumes, a number of quantitative parameters are calculated for the assessment of the LCN, e.g. the porosity and the density of lacunae and canaliculi, the length, width, depth and anisotropy of each lacuna, as well as the ramification of canaliculi per lacuna.

7.2 Materials and methods

7.2.1 Sample description

Cortical bone samples were cut from the femoral diaphyses of 27 human cadavers provided by the Centre du Don des Corps (University Paris 5) and the Dept. of Anatomy Rockefeller, University Lyon. In accordance with legal clauses stated in the French Code of Public Health Ethical, only the information of sex and age for the donors is available. There are in total 15 females (50–95 years old) and 12 males (66–89 years old) among the donors. Transverse cross-sections with the size of $0.4 \times 0.4 \times 4$ mm^3 for the scan were cut using a water-cooled diamond precision saw (Presi Mecatome T210, Struers Diamond Cut-off Wheel EOD15, Liphy, Grenoble).

In this work, we scanned 27 samples, each sample coming from a different donor. We divided the samples into two groups according to gender: the female (F) and the male (M). Then, we used the number to denote the samples in different groups by the age order from the smallest to the largest. Therefore, we had F1–F15 for the female group and M1–M12 for the male group.

7.2.2 Synchrotron radiation nano-CT

We used magnified X-ray phase nano-CT to image the samples at the beamline ID16B of the ESRF. During the scan, the sample was put in a hybrid stage which could rotate to different angles for 3D data acquisition and control translations along three different axial directions. The pixel size was set to 100nm. Each sample was scanned at 4 different distances between the focus and the sample, and 3400 projections were recorded at each distance over a range of 180°. The X-ray beam energy was set to 29.6

keV for our experiment. The total scanning time for one sample at 4 distances was about 4 hours. Phase retrieval was perfomed using the multi distance Paganin method followed by an iterative step of nonlinear conjugate gradient according to our previous work [Yu et al. (2018)]. The 3D phase maps were then reconstructed by the standard Filtered Back-Projection (FBP) algorithm [Mirone et al. (2014)]. The volumes are made of 2560 × 2560 × 2160 voxels corresponding to a field of view of 256 µm × 256 µm × 216 µm.

7.2.3 Image processing

Before calculating the quantitative parameters, we needed to segment the lacunae and canaliculi from the reconstructed images. The segmentations of both structures were performed sequentially. The first step was the segmentation of lacunae. In the beginning, we used a median filter to remove some structures whose sizes were smaller than lacunae. The filter size was 10 voxels chosen from a previous report of our group [Dong, Haupert, et al. (2014)]. They could be canaliculi, collagen fibers or some speckle noise but had the same gray level than lacunae. Then, we used a hysteresis thresholding to obtain the segmented binary images of lacunae based on setting two thresholds: one for the initial segmentation with high-confidence and the other for the refinement by detecting the connectivity of voxels. The method of selecting the two thresholds has been described in Chapter 5. Finally, a connected component analysis was used to filter out Haversian or Volkmann canals, which were kept in the binary results and had much larger sizes than lacunae. The threshold was 2,000,000 voxels i.e. the physical size of 2000 µm^3.

The second step was the segmentation of canaliculi. Due to the slender tubular structures of canaliculi, it was difficult to extract them from the reconstructed images directly. Actually, some Hessian-based filters have been proposed to enhance tube-like features such as vessels in the field of medical image processing [Olabarriaga et al. (2003)], [Annunziata et al. (2016)]. Therefore, we first used Sato's vesselness enhancement method [Sato et al. (1998)] to improve the visibility of line structures which were mainly canaliculi in our work. After this, we also used the hysteresis thresholding method to segment canaliculi from the line-filter images by setting the two thresholds respectively to 3.0 and 4.5. Finally, we used a connected components analysis to filter out residual noise. The thresholds were 75 voxels based on the previous work of our group [Pacureanu (2012)].

7.2.4 Quantitative analysis

7.2.4.1 Quantification of lacunae

In order to quantify lacunae, the number of lacunae ($Lc.N$), the total volume of lacunae ($Lc.TV$), the bone volume (BV), the density of lacunae ($Lc.N/BV$) and the lacunar porosity ($Lc.TV/BV$) and the average volume of lacunae ($Lc.V$), were first calculated on the entire binary segmented images. Then, we computed some lacunae parameters within local regions. To this aim, the original volume was partitioned into different cells according to a Voronoi tessellation, where each cell contained only one lacuna. We then calculated the average volume of each cell ($Cell.V$) and the local lacunar porosity ($Lc.V/Cell.V$). Besides, we calculated the length, width and depth of lacuna ($Lc.L_1$, $Lc.L_2$, and $Lc.L_3$), and the anisotropy of lacuna detected by the ratios between different axes ($Lc.L_1/Lc.L_2$ and $Lc.L_2/Lc.L_3$) by the moment analysis [Dong, Haupert, et al. (2014)], as well as the average surface area of lacuna ($Lc.S$) and the structure model index of lacuna ($Lc.SMI$) by Ohser's method [Ohser et al. (2009)].

7.2.4.2 Quantification of canaliculi

Similarly to lacunae parameters, we calculated the total volume of canaliculi ($Ca.TV$) and the porosity of canaliculi ($Ca.TV/BV$) on the whole volume, as well as the average volume of canaliculi ($Ca.V$), the local porosity of canaliculi ($Ca.V/Cell.V$) and the ratio between the average volume of canaliculi and lacunae ($Ca.V/Lc.V$) within each Voronoi cell. Moreover, the total volume of the LCN ($LCN.TV$) and the porosity of the LCN ($LCN.TV/BV$) were computed to assess the properties of the whole network. In addition, we calculated the number of canaliculi per lacuna at different distances from the surface of the lacuna ($Ca.N(r)$, where r is the distance) [Dong, Haupert, et al. (2014)] and the ratio between the number of canaliculi per lacuna and the average volume of lacuna located in the same cell ($Ca.N/Lc.V$) to evaluate the ramification and the density of canaliculi.

7.2.5 Statistics analysis

The statistics analysis was performed by the software Statview® (SAS Institute Inc., Cary, NC, USA). If the parameters could pass the Kolmogorov-Smirnov (K-S) test for the normality and the F-test for the homogeneity of variances, we used the unpaired t-test to check the significance between groups. If not, Mann-Whitney U test was used for the evaluation. Besides, the Spearman correlation coefficients (R^2) and the p-values by the Fisher's r to z transformation were calculated to evaluate correlations between different parameters. P-values less than 0.05 were considered as significant.

7.3 Results

7.3.1 3D rendering

In Fig. 7.1 (a) and (c), we show the MIPs along the Y-axis of 100 middle slices from the reconstructed volumes of the samples F8 and M4. And the 3D displays of the segmented lacunae and canaliculi rendered by VGStudioMax® are also given in Fig. 7.1 (b) and (d), respectively.

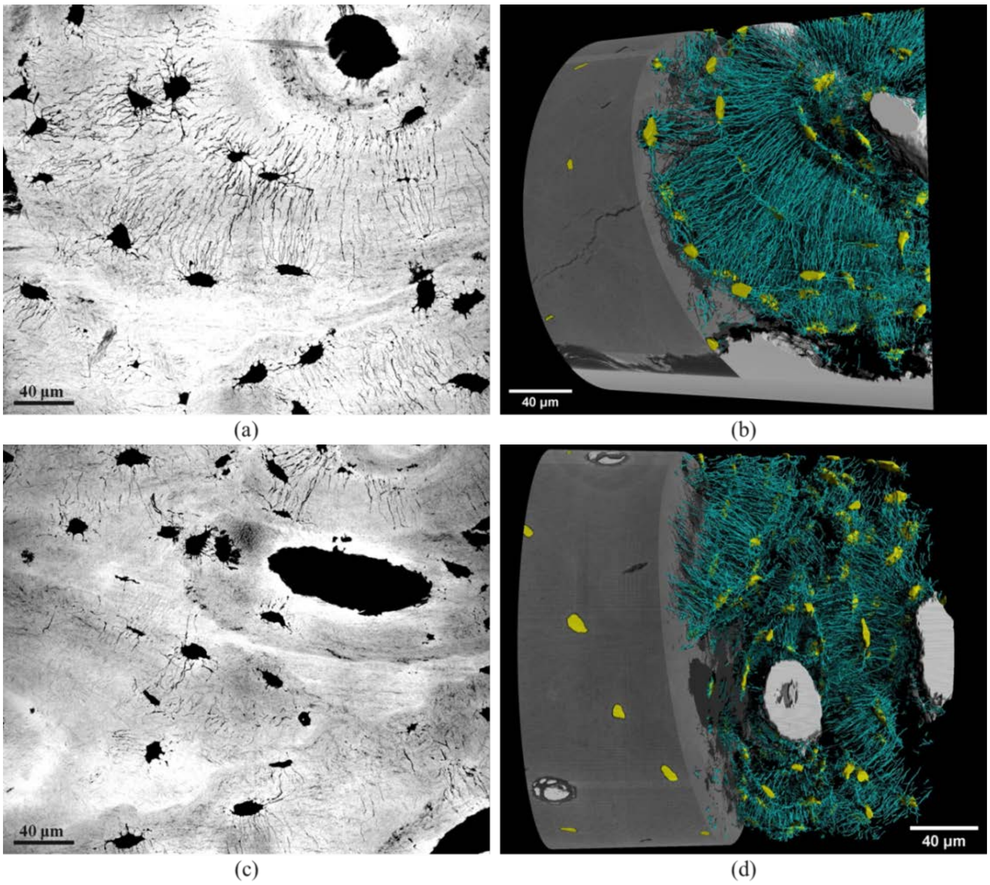

Figure 7.1 Segmentation results for the volumes F8 and M4. (a) and (c) MIPs along the Y-axis of 100 middle slices from the reconstructed volumes F8 and M4, respectively; (b) and (d) 3D rendering of the segmented lacunae and canaliculi corresponding to (a) and (c).

7.3.2 Quantification of the LCN

7.3.2.1 Morphometric parameters of lacunae

We scanned 27 samples at the voxel size of 100 nm: 15 for female and 12 for male. Table 7.1 illustrates the morphometric parameters of lacunae. The average number of lacuna is 224.5 and the average total volume of lacunae is 7.7×10^{-5} mm^3. The average bone volume is 10.4×10^{-3} mm3 with the average lacunar porosity 0.73% and the average density of lacunae 2.1×10^4 mm^{-3}. The average volume of each lacuna is 343.0 µm^3 and the average surface area is 342.5 µm^2. The average volume of each cell is 4.7×10^4 µm^3 and the ratio between the average volume of each lacuna and its belonging cell is 0.87%. The average length, width and depth of each lacuna are 17.9 µm, 9.4 µm and 4.5 µm, respectively. To describe the flatness of the lacunae, we calculated the ratio between the length and the width 2.0, the ratio between the width and the depth 2.2 and the structural model index 3.1.

Figure 7.2 show several morphologic parameters of lacuna for the female and male groups at the voxel size of 100 nm, such as $Lc.N/BV$, $Lc.TV/BV$, $Lc.V/Cell.V$, $Lc.V$, $Lc.L_1$ and $Lc.L_1/Lc.L_2$.

Table 7.1 Morphometric parameters of lacunae at the voxel size of 100 nm

Sample ID	Lc.N	Lc.TV (×10^{-5} mm^3)	BV (×10^{-3} mm^3)	Lc.TV/BV (%)	Lc.N/BV (×10^4 mm^{-3})	Lc.V (µm^3)	Cell.V (×10^4 µm^3)	Lc.V/Cell.V (%)
Mean F	231.1	8.3	10.4	0.79	2.2	358.5	4.7	0.93
Std. F	47.6	1.8	0.8	0.14	0.4	161.2	2.4	0.64
Mean M	216.3	6.9	10.5	0.66	2.1	323.6	4.7	0.81
Std. M	15.9	0.5	0.4	0.05	0.1	135.4	2.2	0.52
Mean All	224.5	7.7	10.4	0.73	2.1	343	4.7	0.87
Std. All	37.8	1.5	0.7	0.12	0.3	151.8	2.3	0.59

Sample ID	Lc.S (µm^2)	Lc.L1 (µm)	Lc.L2 (µm)	Lc.L3 (µm)	Lc.L1 /Lc.L2	Lc.L2 /Lc.L3	Lc.SMI
Mean F	354.9	18.3	9.6	4.5	2.0	2.3	3.1
Std. F	109.3	4.8	2.3	1.3	0.8	0.8	0.4
Mean M	327.1	17.4	9.3	4.5	2.0	2.2	3.1
Std. M	95.2	4.4	2.1	1.2	0.8	0.8	0.4
Mean All	342.5	17.9	9.4	4.5	2.0	2.2	3.1
Std. All	104.3	4.6	2.2	1.3	0.8	0.8	0.4

Lc.N – number of lacunae
Lc.TV – total volume of lacunae (mm^3)
BV – bone volume (mm^3)
Lc.TV/BV – lacunar porosity (%)
Lc.N/BV – density of lacunae (mm^{-3})
Lc.V – average volume of lacuna (µm^3)
Cell.V – average volume of each cell (µm^3)
Lc.V/Cell.V – ratio between the average volume of lacuna and its belonging cell (%)
Lc.S – average surface area of lacuna (µm^2)
Lc.L1, Lc.L2 and Lc.L3 – average length, width and depth of lacuna (µm)
Lc.L1/Lc.L2 and Lc.L2/Lc.L3 – average anisotropy of lacuna
Lc.SMI – average structural model index of lacuna

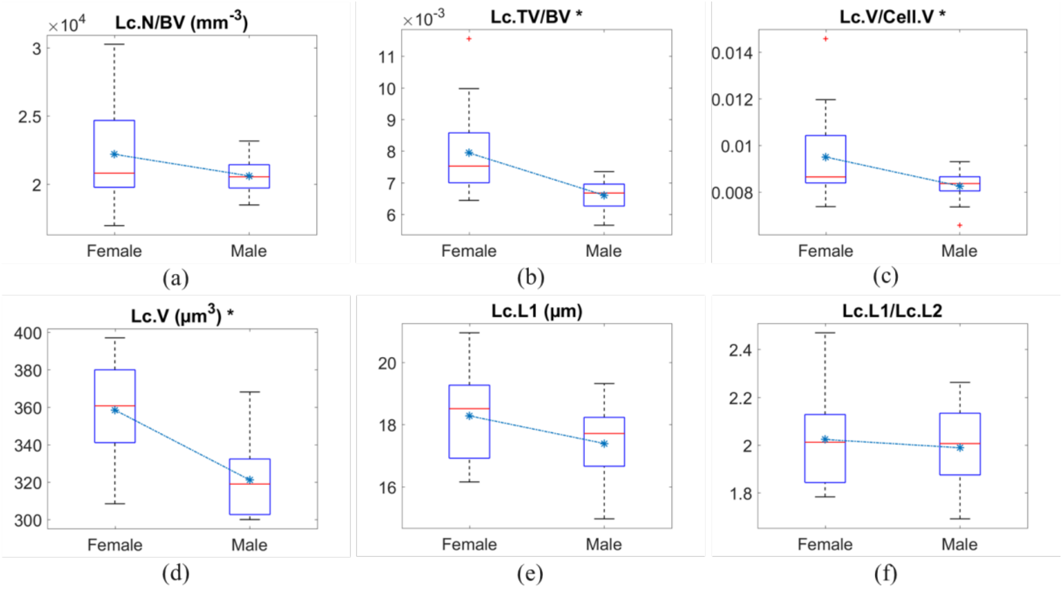

Figure 7.2 Some descriptors for the morphology of lacuna at the voxel size of 100 nm from female and male groups.

7.3.2.2 Morphometric parameters of canaliculi

Table 7.2 shows the morphometric parameters of canaliculi. We can see that the average total volume of canaliculi is 4.2×10^{-5} mm^3 and the average porosity of canaliculi is 0.40%. The average volume of canaliculi per cell is 187.1 μm^3 with the ratio of 0.44% between the average volume of canaliculi per cell and its belonging cell. Also, the average ratio between the volume of canaliculi and the lacuna in the same cell is 59.4%. The average total volume of the LCN is 11.9×10^{-5} mm^3 and the average porosity of the LCN is 1.14%.

Table 7.3 displays the quantitative results of the ramification of canaliculi. At 7 distances from the surface of lacuna ranging from 1.2 μm to 12.0 μm, the average number of canaliculi per lacuna is 54.5, 57.4, 58.0, 59.5, 62.2, 65.6 and 71.3. The corresponding ratio between the number of canaliculi per lacuna and the volume of lacuna in the same cell is 0.16 μm^{-3}, 0.17 μm^{-3}, 0.18 μm^{-3}, 0.18 μm^{-3}, 0.19 μm^{-3}, 0.20 μm^{-3} and 0.22 μm^{-3}, respectively.

Figure 7.3 present several quantitative parameters of canaliculi for female and male groups at the voxel size of 100 nm, such as $Ca.TV/BV$, $Ca.V/Cell.V$, $Ca.V/Lc.V$, $Ca.V$, $Ca.N$ and $Ca.N/Lc.V$.

Table 7.2 Morphometric parameters of canaliculi at the voxel size of 100 nm

Sample ID	Ca.TV (10^{-5} mm^3)	LCN.TV (10^{-5} mm^3)	Ca.TV/BV (%)	LCN.TV/BV (%)	Ca.V (μm^3)	Ca.V/Cell.V (%)	Ca.V/Lc.V (%)
Mean F	4.6	12.9	0.44	1.23	198.3	0.47	60.0
Std. F	1.5	3.0	0.13	0.23	129.0	0.32	40.3
Mean M	3.7	10.7	0.36	1.02	173.2	0.40	58.7
Std. M	1.1	1.3	0.12	0.14	117.6	0.26	43.6
Mean All	4.2	11.9	0.40	1.14	187.1	0.44	59.4
Std. All	1.4	2.6	0.13	0.23	124.9	0.30	41.7

Ca.TV – total volume of canaliculi (mm^3)
LCN.TV – total volume of the LCN (mm^3)
Ca.TV/BV – the porosity of canaliculi (%)
LCN.TV/BV – the porosity of the LCN (%)
Ca.V – average volume of canaliculi per cell (μm^3)

Ca.V/Cell.V – ratio between the average volume of canaliculi and the average volume of cell
Ca.V/Lc.V – ratio between the average volume of canaliculi and the average volume of lacuna

Table 7.3 Number of canaliculi per lacuna at 7 different distances from the surface of the lacuna and the ratio between the number and the average volume of lacuna at the voxel size of 100 nm

Sample ID	Ca.N (r=1.2 μm)	Ca.N (r=3.0 μm)	Ca.N (r=4.8 μm)	Ca.N (r=6.6 μm)	Ca.N (r=8.4 μm)	Ca.N (r=10.2 μm)	Ca.N (r=12.0 μm)
Mean F	58.4	61.8	62.7	64.4	67.1	70.6	76.6
Std. F	36.9	40.2	41.5	44.0	47.4	50.8	56.2
Mean M	49.6	51.9	52.1	53.3	56.0	59.3	64.5
Std. M	31.5	34.8	36.5	38.9	41.8	44.6	48.4
Mean All	54.5	57.4	58.0	59.5	62.2	65.6	71.3
Std. All	35.0	38.3	39.8	42.3	45.5	48.6	53.4
Sample ID	**Ca.N/Lc.V (μm^{-3}, r=1.2 μm)**	**Ca.N/Lc.V (μm^{-3}, r=3.0 μm)**	**Ca.N/Lc.V (μm^{-3}, r=4.8 μm)**	**Ca.N/Lc.V (μm^{-3}, r=6.6 μm)**	**Ca.N/Lc.V (μm^{-3}, r=8.4 μm)**	**Ca.N/Lc.V (μm^{-3}, r=10.2 μm)**	**Ca.N/Lc.V (μm^{-3}, r=12.0 μm)**
Mean F	0.17	0.18	0.18	0.19	0.20	0.21	0.23
Std. F	0.10	0.11	0.11	0.13	0.14	0.15	0.17
Mean M	0.16	0.17	0.17	0.17	0.18	0.20	0.22
Std. M	0.10	0.11	0.12	0.13	0.14	0.15	0.17
Mean All	0.16	0.17	0.18	0.18	0.19	0.20	0.22
Std. All	0.10	0.11	0.12	0.13	0.14	0.15	0.17

Ca.N – number of canaliculi per lacuna
Ca.N/Lc.V – ratio between the number of canaliculi per lacuna and the average volume of lacuna

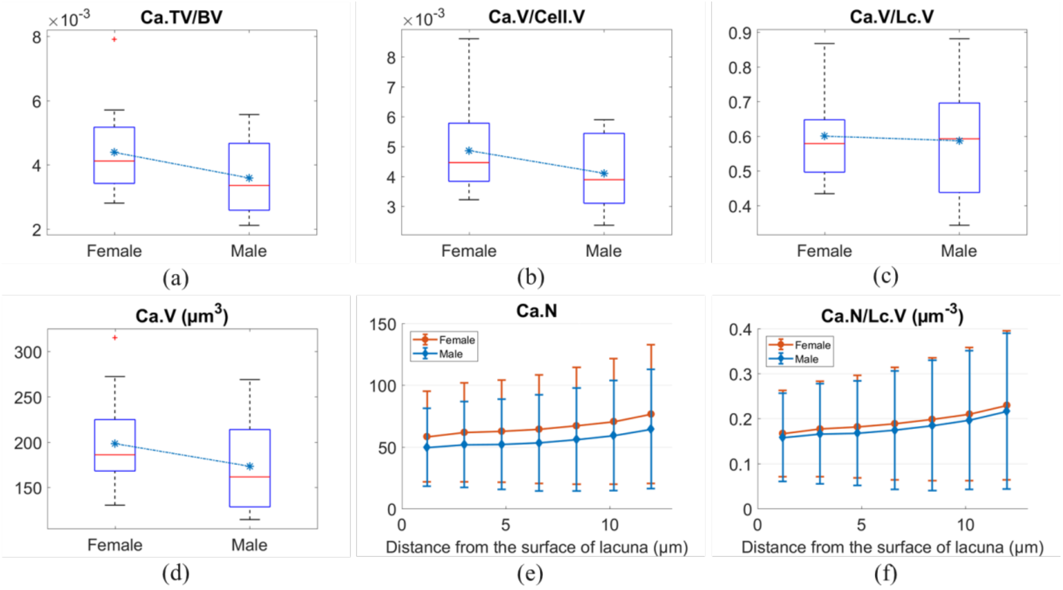

(a) (b) (c)

(d) (e) (f)

Figure 7.3 Some quantitative parameters of canaliculi at the voxel size of 100 nm from female and male groups.

7.3.2.3 Statistical analysis in association with sex

In this section, the statistical differences of parameters with sex are studied. For the parameters which passed the test of the homogeneity of variances, we used the unpaired t-test for the evaluation and the calculated p-values; for the others, we used the Mann-Whitney U test for the analysis as shown in Table 7.4. Between the two groups (female and male), there were no significant differences for most of parameters. But the results of $Lc.TV/BV$, $Lc.V$, $Lc.S$, $LCN.TV/BV$ in the female group are significantly different from those in the male group.

Table 7.4 P-values of F-test, unpaired t-test and Mann-Whitney U test for the two groups

		P-values		
		F-test	Unpaired t-test	Mann-Whitney
Lc.N/BV		0.0015	#	0.3798
Lc.TV/BV		0.0006	#	0.0021
Lc.V		0.4311	0.0009	#
Cell.V		0.0050	#	0.6605
Lc.V/Cell.V		0.0012	#	0.0454
Lc.S		0.9841	0.0045	#
Lc.L1		0.6145	0.1057	#
Lc.L2		0.9764	0.0688	#
Lc.L3		0.2087	0.6080	#
Lc.L1/Lc.L2		0.6352	0.6579	#
Lc.L2/Lc.L3		0.2966	0.5096	#
Lc.SMI		0.8288	0.7138	#
Ca.TV/BV		0.7637	0.1207	#
LCN.TV/BV		0.0952	0.0131	#
Ca.V		0.7518	0.2320	#
Ca.V/Cell.V		0.5055	0.1630	#
Ca.V/Lc.V		0.3933	0.8280	#
Ca.N	r=1.2 µm	0.9653	0.0926	#
	r=3.0 µm	0.8484	0.1006	#
	r=4.8 µm	0.6710	0.0930	#
	r=6.6 µm	0.5244	0.1000	#
	r=8.4 µm	0.5172	0.1229	#
	r=10.2 µm	0.6249	0.1404	#
	r=12.0 µm	0.8352	0.1585	#
Ca.N/Lc.V	r=1.2 µm	0.5412	0.5313	#
	r=3.0 µm	0.3992	0.5155	#
	r=4.8 µm	0.2694	0.4206	#
	r=6.6 µm	0.1865	0.4465	#
	r=8.4 µm	0.1702	0.5054	#
	r=10.2 µm	0.2355	0.5461	#
	r=12.0 µm	0.3302	0.5970	#

7.3.3 Association with age

7.3.3.1 Quantification of the LCN

In order to figure out the association between the quantitative parameters and age, we sort all the samples by the order of age from the youngest to the oldest. Then, we divide them into two groups based on the ages: the young group (≤ 75 years old) and the old group (> 75 years old). The young group contains 11 samples: F1, F2, F3, M1, M2, F4, F5, F6, F7, M3 and F8; the old group contains 16 samples: M4, F9, M5, M6, M7, M8, M9, M10, F10, F11, F12, M11, M12, F13, F14 and F15. In Table 7.5, we give the average results of parameters of lacunae and canaliculi for the two groups.

Similar with the plots for groups of different sex, Fig. 7.4 show several morphologic parameters of lacuna for samples from the young and old groups at the voxel size of 100 nm, such as $Lc.N/BV$, $Lc.TV/BV$, $Lc.V/Cell.V$, $Lc.V$, $Lc.L_1$ and $Lc.L_1/Lc.L_2$. Fig. 7.5 presents some quantitative parameters of canaliculi for different samples of the young and old groups, such as $Ca.TV/BV$, $Ca.V/Cell.V$, $Ca.V/Lc.V$, $Ca.V$, $Ca.N$ and $Ca.N/Lc.V$.

Table 7.5 Average results of parameters of lacunae and canaliculi for volumes from the young and old groups at the voxel size of 100 nm

Sample ID	Lc.N	Lc.TV (×10^{-5} mm^3)	BV (×10^{-3} mm^3)	Lc.TV/BV (%)	Lc.N/BV (×10^4 mm^{-3})	Lc.V (µm^3)	Cell.V (×10^4 µm^3)	Lc.V/Cell.V (%)

Mean Y	219	7.5	10.2	0.74	2.1	348.6	4.9	0.86
Std. Y	42.2	1.4	0.9	0.10	0.3	142.0	2.7	0.54
Mean O	228.3	7.8	10.6	0.73	2.2	339.1	4.6	0.88
Std. O	33.9	1.6	0.4	0.14	0.3	158.0	2.0	0.63

Sample ID	Lc.S (μm^2)	Lc.L1 (μm)	Lc.L2 (μm)	Lc.L3 (μm)	Lc.L1 /Lc.L2	Lc.L2 /Lc.L3	Lc.SMI
Mean Y	350.5	18.5	9.4	4.4	2.1	2.3	3.0
Std. Y	102.3	4.8	2.2	1.2	0.8	0.8	0.4
Mean O	337.1	17.4	9.5	4.5	1.9	2.2	3.1
Std. O	105.4	4.5	2.2	1.3	0.7	0.8	0.4

Sample ID	Ca.TV (10^{-5} mm^3)	LCN.TV (10^{-5} mm^3)	Ca.TV/BV (%)	LCN.TV/BV (%)	Ca.V (μm^3)	Ca.V/Cell.V (%)	Ca.V/Lc.V (%)
Mean Y	4.6	12.2	0.45	1.19	210.2	0.48	65.2
Std. Y	1.8	3.0	0.16	0.23	141.1	0.32	44.8
Mean O	3.9	11.7	0.37	1.10	171.3	0.41	55.5
Std. O	1.0	2.4	0.09	0.22	110.1	0.28	39.1

Sample ID	Ca.N (r=1.2 μm)	Ca.N (r=3.0 μm)	Ca.N (r=4.8 μm)	Ca.N (r=6.6 μm)	Ca.N (r=8.4 μm)	Ca.N (r=10.2 μm)	Ca.N (r=12.0 μm)
Mean Y	60.2	64.1	64.8	66.4	69.2	72.1	77.8
Std. Y	35.7	39.3	41.2	44.4	48.4	52.1	57.8
Mean O	50.6	52.8	53.3	54.7	57.4	61.0	66.7
Std. O	34.0	37.1	38.3	40.2	42.9	45.7	49.8

Sample ID	Ca.N/Lc.V (μm^{-3}, r=1.2 μm)	Ca.N/Lc.V (μm^{-3}, r=3.0 μm)	Ca.N/Lc.V (μm^{-3}, r=4.8 μm)	Ca.N/Lc.V (μm^{-3}, r=6.6 μm)	Ca.N/Lc.V (μm^{-3}, r=8.4 μm)	Ca.N/Lc.V (μm^{-3}, r=10.2 μm)	Ca.N/Lc.V (μm^{-3}, r=12.0 μm)
Mean Y	0.18	0.19	0.19	0.20	0.21	0.22	0.24
Std. Y	0.09	0.11	0.11	0.13	0.14	0.16	0.17
Mean O	0.15	0.16	0.16	0.17	0.18	0.19	0.21
Std. O	0.10	0.11	0.11	0.13	0.14	0.15	0.17

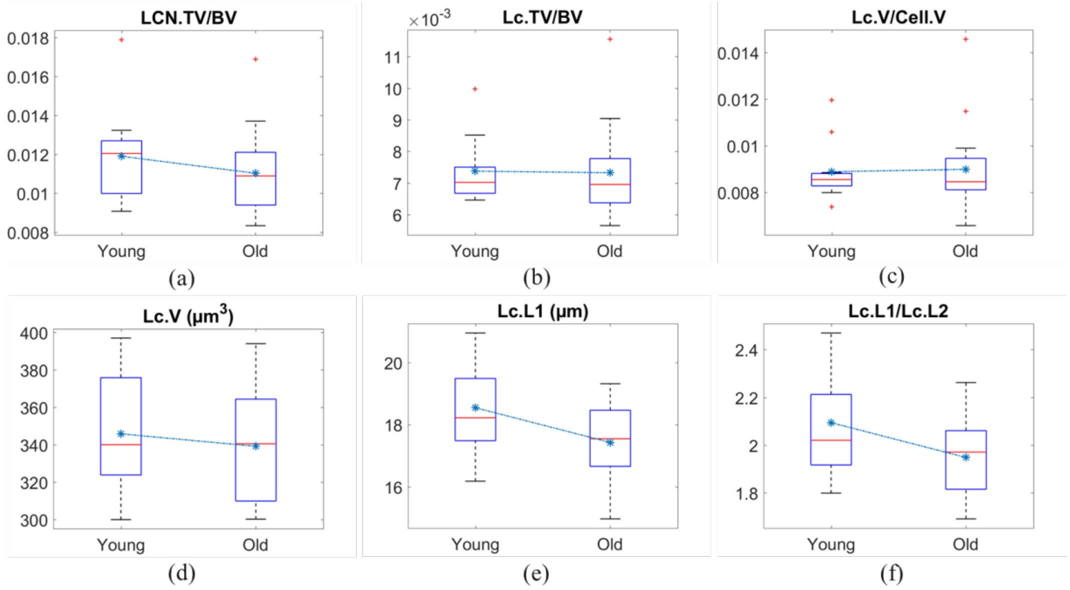

Figure 7.4 Some descriptors for the morphology of lacuna at the voxel size of 100 nm from the groups of different ages.

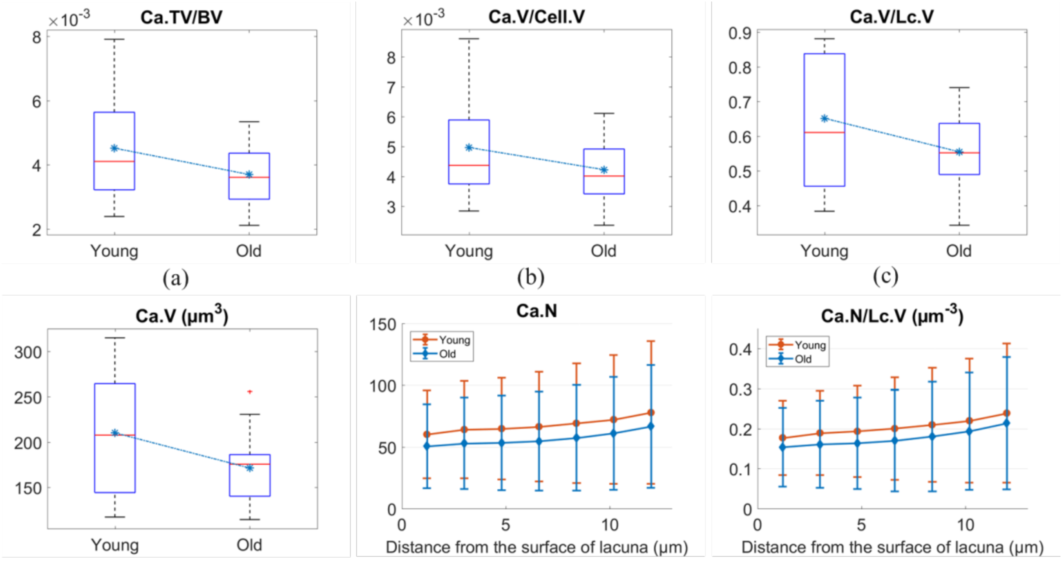

(a) (b) (c)

(d) (e) (f)

Figure 7.5 Some quantitative parameters of canaliculi at the voxel size of 100 nm from the groups of different ages.

7.3.3.2 Statistical analysis

Table 7.5 presents the calculated p-values based on F-test, unpaired t-test and Mann-Whitney U test to compare the young and old groups. From the results, it can be seen that there were no significant differences for most of parameters. But the measurements of $Lc.L1$ in the young group are significantly different from those in the old group.

Table 7.5 P-values of F-test, unpaired t-test and Mann-Whitney U test for the two groups

		P-values		
		F-test	Unpaired t-test	Mann-Whitney
Lc.N/BV		0.9145	0.9313	#
Lc.TV/BV		0.2609	0.9228	#
Lc.V		0.8814	0.4205	#
Cell.V		0.0690	0.2506	#
Lc.V/Cell.V		0.3814	0.7061	#
Lc.S		0.8401	0.2053	#
Lc.L1		0.6714	0.0410	#
Lc.L2		0.1633	0.7876	#
Lc.L3		0.5377	0.3294	#
Lc.L1/Lc.L2		0.3481	0.0561	#
Lc.L2/Lc.L3		0.0517	0.7808	#
Lc.SMI		0.2978	0.1786	#
Ca.TV/BV		0.0670	0.1143	#
LCN.TV/BV		0.7814	0.3422	#
Ca.V		0.0593	0.0607	#
Ca.V/Cell.V		0.1045	0.2238	#
Ca.V/Lc.V		0.0348	#	0.3001
Ca.N	r=1.2 μm	0.1371	0.0687	#
	r=3.0 μm	0.1756	0.0640	#
	r=4.8 μm	0.2019	0.0719	#
	r=6.6 μm	0.2200	0.0840	#
	r=8.4 μm	0.1763	0.1068	#
	r=10.2 μm	0.1239	0.1544	#
	r=12.0 μm	0.0828	0.2028	#
Ca.N/Lc.V	r=1.2 μm	0.0611	0.0927	#
	r=3.0 μm	0.0875	0.0832	#
	r=4.8 μm	0.0936	0.0869	#
	r=6.6 μm	0.0973	0.1147	#

	r=8.4 µm	0.0708	0.1587	#
	r=10.2 µm	0.0412	#	0.4592
	r=12.0 µm	0.0376	#	0.6930

7.3.4 Correlation between parameters

In this section, we show the results of the Spearman correlation coefficients and the corresponding p-values between measured parameters for all the samples. We want to check whether there are good correlation between these quantitative parameters of the lacunae and canaliculi. We listed the results with good correlation ($R^2 > 0.5$ and $p < 0.05$) in Table 8.6 and the regression plots of these parameters were shown in Fig. 7.6 and Fig. 7.7.

Table 7.6 Spearman correlation detection between some parameters for all the samples

Parameter 1	Parameter 2	R^2	p-value
Lc.N/BV	Cell.V	0.7284	<0.0001
Lc.TV/BV	Lc.V/Cell.V	0.9007	<0.0001
Lc.V	Lc.S	0.8189	<0.0001
Lc.L1	Lc.S	0.7400	<0.0001
Lc.L2/Lc.L3	Lc.SMI	0.8173	<0.0001
Ca.TV/BV	Ca.V/Cell.V	0.9688	<0.0001
Ca.V	Ca.N (r=1.2 µm)	0.8717	<0.0001
	Ca.N (r=3.0 µm)	0.8846	<0.0001
	Ca.N (r=4.8 µm)	0.8849	<0.0001
	Ca.N (r=6.6 µm)	0.8747	<0.0001
	Ca.N (r=8.4 µm)	0.8573	<0.0001
	Ca.N (r=10.2 µm)	0.8274	<0.0001
	Ca.N (r=12.0 µm)	0.7936	<0.0001

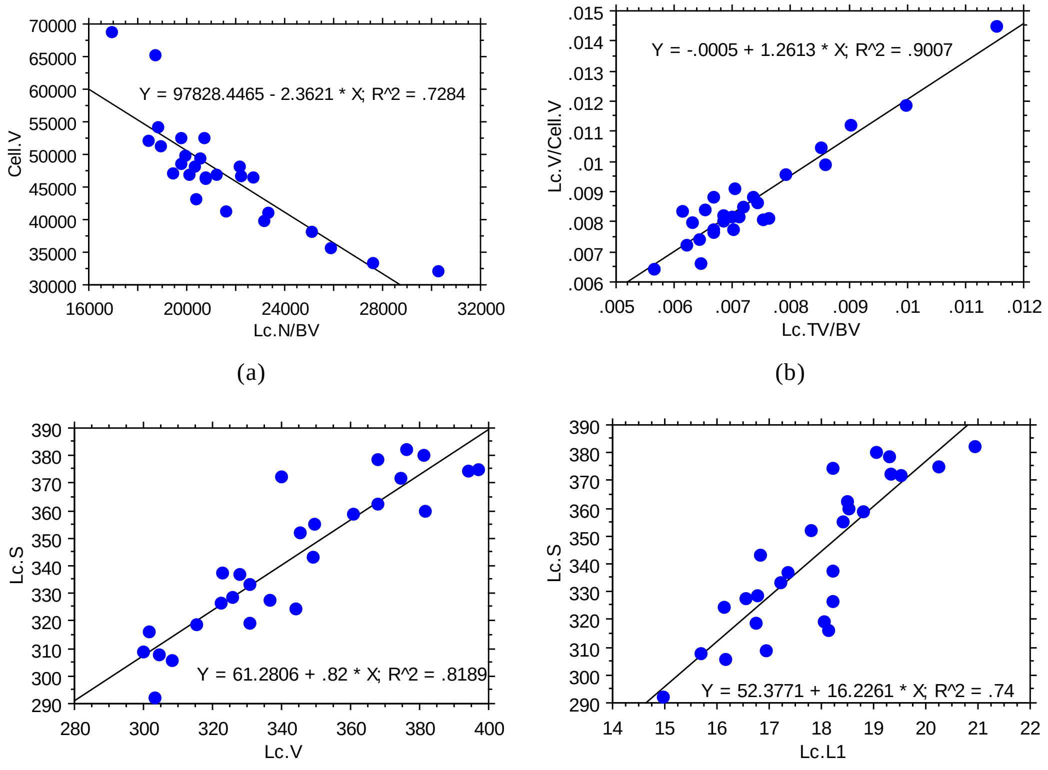

(a) (b)

(c) (d)

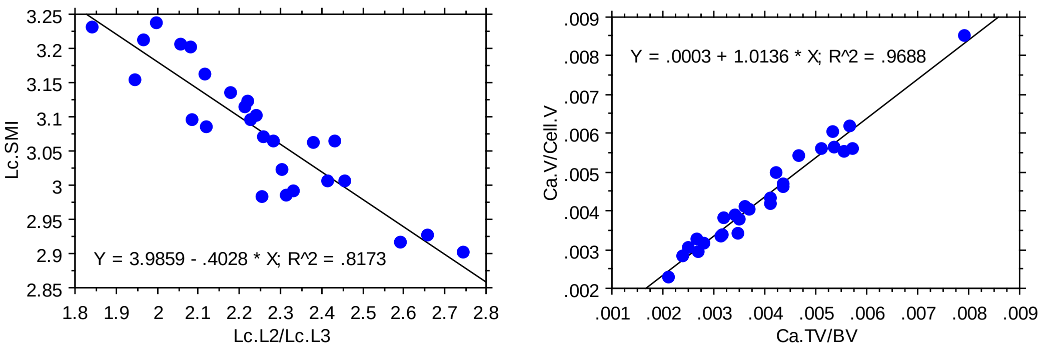

(e) (f)

Figure 7.6 Regression of parameters for the results of the voxel size of 100 nm. (a) correlation between $Cell.V$ (µm^3) and $Lc.N/BV$ (mm^{-3}); (b) correlation between $Lc.V/Cell.V$ and $Lc.TV/BV$;(c) correlation between $Lc.S$ (µm^2) and $Lc.V$ (µm^3); (d) correlation between $Lc.S$ (µm^2) and $Lc.L1$ (µm); (e) correlation between $Lc.SMI$ and $Lc.L1/Lc.L2$; (f) correlation between $Ca.V/Cell.V$ and $Ca.TV/BV$.

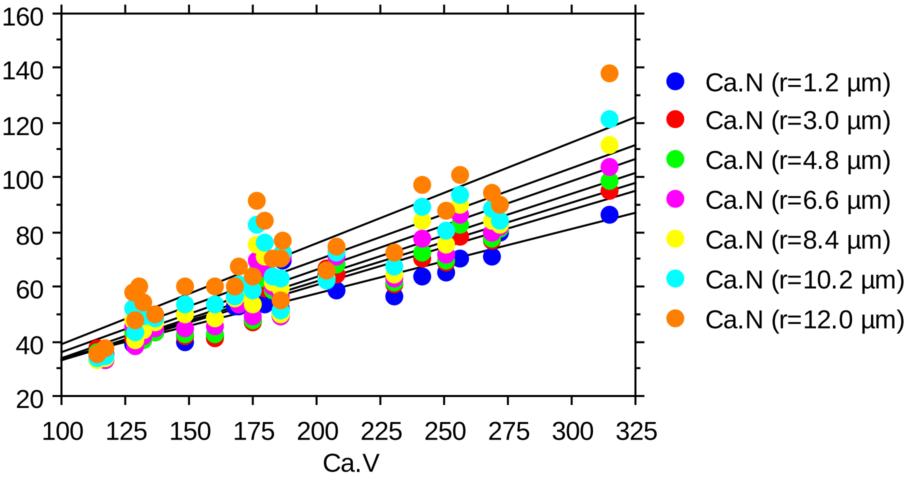

Figure 7.7 Regression between $Ca.N$ at 7 different distances and $Ca.V$ (µm^3) for all the samples at the voxel size of 100 nm.

7.4 Discussion

In this chapter, we reported 3D quantitative parameters obtained on the LCN of 27 human samples taken from the femoral diaphysis. Today, there are no comparative data obtained from such a large data basis on human at such a high spatial resolution in 3D. Conversely to other works using confocal microscopy [Sharma et al. (2012)], [Ashique et al. (2017)], [Kollmannsberger et al. (2017)], our data are extracted from 3D X-ray phase nano-CT images at a voxel size of 100 nm.

Considering the whole group, pooling all the 27 samples together; the he average number of analyzed lacunae in each sample was 224.5 and the density of lacunae ($Lc.N/BV$), 2.6×10^4 mm^{-3} was in the range of 1.5×10^4–3.5×10^4 mm^{-3} as found for instance in [Carter et al. (2013)]. The average lacunar porosity ($Lc.TV/BV$) was 0.73%, canalicular porosity ($Ca.TV/BV$) 0.40%, and the average porosity of the whole network ($LCN.TV/BV$) was 1.14%. These values are a little lower than that of previous research in our group where the lacunar porosity was 0.84% [Dong, Haupert, et al. (2014)], and the canalicular porosity was 0.57% [Varga et al. (2015)]. These differences may be due to the location of the analyzed VOIs. Moreover, we introduced in the present work a local porosity lacuna and canaliculi porosity within their belonging Voronoi cells. The average cell volume $Cell.V$ was 4.7×10^4 μm^3 with a ratio $Lc.V/Cell.V$ being 0.87%. The average canalicular volume within one cell $Ca.V$ was 187.1 μm^3 with a ratio $Ca.V/Cell.V$ of 0.44% and a ratio $Ca.V/Lc.V$ of 59.4%. These parameters permit to quantify the properties of the LCN in a local region instead of the total volume. The value of $Lc.V$ 343.0 μm^3 is in agreement with previous reports (50–730 μm^3) [Remaggi et al. (1998)], [Carter et al. (2013)]. Based on the second-order moments matrix, we calculated the average length (17.9 µm), the width (9.4 µm) and the depth (4.5 µm) of lacuna for our data, as well as the anisotropy of lacuna $Lc.L1/Lc.L2$ (2.0) and $Lc.L2/Lc.L3$ (2.2). These results are consistent with previous reports (~ 17 µm, 9 µm and 4 µm) and the ratio between the length of different axes is about 4:2:1 [van Hove et al. (2009)], [Dong, Haupert, et al. (2014)]. Meanwhile, we got the average surface area $Lc.S$ 342.5 μm^2 which is in agreement with the one 336.2±94.5 μm^2 reported in [Dong, Haupert, et al. (2014)], but lower than 430.4±68.46 μm^2 [Varga et al. (2015)]. The structure model index $Lc.SMI$ was 3.1, which is comparable with previous work of our group [Dong, Haupert, et al. (2014)]. Besides, we quantified the ramification of canaliculi in all volumes. At 7 different physical distances from the surface of each lacuna ranging from 1.2 µm to 12.0 µm, the number of canaliculi of $Ca.N$ increased from 54.5 to 71.3, and the density of canaliculi $Ca.N/Lc.V$ from 0.16 μm^{-3} to 0.22 μm^{-3}. Only few studies reported the number of canaliculi per lacunae. In a previous study using SR nCT, the number of canali per lacuna was found to be 88.5±24.9 in human donors, but the study was limited to 3.3 lacunae per donor compared to 224 in our study [Varga et al. (2015)]. By using CLSM, the number of canali per lacuna was found to be 89.7±15 for rat tibia samples [Sharma et al. (2012)] and 77.5±12.0 for mice femoral samples [Lai et al. (2015)]. In all these works the authors only counted the number of canaliculi per lacuna at one fixed distance, and the evaluation was performed on a much smaller number of lacunae.

We divided the results into two groups according to the sex (i.e. female and male) and compared the measurements between groups. Firstly, we can see that the average number of lacunae in the female group is 231.1 and the density of lacunae is 2.2×10^4 mm^{-3}, both of which are slightly higher than those in the male group 216.3 and 2.1×10^4. The lacunar porosity ($Lc.TV/BV$), the porosity of canaliculi ($Ca.TV/BV$) and the porosity of the LCN ($LCN.TV/BV$) in the female group were 0.79%, 0.44% and 1.23%, and are all higher than those in the male group 0.66%, 0.36% and 1.02%. For the local parameters based on Voronoi cells around each lacuna, the average volume of each cell in the female group 4.7×10^4 μm^3 is equal to that in the male group 4.7×10^4 μm^3, but the average volume of canaliculi per cell was higher in the female group (198.3 μm^3 versus 173.2 μm^3). Also, the local porosity of lacunae and canaliculi $Lc.V/Cell.V$ 0.93%, $Ca.V/Cell.V$ 0.47% and $Ca.V/Lc.V$ 60.0% in the female group are all higher than those in the male group 0.81%, 0.40% and 58.7%, respectively.

Moreover, we calculated parameters to describe the morphology and anisotropy of lacuna. The average volume and surface area of lacuna in the female group respectively 358.5 μm^3 and 354.9 μm^2, are larger than those in the male group, respectively 323.6 μm^3 and 327.14 μm^2). Similarly, the values of $Lc.L1$ and $Lc.L2$ in the female group, respectively 18.3 µm and 9.6 µm are larger than those in the male group, respectively 17.9 µm, 9.4 µm, while the values of $Lc.L3$ are the same 4.5 µm in the two groups. The ratio $Lc.L1/Lc.L2$, $Lc.L2/Lc.L3$ and the structure model index $Lc.SMI$ between groups are quite close, 2.0, 2.3 and 3.1 in the female group, versus 2.0, 2.3 and 3.3 in the male group. These results suggest that the lacunae maintain a similar shape between groups, although their sizes are larger in the female group than those of the male group.

Besides, we computed the number of canaliculi per lacuna at 7 distances from the surface of lacuna. When the distance changes from 1.2 µm to 12.0 µm, we can see that the average number of canaliculi per lacuna ($Ca.N$) in the female group increases from 58.4 to 76.6, and in the male group, we observe a similar growth from 49.6 to 64.5. The local density of canaliculi expressed by the ratio between the number of canaliculi per lacuna and the average volume of lacuna ($Ca.N/Lc.V$) also increases from 0.17 μm^{-3} to 0.23 μm^{-3} in the female group while those in the male group rises up from 0.16 μm^{-3} to 0.22 μm^{-3}.

For a statistical point of view, there are quite few investigations for the influence of sex on the lacunar properties. Using 2D imaging techniques, Mullender et al. found that the lacunar porosity ($Lc.TA/BA$) were significantly increased in healthy women compared to healthy men [Mullender et al. (2005)], while Vashishth et al. and Busse et al. presented that no significant differences in lacunar density were found between women and men [Vashishth et al. (2000)], [Busse et al. (2010)]. Based on SR µCT in 3D, Bach-Gansmo et al. also reported that no significant difference was detected for the lacunar density and the average volume of lacuna, while a non-significant trend of slightly higher values of the average volume of lacuna in women was observed than those in men [Bach-Gansmo et al. (2016)]. Compared with our case, the porosity of lacunae $Lc.TV/BV$ was significantly larger in the female group than those in the male group. Meanwhile, $Lc.V$ and $Lc.S$ which describe the average volume and surface area of lacuna were also significantly higher in the female group. However, there is no significant difference for the lacunar density ($Lc.N/BV$) in two groups, although the average value of $Lc.N/BV$ in the female group (2.22×10^4 mm^{-3}) is non-significantly higher than that in the male group (2.06×10^4 mm^{-3}).

To check the effect of age, we divided the sample into another two groups: the young group and the old group, with threshold at 75 years old. The density of lacunae and the lacunar porosity were quite comparable, while the canaliculi porosity 0.45% was higher in the young group than in the old group 0.37%. The average volume of lacuna and canaliculi within each Voronoi cell, 348.6 μm^3 and 210.2 μm^3 were both larger in the young group than those in the old group 339.1 μm^3 and 171.3 μm^3. The average length of lacuna $Lc.L1$ (18.3 µm) is larger in the young group than that in the old group (17.4 µm), and this difference was statistically significant. There was also a trend to have a larger $Lc.L1/Lc.L2$ ratio in the young group (2.1) compared to that in the old group (1.9). Besides, for the ramification, we also see that the number of canaliculi and the density of canaliculi at 7 different distances from the surface area of lacuna in the young group are both larger than those in the old group.

In previous works, Vashishth et al. and Busse et al. showed that the lacunar density decreased significantly with increasing age in both men and women [Vashishth et al. (2000)], [Busse et al. (2010)]. Bach-Gansmo et al. found that no significant change occurred for the average volume of lacuna with age, while the lacunar density only showed a significant decrease with age when pooling the data for both sexes instead of in separate sex group [Bach-Gansmo et al. (2016)]. By confocal imaging of femoral bone sections in 2D, Ashique et al. reported that the lacunar density ($Lc.N/BA$) and the canalicular porosity ($Ca.TA/BA$) decreased significantly in aged women [Ashique et al. (2017)]. However, in our case, we found some differences between the two groups but none of them was found statistically different except the average lacunae length $Lc.L1$. The average volume of lacuna ($Lc.V$) and the canalicular porosity ($Ca.TV/BV$) were non-significantly higher in the young group than those in the old group, while the lacunar density ($Lc.N/BV$) of two groups was quite close. We acknowledge the limitation of this study considering the effect of age, since all donors were relatively old (> 50 years old) and no information was available regarding the health condition of the donors.

Finally, we showed the Spearman correlation coefficients and the p-values between some measured parameters of two groups. Similarly with the results in Chapter 6, we notice that there are good correlations between some pairs of parameters, such as $Cell.V$ and $Lc.N/BV$, $Lc.S$ and $Lc.V$, $Lc.S$ and $Lc.L1$, $Lc.L2/Lc.L3$ and $Lc.SMI$, $Lc.V/Cell.V$

and $Lc.TV/BV$, $Ca.V/Cell.V$ and $Ca.TV/BV$. Furthermore, we find that the number of canaliculi per lacuna $Ca.N$ at all 7 distances is highly related to the average volume of canaliculi per Voronoi cell. This means that we count a larger number of canaliculi per lacuna when we segment more volumes of canaliculi within each cell.

In conclusion, we used magnified X-ray phase nano-CT for the investigation and analysis of the LCN in 27 human femoral samples from female and male donors. All the data were scanned at the voxel size of 100 nm in the beamline ID16B of the ESRF. To check the association with sex and age, we divided the reconstructed volumes into different groups: female and male, young and old. After comparison, we found that the average volume and the geometrical size of lacuna in the female group are all larger than those in the male group. And the average volume and density of canaliculi per Voronoi cell tended to increase in the female group compared those in the male group, although these results did not reach significance. Considering the influence of age, there was a non-significant trend of larger values of the morphology of lacuna, the average volume and density of canaliculi in the young group than those in the old group. We expect that these parameters of the lacunae and canaliculi can help to analyze and understand bone microstructures and provide references for other researchers for the mechanisms of bone fragility in disease.

Conclusion and perspective

The objective of this thesis was to quantify the LCN in a large number of human bone samples from magnified X-ray phase nano-CT at the ESRF.

Compared with conventional attenuation-based X-ray CT, X-ray phase CT offers a higher sensitivity and permits to image weakly absorbing samples such as soft tissue and materials with small changes in attenuation. Phase contrast can be obtained experimentally by various techniques on either synchrotron radiation or laboratory sources. Synchrotron radiation sources permits to have high brilliance and coherent beams enabling the implementation of propagation based phase contrast imaging. In this thesis, we used magnified X-ray phase nano-CT, which belongs to class of techniques on beamlines optimized to reach very high spatial resolution (up to a few tenths of nanometers).

Our first contribution concerned the study of phase retrieval algorithms when performing quantitative X-ray phase CT. We extended Paganin's single distance formula to multiple distance acquisitions and made a comparison with the homogeneous CTF method using a single or multiple distances. The two phase retrieval methods were applied to data sets of bone samples acquired at the voxel size of 120 nm and 30 nm. We investigated the gain of using several propagation distances instead of one and, of using an iterative method (NLCG) to refine further the retrieved phase maps. The SNR and spatial resolution were calculated to evaluate the quality of the reconstructed images. From a visual point of view, we found that the images reconstructed from the multiple distances methods are sharper than those reconstructed from only one propagation distance. This result was corroborated by the quantitative computation, which showed an increase in estimated spatial resolution when using images recorded at several propagation distances. Thus, we verified the feasibility of using magnified X-ray phase nano-CT to image the LCN in human bone samples and illustrated the benefits of applying the extended Paganin's method followed by NLCG. In the remaining of this work, we used this approach for the acquisition and reconstruction of all images in this thesis.

Our second contribution concerns the acquisition of images of human femoral samples at the two beamlines ID16A and ID16B of the ESRF. Typically, 2000 projections at ID16A and 3400 projections at ID16B were recorded over a range of 180° at 4 different sample-to-detector distances. In total, we scanned 13 samples from female donors at ID16A. Because sometimes the samples from the same donor was scanned more than once at different voxel sizes, we obtained 8 reconstructed volumes at the voxel size of 120 nm, 9 volumes at 50 nm and 14 volumes at 30 nm. Each sample was scanned at voxel sizes of 120 nm, 50 nm or 30 nm under two specific energies 17 or 33.6 keV, and the size of one reconstructed volume was 2048×2048×2048 voxels. At ID16B, we scanned 27 samples from 15 female and 12 male donors, where one sample corresponded to one donor. The voxel size was 100 nm and the energy was 29.6 keV. The volume size was 2560×2560×2160 voxels.

Our third contribution was the development of the processing workflow to analyze these data. The segmentation methods are illustrated in Chapter 5. Actually, we met several challenges in the beginning and the most important one was the large size of the dataset which influenced the computing efficiency. For example, the size of each reconstructed volume at ID16A was 32 GB and that at ID16B was 52.7 GB. Therefore, we needed to consider the usage of computer memory and the running time of programs when we selected processing methods. In order to segment lacunae, we chose some classical and efficient image processing methods such as the median filter, the hysteresis thresholding method and connected components analysis. To segment canaliculi, we made use of the vesselness enhancement to improve the visibility of line structures, the variational region growing to extract canaliculi and connected components analysis to remove residual noise. The results in Chapter 5 proved that these methods could cope with large datasets and maintain quality of segmentation within accessible limit of running time. It might provide a reference for other researchers who encountered similar problems.

In Chapter 5 and Chapter 6, we presented a number of quantitative parameters that can be used to analyze the LCN at different voxel sizes. We first calculated some classical parameters e.g. the porosity and density of lacunae and canaliculi. We introduced local porosity and density lacunae and canaliculi parameters calculated on Voronoi cells after a Voronoi tessellation of the volume. Morphological descriptors for each lacuna were calculated from 3D image moments and intrinsic volumes. We also computed the numbers of canaliculi per lacuna at different distances from the surface of the lacuna and the ratio between the number of canaliculi per lacuna and the average surface area of lacuna located in the same cell. All the parameters were used to evaluate the properties LCN and were compared with those in previous studies to verify the reliability of the measurements. Besides, we compared the quantitative results of reconstructions at different voxel sizes but located in the same volume of interest. The porosity and density of lacunae and canaliculi for the reconstructed volumes at 30 nm are all higher than those at 120 nm. However, we can much less number of lacunae (~ 5) at 30 nm compared with that (~ 260) at 120 nm. Therefore, we found that using the voxel size of 30 nm could achieve better observation and quantification of canaliculi, but the voxel size of 120 nm was more suitable to investigate and analyze the 3D properties of the whole network with a larger field of view.

We reported the quantitative results of reconstructed volumes of ID16B at the voxel size of 100 nm in Chapter 7. We analyzed 27 volumes, 15 volumes from female donors and 12 from male donors, providing more samples to perform statistical analysis. The lacunae and canaliculi were segmented by the methods described in Chapter 5. To check the association with sex and age, we divided the reconstructed volumes into different groups: female and male, young and old. After comparison, we find that the average volume and the geometrical size of lacuna, the average volume and the density of canaliculi per Voronoi cell in the female group are all larger than those in the male group. Similarly, there are more volumes of lacunae and larger number of canaliculi in the young group than those in the old group. Also, our quantifications maintained consistent with those results in previous references after comparison.

Our works belong to a part of the MULTIPS project whose main purposes were to investigate the properties of cortical bone including stiffness and toughness, micro- and nanostructure and the characteristics of mineral crystals and of the collagen. We achieved the observation and quantification of the lacunae and canaliculi at the nano scale by using synchrotron radiation nano-CT. All our quantitative results are expected to help understand nanostructures of cortical bone can research further the 3D properties of bone with collaboration with other studies of our colleagues such as stiffness and mineralization in the MULTIPS project.

One challenge in our work was the segmentation of canaliculi, which will directly influence the subsequent quantification and analysis. Conversely to the segmentation of lacunae for which there exist mature methods, the segmentation of canaliculi was difficult due to several reasons. First of all, the physical size of canaliculi is at the nano scale e.g. the diameter of canaliculi is about in the range of 100–500 nm. Therefore, it needs imaging techniques which can provide a high spatial resolution. This requirement was fulfilled when using magnified phase nano CT with voxel sizes smaller than 120nm. However, at this scale other micro structures such as collagen fibers and speckle noise were found to influence the segmentation because they shared similar same gray levels and geometrical structures. This means that more space and feature information should be used when implementing segmentation. The last problem is how to keep the connectivity of canaliculi after segmentation. Because of the operation of filtering, the connection of canaliculi could be broken after processing. Therefore, a perspective could be to further develop segmentation methods dedicated to canaliculi by trying to preserve the connectivity of canaliculi without introducing false channels.

Concerning the quantification of lacunae and canaliculi, it is still meaningful to find or design some descriptors for the 3D structures of the LCN. There may be a lot of parameters for the quantification of lacunae such as porosity, density, morphology, anisotropy and orientation. However, the classes of parameters to quantify canaliculi are still limited except some usual ones like diameter, porosity and ramification. In this thesis, we calculated the density of canaliculi by the ratio between the number of canaliculi per lacuna and the volume of lacuna located in the same Voronoi cell. Besides, it is meaningful to compute some parameters to evaluate the properties of the whole network instead of lacunae and canaliculi separately. Not just the volume and porosity, but some new parameters may help to figure out the spatial distribution and the topological structure of the LCN. From a bone research point of view, a perspective would also be to use the developed method to assess the LCN properties in different disease or in animal models.

In conclusion, in this work a complete workflow, going from data acquisition in magnified X-ray phase nano-CT to quantitative analysis was developed. s. Although only some classical image processing methods were used in this work, it is still worth considering when researchers meet the same conditions of dealing with large datasets or extracting channel structures. Meanwhile, the quantitative results discussed in Chapter 5, Chapter 6 and Chapter 7 are able to offer references for the study in the same biological or medical field. Also, all the work in this thesis illustrating the evaluation of 3D structures of lacunae and canaliculi are expected to offer a better understanding of bone microarchitectures and help to research the mechanisms of bone fragility in disease cooperating with other studies.

Annex 1

In this annex, we attached the MIPs along the Y-axis from the reconstructed volumes of all the samples scanned at the beamlines ID16A and ID16B. For the samples scanned at ID16A, we showed the MIPs along the Y-axis of 100 middle slices for 8 reconstructed volumes at the voxel size of 120 nm, and we gave the MIPs along the Y-axis of all the slices for 9 reconstructed volumes at the voxel size of 50 nm and 7 volumes at 30 nm. For the samples at ID16B, we presented the MIPs along the Y-axis of 100 middle slices for 27 reconstructed volumes at the voxel size of 100 nm.

Beamline: ID16A

Voxel size: 120 nm

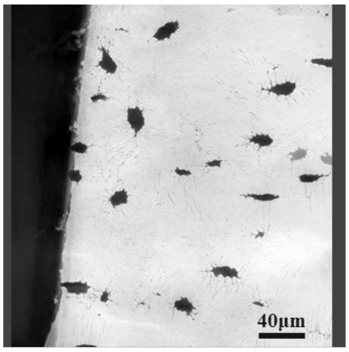

A2 (#166)

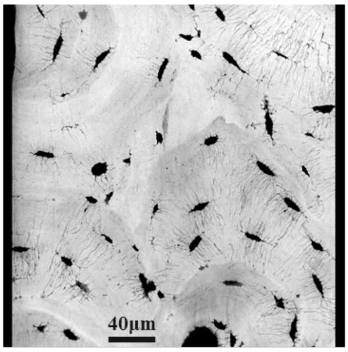

A3 (#204)

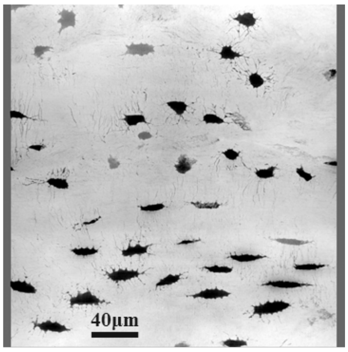

A6 (#246)

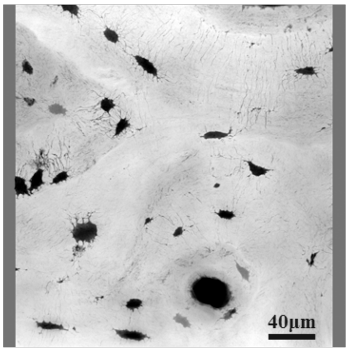

A8 (#067)

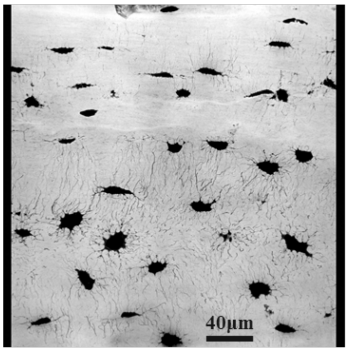

A9 (#213)

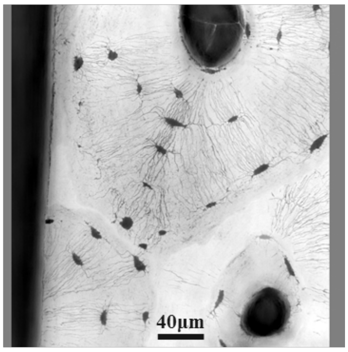

A11 (#214)

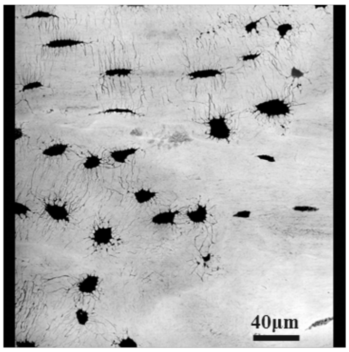

A12 (#234)

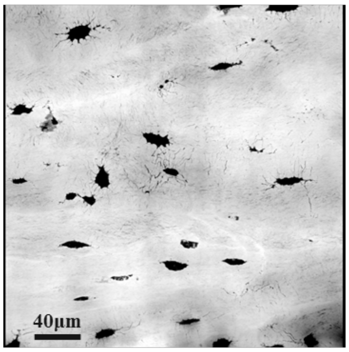

A13 (#239)

Beamline: ID16A

Voxel size: 50 nm

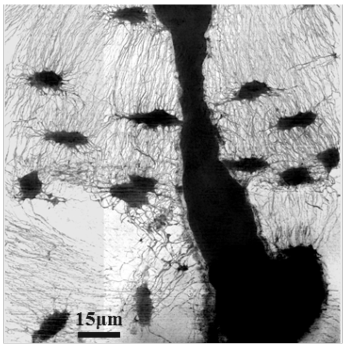

B1 (#166)

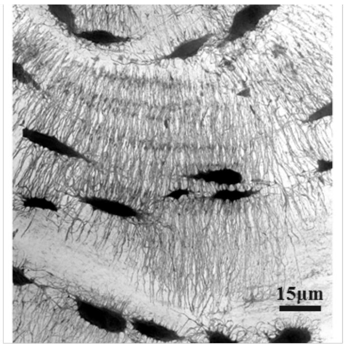

B4-1 (#240)

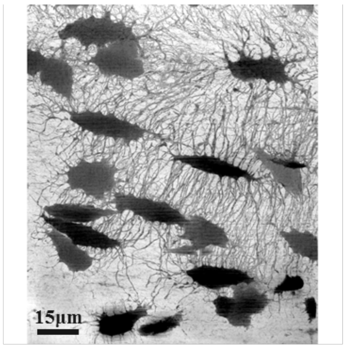

B4-2 (#240)

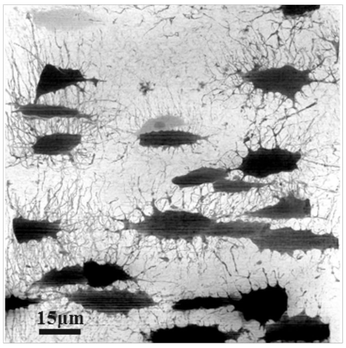

B4-3 (#240)

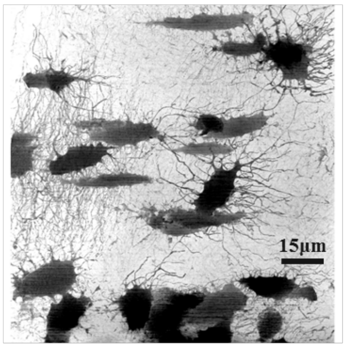

B4-4 (#240)

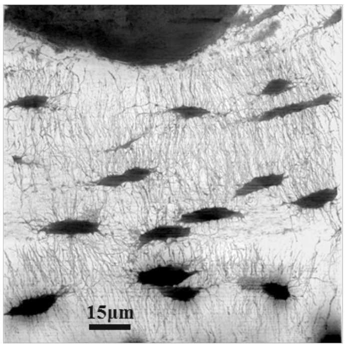

B5 (#024)

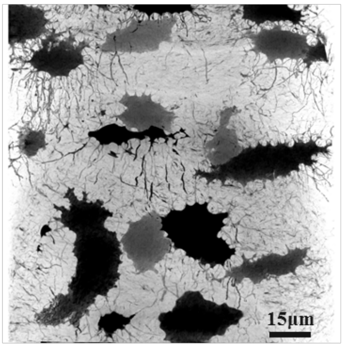

B7 (#013)

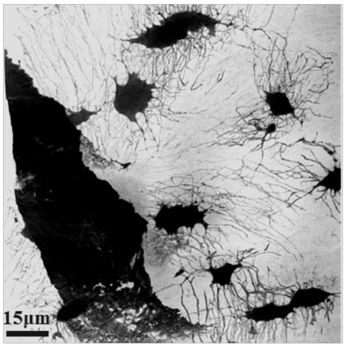

B10 (#245)

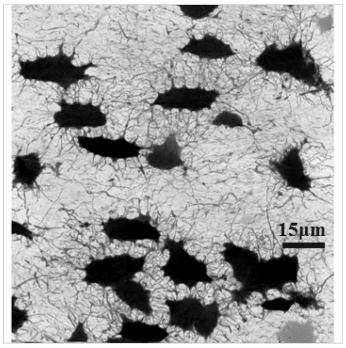

B11 (#214)

Beamline: ID16A

Voxel size: 30 nm

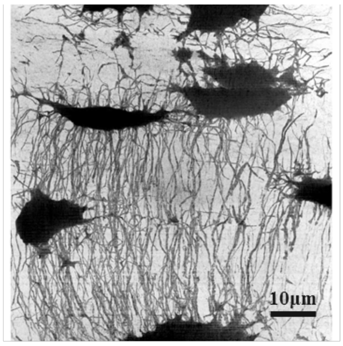

C2 (#166)

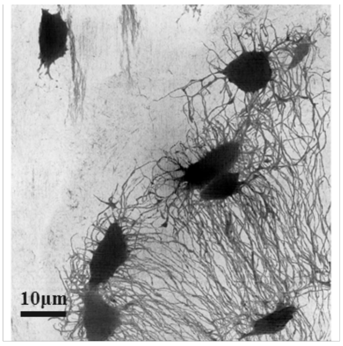

C3 (#204)

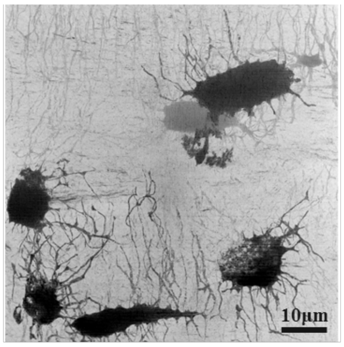

C6 (#246)

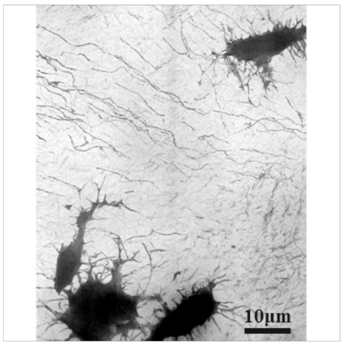

C8 (#067)

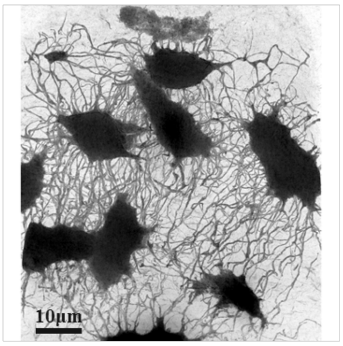

C9 (#213)

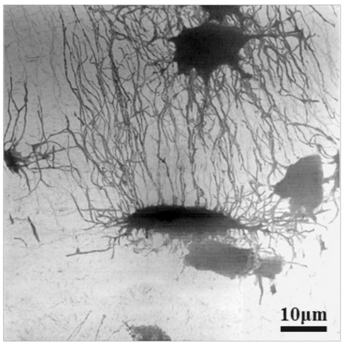

C12 (#234)

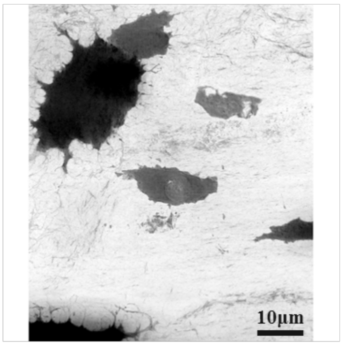

C13 (#239)

Beamline: ID16B

Voxel size: 100 nm

Sex: Female

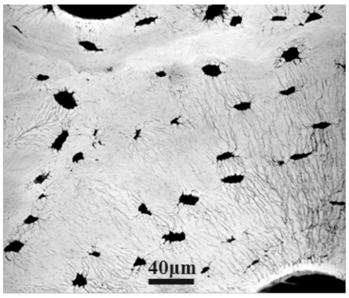

F1 (#154)

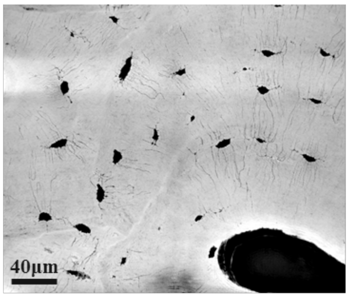

F2 (#166)

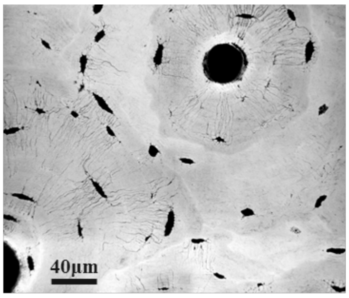

F3 (#204)

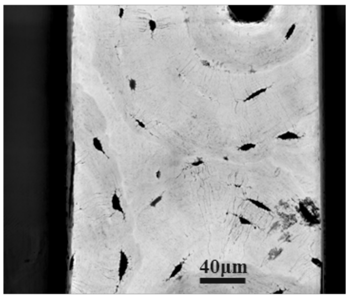

F4 (#240)

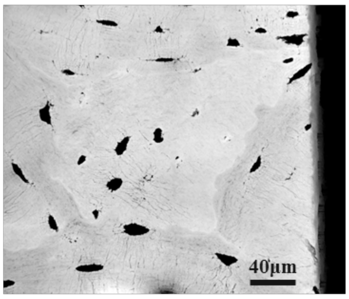

F5 (#024)

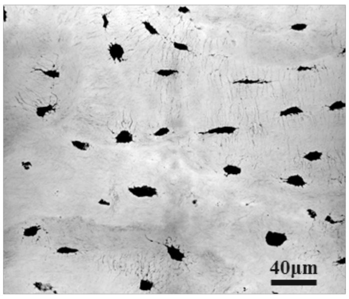

F6 (#246)

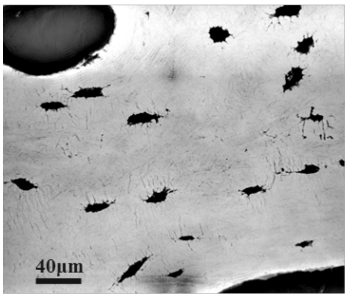

F7 (#013)

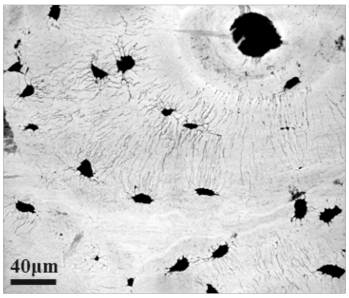

F8 (#067)

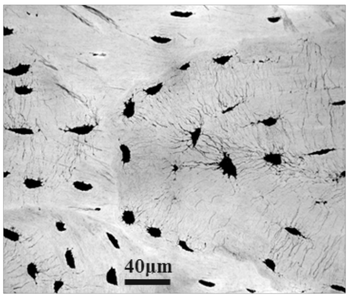

F9 (#213)

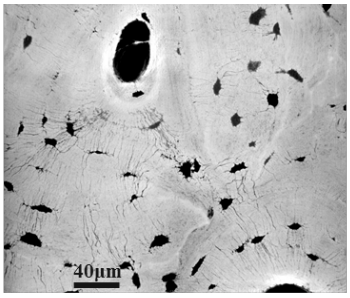

F10 (#229)

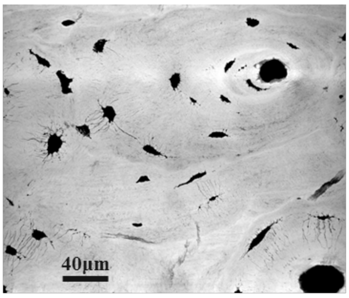

F11 (#232)

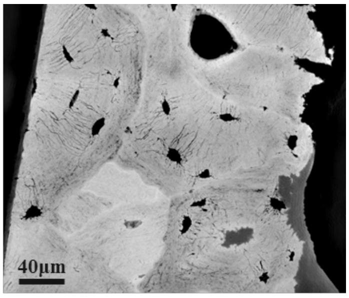

F12 (#214)

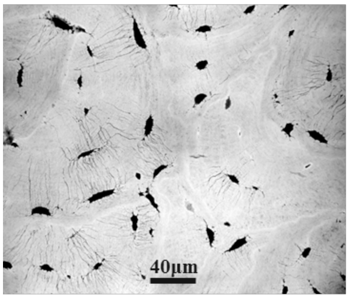

F13 (#222)

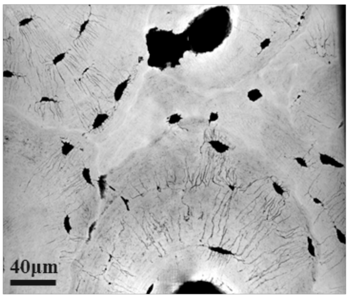

F14 (#234)

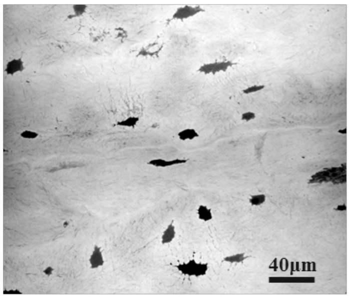

F15 (#239)

Beamline: ID16B

Voxel size: 100 nm

Sex: Male

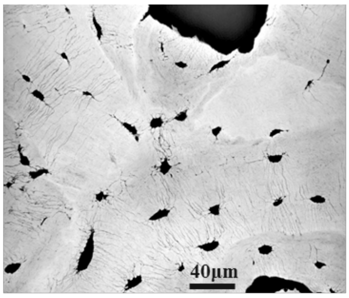

M1 (#121)

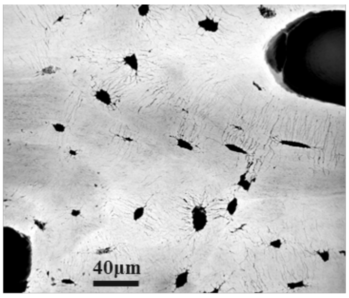

M2 (#206)

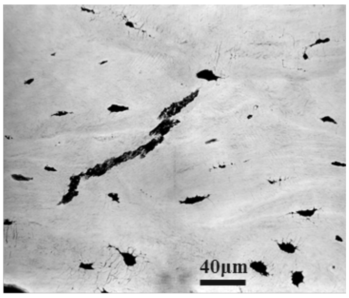

M3 (#056)

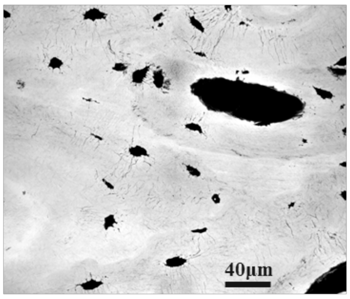

M4 (#161)

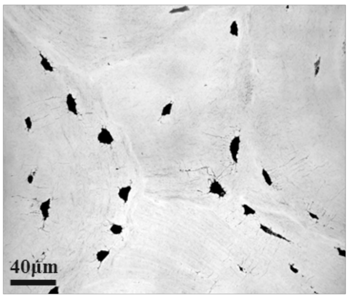

M5 (#138)

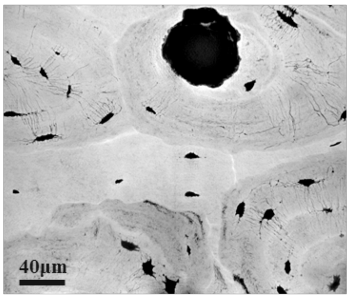

M6 (#245)

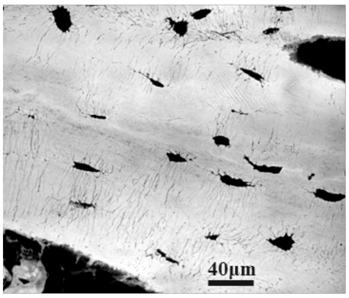

M7 (#215)

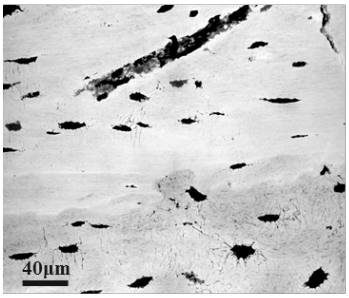

M8 (#211)

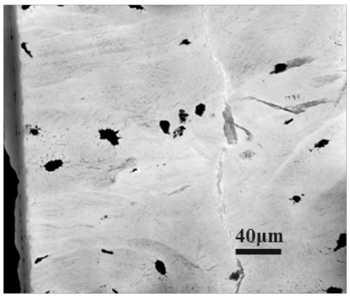

M9 (#250)

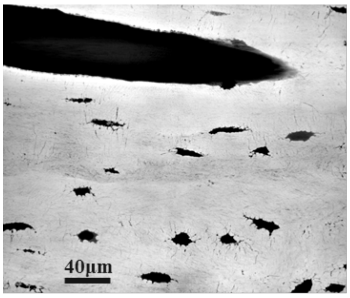

M10 (#244)

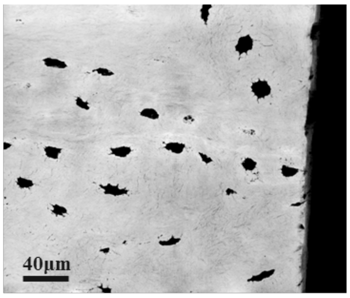

M11 (#230)

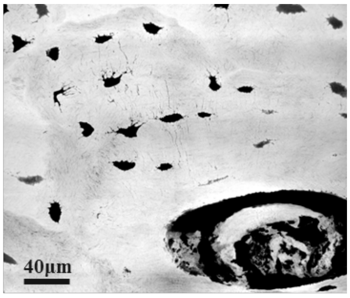

M12 (#090)

Annex 2

In this annex, we attached the plots of parameters for the reconstructed volumes at the voxel size of 30 nm and the PCM volumes together as a supplement of the contexts in Chapter 6. Fig. 1 shows some parameters of the morphology of lacuna, such as the average length, width and depth, as well as the descriptors of the flatness ($Lc.L1/Lc.L2$, $Lc.L1/Lc.L2$ and $Lc.SMI$). Figure 2 presents the average porosity of lacunae and canaliculi within their belonging cells. We show the average volume of lacuna, canaliculi and the cell, as well as the ratios between these values of volumes ($Lc.V/Cell.V$, $Ca.V/Cell.V$ and $Ca.V/Lc.V$). Figure 3 presents the average number and density of canaliculi at 7 distances from the surface of lacuna among two groups.

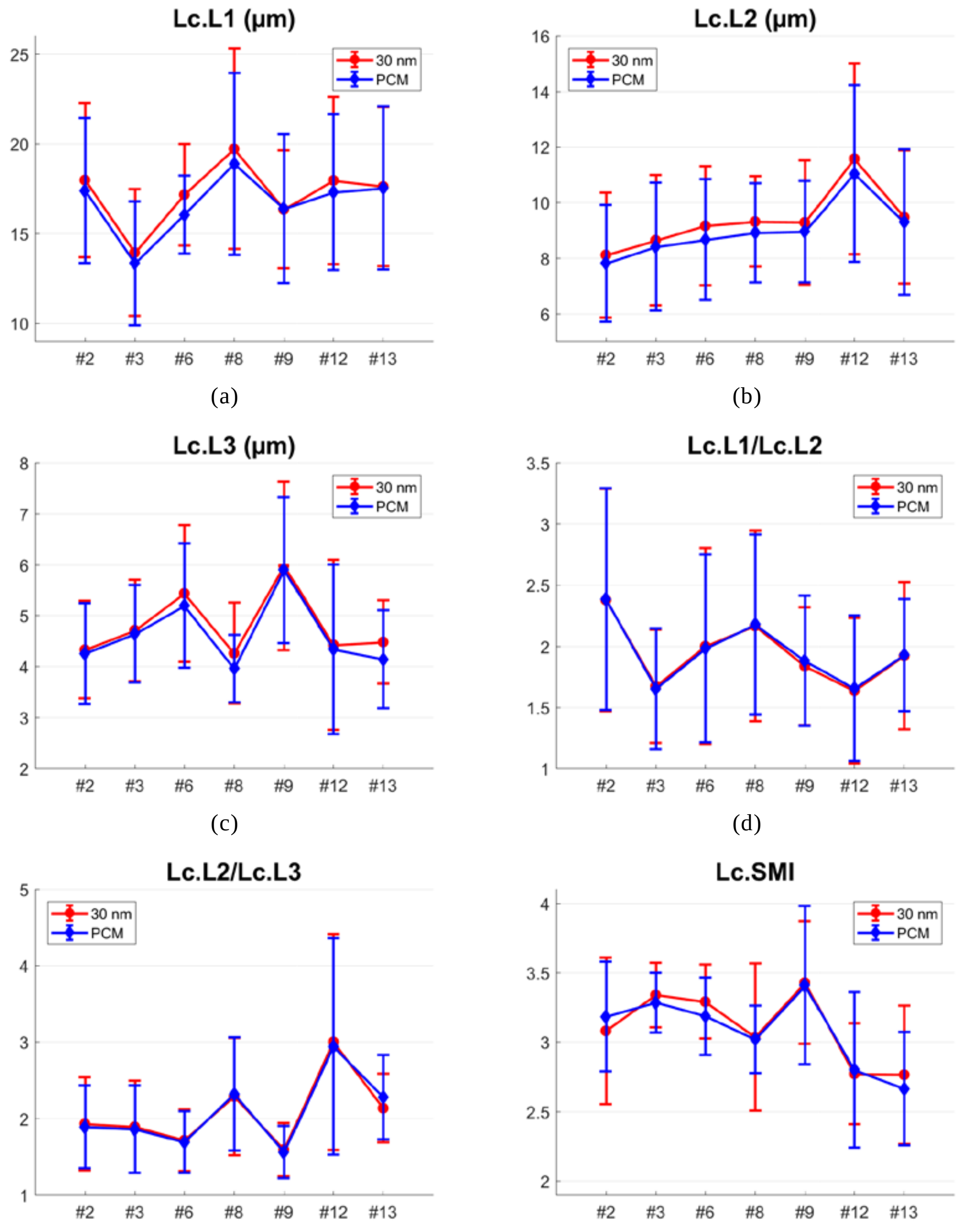

(a) (b)

(c) (d)

(e) (f)

Figure 1 Some descriptors for the morphology of lacuna for the reconstructed volumes at the voxel size of 30 nm and the cropped volumes at 120 nm.

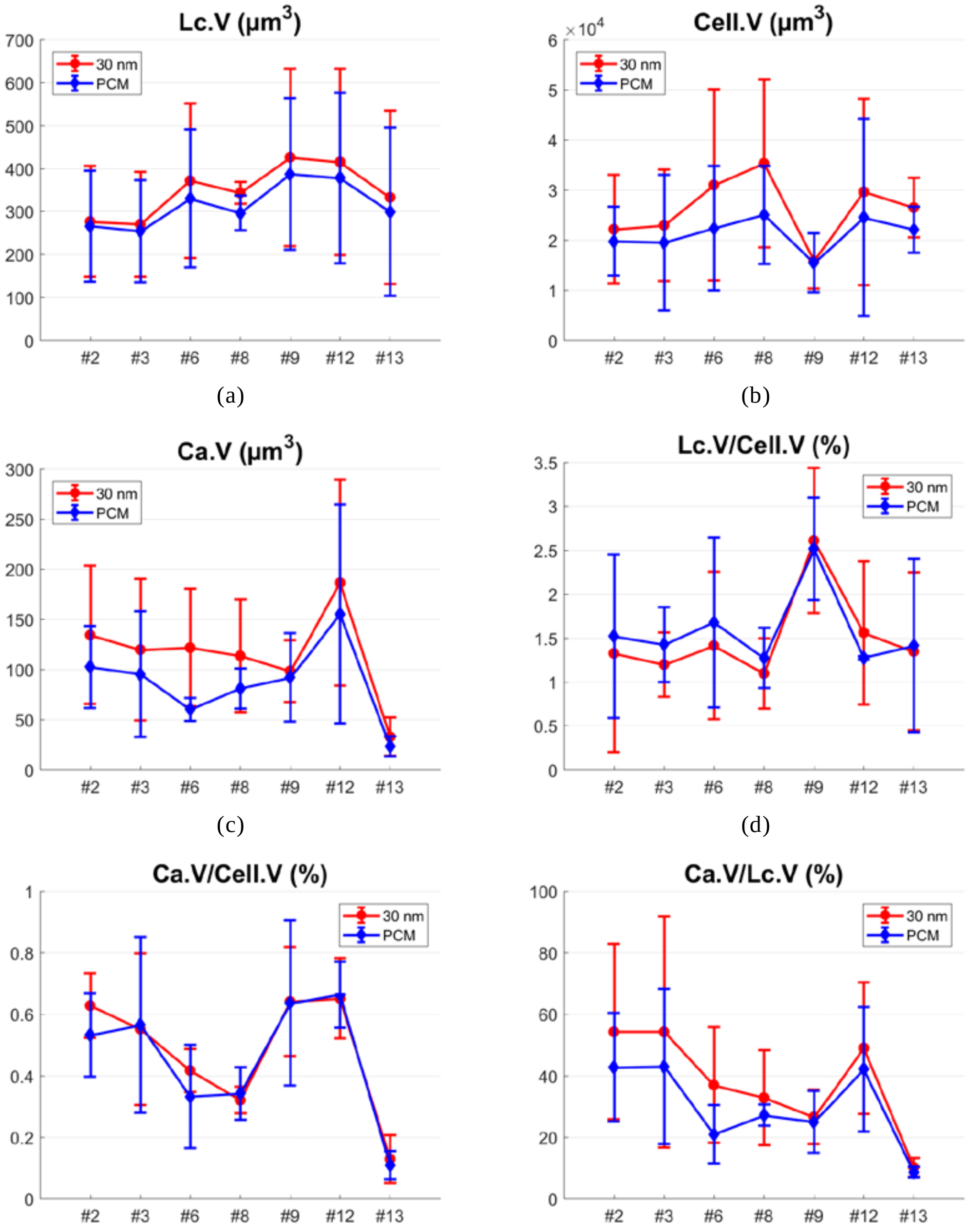

(a) (b)

(c) (d)

(e) (f)

Figure 2 Average porosity of lacunae and canaliculi within different cells for the reconstructed volumes at the voxel size of 30 nm and the cropped volumes at 120 nm.

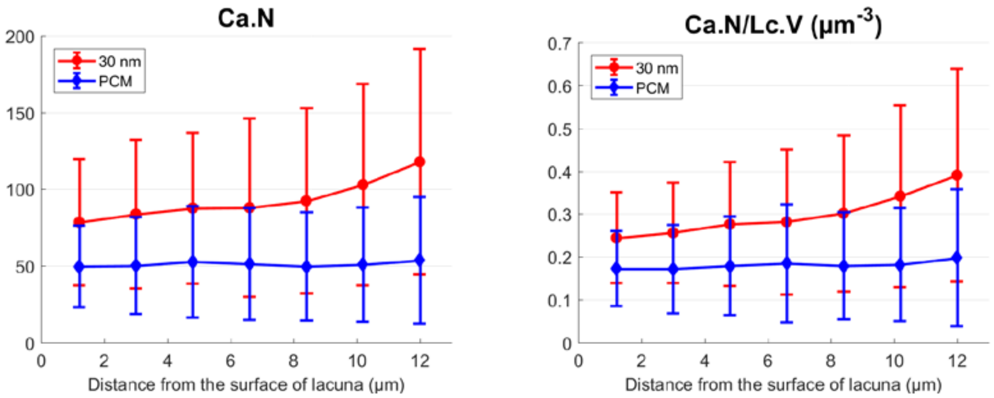

(a) (b)

Figure 3 Number of canaliculi per lacuna at 7 distances from the surface of lacuna and the ratio between the number of canaliculi and the average volume of lacuna for the reconstructed volumes at the voxel size of 30 nm and the cropped volumes at 120 nm.

Annex 3

In this annex, we attached the quantitative results for all the reconstructed volumes at the voxel size of 100 nm scanned in ID16B. Table 1 illustrates the morphometric parameters of lacunae for all the samples; Table 2 shows the morphometric parameters of canaliculi; Table 3 displays the quantitative results of the ramification of canaliculi.

Table 1 Morphometric parameters of lacunae at the voxel size of 100 nm.

Sample ID	Lc.N	Lc.TV ($\times10^{-5}$ mm^3)	BV ($\times10^{-3}$ mm^3)	Lc.TV/BV (%)	Lc.N/BV ($\times10^4$ mm^{-3})	Lc.V (μm^3)	Cell.V ($\times10^4$ μm^3)	Lc.V/Cell.V (%)
F1	274	10.9	10.9	1.00	2.5	397.1±177.3	3.8±1.4	1.19±0.77
F2	210	7.9	10.6	0.74	2.0	376.4±159.3	5.3±2.8	0.86±0.52
F3	227	7.8	10.9	0.72	2.1	345.5±114.7	4.6±1.8	0.85±0.40
F4	151	5.8	8.9	0.65	1.7	381.1±136.3	6.9±3.5	0.66±0.33
F5	151	5.7	8.1	0.70	1.9	374.4±169.0	6.5±5.3	0.78±0.51
F6	302	9.3	10.9	0.85	2.8	308.3±105.5	3.3±1.2	1.05±0.58
F7	211	7.2	10.3	0.7	2.1	340.0±142.9	4.9±2.6	0.82±0.46
F8	229	7.6	10.1	0.75	2.3	330.9±141.1	4.6±1.9	0.81±0.44
F9	272	9.5	10.5	0.90	2.6	349.0±123.9	3.6±1.5	1.12±0.54
F10	328	12.5	10.8	1.15	3.0	381.6±202.5	3.2±1.3	1.45±1.11
F11	222	8.7	11.0	0.79	2.0	394.1±187.1	4.7±1.7	0.96±0.60
F12	218	7.5	9.8	0.76	2.2	344.2±174.5	4.8±2.0	0.81±0.48
F13	260	9.6	11.1	0.86	2.3	368.0±186.7	4.1±1.4	0.99±0.55
F14	205	7.4	10.8	0.68	1.9	360.7±141.8	5.1±2.0	0.80±0.43
F15	206	6.7	10.4	0.64	2.0	325.9±177.6	4.9±2.1	0.74±0.45
M1	208	6.7	10.0	0.67	2.1	322.4±121.6	5.3±2.6	0.76±0.46
M2	221	6.6	9.9	0.67	2.2	330.9±99.8	4.7±3.2	0.77±0.38
M3	225	7.4	11.0	0.67	2.0	327.8±146.9	4.3±1.7	0.88±0.56
M4	250	7.6	10.8	0.70	2.3	304.4±136.1	4.0±1.7	0.91±0.59
M5	196	6.6	10.6	0.62	1.8	336.8±132.6	5.2±2.0	0.72±0.40
M6	200	6.0	10.6	0.57	1.9	300.2±125.4	5.4±2.2	0.64±0.36
M7	204	7.5	10.2	0.74	2.0	368.1±158.0	5.0±2.1	0.88±0.55
M8	237	7.2	11.0	0.65	2.2	301.9±152.3	4.1±1.5	0.84±0.73
M9	225	6.8	10.8	0.63	2.1	303.3±132.8	4.6±2.3	0.80±0.50
M10	224	7.2	10.6	0.69	2.1	323.1±134.8	4.7±1.9	0.82±0.51
M11	202	7.1	9.9	0.71	2.0	349.6±126.1	4.8±2.0	0.82±0.39
M12	204	6.4	10.5	0.61	1.9	315.4±131.0	4.7±2.4	0.83±0.51

Sample ID	Lc.S (μm^2)	Lc.L1 (μm)	Lc.L2 (μm)	Lc.L3 (μm)	Lc.L1 /Lc.L2	Lc.L2 /Lc.L3	Lc.SMI
F1	374.7±104.8	20.3±5.7	8.9±2.2	4.9±1.5	2.5±1.1	1.9±0.7	3.2±0.4
F2	382.0±117.7	20.9±4.9	9.2±2.3	4.2±0.9	2.4±0.8	2.3±0.7	3.0±0.4
F3	352.2±84.7	17.8±3.6	10.3±1.9	4.1±1.1	1.8±0.5	2.7±0.8	2.9±0.4
F4	380.0±95.3	19.1±4.4	10.1±2.3	4.4±1.2	2.0±0.8	2.5±0.8	3.0±0.4
F5	371.9±118.9	19.5±4.8	9.6±2.6	4.4±1.1	2.2±0.8	2.3±0.8	3.0±0.4
F6	305.8±75.8	16.2±4.5	8.7±1.8	5.0±1.2	2.0±0.8	1.8±0.5	3.2±0.4
F7	372.4±126.3	19.3±4.3	10.2±2.6	3.8±0.8	2.0±0.7	2.7±0.9	2.9±0.4
F8	333.4±101.9	17.2±4.1	9.6±2.2	4.5±1.3	1.9±0.7	2.3±0.8	3.1±0.4
F9	343.3±88.4	16.8±4.0	9.8±2.0	4.7±1.1	1.8±0.6	2.2±0.8	3.1±0.4
F10	359.6±118.5	18.5±5.5	9.3±2.2	4.9±1.8	2.1±0.9	2.1±0.7	3.2±0.4
F11	374.2±121.3	18.2±4.8	10.0±2.4	4.7±1.3	1.9±0.7	2.2±0.7	3.1±0.4
F12	324.3±106.2	16.2±3.7	9.4±2.2	4.9±1.5	1.8±0.6	2.1±0.8	3.2±0.4
F13	362.6±120.1	18.5±5.0	9.8±2.5	4.4±1.3	2.0±0.8	2.4±0.8	3.1±0.4
F14	358.7±100.9	18.8±4.4	9.4±2.4	4.5±1.2	2.1±0.8	2.2±0.8	3.1±0.4
F15	328.4±119.4	16.8±4.0	9.7±2.5	4.3±1.3	1.8±0.6	2.4±0.9	3.1±0.4
M1	326.5±83.9	18.2±4.7	8.7±1.9	4.6±1.1	2.2±0.8	2.0±0.6	3.2±0.3
M2	319.3±81.8	18.0±4.9	8.8±1.8	4.3±1.0	2.2±0.8	2.1±0.6	3.1±0.3
M3	336.8±97.8	17.4±4.3	9.6±2.2	4.4±1.2	1.9±0.7	2.3±0.8	3.0±0.4
M4	307.9±82.5	15.7±3.1	9.6±1.9	4.3±1.4	1.7±0.5	2.4±0.9	3.0±0.4
M5	327.4±79.4	16.6±3.8	9.4±2.0	4.9±1.5	1.8±0.7	2.1±0.8	3.2±0.4
M6	308.7±87.1	16.9±3.9	9.0±2.1	4.2±1.0	2.0±0.8	2.2±0.7	3.1±0.4

M7	378.7±116.3	19.3±4.6	10.1±2.3	4.2±1.2	2.0±0.7	2.6±0.9	2.9±0.4
M8	316.1±109.0	18.1±5.3	8.5±2.0	4.3±1.2	2.3±0.9	2.1±0.6	3.1±0.3
M9	292.3±82.3	15.0±3.6	9.1±1.9	4.9±1.3	1.7±0.6	2.0±0.7	3.2±0.4
M10	337.4±104.9	18.2±3.8	9.2±2.3	4.3±1.1	2.1±0.7	2.3±0.8	3.1±0.4
M11	355.0±88.2	18.4±4.5	9.7±2.0	4.5±1.2	2.0±0.7	2.3±0.7	3.0±0.4
M12	318.6±90.7	16.8±4.0	9.3±2.2	4.6±1.2	1.9±0.9	2.2±0.8	3.1±0.4

Lc.N – number of lacunae
Lc.TV – total volume of lacunae (mm^3)
BV – bone volume (mm^3)
Lc.TV/BV – lacunar porosity (%)
Lc.N/BV – density of lacunae (mm^{-3})
Lc.V – average volume of lacuna (μm^3)
Cell.V – average volume of each cell (μm^3)
Lc.V/Cell.V – ratio between the average volume of lacuna and its belonging cell (%)
Lc.S – average surface area of lacuna (μm^2)
Lc.L1, Lc.L2 and Lc.L3 – average length, width and depth of lacuna (μm)
Lc.L1/Lc.L2 and Lc.L2/Lc.L3 – average anisotropy of lacuna
Lc.SMI – average structural model index of lacuna

Table 2 Morphometric parameters of canaliculi at the voxel size of 100 nm.

Sample ID	Ca.TV (10^{-5} mm^3)	LCN.TV (10^{-5} mm^3)	Ca.TV/BV (%)	LCN.TV/BV (%)	Ca.V (μm^3)	Ca.V/Cell.V (%)	Ca.V/Lc.V (%)
F1	8.6	19.5	0.79	1.79	315.1±181.3	0.85±0.46	86.7±50.4
F2	4.4	12.3	0.41	1.15	207.6±89.7	0.43±0.19	61.1±33.7
F3	6.2	14.0	0.57	1.28	272.2±160.1	0.62±0.34	82.5±56.7
F4	3.1	8.8	0.35	0.99	204.2±86.0	0.34±0.16	57.9±31.9
F5	2.5	8.2	0.31	1.02	167.6±103.2	0.33±0.25	48.5±28.5
F6	3.9	13.2	0.36	1.21	130.4±83.3	0.41±0.26	44.6±29.0
F7	2.9	10.1	0.28	0.98	136.5±63.3	0.32±0.17	43.4±21.8
F8	5.7	13.3	0.57	1.32	251.1±154.7	0.56±0.27	81.5±49.4
F9	4.9	14.4	0.47	1.37	180.1±124.6	0.54±0.38	53.1±35.0
F10	5.8	18.3	0.53	1.69	176.5±86.2	0.61±0.33	54.8±35.6
F11	3.8	12.5	0.34	1.13	169.5±103.0	0.39±0.24	46.5±27.2
F12	4.1	11.6	0.41	1.17	185.9±106.0	0.42±0.25	60.7±36.3
F13	4.8	14.4	0.44	1.29	186.5±115.7	0.47±0.26	54.7±34.6
F14	4.7	12.1	0.44	1.12	230.5±149.3	0.46±0.26	66.0±38.5
F15	3.3	10.0	0.32	0.96	160.4±91.5	0.34±0.15	58.4±39.8
M1	5.6	12.3	0.56	1.22	269.0±146.0	0.56±0.26	88.1±47.0
M2	5.3	12.0	0.54	1.20	241.3±132.1	0.56±0.27	84.2±46.1
M3	2.6	10.0	0.24	0.91	117.3±86.7	0.28±0.19	38.3±27.8
M4	4.6	12.2	0.42	1.13	182.6±111.3	0.50±0.28	64.5±40.0
M5	2.2	8.8	0.21	0.83	114.4±74.8	0.23±0.14	34.3±19.0
M6	3.7	9.7	0.35	0.92	186.3±106.2	0.38±0.23	65.1±37.5
M7	5.2	12.7	0.51	1.25	255.9±150.3	0.56±0.33	74.0±44.2
M8	3.5	10.7	0.32	0.97	148.4±114.3	0.38±0.28	55.6±48.2
M9	2.9	9.7	0.27	0.90	128.9±79.9	0.33±0.28	48.4±42.9
M10	3.9	11.1	0.37	1.06	174.7±77.4	0.40±0.17	62.9±44.4
M11	2.7	9.7	0.27	0.98	132.2±71.6	0.29±0.16	39.2±19.6
M12	2.6	9.0	0.25	0.86	128.0±68.4	0.31±0.18	49.5±49.5

Ca.TV – total volume of canaliculi (mm^3)
LCN.TV – total volume of the LCN (mm^3)
Ca.TV/BV – the porosity of canaliculi (%)
LCN.TV/BV – the porosity of the LCN (%)
Ca.V – average volume of canaliculi per cell (μm^3)
Ca.V/Cell.V – ratio between the average volume of canaliculi and the average volume of cell
Ca.V/Lc.V – ratio between the average volume of canaliculi and the average volume of lacuna

Table 3 Number of canaliculi per lacuna at 7 different distances from the surface of the lacuna and the ratio between the number and the average volume of lacuna at the voxel size of 100 nm.

Sample ID	Ca.N (r=1.2 μm)	Ca.N (r=3.0 μm)	Ca.N (r=4.8 μm)	Ca.N (r=6.6 μm)	Ca.N (r=8.4 μm)	Ca.N (r=10.2 μm)	Ca.N (r=12.0 μm)
F1	86.6±37.7	95.2±42.5	99.0±48.3	103.9±55.1	111.6±63.3	121.7±72.0	138.1±85.3
F2	58.9±29.1	64.7±33.1	68.1±35.0	70.9±38.4	73.1±39.9	72.2±40.3	74.5±41.5
F3	79.5±40.7	83.4±44.4	81.3±45.2	81.7±46.8	82.8±50.5	84.3±53.0	89.9±56.6
F4	64.1±30.8	67.0±31.7	65.6±32.3	63.2±31.9	62.7±33.1	62.3±32.2	65.6±32.8
F5	52.9±34.6	56.0±38.1	56.1±36.9	55.9±38.7	55.8±39.8	56.7±42.6	60.1±44.5
F6	41.0±30.5	44.8±33.5	45.9±35.0	47.7±37.3	51.0±40.2	55.3±43.1	60.0±46.1
F7	43.3±24.7	43.0±25.4	43.6±27.3	45.0±31.7	46.6±36.7	48.2±36.1	50.2±37.6
F8	65.3±30.5	68.6±32.9	69.7±34.3	71.6±36.0	75.5±37.1	80.8±39.1	87.8±43.3
F9	53.9±39.7	59.0±45.0	62.7±48.4	66.4±52.3	70.7±56.4	76.4±59.0	84.5±63.8
F10	57.5±34.9	62.0±37.6	64.8±40.0	69.9±43.6	75.3±48.0	82.8±54.5	91.4±59.1
F11	52.8±44.2	53.6±46.1	53.4±44.6	53.9±42.5	57.1±43.4	61.1±42.4	67.5±46.5
F12	52.4±28.7	55.1±31.5	55.4±32.2	56.7±32.5	59.7±36.0	63.2±37.9	70.0±44.1
F13	69.8±40.8	72.6±44.1	71.5±42.4	70.9±44.3	72.5±46.4	72.8±48.1	77.1±51.1
F14	56.2±30.8	61.0±34.3	61.3±34.8	62.7±36.3	64.1±37.9	67.7±41.2	72.4±44.2
F15	41.7±29.3	41.1±28.3	42.5±28.2	45.7±29.0	48.6±30.2	53.6±32.1	60.3±35.5
M1	70.9±31.1	76.8±33.2	77.3±34.0	79.8±37.0	84.2±40.5	88.5±45.0	94.5±47.1
M2	63.7±30.5	70.1±35.0	72.8±37.4	77.8±41.6	83.9±45.3	89.1±48.5	97.6±52.3
M3	35.6±26.4	35.1±27.6	33.4±27.0	33.2±27.2	33.6±28.6	34.5±29.2	37.8±31.5
M4	57.7±32.6	60.3±36.0	58.7±36.3	60.1±37.5	61.5±39.3	63.6±40.0	70.0±42.4
M5	36.8±25.6	37.7±27.6	36.0±27.2	34.3±27.2	33.3±25.9	34.1±25.7	35.0±26.3
M6	48.9±31.1	50.8±34.0	49.9±34.0	49.0±35.6	50.1±35.8	51.1±36.5	54.8±39.4
M7	70.3±36.6	78.2±40.5	82.4±44.6	86.3±48.7	90.2±51.9	94.0±56.3	100.6±59.9
M8	39.7±29.5	41.6±33.2	42.5±35.0	44.8±38.2	49.8±43.6	53.6±48.0	60.1±54.7
M9	41.3±29.0	41.9±30.9	40.6±31.3	38.3±31.0	40.2±33.4	43.2±35.6	47.9±41.6
M10	47.8±22.6	47.3±24.3	47.9±27.0	49.2±27.4	53.2±30.4	58.6±33.4	63.6±34.7
M11	43.3±28.3	41.5±27.7	40.4±28.1	41.6±28.3	44.3±30.9	49.0±34.7	54.1±39.0
M12	39.2±23.1	41.3±24.9	43.2±27.8	45.3±30.9	47.9±33.2	51.7±37.5	58.3±41.7

Sample ID	Ca.N/Lc.V (μm^{-3}, r=1.2 μm)	Ca.N/Lc.V (μm^{-3}, r=3.0 μm)	Ca.N/Lc.V (μm^{-3}, r=4.8 μm)	Ca.N/Lc.V (μm^{-3}, r=6.6 μm)	Ca.N/Lc.V (μm^{-3}, r=8.4 μm)	Ca.N/Lc.V (μm^{-3}, r=10.2 μm)	Ca.N/Lc.V (μm^{-3}, r=12.0 μm)
F1	0.23±0.08	0.25±0.09	0.26±0.12	0.28±0.14	0.30±0.16	0.33±0.18	0.37±0.22
F2	0.16±0.06	0.18±0.08	0.19±0.08	0.20±0.10	0.20±0.10	0.20±0.10	0.21±0.11
F3	0.23±0.12	0.24±0.13	0.24±0.13	0.24±0.15	0.25±0.16	0.25±0.16	0.27±0.18
F4	0.17±0.07	0.18±0.08	0.18±0.09	0.17±0.09	0.17±0.10	0.17±0.10	0.19±0.11
F5	0.14±0.08	0.15±0.09	0.16±0.09	0.16±0.09	0.15±0.09	0.16±0.10	0.17±0.11
F6	0.13±0.09	0.14±0.10	0.15±0.11	0.16±0.12	0.17±0.13	0.18±0.14	0.20±0.15
F7	0.13±0.07	0.13±0.07	0.13±0.07	0.14±0.08	0.14±0.09	0.15±0.10	0.15±0.11
F8	0.21±0.08	0.22±0.09	0.22±0.10	0.23±0.11	0.25±0.13	0.27±0.15	0.30±0.17
F9	0.15±0.10	0.17±0.12	0.18±0.13	0.19±0.14	0.20±0.15	0.22±0.17	0.25±0.18
F10	0.16±0.10	0.18±0.11	0.19±0.11	0.20±0.13	0.22±0.14	0.24±0.16	0.27±0.18
F11	0.13±0.10	0.14±0.10	0.14±0.10	0.14±0.10	0.16±0.11	0.17±0.13	0.19±0.15
F12	0.16±0.10	0.17±0.10	0.18±0.11	0.18±0.11	0.19±0.12	0.20±0.13	0.23±0.14
F13	0.20±0.10	0.21±0.12	0.21±0.12	0.21±0.13	0.21±0.14	0.22±0.15	0.23±0.16
F14	0.16±0.07	0.17±0.07	0.17±0.08	0.18±0.09	0.18±0.10	0.19±0.11	0.21±0.12
F15	0.14±0.09	0.14±0.10	0.14±0.11	0.16±0.14	0.17±0.13	0.19±0.15	0.22±0.16
M1	0.22±0.08	0.24±0.08	0.25±0.10	0.26±0.12	0.28±0.14	0.29±0.16	0.31±0.16
M2	0.21±0.09	0.24±0.10	0.25±0.11	0.27±0.14	0.29±0.15	0.31±0.17	0.34±0.19
M3	0.11±0.07	0.11±0.08	0.10±0.08	0.10±0.09	0.10±0.09	0.11±0.09	0.12±0.10
M4	0.19±0.10	0.20±0.12	0.20±0.12	0.21±0.14	0.22±0.15	0.22±0.15	0.25±0.17
M5	0.11±0.06	0.11±0.07	0.10±0.07	0.10±0.07	0.10±0.07	0.10±0.08	0.10±0.08
M6	0.16±0.08	0.17±0.10	0.17±0.10	0.16±0.11	0.17±0.12	0.18±0.13	0.19±0.15
M7	0.19±0.08	0.22±0.10	0.23±0.11	0.24±0.12	0.26±0.14	0.27±0.15	0.29±0.17
M8	0.14±0.11	0.15±0.14	0.15±0.14	0.16±0.16	0.18±0.19	0.20±0.18	0.22±0.21
M9	0.15±0.12	0.15±0.13	0.14±0.13	0.14±0.14	0.15±0.15	0.16±0.16	0.18±0.19
M10	0.16±0.08	0.16±0.09	0.16±0.09	0.17±0.10	0.18±0.11	0.20±0.12	0.22±0.15
M11	0.12±0.07	0.12±0.07	0.12±0.08	0.12±0.09	0.13±0.09	0.14±0.11	0.16±0.12
M12	0.14±0.11	0.14±0.11	0.15±0.10	0.16±0.12	0.17±0.12	0.18±0.14	0.20±0.16

Ca.N – number of canaliculi per lacuna

Ca.N/Lc.V – ratio between the number of canaliculi per lacuna and the average volume of lacuna

Publications

Journal article

[1] **B. Yu**, L. Weber, A. Pacureanu, M. Langer, C. Olivier, P. Cloetens, and F. Peyrin, “Evaluation of phase retrieval approaches in magnified X-ray phase nano computerized tomography applied to bone tissue,” Opt. Express 26(9), 11110, 2018.

Conference paper

[2] **B. Yu**, L. Weber, A. Pacureanu, M. Langer, C. Olivier, P. Cloetens, and F. Peyrin, “Phase retrieval in 3D X-ray magnified phase nano CT: Imaging bone tissue at the nanoscale,” in *2017 IEEE 14th International Symposium on Biomedical Imaging (ISBI 2017)*, IEEE, pp. 56–59, 2017.

[3] **B. Yu**, M. Langer, A. Pacureanu, R. Gauthier, H. Follet, D. Mitton, C. Olivier, P. Cloetens, and F. Peyrin, “Assessment of imaging quality in magnified phase CT of human bone tissue at the nanoscale,” in *Developments in X-Ray Tomography XI*, Proc. SPIE 103910L, 2017.

[4] X. Cai, R. Gauthier, L. Peralta, H. Follet, E. Gineyts, M. Langer, **B. Yu**, C. Olivier, F. Peyrin, D. Mitton, Q. Grimal, and P. Laugier, “Relationships between cortical bone quality biomarkers: Stiffness, toughness, microstructure, mineralization, cross-links and collagen,” in *2017 IEEE International Ultrasonics Symposium (IUS)*, IEEE, pp. 1–1, 2017.

International conferences (abstracts)

[5] **B. Yu**, L. Weber, A. Pacureanu, R. Gauthier, C. Olivier, M. Langer, H. Follet, D. Mitton, P. Cloetens and F. Peyrin, “Synchrotron radiation phase CT for the investigation of nano properties in femoral human bone,” in *22nd Congress of the European Society of Biomechanics (ESB)*, Lyon, 2016.

[6] **B. Yu**, M. Langer, A. Pacureanu, C. Olivier, P-J. Gouttenoire, P. Cloetens, and F. Peyrin, “Assessment of the lacuno-canalicular network in human bone from magnified phase nano-CT images,” in *21st International Bone Densitometry Workshop IBDW/ESUCB*, Germany, 2017.

[7] D. Fiole, **B. Yu**, A. Pacureanu, P. Varga, C. Olivier, P-J. Gouttenoire, M. Langer, P. Cloetens, F. Peyrin, “Evaluation of bone collagen fibril three-dimensional orientation in nano-CT images using a refined autocorrelation-based method,” in *8th World Congress of Biomechanics (WCB)*, Dublin, 2018.

Bibliography

A. Al Hassan, R. B. Lewis, H. Küpers, W.-H. Lin, D. Bahrami, T. Krause, D. Salomon, A. Tahraoui, M. Hanke, L. Geelhaar, and U. Pietsch. "Determination of indium content of GaAs/(In,Ga)As/(GaAs) core-shell(-shell) nanowires by x-ray diffraction and nano x-ray fluorescence," *Phys. Rev. Mater.*, 2(1), 2018.

J. C. Andrews, E. Almeida, M. C. H. van der Meulen, J. S. Alwood, C. Lee, Y. Liu, J. Chen, F. Meirer, M. Feser, J. Gelb, J. Rudati, A. Tkachuk, W. Yun, and P. Pianetta. "Nanoscale X-Ray Microscopic Imaging of Mammalian Mineralized Tissue," *Microsc. Microanal.*, 16(03), 327–336, 2010.

J. M. Andronowski, A. Z. Mundorff, I. V. Pratt, J. M. Davoren, and D. M. L. Cooper. "Evaluating differential nuclear DNA yield rates and osteocyte numbers among human bone tissue types: A synchrotron radiation micro-CT approach," *Forensic Sci. Int. Genet.*, 28, 211–218, 2017.

R. Annunziata, A. Garzelli, L. Ballerini, A. Mecocci, and E. Trucco. "Leveraging Multiscale Hessian-Based Enhancement With a Novel Exudate Inpainting Technique for Retinal Vessel Segmentation," *IEEE J. Biomed. Health Inform.*, 20(4), 1129–1138, 2016.

N. Asada, M. Sato, and Y. Katayama. "Communication of bone cells with hematopoiesis, immunity and energy metabolism," *BoneKEy Rep.*, 4, 2015.

A. M. Ashique, L. S. Hart, C. D. L. Thomas, J. G. Clement, P. Pivonka, Y. Carter, D. D. Mousseau, and D. M. L. Cooper. "Lacunar-canalicular network in femoral cortical bone is reduced in aged women and is predominantly due to a loss of canalicular porosity," *Bone Rep.*, 7, 9–16, 2017.

F. L. Bach-Gansmo, A. Brüel, M. V. Jensen, E. N. Ebbesen, H. Birkedal, and J. S. Thomsen. "Osteocyte lacunar properties and cortical microstructure in human iliac crest as a function of age and sex," *Bone*, 91, 11–19, 2016.

F. L. Bach-Gansmo, J. C. Weaver, M. H. Jensen, H. Leemreize, K. S. Mader, M. Stampanoni, A. Brüel, J. S. Thomsen, and H. Birkedal. "Osteocyte lacunar properties in rat cortical bone: Differences between lamellar and central bone," *J. Struct. Biol.*, 191(1), 59–67, 2015.

F. L. Bach-Gansmo, N. K. Wittig, A. Brüel, J. S. Thomsen, and H. Birkedal. "Immobilization and long-term recovery results in large changes in bone structure and strength but no corresponding alterations of osteocyte lacunar properties," *Bone*, 91, 139–147, 2016.

A. Balles, S. Zabler, T. Ebensperger, C. Fella, and R. Hanke. "Propagator based formalism for optimizing in-line phase contrast imaging in laboratory X-ray setups," *Rev. Sci. Instrum.*, 87(9), 093707, 2016.

R. Barrett, R. Baker, P. Cloetens, C. Morawe, R. Tucoulou, and A. Vivo. "Reflective Optics for Hard X-ray Nanofocusing Applications at the ESRF," *Synchrotron Radiat. News*, 29(4), 10–15, 2016.

M. A. Beltran, D. M. Paganin, K. Uesugi, and M. J. Kitchen. "2D and 3D X-ray phase retrieval of multi-material objects using a single defocus distance," *Opt. Express*, 18(7), 6423, 2010.

J. C. Biasci, J. F. Bouteille, N. Carmignani, J. Chavanne, D. Coulon, Y. Dabin, F. Ewald, L. Farvacque, L. Goirand, M. Hahn, J. Jacob, G. LeBec, S. Liuzzo, B. Nash, H. Pedroso-Marques, T. Perron, E. Plouviez, P. Raimondi, J. L. Revol, K. Scheidt, and V. Serrière. "A Low-Emittance Lattice for the ESRF," *Synchrotron Radiat. News*, 27(6), 8–12, 2014.

R. Boistel, T. Aubin, P. Cloetens, F. Peyrin, T. Scotti, P. Herzog, J. Gerlach, N. Pollet, and J.-F. Aubry. "How minute sooglossid frogs hear without a middle ear," *Proc. Natl. Acad. Sci.*, 110(38), 15360–15364, 2013.

L. F. Bonewald. "The amazing osteocyte," *J. Bone Miner. Res.*, 26(2), 229–238, 2011.

U. Bonse and M. Hart. "An X-ray interferometer," *Appl. Phys. Lett.*, 6(8), 155–156, 1965.

M. N. Boone, W. Devulder, M. Dierick, L. Brabant, E. Pauwels, and L. Van Hoorebeke. "Comparison of two single-image phase-retrieval algorithms for in-line x-ray phase-contrast imaging," *J. Opt. Soc. Am. A*, 29(12), 2667, 2012.

C. B. Bozal, L. M. Sánchez, and A. M. Ubios. "The lacuno-canalicular system (LCS) and osteocyte network of alveolar bone by confocal laser scanning microscopy (CLSM).," *Acta Odontol. Latinoam. AOL*, 25(1), 123–131, 2011.

A. Bravin, P. Coan, and P. Suortti. "X-ray phase-contrast imaging: from pre-clinical applications towards clinics," *Phys. Med. Biol.*, 58(1), R1–R35, 2013.

G. R. Brock, G. Kim, A. R. Ingraffea, J. C. Andrews, P. Pianetta, and M. C. H. van der Meulen. "Nanoscale Examination of Microdamage in Sheep Cortical Bone Using Synchrotron Radiation Transmission X-Ray Microscopy," *PLoS ONE*, 8(3), e57942, 2013.

A. V. Bronnikov. "Theory of quantitative phase-contrast computed tomography," *J. Opt. Soc. Am. A*, 19(3), 472, 2002.

P. R. Buenzli and N. A. Sims. "Quantifying the osteocyte network in the human skeleton," *Bone*, 75, 144–150, 2015.

A. Burvall, U. Lundström, P. A. C. Takman, D. H. Larsson, and H. M. Hertz. "Phase retrieval in X-ray phase-contrast imaging suitable for tomography," *Opt. Express*, 19(11), 10359, 2011.

B. Busse, D. Djonic, P. Milovanovic, M. Hahn, K. Püschel, R. O. Ritchie, M. Djuric, and M. Amling. "Decrease in the osteocyte lacunar density accompanied by hypermineralized lacunar occlusion reveals failure and delay of remodeling in aged human bone: Osteocyte lacunar density and composition in aging," *Aging Cell*, 9(6), 1065–1075, 2010.

X. Cai, L. Peralta, A. Giron, L. Helfen, C. Olivier, F. Peyrin, P. Laugier, and Q. Grimal. "Cortical bone elasticity measured by resonant ultrasound spectroscopy is not altered by defatting and synchrotron X-ray imaging," *J. Mech. Behav. Biomed. Mater.*, 72, 241–245, 2017.

M. Capulli, R. Paone, and N. Rucci. "Osteoblast and osteocyte: Games without frontiers," *Arch. Biochem. Biophys.*, 561, 3–12, 2014.

A. J. Carroll, G. A. van Riessen, E. Balaur, I. P. Dolbnya, G. N. Tran, and A. G. Peele. "An iterative method for robust in-line phase contrast imaging," *New J. Phys.*, 18(4), 043003, 2016.

Y. Carter, C. D. L. Thomas, J. G. Clement, and D. M. L. Cooper. "Femoral osteocyte lacunar density, volume and morphology in women across the lifespan," *J. Struct. Biol.*, 183(3), 519–526, 2013.

Y. Carter, C. D. L. Thomas, J. G. Clement, A. G. Peele, K. Hannah, and D. M. L. Cooper. "Variation in osteocyte lacunar morphology and density in the human femur — a synchrotron radiation micro-CT study," *Bone*, 52(1), 126–132, 2013.

H. A. Castillo-Michel, C. Larue, A. E. Pradas del Real, M. Cotte, and G. Sarret. "Practical review on the use of synchrotron based micro- and nano- X-ray fluorescence mapping and X-ray absorption spectroscopy to investigate the interactions between plants and engineered nanomaterials," *Plant Physiol. Biochem.*, 110, 13–32, 2017.

J. Cesar da Silva, A. Pacureanu, Y. Yang, S. Bohic, C. Morawe, R. Barrett, and P. Cloetens. "Efficient concentration of high-energy x-rays for diffraction-limited imaging resolution," *Optica*, 4(5), 492, 2017.

T. F. Chan and L. A. Vese. "Active contours without edges," *IEEE Trans. Image Process.*, 10(2), 266–277, 2001.

A. Ciani, M. Guizar-Sicairos, A. Diaz, M. Holler, S. Pallu, Z. Achiou, R. Jennane, H. Toumi, E. Lespessailles, and C. M. Kewish. "Segmentation of nanotomographic cortical bone images for quantitative characterization of the osteoctyte lacuno-canalicular network," in p. 020040, 2016.

P. Cloetens, W. Ludwig, J. Baruchel, D. Van Dyck, J. Van Landuyt, J. P. Guigay, and M. Schlenker. "Holotomography: Quantitative phase tomography with micrometer resolution using hard synchrotron radiation x rays," *Appl. Phys. Lett.*, 75(19), 2912, 1999.

P. Cloetens, M. Pateyron-Salomé, J. Y. Buffière, G. Peix, J. Baruchel, F. Peyrin, and M. Schlenker. "Observation of microstructure and damage in materials by phase sensitive radiography and tomography," *J. Appl. Phys.*, 81(9), 5878–5886, 1997.

C. Colnot. "Skeletal Cell Fate Decisions Within Periosteum and Bone Marrow During Bone Regeneration," *J. Bone Miner. Res.*, 24(2), 274–282, 2009.

M.-E. Couprie and J.-M. Filhol. "X radiation sources based on accelerators," *Comptes Rendus Phys.*, 9(5)–(6), 487–506, 2008.

M. E. Couprie. "New generation of light sources: Present and future," *J. Electron Spectrosc. Relat. Phenom.*, 196, 3–13, 2014.

Y. H. Dai and Y. Yuan. "A Nonlinear Conjugate Gradient Method with a Strong Global Convergence Property," *SIAM J. Optim.*, 10(1), 177–182, 1999.

N. K. H. Dalasm, T. Kotaka, Y. Tabuchi, and U. Pasaogullari. "A Comparison of Laboratory Based and Synchrotron Based Nano X-ray CT for PEFC Micro Porous Layer," *ECS Trans.*, 58(1), 345–352, 2013.

S. L. Dallas, M. Prideaux, and L. F. Bonewald. "The Osteocyte: An Endocrine Cell … and More," *Endocr. Rev.*, 34(5), 658–690, 2013.

M. Dierolf, A. Menzel, P. Thibault, P. Schneider, C. M. Kewish, R. Wepf, O. Bunk, and F. Pfeiffer. "Ptychographic X-ray computed tomography at the nanoscale," *Nature*, 467(7314), 436–439, 2010.

N. S. Dole, C. M. Mazur, C. Acevedo, J. P. Lopez, D. A. Monteiro, T. W. Fowler, B. Gludovatz, F. Walsh, J. N. Regan, S. Messina, D. S. Evans, T. F. Lang, B. Zhang, R. O. Ritchie, K. S. Mohammad, and T. Alliston. "Osteocyte-Intrinsic TGF-β Signaling Regulates Bone Quality through Perilacunar/Canalicular Remodeling," *Cell Rep.*, 21(9), 2585–2596, 2017.

P. Dong, S. Haupert, B. Hesse, M. Langer, P.-J. Gouttenoire, V. Bousson, and F. Peyrin. "3D osteocyte lacunar morphometric properties and distributions in human femoral cortical bone using synchrotron radiation micro-CT images," *Bone*, 60, 172–185, 2014.

P. Dong, A. Pacureanu, M. A. Zuluaga, C. Olivier, Q. Grimal, and F. Peyrin. "Quantification of the 3D morphology of the bone cell network from synchrotron micro-CT images," *Image Anal. Stereol.*, 33(2), 157, 2014.

N. Eliaz and N. Metoki. "Calcium Phosphate Bioceramics: A Review of Their History, Structure, Properties, Coating Technologies and Biomedical Applications," *Materials*, 10(4), 334, 2017.

M. Fakhry. "Molecular mechanisms of mesenchymal stem cell differentiation towards osteoblasts," *World J. Stem Cells*, 5(4), 136, 2013.

R. Fletcher. "Function minimization by conjugate gradients," *Comput. J.*, 7(2), 149–154, 1964.

R. Florencio-Silva, G. R. da S. Sasso, E. Sasso-Cerri, M. J. Simões, and P. S. Cerri. "Biology of Bone Tissue: Structure, Function, and Factors That Influence Bone Cells," *BioMed Res. Int.*, 2015, 1–17, 2015.

J. Flusser, T. Suk, and B. Zitov. Moments and Moment Invariants in Pattern Recognition, *J. Wiley*, 2009.

H. Fonseca, D. Moreira-Gonçalves, H.-J. A. Coriolano, and J. A. Duarte. "Bone Quality: The Determinants of Bone Strength and Fragility," *Sports Med.*, 44(1), 37–53, 2014.

H. Foroosh, J. B. Zerubia, and M. Berthod. "Extension of phase correlation to subpixel registration," *IEEE Trans. Image Process.*, 11(3), 188–200, 2002.

P. Fratzl and R. Weinkamer. "Nature’s hierarchical materials," *Prog. Mater. Sci.*, 52(8), 1263–1334, 2007.

H. Fujita. "Ultra-high voltage electron microscopy: Past, present, and future," *J. Electron Microsc. Tech.*, 3(3), 243–304, 1986.

K. Fulzele, F. Lai, C. Dedic, V. Saini, Y. Uda, C. Shi, P. Tuck, J. L. Aronson, X. Liu, J. M. Spatz, M. N. Wein, and P. Divieti Pajevic. "Osteocyte-secreted Wnt signaling inhibitor sclerostin contributes to beige adipogenesis in peripheral fat depots," *J. Bone Miner. Res.*, 32(2), 373–384, 2017.

V. Gatti, E. M. Azoulay, and S. P. Fritton. "Microstructural changes associated with osteoporosis negatively affect loading-induced fluid flow around osteocytes in cortical bone," *J. Biomech.*, 66, 127–136, 2018.

R. Genthial, E. Beaurepaire, M.-C. Schanne-Klein, F. Peyrin, D. Farlay, C. Olivier, Y. Bala, G. Boivin, J.-C. Vial, D. Débarre, and A. Gourrier. "Label-free imaging of bone multiscale porosity and interfaces using third-harmonic generation microscopy," *Sci. Rep.*, 7(1), 2017.

P. M. Goggin, K. C. Zygalakis, R. O. Oreffo, and P. Schneider. "High-resolution 3D imaging of osteocytes and computational modelling in mechanobiology: insights on bone development, ageing, health and disease.," *Eur. Cell. Mater.*, 31, 264, 2016.

J. W. Goodman. Introduction to Fourier Optics, 3rd ed, *Roberts & Co*, 2005.

J. P. Guigay, M. Langer, R. Boistel, and P. Cloetens. "Mixed transfer function and transport of intensity approach for phase retrieval in the Fresnel region," *Opt. Lett.*, 32(12), 1617, 2007.

T. E. Gureyev, Y. I. Nesterets, A. Kozlov, D. M. Paganin, and H. M. Quiney. "On the “unreasonable” effectiveness of transport of intensity imaging and optical deconvolution," *J. Opt. Soc. Am. A*, 34(12), 2251, 2017.

D. J. Hadjidakis and I. I. Androulakis. "Bone Remodeling," *Ann. N. Y. Acad. Sci.*, 1092(1), 385–396, 2006.

C. K. Hagen, P. Maghsoudlou, G. Totonelli, P. C. Diemoz, M. Endrizzi, L. Rigon, R.-H. Menk, F. Arfelli, D. Dreossi, E. Brun, P. Coan, A. Bravin, P. De Coppi, and A. Olivo. "High contrast microstructural visualization of natural acellular matrices by means of phase-based x-ray tomography," *Sci. Rep.*, 5, 18156, 2015.

T. Hasegawa, T. Yamamoto, H. Hongo, Z. Qiu, M. Abe, T. Kanesaki, K. Tanaka, T. Endo, P. H. L. de Freitas, M. Li, and N. Amizuka. "Three-dimensional ultrastructure of osteocytes assessed by focused ion beam-scanning electron microscopy (FIB-SEM)," *Histochem. Cell Biol.*, 2018.

J. Haubrich, G. Requena, J. C. da Silva, P. Cloetens, A. Pacureanu, L. Bloch, Y. Yang, and M. Hubert. "High energy near- and far-field ptychographic tomography at the ESRF," in B. Müller and G. Wang, eds., SPIE, p. 5, 2017.

H. Hemmatian, M. R. Laurent, S. Ghazanfari, D. Vanderschueren, A. D. Bakker, J. Klein-Nulend, and G. H. van Lenthe. "Accuracy and reproducibility of mouse cortical bone microporosity as quantified by desktop microcomputed tomography," *PLOS ONE*, 12(8), e0182996, 2017.

E. Hernlund, A. Svedbom, M. Ivergård, J. Compston, C. Cooper, J. Stenmark, E. V. McCloskey, B. Jönsson, and J. A. Kanis. "Osteoporosis in the European Union: medical management, epidemiology and economic burden: A report prepared in collaboration with the International Osteoporosis Foundation (IOF) and the European Federation of Pharmaceutical Industry Associations (EFPIA)," *Arch. Osteoporos.*, 8(1)–(2), 2013.

B. Hesse, P. Varga, M. Langer, A. Pacureanu, S. Schrof, N. Männicke, H. Suhonen, P. Maurer, P. Cloetens, F. Peyrin, and K. Raum. "Canalicular Network Morphology Is the Major Determinant of the Spatial Distribution of Mass Density in Human Bone Tissue: Evidence by Means of Synchrotron Radiation Phase-Contrast nano-CT," *J. Bone Miner. Res.*, 30(2), 346–356, 2015.

M. R. Hestenes and E. Stiefel. "Methods of conjugate gradients for solving linear systems," *J. Res. Natl. Bur. Stand.*, 49(6), 2379, 1952.

T. Hildebrand and P. RüEgsegger. "Quantification of Bone Microarchitecture with the Structure Model Index," *Comput. Methods Biomech. Biomed. Engin.*, 1(1), 15–23, 1997.

G. Holzer, G. von Skrbensky, L. A. Holzer, and W. Pichl. "Hip Fractures and the Contribution of Cortical Versus Trabecular Bone to Femoral Neck Strength," *J. Bone Miner. Res.*, 24(3), 468–474, 2009.

R. P. van Hove, P. A. Nolte, A. Vatsa, C. M. Semeins, P. L. Salmon, T. H. Smit, and J. Klein-Nulend. "Osteocyte morphology in human tibiae of different bone pathologies with different bone mineral density — Is there a role for mechanosensing?," *Bone*, 45(2), 321–329, 2009.

S. Jehan-Besson, M. Barlaud, and G. Aubert. "DREAM2S: Deformable Regions Driven by an Eulerian Accurate Minimization Method for Image and Video Segmentation," *Int. J. Comput. Vis.*, 53(1), 45–70, 2003.

R. L. Jilka and C. A. O'Brien. "The Role of Osteocytes in Age-Related Bone Loss," *Curr. Osteoporos. Rep.*, 14(1), 16–25, 2016.

K. S. Joeng, Y.-C. Lee, J. Lim, Y. Chen, M.-M. Jiang, E. Munivez, C. Ambrose, and B. H. Lee. "Osteocyte-specific WNT1 regulates osteoblast function during bone homeostasis," *J. Clin. Invest.*, 127(7), 2678–2688, 2017.

A. Johannes, D. Salomon, G. Martinez-Criado, M. Glaser, A. Lugstein, and C. Ronning. "In operando x-ray imaging of nanoscale devices: Composition, valence, and internal electrical fields," *Sci. Adv.*, 3(12), eaao4044, 2017.

G. R. Jordan, N. Loveridge, J. Power, M. T. Clarke, M. Parker, and J. Reeve. "The Ratio of Osteocytic Incorporation to Bone Matrix Formation in Femoral Neck Cancellous Bone: An Enhanced Osteoblast Work Rate in the Vicinity of Hip Osteoarthritis," *Calcif. Tissue Int.*, 72(3), 190–196, 2003.

A. C. Kak and M. Slaney. Principles of Computerized Tomographic Imaging, *IEEE Press*, 1988.

H. Kamioka, T. Honjo, and T. Takano-Yamamoto. "A three-dimensional distribution of osteocyte processes revealed by the combination of confocal laser scanning microscopy and differential interference contrast microscopy," *Bone*, 28(2), 145–149, 2001.

H. Kamioka. "Osteocyte bioimaging," *J. Oral Biosci.*, 57(2), 61–64, 2015.

J. A. Kanis, N. C. Harvey, C. Cooper, H. Johansson, A. Odén, and E. V. McCloskey. "A systematic review of intervention thresholds based on FRAX: A report prepared for the National Osteoporosis Guideline Group and the International Osteoporosis Foundation," *Arch. Osteoporos.*, 11(1), 2016.

R. Karazija. Introduction to the Theory of X-Ray and Electronic Spectra of Free Atoms., *Springer-Verlag New York*, 2013.

O. L. Katsamenis, H. M. H. Chong, O. G. Andriotis, and P. J. Thurner. "Load-bearing in cortical bone microstructure: Selective stiffening and heterogeneous strain distribution at the lamellar level," *J. Mech. Behav. Biomed. Mater.*, 17, 152–165, 2013.

P. Ke, X.-N. Jiao, X.-H. Ge, W.-M. Xiao, and B. Yu. "From macro to micro: structural biomimetic materials by electrospinning," *RSC Adv*, 4(75), 39704–39724, 2014.

M. L. Knothe Tate, J. R. Adamson, A. E. Tami, and T. W. Bauer. "The osteocyte," *Int. J. Biochem. Cell Biol.*, 36(1), 1–8, 2004.

P. Kollmannsberger, M. Kerschnitzki, F. Repp, W. Wagermaier, R. Weinkamer, and P. Fratzl. "The small world of osteocytes: connectomics of the lacuno-canalicular network in bone," *New J. Phys.*, 19(7), 073019, 2017.

H. Komaba, J. Kaludjerovic, D. Z. Hu, K. Nagano, K. Amano, N. Ide, T. Sato, M. J. Densmore, J. Hanai, H. Olauson, T. Bellido, T. E. Larsson, R. Baron, and B. Lanske. "Klotho expression in osteocytes regulates bone metabolism and controls bone formation," *Kidney Int.*, 92(3), 599–611, 2017.

R. D. Kongskov, J. S. Jørgensen, H. F. Poulsen, and P. C. Hansen. "Noise robustness of a combined phase retrieval and reconstruction method for phase-contrast tomography," *J. Opt. Soc. Am. A*, 33(4), 447, 2016.

A. Kostenko, K. J. Batenburg, A. King, S. E. Offerman, and L. J. van Vliet. "Total variation minimization approach in in-line x-ray phase-contrast tomography," *Opt. Express*, 21(10), 12185, 2013.

M. Krenkel, A. Markus, M. Bartels, C. Dullin, F. Alves, and T. Salditt. "Phase-contrast zoom tomography reveals precise locations of macrophages in mouse lungs," *Sci. Rep.*, 5(1), 2015.

M. Krenkel, M. Toepperwien, F. Alves, and T. Salditt. "Three-dimensional single-cell imaging with X-ray waveguides in the holographic regime," *Acta Crystallogr. Sect. Found. Adv.*, 73(4), 282–292, 2017.

B. Laforce, S. Schmitz, B. Vekemans, J. Rudloff, J. Garrevoet, R. Tucoulou, F. E. Brenker, G. Martinez-Criado, and L. Vincze. "Nanoscopic X-ray Fluorescence Imaging of Meteoritic Particles and Diamond Inclusions," *Anal. Chem.*, 86(24), 12369–12374, 2014.

X. Lai, C. Price, S. Modla, W. R. Thompson, J. Caplan, C. B. Kirn-Safran, and L. Wang. "The dependences of osteocyte network on bone compartment, age, and disease," *Bone Res.*, 3, 2015.

M. Langer, P. Cloetens, J.-P. Guigay, and F. Peyrin. "Quantitative comparison of direct phase retrieval algorithms in in-line phase tomography," *Med. Phys.*, 35(10), 4556, 2008.

M. Langer, A. Pacureanu, H. Suhonen, Q. Grimal, P. Cloetens, and F. Peyrin. "X-Ray Phase Nanotomography Resolves the 3D Human Bone Ultrastructure," *PLoS ONE*, 7(8), e35691, 2012.

M. Langer, P. Cloetens, B. Hesse, H. Suhonen, A. Pacureanu, K. Raum, and F. Peyrin. "Priors for X-ray in-line phase tomography of heterogeneous objects," *Philos. Trans. R. Soc. Math. Phys. Eng. Sci.*, 372(2010), 20130129–20130129, 2014.

M. Langer, P. Cloetens, and F. Peyrin. "Regularization of Phase Retrieval With Phase-Attenuation Duality Prior for 3-D Holotomography," *IEEE Trans. Image Process.*, 19(9), 2428–2436, 2010.

P. T. Leali, C. D. FBSE, A. Zachos, A. Ruggiu, F. Milia, and F. Barca. "Bone fragility: current reviews and clinical features," *Clin. Cases Miner. Bone Metab.*, 6(2), 109, 2009.

Y. Lin and S. Xu. "AFM analysis of the lacunar-canalicular network in demineralized compact bone: AFM FOR 3D TISSUE NANOSTRUCTURE," *J. Microsc.*, 241(3), 291–302, 2011.

K. S. Mader, P. Schneider, R. Müller, and M. Stampanoni. "A quantitative framework for the 3D characterization of the osteocyte lacunar system," *Bone*, 57(1), 142–154, 2013.

M. Marenzana and T. R. Arnett. "The Key Role of the Blood Supply to Bone," *Bone Res.*, 1(3), 203–215, 2013.

E. N. Marieb and K. Hoehn. Human Anatomy & Physiology, *Pearson*, 2013.

E. N. Marieb and S. M. Keller. Essentials of Human Anatomy & Physiology, 2018.

M. Marinescu, M. Langer, A. Durand, C. Olivier, A. Chabrol, H. Rositi, F. Chauveau, T. H. Cho, N. Nighoghossian, Y. Berthezène, F. Peyrin, and M. Wiart. "Synchrotron Radiation X-Ray Phase Micro-computed Tomography as a New Method to Detect Iron Oxide Nanoparticles in the Brain," *Mol. Imaging Biol.*, 15(5), 552–559, 2013.

G. Marotti, M. Ferretti, F. Remaggi, and C. Palumbo. "Quantitative evaluation on osteocyte canalicular density in human secondary osteons," *Bone*, 16(1), 125–128, 1995.

G. Martínez-Criado, B. Alén, J. A. Sans, A. D. Lozano-Gorrín, P. Haro-González, I. R. Martín, and V. Lavín. "X-ray nanoimaging of Nd^3+ optically active ions embedded in Sr_05Ba_05Nb_2O_6 nanocrystals," *Opt. Mater. Express*, 7(7), 2424, 2017.

G. Martínez-Criado, J. Villanova, R. Tucoulou, D. Salomon, J.-P. Suuronen, S. Labouré, C. Guilloud, V. Valls, R. Barrett, E. Gagliardini, Y. Dabin, R. Baker, S. Bohic, C. Cohen, and J. Morse. "ID16B: a hard X-ray nanoprobe beamline at the ESRF for nano-analysis," *J. Synchrotron Radiat.*, 23(1), 344–352, 2016.

C. Menaa, N. Kurihara, and G. D. Roodman. "CFU-GM-Derived Cells Form Osteoclasts at a Very High Efficiency," *Biochem. Biophys. Res. Commun.*, 267(3), 943–946, 2000.

A. Mirone, E. Brun, E. Gouillart, P. Tafforeau, and J. Kieffer. "The PyHST2 hybrid distributed code for high speed tomographic reconstruction with iterative reconstruction and a priori knowledge capabilities," *Nucl. Instrum. Methods Phys. Res. Sect. B Beam Interact. Mater. At.*, 324, 41–48, 2014.

S. Mobilio, F. Boscherini, C. Meneghini, and Società Italiana Luce di Sincrotrone, eds. Synchrotron Radiation: Basics, Methods and Applications, *Springer*, 2015.

R. Mokso, P. Cloetens, E. Maire, W. Ludwig, and J.-Y. Buffière. "Nanoscale zoom tomography with hard x rays using Kirkpatrick-Baez optics," *Appl. Phys. Lett.*, 90(14), 144104, 2007.

A. Momose. "Phase-contrast radiographs of nonstained rat cerebellar specimen," *Med. Phys.*, 22(4), 375, 1995.

C. Morawe, R. Barrett, P. Cloetens, B. Lantelme, J.-C. Peffen, and A. Vivo. "Graded multilayers for figured Kirkpatrick-Baez mirrors on the new ESRF end station ID16A," in S. Goto, C. Morawe, and A. M. Khounsary, eds., p. 958803, 2015.

M. G. Mullender, D. D. van der Meer, R. Huiskes, and P. Lips. "Osteocyte density changes in aging and osteoporosis," *Bone*, 18(2), 109–113, 1996.

M. G. Mullender, S. D. Tan, L. Vico, C. Alexandre, and J. Klein-Nulend. "Differences in Osteocyte Density and Bone Histomorphometry Between Men and Women and Between Healthy and Osteoporotic Subjects," *Calcif. Tissue Int.*, 77(5), 291–296, 2005.

T. Nakashima, M. Hayashi, T. Fukunaga, K. Kurata, M. Oh-hora, J. Q. Feng, L. F. Bonewald, T. Kodama, A. Wutz, E. F. Wagner, J. M. Penninger, and H. Takayanagi. "Evidence for osteocyte regulation of bone homeostasis through RANKL expression," *Nat. Med.*, 17, 1231, 2011.

P. Narducci, R. Bortul, R. Bareggi, and V. Nicolin. "Clathrin-dependent endocytosis of membrane-bound RANKL in differentiated osteoclasts," *Eur. J. Histochem.*, 54(1), 6, 2010.

Y. I. Nesterets, S. W. Wilkins, T. E. Gureyev, A. Pogany, and A. W. Stevenson. "On the optimization of experimental parameters for x-ray in-line phase-contrast imaging," *Rev. Sci. Instrum.*, 76(9), 093706, 2005.

A. Odgaard. "Three-dimensional methods for quantification of cancellous bone architecture," *Bone*, 20(4), 315–328, 1997.

J. Ohser, W. Nagel, and K. Schladitz. "Miles formulae for Boolean models observed on lattices," *Image Anal. Stereol.*, 28(2), 77, 2009.

J. Ohser and K. Schladitz. 3D Images of Materials Structures: Processing and Analysis, *Wiley-VCH*, 2009.

S. . Olabarriaga, M. Breeuwer, and W. . Niessen. "Evaluation of Hessian-based filters to enhance the axis of coronary arteries in CT images," *Int. Congr. Ser.*, 1256, 1191–1196, 2003.

M. J. Olszta, X. Cheng, S. S. Jee, R. Kumar, Y.-Y. Kim, M. J. Kaufman, E. P. Douglas, and L. B. Gower. "Bone structure and formation: A new perspective," *Mater. Sci. Eng. R Rep.*, 58(3)–(5), 77–116, 2007.

A. Pacureanu. "Imaging the bone cell network with nanoscale synchrotron computed tomography," PhD Thesis, *INSA de Lyon*, 2012.

A. Pacureanu, M. Langer, E. Boller, P. Tafforeau, and F. Peyrin. "Nanoscale imaging of the bone cell network with synchrotron X-ray tomography: optimization of acquisition setup: Synchrotron x-ray tomography reveals the bone cell network," *Med. Phys.*, 39(4), 2229–2238, 2012.

A. Pacureanu, A. Larrue, Z. Peter, and F. Peyrin. "3D non-linear enhancement of tubular microscopic bone porosities," in *2009 IEEE International Symposium on Biomedical Imaging: From Nano to Macro*, IEEE, pp. 602–605, 2009.

A. Pacureanu, C. Revol-Muller, J.-L. Rose, M. S. Ruiz, and F. Peyrin. "Vesselness-guided variational segmentation of cellular networks from 3D micro-CT," in *Biomedical Imaging: From Nano to Macro, 2010 IEEE International Symposium on*, IEEE, pp. 912–915, 2010.

D. Paganin, S. C. Mayo, T. E. Gureyev, P. R. Miller, and S. W. Wilkins. "Simultaneous phase and amplitude extraction from a single defocused image of a homogeneous object," *J. Microsc.*, 206(1), 33–40, 2002.

D. Paganin and K. A. Nugent. "Noninterferometric Phase Imaging with Partially Coherent Light," *Phys. Rev. Lett.*, 80(12), 2586–2589, 1998.

P. E. Palacio-Mancheno, A. I. Larriera, S. B. Doty, L. Cardoso, and S. P. Fritton. "3D Assessment of Cortical Bone Porosity and Tissue Mineral Density Using High-Resolution µCT: Effects of Resolution and Threshold Method," *J. Bone Miner. Res.*, 29(1), 142–150, 2014.

C. Palumbo, M. Ferretti, A. Ardizzoni, D. Zaffe, and G. Marotti. "Osteocyte-osteoclast morphological relationships and the putative role of osteocytes in bone remodeling," *J Musculoskelet Neuronal Interact*, 1(4), 327–32, 2001.

F. Peyrin and K. Engelke. "CT Imaging: Basics and New Trends," in *Handbook of Particle Detection and Imaging*, C. Grupen and I. Buvat, eds., Springer Berlin Heidelberg, pp. 883–915, 2012.

R. J. Pignolo and M. A. Mukaddam. "Evaluation of Bone Fragility and Fracture Prevention," in *Fractures in the Elderly*, R. J. Pignolo and J. Ahn, eds., Springer International Publishing, pp. 285–301, 2018.

L. I. Plotkin. "Apoptotic Osteocytes and the Control of Targeted Bone Resorption," *Curr. Osteoporos. Rep.*, 12(1), 121–126, 2014.

E. Polak and G. Ribiere. "Note sur la convergence de méthodes de directions conjuguées," *Rev. Fr. Inform. Rech. Opérationnelle Sér. Rouge*, 3(1), 35–43, 1969.

S. Qiu, D. S. Rao, S. Palnitkar, and A. M. Parfitt. "Differences in osteocyte and lacunar density between Black and White American women," *Bone*, 38(1), 130–135, 2006.

P. Raimondi. "ESRF-EBS: The Extremely Brilliant Source Project," *Synchrotron Radiat. News*, 29(6), 8–15, 2016.

S. H. Ralston. "Bone structure and metabolism," *Medicine (Baltimore)*, 45(9), 560–564, 2017.

F. Rauch. "The brains of the bones: how osteocytes use WNT1 to control bone formation," *J. Clin. Invest.*, 127(7), 2539–2540, 2017.

F. Remaggi, V. Canè, C. Palumbo, and M. Ferretti. "Histomorphometric study on the osteocyte lacuno-canalicular network in animals of different species. I. Woven-fibered and parallel-fibered bones," *Ital. J. Anat. Embryol. Arch. Ital. Anat. Ed Embriologia*, 103(4), 145–155, 1998.

F. Repp, P. Kollmannsberger, A. Roschger, A. Berzlanovich, G. M. Gruber, P. Roschger, W. Wagermaier, and R. Weinkamer. "Coalignment of osteocyte canaliculi and collagen fibers in human osteonal bone," *J. Struct. Biol.*, 199(3), 177–186, 2017.

F. Repp, P. Kollmannsberger, A. Roschger, M. Kerschnitzki, A. Berzlanovich, G. M. Gruber, P. Roschger, W. Wagermaier, and R. Weinkamer. "Spatial heterogeneity in the canalicular density of the osteocyte network in human osteons," *Bone Rep.*, 6, 101–108, 2017.

J.-Y. Rho, L. Kuhn-Spearing, and P. Zioupos. "Mechanical properties and the hierarchical structure of bone," *Med. Eng. Phys.*, 20(2), 92–102, 1998.

M. S. del Rio and R. J. Dejus. "Status of XOP: an x-ray optics software toolkit," in *Optical Science and Technology, the SPIE 49th Annual Meeting*, International Society for Optics and Photonics, pp. 171–174, 2004.

G. Y. Rochefort, S. Pallu, and C. L. Benhamou. "Osteocyte: the unrecognized side of bone tissue," *Osteoporos. Int.*, 21(9), 1457–1469, 2010.

T. Rolvien, M. Krause, A. Jeschke, T. Yorgan, K. Püschel, T. Schinke, B. Busse, M. B. Demay, and M. Amling. "Vitamin D regulates osteocyte survival and perilacunar remodeling in human and murine bone," *Bone*, 103, 78–87, 2017.

J.-L. Rose, T. Grenier, C. Revol-Muller, and C. Odet. "Unifying variational approach and region growing segmentation," in *Signal Processing Conference, 2010 18th European*, IEEE, pp. 1781–1785, 2010.

M. A. Rubin and I. Jasiuk. "The TEM characterization of the lamellar structure of osteoporotic human trabecular bone," *Micron*, 36(7)–(8), 653–664, 2005.

P. Rüegsegger, B. Koller, and R. Müller. "A microtomographic system for the nondestructive evaluation of bone architecture," *Calcif. Tissue Int.*, 58(1), 24–29, 1996.

A. Ruhlandt, M. Krenkel, M. Bartels, and T. Salditt. "Three-dimensional phase retrieval in propagation-based phase-contrast imaging," *Phys. Rev. A*, 89(3), 2014.

M. Salomé, F. Peyrin, P. Cloetens, C. Odet, A.-M. Laval-Jeantet, J. Baruchel, and P. Spanne. "A synchrotron radiation microtomography system for the analysis of trabecular bone samples," *Med. Phys.*, 26(10), 2194–2204, 1999.

C. Sanchez-Cano, I. Romero-Canelón, Y. Yang, I. J. Hands-Portman, S. Bohic, P. Cloetens, and P. J. Sadler. "Synchrotron X-Ray Fluorescence Nanoprobe Reveals Target Sites for Organo-Osmium Complex in Human Ovarian Cancer Cells," *Chem. - Eur. J.*, 23(11), 2512–2516, 2017.

M. Sasaki, S. Kuroshima, Y. Aoki, N. Inaba, and T. Sawase. "Ultrastructural alterations of osteocyte morphology via loaded implants in rabbit tibiae," *J. Biomech.*, 48(15), 4130–4141, 2015.

Y. Sato, S. Nakajima, N. Shiraga, H. Atsumi, S. Yoshida, T. Koller, G. Gerig, and R. Kikinis. "Three-dimensional multi-scale line filter for segmentation and visualization of curvilinear structures in medical images," *Med. Image Anal.*, 2(2), 143–168, 1998.

M. Sayab, J.-P. Suuronen, F. Molnár, J. Villanova, A. Kallonen, H. O'Brien, R. Lahtinen, and M. Lehtonen. "Three-dimensional textural and quantitative analyses of orogenic gold at the nanoscale," *Geology*, 44(9), 739–742, 2016.

M. B. Schaffler, W.-Y. Cheung, R. Majeska, and O. Kennedy. "Osteocytes: Master Orchestrators of Bone," *Calcif. Tissue Int.*, 94(1), 5–24, 2014.

P. Schneider, M. Meier, R. Wepf, and R. Müller. "Towards quantitative 3D imaging of the osteocyte lacuno-canalicular network," *Bone*, 47(5), 848–858, 2010.

P. Schneider, M. Meier, R. Wepf, and R. Müller. "Serial FIB/SEM imaging for quantitative 3D assessment of the osteocyte lacuno-canalicular network," *Bone*, 49(2), 304–311, 2011.

P. Schöppe, C. S. Schnohr, M. Oertel, A. Kusch, A. Johannes, S. Eckner, M. Burghammer, G. Martínez-Criado, U. Reislöhner, and C. Ronning. "Improved Ga grading of sequentially produced $Cu(In,Ga)Se_2$ solar cells studied by high resolution X-ray fluorescence," *Appl. Phys. Lett.*, 106(1), 013909, 2015.

F. A. Shah, B. R. Johansson, P. Thomsen, and A. Palmquist. "Ultrastructural evaluation of shrinkage artefacts induced by fixatives and embedding resins on osteocyte processes and pericellular space dimensions: Ultrastructural Evaluation of Shrinkage Artefacts," *J. Biomed. Mater. Res. A*, 103(4), 1565–1576, 2015.

F. A. Shah and A. Palmquist. "Evidence that Osteocytes in Autogenous Bone Fragments can Repair Disrupted Canalicular Networks and Connect with Osteocytes in de novo Formed Bone on the Fragment Surface," *Calcif. Tissue Int.*, 101(3), 321–327, 2017.

F. A. Shah, A. Snis, A. Matic, P. Thomsen, and A. Palmquist. "3D printed Ti6Al4V implant surface promotes bone maturation and retains a higher density of less aged osteocytes at the bone-implant interface," *Acta Biomater.*, 30, 357–367, 2016.

F. Shapiro. "Cortical bone repair. The relationship of the lacunar-canalicular system and intercellular gap junctions to the repair process," *J. Bone Joint Surg. Am.*, 70(7), 1067–1081, 1988.

D. Sharma, C. Ciani, P. A. R. Marin, J. D. Levy, S. B. Doty, and S. P. Fritton. "Alterations in the osteocyte lacunar–canalicular microenvironment due to estrogen deficiency," *Bone*, 51(3), 488–497, 2012.

D. Sharma, A. I. Larriera, P. E. Palacio-Mancheno, V. Gatti, J. C. Fritton, T. G. Bromage, L. Cardoso, S. B. Doty, and S. P. Fritton. "The effects of estrogen deficiency on cortical bone microporosity and mineralization," *Bone*, 110, 1–10, 2018.

J. C. da Silva, A. Pacureanu, Y. Yang, F. Fus, M. Hubert, L. Bloch, M. Salome, S. Bohic, and P. Cloetens. "High-energy cryo x-ray nano-imaging at the ID16A beamline of ESRF," in B. Lai and A. Somogyi, eds., SPIE, p. 14, 2017.

V. Singh. General Anatomy, *ELSEVIER INDIA*, 2015.

H. A. Sissons, G. J. Kelman, L. Ling, G. Marotti, V. Cane, and M. A. Muglia. "A light and scanning electron microscopic study of osteocyte activity in calcium-deficient rats," *Calcif. Tissue Int.*, 46(1), 33–37, 1990.

Song Chun Zhu and A. Yuille. "Region competition: unifying snakes, region growing, and Bayes/MDL for multiband image segmentation," *IEEE Trans. Pattern Anal. Mach. Intell.*, 18(9), 884–900, 1996.

B. Subashi, D. S. Butt, F. Kamberi, G. Sinanaj, and Y. Bilushi. "Physical Activity Recommended for Osteoporosis Prevention," *Durreesamin J.*, 3(3), 2017.

Y. Sugawara, R. Ando, H. Kamioka, Y. Ishihara, T. Honjo, N. Kawanabe, H. Kurosaka, T. Takano-Yamamoto, and T. Yamashiro. "The Three-Dimensional Morphometry and Cell–Cell Communication of the Osteocyte Network in Chick and Mouse Embryonic Calvaria," *Calcif. Tissue Int.*, 88(5), 416–424, 2011.

R. Tannert, M. Schwan, A. Rege, M. Eggeler, J. C. da Silva, M. Bartsch, B. Milow, M. Itskov, and L. Ratke. "The three-dimensional structure of flexible resorcinol-formaldehyde aerogels investigated by means of holotomography," *J. Sol-Gel Sci. Technol.*, 84(3), 391–399, 2017.

M. R. Teague. "Irradiance moments: their propagation and use for unique retrieval of phase," *J. Opt. Soc. Am.*, 72(9), 1199, 1982.

A. Thiel, M. K. Reumann, A. Boskey, J. Wischmann, R. von Eisenhart-Rothe, and P. Mayer-Kuckuk. "Osteoblast migration in vertebrate bone: Osteoblast migration in vertebrate bone," *Biol. Rev.*, 93(1), 350–363, 2018.

J. Toriwaki and T. Yonekura. "Euler number and connectivity indexes of a three dimensional digital picture," *Forma*, 17(3), 183–209, 2002.

G. J. Tortora and B. Derrickson. Principles of Anatomy & Physiology, 13th ed, *Wiley*, 2012.

L. D. Turner, B. B. Dhal, J. P. Hayes, A. P. Mancuso, K. A. Nugent, D. Paterson, R. E. Scholten, C. Q. Tran, and A. G. Peele. "X-ray phase imaging: Demonstration of extended conditions with homogeneous objects," *Opt. Express*, 12(13), 2960, 2004.

M. Ullherr and S. Zabler. "Correcting multi material artifacts from single material phase retrieved holo-tomograms with a simple 3D Fourier method," *Opt. Express*, 23(25), 32718, 2015.

M. Ullherr, A. Balles, C. Fella, and S. Zabler. "Using measurements of the spatial SNR to optimize phase contrast X-ray imaging," *Nucl. Instrum. Methods Phys. Res. Sect. Accel. Spectrometers Detect. Assoc. Equip.*, 877, 44–50, 2018.

P. Varga, B. Hesse, M. Langer, S. Schrof, N. Männicke, H. Suhonen, A. Pacureanu, D. Pahr, F. Peyrin, and K. Raum. "Synchrotron X-ray phase nano-tomography-based analysis of the lacunar–canalicular network morphology and its relation to the strains experienced by osteocytes in situ as predicted by case-specific finite element analysis," *Biomech. Model. Mechanobiol.*, 14(2), 267–282, 2015.

D. Vashishth, O. Verborgt, G. Divine, M. B. Schaffler, and D. P. Fyhrie. "Decline in osteocyte lacunar density in human cortical bone is associated with accumulation of microcracks with age," *Bone*, 26(4), 375–380, 2000.

L. Wang, Y. Wang, Y. Han, S. C. Henderson, R. J. Majeska, S. Weinbaum, and M. B. Schaffler. "In situ measurement of solute transport in the bone lacunar-canalicular system," *Proc. Natl. Acad. Sci.*, 102(33), 11911–11916, 2005.

Y. Wang, L. M. McNamara, M. B. Schaffler, and S. Weinbaum. "A model for the role of integrins in flow induced mechanotransduction in osteocytes," *Proc. Natl. Acad. Sci.*, 104(40), 15941–15946, 2007.

P. Willmott. An Introduction to Synchrotron Radiation: Techniques and Applications, *John Wiley*, 2011.

M. P. Yavropoulou and J. G. Yovos. "Osteoclastogenesis--current knowledge and future perspectives," *J. Musculoskelet. Neuronal Interact.*, 8(3), 204–216, 2008.

L.-D. You, S. Weinbaum, S. C. Cowin, and M. B. Schaffler. "Ultrastructure of the osteocyte process and its pericellular matrix," *Anat. Rec.*, 278A(2), 505–513, 2004.

B. Yu, L. Weber, A. Pacureanu, M. Langer, C. Olivier, P. Cloetens, and F. Peyrin. "Evaluation of phase retrieval approaches in magnified X-ray phase nano computerized tomography applied to bone tissue," *Opt. Express*, 26(9), 11110, 2018.

S. Zabler, P. Cloetens, J.-P. Guigay, J. Baruchel, and M. Schlenker. "Optimization of phase contrast imaging using hard x rays," *Rev. Sci. Instrum.*, 76(7), 073705, 2005.

R. M. Zebaze, A. Ghasem-Zadeh, A. Bohte, S. Iuliano-Burns, M. Mirams, R. I. Price, E. J. Mackie, and E. Seeman. "Intracortical remodelling and porosity in the distal radius and post-mortem femurs of women: a cross-sectional study," *The Lancet*, 375(9727), 1729–1736, 2010.

G. L. Zeng. Medical Image Reconstruction: A Conceptual Tutorial, *Higher Education Press*, 2010.

M. A. Zuluaga, M. Orkisz, P. Dong, A. Pacureanu, P.-J. Gouttenoire, and F. Peyrin. "Bone canalicular network segmentation in 3D nano-CT images through geodesic voting and image tessellation," *Phys. Med. Biol.*, 59(9), 2155–2171, 2014.

FOLIO ADMINISTRATIF

THESE DE L'UNIVERSITE DE LYON OPEREE AU SEIN DE L'INSA LYON

NOM : YU
(avec précision du nom de jeune fille, le cas échéant)

DATE de SOUTENANCE : 13/03/2019

Prénoms : Boliang

TITRE : 3D analysis of bone ultra structure from phase nano-CT imaging

NATURE : Doctorat

Numéro d'ordre : 2019LYSEI016

Ecole doctorale : E.E.A. (Électronique, Électrotechnique, Automatique)

Spécialité : Traitement du Signal et de l'Image

RESUME :

Osteoporosis is a bone fragility disease resulting in abnormalities in bone mass and density. In order to prevent osteoporotic fractures, it is important to have a better understanding of the processes involved in fracture at various scales. As the most abundant bone cells, osteocytes may act as orchestrators of bone remodeling which regulate the activities of both osteoclasts and osteoblasts. The osteocyte system is deeply embedded inside the bone matrix and also called lacuno-canalicular network (LCN). The network is organized as a complex mesh structure where lacunae serve as nodes housing the osteocytes connected with each other through processes included in the canaliculi. Although several imaging techniques have recently been proposed, the 3D observation and analysis of the LCN at high spatial resolution is still challenging.

The aim of this work was to investigate and analyze the LCN in human cortical bone in three dimensions with an isotropic spatial resolution using magnified X-ray phase nano-CT. We performed image acquisition at different voxel sizes of 120 nm, 100 nm, 50 nm and 30 nm in the beamlines ID16A and ID16B of the European Synchrotron Radiation Facility (ESRF). Our first study concerned phase retrieval, which is the first step of data processing and consists in solving a non-linear inverse problem. We proposed an extension of Paganin's method suited to multi-distance acquisitions, which has been used to retrieve phase maps in our experiments. The method was compared theoretically and experimentally to the contrast transfer function (CTF) approach for homogeneous object.

The analysis of the 3D reconstructed images requires first to segment the LCN, including both the segmentation of lacunae and of canaliculi. We developed a workflow based on median filter, hysteresis thresholding and morphology filters to segment lacunae. Concerning the segmentation of canaliculi, we made use of the vesselness enhancement to improve the visibility of line structures, the variational region growing to extract canaliculi and connected components analysis to remove residual noise.

For the quantitative assessment of the LCN, we calculated morphological descriptors based on an automatic and efficient 3D analysis method developed in our group. For the lacunae, we calculated some parameters like the number of lacunae, the bone volume, the total volume of all lacunae, the lacunar volume density, the average lacunae volume, the average lacunae surface, the average length, width and depth of lacunae. For the canaliculi, we first computed the total volume of all the canaliculi and canalicular volume density. Moreover, we counted the number of canaliculi at different distances from the surface of each lacuna by an automatic method, which could be used to evaluate the ramification of canaliculi. We reported the statistical results obtained on the different groups and at different spatial resolutions, providing unique information about the organization of the LCN in human bone in three dimensions.

MOTS-CLÉS : X-ray imaging, phase contrast, computed tomography, phase nano-CT, bone, phase retrieval, tomographic reconstruction, quantitative analysis.

Laboratoire (s) de recherche : Centre de Recherche en Acquisition et Traitement de l'Image pour la Santé (CREATIS), CNRS UMR 5220, INSERM U1206.

Directeur de thèse: PEYRIN Françoise

Président de jury : LAUGIER Pascal

Composition du jury : ROUSSEAU David (Rapporteur), VAN LENTHE Harry (Rapporteur), VICO Laurence (Examinateur), LAUGIER Pascal (Examinateur), GOURRIER Aurelien (Examinateur), CLOETENS Peter (Examinateur), PEYRIN Françoise (Directrice de thèse)